UCLA-ENG-7537
AUGUST 1975

FINAL REPORT

Prepared for
Department of the Navy
Naval Air Systems Command

AN EXPERIMENTAL STUDY ON THE COMPRESSIVE BIAXIAL STRENGTH OF CERAMICS

M. ADAMS
G. SINES

Contract No. N00019-73-C-0294 Mod. P00004

UCLA • SCHOOL OF ENGINEERING AND APPLIED SCIENCE

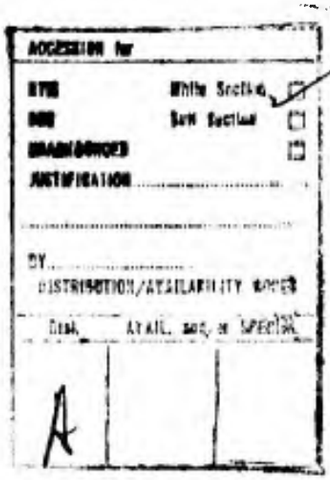
ACCESSION for
NTIS
White Section
DDC
Buff Section
UNANNOUNCED
JUSTIFICATION
BY
DISTRIBUTION/AVAILABILITY CODES
Dist. AVAIL. and/or SPECIAL
A

SECURITY CLASSIFICATION OF THIS PAGE (When Data Entered)

REPORT DOCUMENTATION PAGE

READ INSTRUCTIONS BEFORE COMPLETING FORM

1. REPORT NUMBER: UCLA-ENG-7537	2. GOVT ACCESSION NO.
3. RECIPIENT'S CATALOG NUMBER	
4. TITLE (and Subtitle): An Experimental Study on the Compressive Biaxial Strength of Ceramics.	5. TYPE OF REPORT & PERIOD COVERED: FINAL REPORT, 10 Oct 1970 to 31 Jul 1975
	6. PERFORMING ORG. REPORT NUMBER
7. AUTHOR(s): Marc Adams and George Sines	8. CONTRACT OR GRANT NUMBER(s): N00019-73-C-0294 Mod P00004; N00019-73-C-0294, N00019-72-C-0159, N00019-71-C-0178
9. PERFORMING ORGANIZATION NAME AND ADDRESS: UCLA School of Engineering	10. PROGRAM ELEMENT, PROJECT, TASK AREA & WORK UNIT NUMBERS: 299p.
11. CONTROLLING OFFICE NAME AND ADDRESS	12. REPORT DATE: August 1975
	13. NUMBER OF PAGES
14. MONITORING AGENCY NAME & ADDRESS (if different from Controlling Office): Naval Air Systems Command, Department of the Navy, Washington, D.C. 20360	15. SECURITY CLASS. (of this report): Unclassified
	15a. DECLASSIFICATION/DOWNGRADING SCHEDULE

16. DISTRIBUTION STATEMENT (of this Report)

Approved for public release; distribution unlimited

17. DISTRIBUTION STATEMENT (of the abstract entered in Block 20, if different from Report)

18. SUPPLEMENTARY NOTES

19. KEY WORDS (Continue on reverse side if necessary and identify by block number)

Ceramics	Compression Testing	Flaw Statistics	Crack Initiation
Biaxial Strength	Compressive Strength	Brittle Materials	Crack Propagation
Alumina	Compressive Failure	Fracture	Flaws

20. ABSTRACT (Continue on reverse side if necessary and identify by block number)

A mechanical testing program in which the biaxial compressive strength of WESGO AL-995, high strength alumina was measured has shown that the biaxial compressive strength of such material is only slightly affected by the value of the intermediate principal compressive stress. The average value of the compressive strengths measured in all stress states, excluding the equi-biaxial compression stress state, was 528 ksi. The standard deviation of the individual measured strengths was only a few percent of the average values which is consistent with the predictions of flaw statistics theories. The tensile strengths

DD FORM 1 JAN 73 1473 EDITION OF 1 NOV 65 IS OBSOLETE S/N 0102-LF 014-6601

Unclassified

SECURITY CLASSIFICATION OF THIS PAGE (When Data Entered)

406 237

measured for the material indicate the ratio of compressive strength to tensile strength is approximately 18. The design and operation of the various testing devices employed is described. Problems were encountered in the equi-biaxial compression stress state tests. These problems and the general problem of performing valid compressive strength measurements are discussed.

It is suggested that the compressive strength of a material is limited by the amount of crack damage which may be sustained in the material without structural collapse occurring. This crack damage is created in the body by cracks extending stably from an increasing number of flaws as the imposed compressive loads are increased. The nature of this crack damage has been characterized for the alumina test specimens by use of a replicating technique which permitted quantitative evaluation of the spalling phenomenon that occurs on the inside surface of the test section. These studies revealed that crack extension from flaws begins to occur at compressive stress levels approximately one quarter of those required to cause compressive failure. The characteristics of this crack damage were evaluated as a function of the applied stress levels up to failure. The particular kind of crack damage produced in the specimen under the stressing conditions imposed is described and related to a structural collapse mechanism.

The general aspects of compressive failure are presented which include a description of the micromechanical mechanisms of crack initiation and extension that can operate in a body subjected to purely compressive loading. Three types of flaws are identified which can initiate cracks. The problem of describing crack initiation and extension in three dimensions is addressed. The results of experimental studies of crack extension from three-dimensional, penny-shaped flaws introduced into blocks of polymethylmethacrylate plastic are presented. These studies indicate crack extension from three-dimensional flaws is more complex than current two-dimensional theories indicate. It is shown that establishing the three-dimensional character of the crack damage produced in a body is necessary to adequately describe compressive failure.

A general theory of compressive failure is presented in terms of functional relationships. Compressive strength criteria must be expressed in terms of a "critical damage figure" produced in the material which results in structural collapse. Theories describing crack initiation at flaws were found to provide only a first step in defining the multiple processes which operate in a compressively loaded body before structural collapse. It became apparent that an understanding of the densities, extended lengths and orientations of cracks produced in the body would be critical to a determination of the extent of the damage.

UCLA-ENG-7537
August 1975

FINAL REPORT

on

AN EXPERIMENTAL STUDY ON THE COMPRESSIVE BIAXIAL STRENGTH OF CERAMICS

by

Marc Adams

George Sines

Prepared under Contract No. N00019-73-C-0294 Mod. P00004

for

Naval Air Systems Command
Department of the Navy

MATERIALS DEPARTMENT
School of Engineering and Applied Science
University of California
Los Angeles, California

FOREWORD

This work was performed by the Materials Department, School of Engineering and Applied Science, University of California, Los Angeles, California under Contracts Numbered N00019-71-C-0178, N00019-72-C-0159, N00019-73-C-0294, and N00019-73-C-294 Mod. P00004 with the U. S. Department of the Navy. The work was administered under the direction of the Naval Air Systems Command. Mr. Charles Bersch was the project monitor.

This final report describes the work conducted between 10 October 1970 and 31 July 1975. Personnel responsible for carrying out the research were George Sines and Marc Adams. The manuscript was released by the authors August 1975 for publication as the Final Contract Report.

This research is continuing under NSF sponsorship.

ABSTRACT

A mechanical testing program in which the biaxial compressive strength of WESGO AL-995, high strength alumina was measured has shown that the biaxial compressive strength of such material is only slightly affected by the value of the intermediate principal compressive stress. The average value of the compressive strengths measured in all stress states, excluding the equi-biaxial compression stress state, was 528 ksi. The standard deviation of the individual measured strengths was only a few percent of the average values which is consistent with the predictions of flaw statistics theories. The tensile strengths measured for the material indicate the ratio of compressive strength to tensile strength is approximately 18. The design and operation of the various testing devices employed is described. Problems were encountered in the equi-biaxial compression stress state tests. These problems and the general problem of performing valid compressive strength measurements are discussed.

It is suggested that the compressive strength of a material is limited by the amount of crack damage which may be sustained in the material without structural collapse occurring. This crack damage is created in the body by cracks extending stably from an increasing number of flaws as the imposed compressive loads are increased. The nature of this crack damage has been characterized for the alumina test specimens by use of a replicating technique which permitted quantitative evaluation of the spalling phenomenon that occurs on the inside surface of the test section. These studies revealed that crack

extension from flaws begins to occur at compressive stress levels approximately one quarter of those required to cause compressive failure. The characteristics of this crack damage were evaluated as a function of the applied stress levels up to failure. The particular kind of crack damage produced in the specimen under the stressing conditions imposed is described and related to a structural collapse mechanism.

The general aspects of compressive failure are presented which include a description of the micromechanical mechanisms of crack initiation and extension that can operate in a body subjected to purely compressive loading. Three types of flaws are identified which can initiate cracks. The problem of describing crack initiation and extension in three dimensions is addressed. The results of experimental studies of crack extension from three-dimensional, penny-shaped flaws introduced into blocks of polymethylmethacrylate plastic are presented. These studies indicate crack extension from three-dimensional flaws is more complex than current two-dimensional theories indicate. It is shown that establishing the three-dimensional character of the crack damage produced in a body is necessary to adequately describe compressive failure.

A general theory of compressive failure is presented in terms of functional relationships. Compressive strength criteria must be expressed in terms of a "critical damage figure" produced in the material which results in structural collapse. Theories describing crack initiation at flaws were found to provide only a first step in defining the multiple processes which operate in a compressively loaded body before structural collapse. It became apparent that an understanding of the densities, extended lengths and orientations of cracks produced in the would be critical to a determination of the extent of the damage.

TABLE OF CONTENTS

CHAPTERS

FIGURES

FIGURES (Cont'd)

FIGURES (Cont'd)

FIGURES (Cont'd)

TABLES

CHAPTER I

INTRODUCTION

There is increasing interest in the accurate determination of the strength of brittle ceramics under compressive stresses, both to enable theoreticians to construct a realistic theory of strength and to provide design information for the optimum use of these materials as load bearing elements. The scope of application of high density, high strength brittle materials as structural elements is increasing rapidly. Materials such as alumina, silicon carbide and silicon nitride are being used in applications where their corrosion resistance, strength at high temperature, light weight, and very high compressive strength can be used to advantage. Potential design applications include biaxially prestressed hypersonic airfoils,[1,2] tiled domed structures beneath the sea,[3] and ceramic turbine engine components.[4,5]

In many applications of these materials as structural, load carrying elements the stress state encountered is more complex than simple uniaxial loading. This situation may arise though intent, as in the biaxial compressive preloading of panels which are to be put into bending, or because specification of even the minimum, unavoidable, dimensional tolerances in the design of a structure can still produce eccentricities or non-uniformities in loading that result in a stress state more complex than the uniaxial one intended. A biaxial stress state is the common one attained in the structural applications of these materials, especially in high temperature applications where thermal stresses are induced. Often failure is from "thermal shock," that is the failure which occurs when the stresses caused by thermal

gradients exceed the material's strength. Numerical analysis is improving so that the stress distribution can be computed with increasing accuracy, but seldom is the strength known to a corresponding accuracy. The critical thermal stresses are often biaxial and little data exists for the biaxial strength of brittle materials.

Even at temperatures of 600-800°C no plastic flow occurs in brittle materials such as alumina to relieve local stress concentrations; consequently, mechanical testing of these materials or design with them is very difficult. Inadvertent, localized high stresses cannot be relieved by plastic flow, and such stresses can cause fracture and failure of the material at values of the gross section stress considerably lower than the actual strength of the material. The extremely high stresses required to break materials like alumina in compression (greater than 500,000 psi) create considerable problems in the design of testing devices and specimens to insure failure of the material in the desired compression stress state. The design of such devices can become quite complex. For these reasons, and because only recently has there been interest in high strength, high performance ceramics, there exists a lack of reliable data on compressive strength for such brittle materials.

Relatively few measurements of compressive strengths have been made. Some of these data are suspect because the unusual difficulty of designing the specimen and loading device to attain the desired stress state may not have been recognized. Failure strengths in the tension-tension and tension-compression quadrants of biaxial stress space have been studied more extensively for various brittle materials,[6-9]

and theories of strength[10-13] have been advanced to explain the observed strengths. The predictions of these theories are successful within their regions of application. The compression-compression biaxial stress quadrant has not been as thoroughly investigated. Since many engineering applications of these materials involve biaxial compressive stress states, there is a need for the accurate determination of the failure envelope for high strength brittle materials in this stress quadrant.

Testing brittle materials is difficult because an inadvertent, localized high stress can cause fracture of the test specimen, thereby giving a false, low value for the strength. Some sources of inadvertent stresses for an axially, compressively loaded specimen are the disparities on the surfaces of the specimen's ends which contact the loading block of the testing machine, and stress concentrations at the transition from the butt section either from too small a radius or lack of smoothness at the point of tangency.

Also care must be taken that bending stresses are not inadvertently introduced.[14] When the loading blocks are rigidly guided to prevent rotation, their surfaces must be parallel and the ends of the specimens equally so. A very small deviation from being parallel can cause bending so that premature failure is caused by the added compressive stress or the bending can easily be great enough to cause a net tensile stress and premature failure from it.

One method used to prevent the application of bending moments is to abandon the precisely guided parallel surfaces and use a flexible load train. This can be accomplished by a spherical joint; however,

such a joint is usually made completely ineffective by friction between the mating surfaces. Therefore, the surfaces must be separated by a pressurized fluid layer.[15] An air bearing has been developed and successfully used,[16] but it is a rather complicated device. Another approach that removes many of the complications is to use a long load train and to replace the bearing by knife edges.[17] The knife edges could be replaced by flexure plates in order to increase the capacity and still retain the benefits of the flexible load train.

Although the load train may be completely flexible, a moment can be applied to the test section if the line of load is not concentric with the axis of the test section. A surprisingly small eccentricity can cause significant bending stress. Concentricity can be assured by careful gaging. Fortunately, electric resistance strain gages can be used to measure the stresses and until one is convinced that the apparatus and techniques successfully eliminate bending, each specimen should have a minimum of three equally spaced, longitudinally oriented, strain gages measuring the stress in the test section.

Most of the difficulties posed by the uniaxial loading of a brittle specimen with a reduced cross-section are avoided by the tensile ring and compressive ring tests developed by Sedlacek.[18-19] For the compressive test a uniform fluid pressure is applied to the external surface of a ring by a rubber bladder. The problems of sealing the ends and eliminating the longitudinal stress have been solved. In the ring tensile test, the fluid pressure is applied to the internal surface through a rubber bladder. Some of the advantages are - no intense localized stresses from the hard steel contacting disparities on the

specimen, no stress concentrations at fillets between the test section and loading area, and no possibility of eccentric loading or applied moments.

In the present study of biaxial compressive strength the specimen tested was a right, circular, cylindrical tube. The localized high stresses were avoided by loading in the radial direction by fluid pressure and in the axial direction by having the wall thickness at the ends three times thicker than at the test section. All mating surfaces were lapped together to eliminate disparities and to insure uniform loading over the circumference. The axiality of the loading was ensured by the radial tolerances on the specimens and in the end devices.

The specimen material was a high density, high purity, moderately fine-grained alumina designated by the manufacturer, Western Gold and Platinum Comp., as AL-995. This material was chosen because it has been tested extensively and is a candidate for several future applications. Its compressive strength behavior under polyaxial stresses should be similar to other high performance ceramics such as silicon nitride and silicon carbide.

The objectives of the mechanical testing program were to determine the compressive strength of the alumina material and to establish whether the magnitude of the intermediate principal compression affected the compressive strength measured in compressive biaxial stress states. During the program, strength measurements were made in the following stress states: 1:1, 1:0.8, 1:0.5, 1:0.1, 1:0.01 compression-compression and 1:0 uniaxial tension (the stress state is designated as $\sigma_{\theta\theta}$:σ_{zz} for cylindrical test specimen coordinates, where $\sigma_{\theta\theta}$ and σ_{zz} are principal

stresses). Since one of the major goals of the program was to establish whether the biaxial compressive strength is greater than the uniaxial compressive strength, the testing of identical specimens in each stress state was imperative. This was accomplished by using the same specimen geometry for every stress state and fabricating all specimens from the same lot of material. Thus, direct comparison of strengths in different stress states can be made without the possibility of an influence of specimen geometry, size, or processing history. A preliminary testing program was executed on a batch of six specimens with 1 inch test sections. All other tests were performed on one batch of specimens which had a 1/2 inch long test section.

The philosophy of the approach to compressive strength measurement was to determine the strength in each stress state by performing very careful tests on a small number of specimens. This is in contrast to the common approach used in testing brittle materials where large numbers of specimens are tested, perhaps not so carefully, and the data are then statistically analyzed to establish some average strength value. It was reasoned that statistical analysis of data from improperly executed tests would be less meaningful. The large standard deviations in the measured strengths which are obtained when brittle materials are tested in tension is attributable, in part, to imperfect testing techniques and, in part, to the sensitivity of the tensile strength of each specimen to minor variations in the distribution of worst flaws in the particular body of material. As will be discussed, in compressive strength tests of high quality ceramic the distribution of most severe flaws has little or no effect on the compressive strength.

This is so because a large portion of the flaws in the body are involved with crack initiation and extension before failure occurs. The shape of the entire flaw distribution curve is important, not just the worst flaws. Strength theories based on the statistics of flaws indicate that such a condition should result in only small strength variations between individual specimens. The nature of the total flaw distribution curve probably does not vary much in specimens fabricated from one lot of material; hence, it was considered that any but a small amount of scatter in the measured strengths would be attributable to improper testing techniques and not to variations in the compressive strength of individual specimens.

A satisfactory theory of compressive strength has not yet been proposed. Geologists studying the compressive failure of rock materials have determined that extensive crack damage is produced in such materials as the compressive load approaches that necessary to cause structural collapse of the body. This crack damage reduces the ability of the body to sustain additional increases in load. At some load, structural collapse of the weakened body occurs. A study was undertaken to determine whether such crack damage was produced in the high density alumina material tested in this study and how this damage might control the strength. The nature of the damage found to occur was characterized and its relationship to structural collapse of the specimen was identified.

The damage produced in the specimen is the result of crack propagation from flaws contained in the body under the action of the applied compressive stresses. Crack propagation from flaws contained in a

body subjected to compression is not well understood. Both theoretical and experimental studies were undertaken to obtain some idea of the nature of this phenomenon.

Combining the observations of this study with the experimental and theoretical results of other investigators, a coherent picture of the process of compressive failure was revealed. Large gaps exist in the understanding of individual mechanisms which comprise this process of failure but a qualitative description of the process is possible. This is presented as a general theory of compressive failure. It is discussed in terms of functional relationships some of which will require considerably better characterization in terms of specific materials before quantitative prediction of compressive strengths are possible.

A Road Map

Chapter II describes the testing concepts and design of the mechanical devices used to measure the biaxial compressive strength. Chapter III outlines the testing procedures and presents the results of the strength determinations. The general problems of compression testing are also addressed. Chapter IV describes the experimental investigation undertaken to characterize the nature of the damage produced in the specimen by compressive loads. The findings of this investigation indicated that crack propagation was occuring in the test specimen at loads less than failure. Such crack propagation was thought to originate at inherent flaws in the material. This led to a theoretical study of the kinds of flaws which may exist in a fabricated ceramic body and the mechanisms by which such flaws can extend cracks. Chapter V outlines the observations and conclusions of the study.

This chapter also presents the results of an experimental investigation into the nature of crack extension in a material containing flaws of controlled shape and size. This work contributes some experimental data in support of the theoretical ideas presented but also raises new questions about flaw behavior. Chapter VI brings together the theoretical concepts and experimental findings of the entire study and focuses them on the specific problem of explaining the process of failure in the test specimen. Lastly, this chapter introduces a theoretical approach to the general problem of describing the compressive failure of brittle materials.

CHAPTER II

DESIGN OF MECHANICAL TESTS

A. General Design Concepts

Many of the problems encountered when trying to compressively load brittle materials with mechanical rams can be overcome by using fluid pressure to apply the load to the test specimen. The problems of load train alignment and parallelism of opposed loading surfaces are eliminated since fluid pressure always applies a uniformly distributed force normal to the surface on which it acts. The external pressurization of a hollow, closed-end cylinder can create very high stresses in a test material with a substantial volume of highly stressed material without requiring the application of excessively high forces. To attain compressive stresses of 600 ksi one needs only 65,000 psi fluid pressure acting externally on a 2 inch inside diameter tube with a 1/8 inch wall thickness. For these reasons the basic approach to compressively loading the test material was to pressurize externally a closed-end, hollow tube.

In all tests the maximum principal compressive stress was in the hoop or circumferential direction ($\sigma_{\theta\theta}$) and arose from the action of the fluid pressure on the tube. The radial principal stress (σ_{rr}) was the same proportion of the applied fluid pressure in all compression tests, varying from a maximum (equal to the fluid pressure) at the outside diameter to zero at the inside diameter. The axial principal stress (σ_{zz}) was varied by two methods to produce the various ratios of biaxial compressive stresses in which the specimen was tested. A cartoon, showing in simplified form the loading schemes and the stress states produced in each test for the test specimen used, is shown in

Figure 1. A brief, conceptual description of how the various stress states were produced is given below.

1. Description of test devices

The simplest test in concept is the 1:0.5 biaxial compression test in which a closed-end, hollow tube is subjected to external pressure. (See Figure 1(a).) The stress distribution developed in the test section of the specimen may be determined from the equations of elasticity for a thick-walled pressure vessel, assuming elastic behavior of the material to failure. These equations are as follows:

circumferential stress: $$\sigma_{\theta\theta} = - p \frac{r_o^2(r_i^2+r^2)}{r^2(r_o^2-r_i^2)} \quad \ldots\ldots \quad (1)$$

$$\sigma_{\theta\theta} = - (4.758)p(1-r^{-2})$$

at inner surface: $$\sigma_{\theta\theta}(\max) = - p \frac{2r_o^2}{(r_o^2-r_i^2)} \quad \ldots\ldots \quad (2)$$

$$\sigma_{\theta\theta}(\max) = - (9.516)p$$

axial stress: $$\sigma_{zz} = - p \frac{r_o^2}{(r_o^2-r_i^2)}$$ constant through wall (3)

$$\sigma_{zz} = - (4.758)p$$

radial stress: $$\sigma_{rr} = - p \frac{r_o^2(r^2-r_i^2)}{r^2(r_o^2-r_i^2)} \quad \ldots\ldots \quad (4)$$

$$\sigma_{rr} = - (4.758)p(1-r^{-2})$$

at outer surface: $$\sigma_{rr}(\max) = - p \quad \ldots\ldots \quad (5)$$

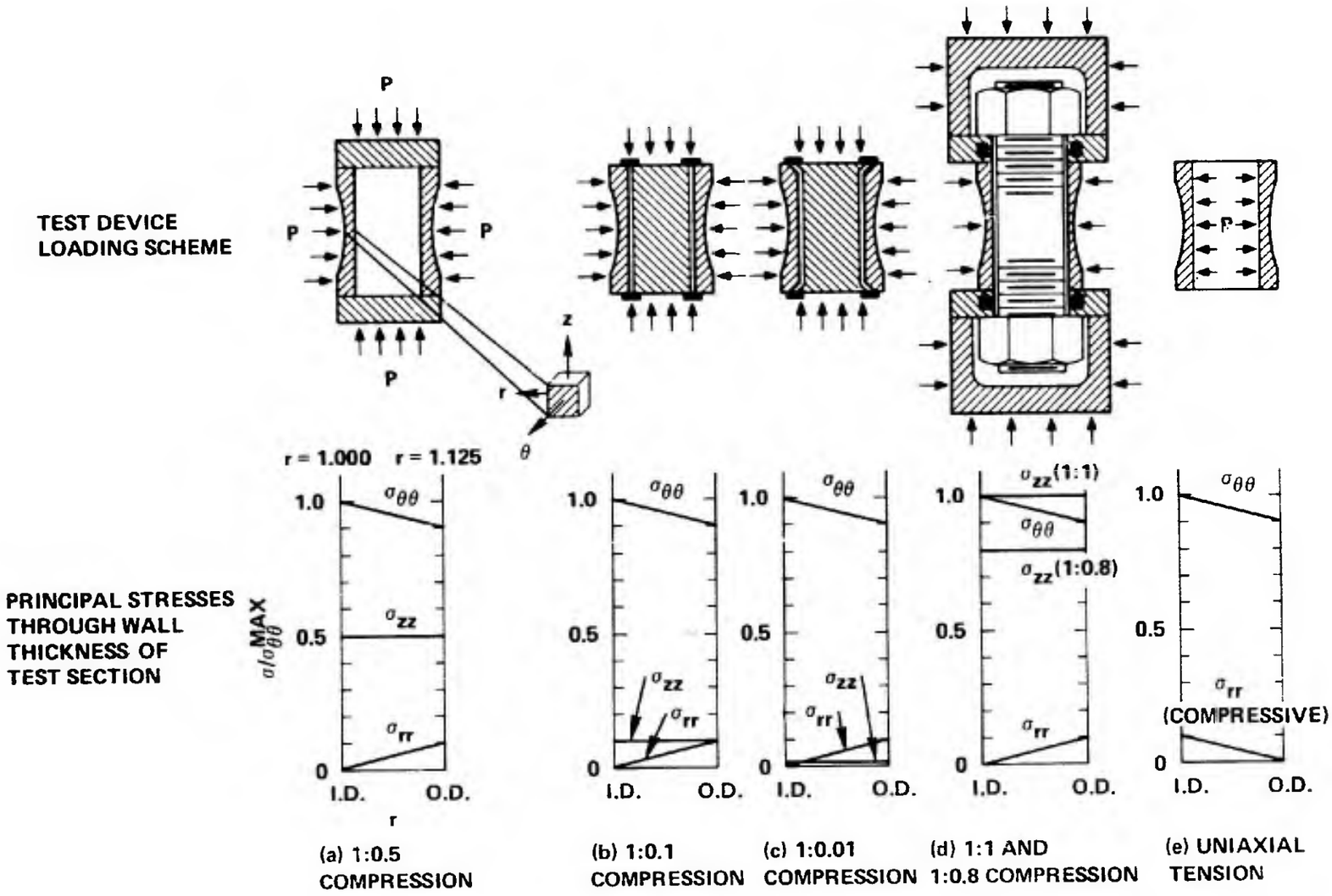

Figure 1. Loading Schemes and Stress States Developed in Test Specimen.

where: p = applied external pressure (positive)

r_o = 1.125 inches = outside radius of test section

r_i = 1.000 inches = inside radius of test section

r = radial position within the wall

$(1.000 \leq r \leq 1.125)$

and calling compressive stresses negative. Under this condition of loading the hoop stress ($\sigma_{\theta\theta}$) is the maximum principal stress and attains its maximum value at the inside diameter, decreasing to a value 90% of its maximum on the outside diameter in an approximately linear fashion. The intermediate principal stress (σ_{zz}) has a value one half that of $\sigma_{\theta\theta}$ and has a constant magnitude through the wall thickness. The minor principal stress (σ_{rr}) is a maximum at the outside diameter where its magnitude is equal to the applied fluid pressure. This radial stress decreases to zero at the inside diameter in an approximately linear fashion.

The stress state in the 1:0.5 compression test specimen (and for all other compression stress state tests) is triaxial compression for all radii except the inside diameter. The largest amount of triaxial compression occurs on the outside diameter where the stress state $\sigma_{\theta\theta} = 0.9\ \sigma_{\theta\theta}^{max}$; $\sigma_{zz} = 0.5\ \sigma_{\theta\theta}^{max}$; $\sigma_{rr} = 0.1\ \sigma_{\theta\theta}^{max}$ prevails. It is believed that fracture initiates on the inside diameter where $\sigma_{rr} = 0$ and $\sigma_{\theta\theta}$ is at its maximum. Strength values are reported as the maximum $\sigma_{\theta\theta}$ stress present in the specimen at failure.

The 1:0.1 biaxial compression stress state is developed in the specimen by a modification of the 1:0.5 test. (See Figure 1(b).) A center post is placed in the specimen equal to the length of the specimen

and an annular pressure seal is made between the specimen ends and the center post. The axial load produced by the fluid pressure acting on the specimen ends is carried by both the center post and specimen wall. The end diameter of the center post and the end, inside diameter of the specimen establish the proportions of the axial load carried by the center post and the specimen. The load carried through the center post decreases the axial, end load which must be carried by the specimen. By careful sizing of the seal area and its position, the majority of the axial load is carried by the center post and a stress state is obtained where $\sigma_{zz} = 0.1\ \sigma_{\theta\theta}$. The failure stress was calculated for $\sigma_{\theta\theta}$ by Equation (2) and σ_{zz} was determined from the constant proportion established by the geometry.

By increasing the inside diameter of the specimen tube at the ends by bevelling as shown and utilizing a seal arrangement similar to the 1:0.1 biaxial compression test, the stress state in the specimen test section could be varied between 1:0.1 biaxial compression and one of compression with a slight tension (i.e. 1:0.1 compression:tension). Because of the interest in stress states near uniaxial compression, the diameters and seal area were sized to give a stress state of 1:0.01 biaxial compression. (See Figure 1(c).) The determination of the stress state at failure is the same as that used for the 1:0.1 test.

To achieve the stress states of 1:0.8 and 1:1 biaxial compression, the stresses developed by an axial compressive load were superimposed upon those caused by a surrounding, external fluid pressure. The axial force was produced by tightening the nuts on a threaded bolt which passes through the specimen. (See Figure 1(d).) After sufficient axial

preload was applied, the specimen was subjected to a surrounding fluid pressure with the ends of the threaded bolt protected from the fluid pressure. By selecting the amount of axial preload introduced, stress states between 1:0.5 and 1:1 can be produced at failure in the specimen. The $\sigma_{\theta\theta}$ stress at failure is calculated from Equation (2). The axial stress (σ_{zz}) is a summation of the σ_{zz} produced by the fluid pressure, which is $\frac{\sigma_{\theta\theta}}{2}$, plus the σ_{zz} developed by the axial preload. The axial preload force is diminished under pressurization because of the displacements produced in the specimen by the fluid pressure. The development of the equations describing this are given in Appendix A.

The uniaxial tensile stress state is produced in the specimen by allowing internal fluid pressure to act against the inside bore surface of the specimen. (See Figure 1(e).) The axial extension of the specimen produced under the internal pressure is unconstrained so $\sigma_{zz} = 0$. The hoop and radial stresses may be obtained from the equations of elasticity for a thick-walled pressure vessel. They are as follows:

circumferential stress: $$\sigma_{\theta\theta} = p \frac{r_i^2(r_o^2+r^2)}{r^2(r_o^2-r_i^2)} \quad \ldots\ldots \quad (6)$$

$$\sigma_{\theta\theta} = 3.765p \left(\frac{1.266}{r^2} + 1\right)$$

at inside surface: $$\sigma_{\theta\theta}(\text{max}) = 8.531p \quad \ldots\ldots \quad (7)$$

radial stress: $$\sigma_{rr} = p \frac{r_i^2(r_o^2-r^2)}{r^2(r_o^2-r_i^2)} = 3.765p\left(\frac{1.266}{r^2} - 1\right) \ldots (8)$$

at inside surface: $$\sigma_{rr}(\text{max}) = p \quad \ldots\ldots \quad (9)$$

where the symbols are defined as those for Equations (1) to (5).

It is seen that the maximum principal stress is $\sigma_{\theta\theta}$ and that it reaches its maximum on the inside diameter surface. The radial stress is compressive and is at a maximum on this surface at a value of approximately one tenth $\sigma_{\theta\theta}$ and decreases to zero at the outside diameter surface.

ii. Specimen design

The shape and dimensions of the specimen tested are shown in Figure 2. The specimen (A) is 2 inches inside diameter by 4 inches long with a 1/2 inch long test section of 1/8 inch wall thickness. The thickness increases smoothly with a 4 inch radius to a thickness of 3/8 inch on the ends of the tube. When the specimen was tested in a stress state which required axial loads to be applied to the ends by the direct bearing of steel parts against the specimen tube (see the sections on 1:0.5, 1:0.8 and 1:1 testing devices), the compliance tubes (B) were used between the steel parts and the specimen tube. These compliance tubes allow the disturbing end effects, which arise from the frictional constraint of the ceramic tube's radial expansion by the steel loading parts, to vanish in regions well outside the test section. The effect of such compliance tubes in creating a uniform stress state in the test section was demonstrated by Filon and Coker[20] using a photoelastic model. The selection of the specimen tube geometry with an externally curved surface and 12° conical ends was based on a study made of different uniaxial compression test specimen geometries by Lambert and Manjoine.[21] A specimen of geometry similar to the one used in this study was used to test zirconia in tension, compression, and tension-compression by Babel and Sines[22] in which very little scatter in the measured strength values was observed.

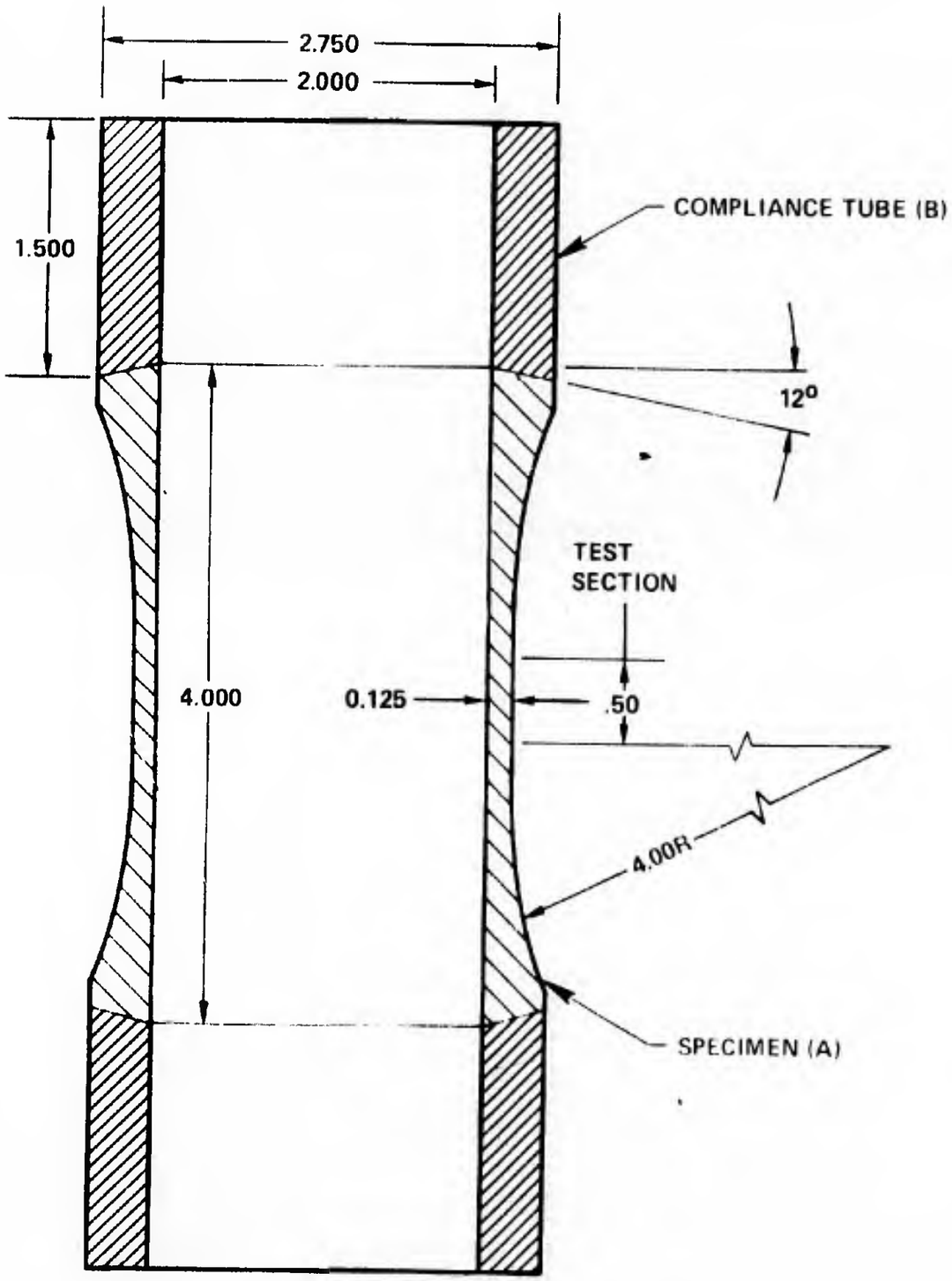

Figure 2. Alumina Test Specimen Dimensions.

When making compressive strength measurements on a hollow tubular specimen which is loaded by external fluid pressure, it must be verified that the specimen is failing in direct compression. Elastic instability can result in circumferential or "out of round" buckling that causes failure of the specimen at a stress below the compressive strength. The required axial load for longitudinal buckling of the specimen is on the order of ten times the stresses reached at failure; hence, this mode of elastic instability is not critical. A good theoretical analysis of circumferential buckling from external fluid pressure of a right, circular, hollow cylinder of varying wall thickness is not available. Southwell's analysis[23] of elastic stability is the only quantitative treatment of such buckling which includes some consideration of a superimposed end load. The difficulty in applying such treatments to the analysis of the specimen, which has a gradually reducing wall thickness ending in a minimum wall thickness in the test section, lies in choosing a length (ℓ) for the idealized cylindrical model which represents the point at which the diameter is constrained to be perfectly circular by the increased wall thickness. The calculations of Appendix B show the specimen tube should not buckle at the pressures necessary to produce direct compressive failure of the specimen. Experimental evidence will be cited below to substantiate the above prediction.

The compliance tubes were not used for the 1:0.1 and 1:0.01 compression tests or the uniaxial tension tests. The uniaxial tension test used only the specimen tube as shown in Figure 2. The ends of the specimen tube were modified for the 1:0.1 and 1:0.01 tests as shown in

Figure 3. All other dimensions of the specimen were the same as in Figure 2. A 1 inch test section specimen was also tested in the 1:0.5 compression stress state with compliance tubes. This specimen had dimensions identical with Figure 2 except the test section was 1 inch long and each compliance tube was 0.250 inches shorter than shown.

B. Design of Test Devices

1. 1:0.5 biaxial compression test device

The 1:0.5 biaxial compressive stress state is produced in the specimen by externally pressurizing an assembly of the specimen and compliance tubes. (See Figure 4.) The ends of the compliance tubes are sealed by two, hardened, tool steel end caps. The assembly is held aligned by screwing the end caps onto the soft brass tie rod. A steel bar (specimen mandrel) is placed in the bore of the specimen which prevents the end caps from moving inward a distance large enough to completely destroy the test section after it fractures. A layer of plasticine is inserted between the bar and the end caps to further absorb energy. The annular space between the bar and the inside diameter of the specimen is also filled with plasticine, but a controlled vacant space is provided to prevent internal pressure arising when the inner volume is reduced during testing. The plasticine reduces the amount of volume change and redistribution necessary in the pressurizing fluid as the specimen fractures. This results in a remarkable degree of preservation of the failed specimen. A polyethylene heat-shrunk plastic sheath is applied to the outside of the assembly to prevent the pressurizing fluid from contacting the specimen. This sheath is sealed on the ends with polyvinyl adhesive tape. A neoprene rubber girdle is also

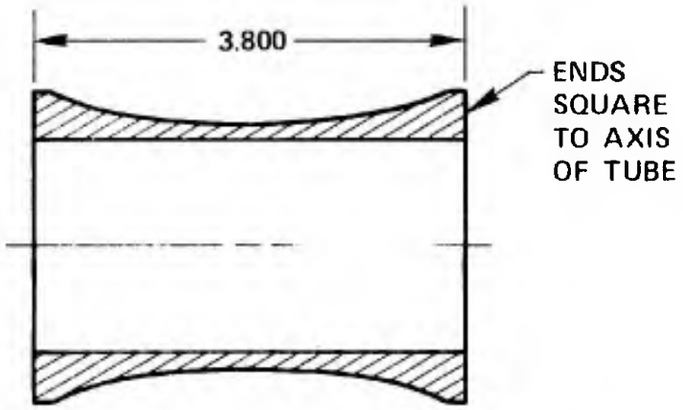

(a) 1:0.1 COMPRESSION TEST SPECIMEN MODIFICATION

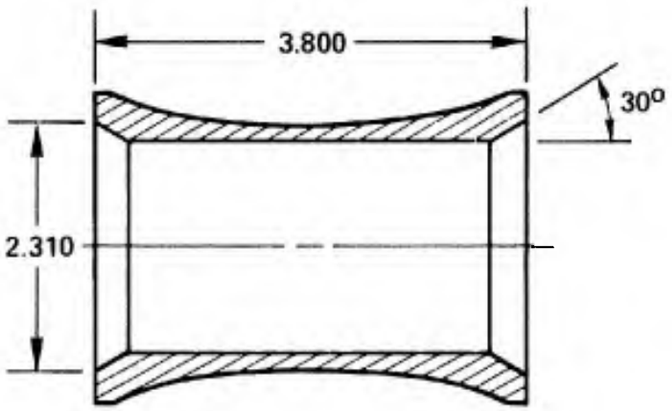

(b) 1:0.01 COMPRESSION TEST SPECIMEN MODIFICATION

Figure 3. Modification of Test Specimens Ends for 1:0.1 and 1:0.01 Compression Tests.

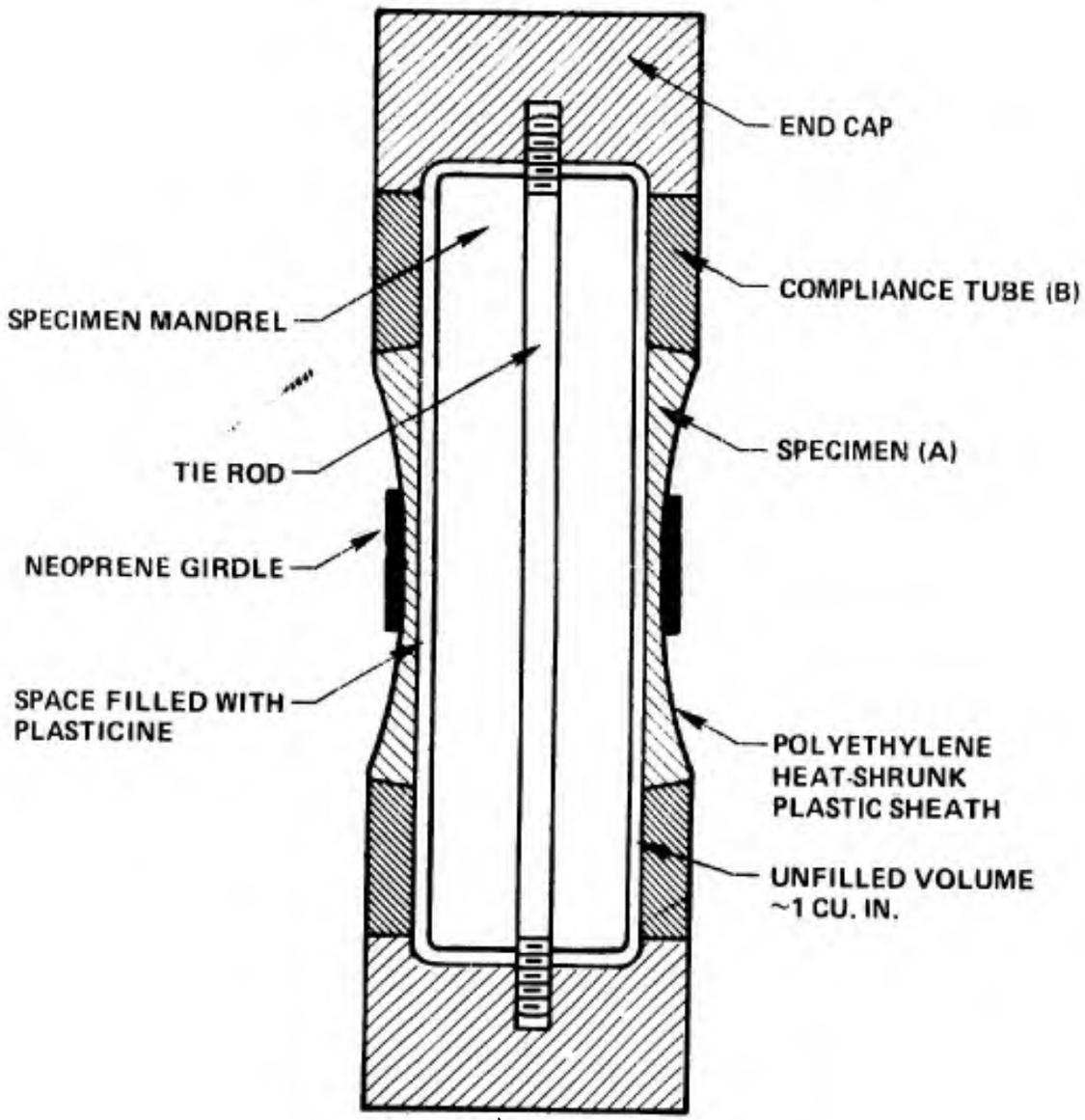

Figure 4. 1:0.5 Biaxial Compression Test Device.

installed around the test section to prevent alumina particles of the fractured test section from entering the pressurization hydraulics.

ii. 1:0.1 biaxial compression test device

The 1:0.1 compression test is performed by sealing the squared ends of the specimen tube with a metal-backed rubber seal (see Figure 5) and subjecting the assembly to surrounding fluid pressure. A center post through the specimen provides internal support for the seal element and carries the majority of the axial load from the fluid pressure acting on the end diameter area of the specimen tube. The annular ring, steel seal element is designed to yield at a fluid pressure less than that necessary to cause failure in the specimen; thus, it can be assumed that the load across the seal gap will be equally shared between the center post and the specimen. By appropriately locating the center of action of the seal gap force, the axial stress produced in the specimen was made to be a value of 0.10 $\sigma_{\theta\theta}$. Yielding of the steel seal element occurred in every test, thereby insuring the equal distribution of load.

The largest principal stress is $\sigma_{\theta\theta}$ and is calculated from the thick-wall pressure vessel equations. The intermediate principal stress (σ_{zz}) arises from the fluid pressure acting on the ends of the specimen and part of the seal area. This force is carried by the area of the test section and is balanced by an equal force on the opposite end of the specimen resulting in σ_{zz} always being 10% of $\sigma_{\theta\theta}$. The stresses in the specimen tube and center post produce axial displacements in both. The axial compliance of the center post was designed such that the axial displacement produced in the center post matched the axial displacement of the specimen. Thus, during application of the fluid pressure a step

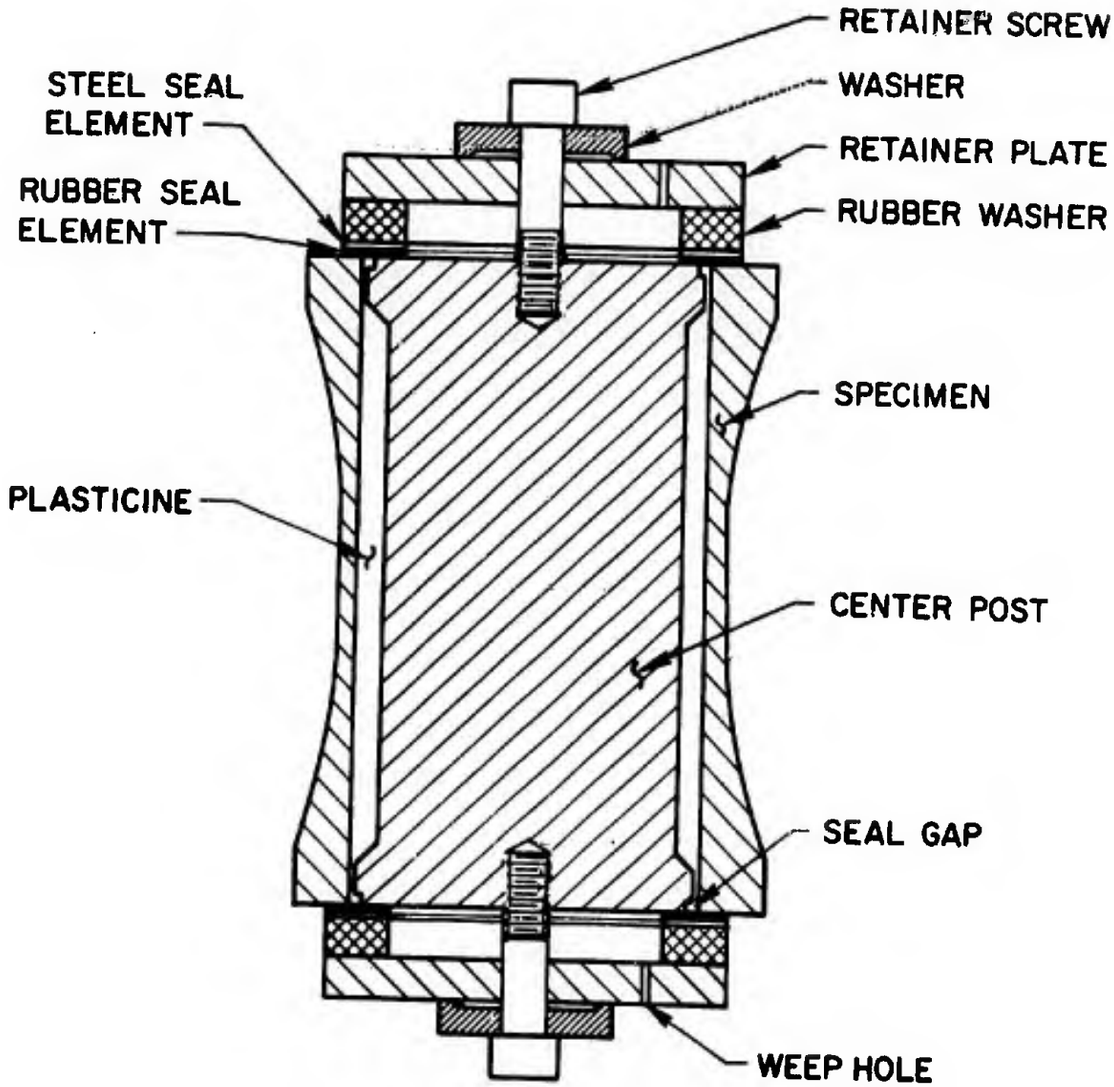

Figure 5. 1:0.1 Biaxial Compression Test Device.

did not form between the specimen end and center post end which would have prevented attaining a high pressure seal between the two. The length of each specimen tested was the same as the center post length to within ± 0.0002 inches.

On assembly, the retainer plate and seal elements are aligned to the specimen tube by use of an alignment ring. The retainer screw in turn aligns the center post to the retainer plate. To set the initial seal and hold the device components aligned, the retainer screws are tightened. The 1/4 inch thick rubber washer distributes the seal setting force uniformly around the seal element surfaces as the retainer screws are tightened. Pressure acts directly on the center post through the weep holes. As in the 1:0.5 test, the internal free volume of the specimen is filled with plasticine to prevent large amounts of fluid redistribution during specimen failure. A controlled free space is left to prevent internal pressure from arising from the volume contraction which occurs on pressurization.

iii. 1:0.01 compression test device

By increasing the inside diameter of the specimen tube on the ends and utilizing a seal arrangement similar to the 1:0.1 biaxial compression test device, the stress state in the test section can be varied between 1:0.1 biaxial compression and one of compression with a small axial principal stress which is tensile. It was decided that the task of achieving a pure uniaxial compressive stress state in the test specimen (one free from any unwanted tensile stresses which can arise from misalignment of parts and eccentricity or lack of concentricity of diameters) would require extremely accurate tolerances of the machining

and assembly alignment of the test device parts. This was judged to be too difficult a task to be certain of attaining the desired stress state. Small eccentricities would easily produce bending moments which would create tensile components in the test section and cause it to fail prematurely in compression-tension. Also, if the end diameters were not sized sufficiently accurately the stress state in the specimen might possibly be compression-tension (with too large an end diameter). This would result in the measured uniaxial compressive strength being below its actual value. Consequently, the design objective was to produce a 1:0.01 biaxial compression stress state in the test section.

The 1:0.01 compression test device is shown in Figure 6. The end diameter of the specimen bore was over-cut with a 30° chamfer and the steel seal element No. 2 was used to establish the area over which the fluid pressure acted to apply the axial load to the specimen tube. The inside radius of this seal element ($r_{i.d.}$) was sized to produce a slight biaxial compression stress state, 1:0.01. A worst case calculation was made which assumed maximum eccentricity of device parts and maximum possible misalignment that could occur during assembly. This calculation verified that under the worst conditions of eccentricity and misalignment no tensile stress components would be produced in the test section, i.e. the stress state in the test section could vary only between 1:0.02 and 1:0.00.

Alignment of the center post axis with the axis of the specimen tube is extremely critical in this device. This was accomplished by very accurate machining and careful inspection of all parts. The center post is aligned to the specimen axis by the following method. The

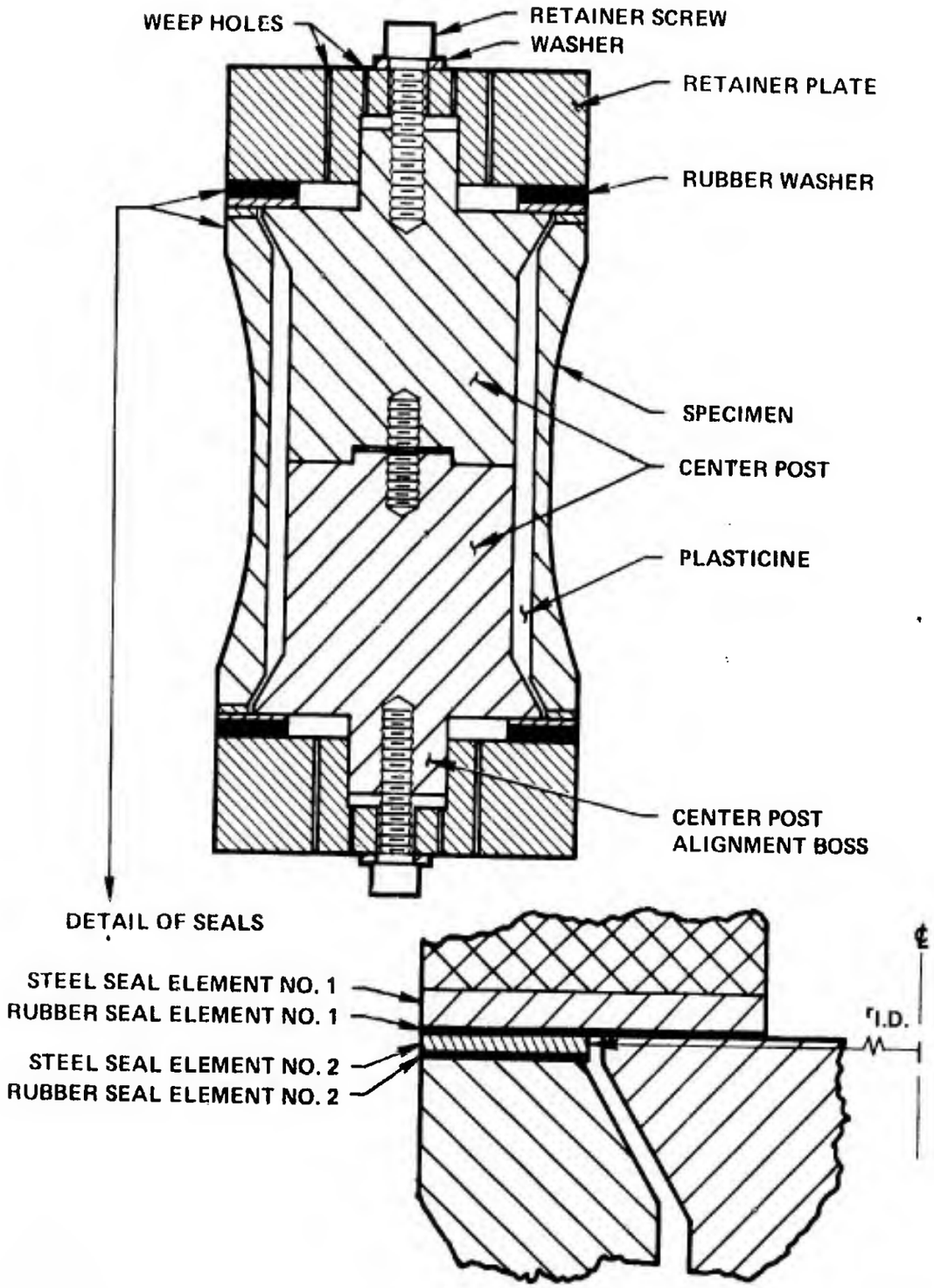

Figure 6. 1:0.01 Compression Test Device.

alignment bosses on the ends of the center post index the center post to the retainer plate. The retainer plate is in turn indexed to the largest O.D. of the specimen tube via an alignment sleeve which slides over the O.D. of the retainer plate and specimen. With the device assembled and the alignment sleeve in place, the retainer screws are tightened to set the initial seal and hold the assembly aligned.

Surrounding fluid pressure is applied which acts directly on the center post through the weep holes. The steel and rubber seal elements No. 1 create a seal between the center post and specimen. As before, the steel seal element No. 1 is designed to yield thus assuring that the axial pressure force is distributed uniformly between the specimen tube and the center post across the seal gap. Steel seal element No. 2 was designed not to yield since this element established the center line of the seal gap and, hence, the stress state.

The problem of matching the axial displacements under pressurization in the specimen tube and center post to prevent a step from forming at the seal is quite complex in this device. Calculations show that the specimen tube becomes slightly longer ($+ \varepsilon_{zz}$) whereas the center post becomes slightly shorter ($- \varepsilon_{zz}$). The difference in the displacements between the two is approximately 0.005 inches at the failure pressure. The second effect to be considered is that which arises from the rubber seal element No. 2. The low modulus of this material results in a much greater axial displacement than for an equivalent thickness of steel. A further complication is that the rubber seal element, being in the form of a thin film, has a higher "effective" modulus under the compressive axial load. A straightforward calculation of the axial compliance

of the specimen side of the seal components was not possible. Instead several trial pressurizations were made with the device using different thicknesses of the No. 2 rubber seal element until a thickness was obtained which matched the displacements of the specimen side and center post side of the seal gap. This was revealed by careful measurement of the permanent deformation produced in the steel seal element No. 1.

iv. 1:1 biaxial compression test device

The 1:1 and 1:0.8 biaxial compressive stress states are achieved in the specimen by superimposing the stresses from an axial load onto those caused by external fluid pressure. A drawing of the 1:1 loading device which was used for both tests is shown in Figure 7. A large bolt (C) passes through the assembly of loading washer (J), specimen and compliance tubes (A) and (B), loading ring (I), loading sleeve (H), and thrust washer (X). There is a large 12-point wrenching nut (D) on each end. Integral with one end of the bolt is a spline (E). The spline end of the bolt is enclosed by the prestress pressure case (G) which seals to the loading washer (I) by means of the "O" ring (U). This seal is set by prestressing the "O" ring with machine screws (P). The opposite end of the bolt is protected from fluid pressure by pressure cap (K) which seals to the loading washer (J). Weep hole (R) allows the surrounding fluid pressure to act directly on the specimen. Parts (O) are lead blocks positioned at each end of the bolt to absorb any impact on collapse of the specimen. A safety sleeve (L) along with extrusion washers (N) and lead washers (M) perform protection and energy dissipating functions in the design. The keys (F) permit the sleeve to slide

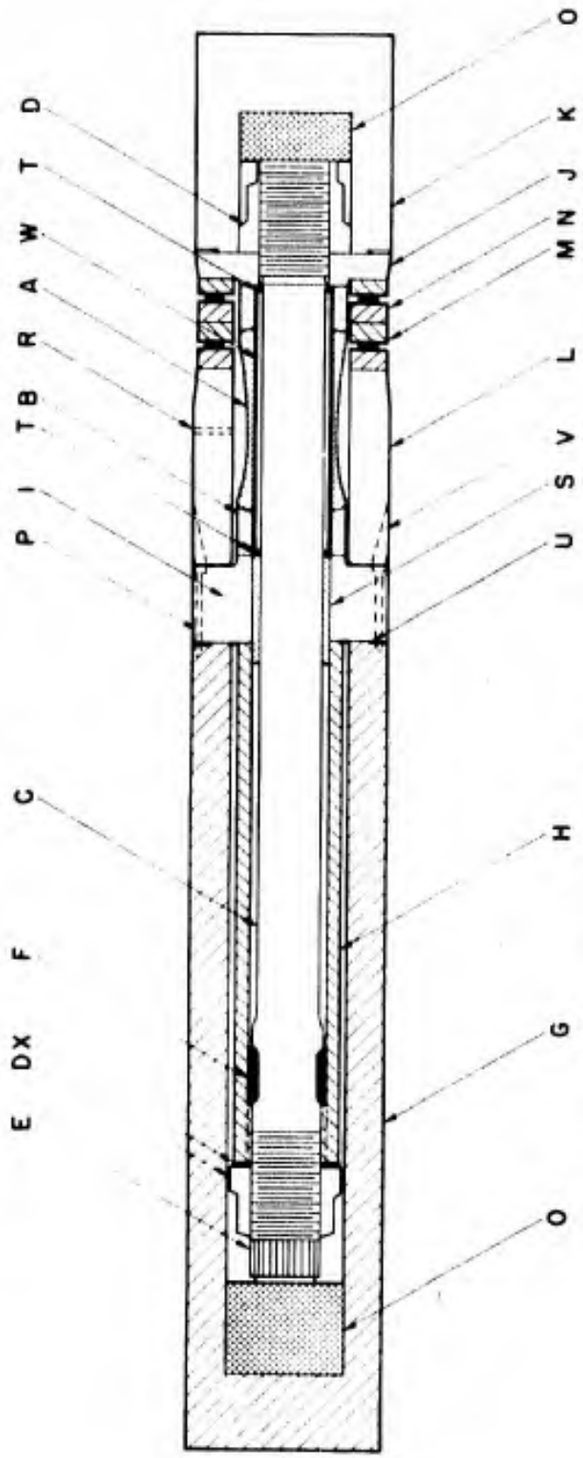

Figure 7. 1:1 Biaxial Compression Test Device.

longitudinally on the bolt but prevent rotation. Sleeves and rings, (W), (S) and (T) are for alignment.

The specimen is axially preloaded by placing the device, without the prestress pressure case and pressure cap, in a large lathe. The spline is grasped in the chuck of the lathe by a special wrench and the opposite end is allowed to slide freely in a modified tail stock of the lathe. A wrench is fixed over the spline-end nut and its force is reacted through a column to the ground. The lathe is hand-turned by a 3 ft. crank attached to the motor and the lowest gear is used. The lathe turns the entire assembly and the wrench holds the spline-end nut stationary. The keys (F) prevent the bolt or loading sleeve from being elastically wound up in torsion and possibly transmitting torsional stresses to the specimen. The torque applied to the spline is reacted a short distance away at the nut. When a sufficient preload has been applied to the specimen, the device is removed from the lathe and the prestress pressure case (G) and the pressure cap (K) are installed. The device is put into the pressure vessel and fluid pressure is applied until the specimen breaks.

The fluid pressure acts over the cylindrical surface of the specimen through weep hole (R) and axially through the pressure cap and loading washer. The prestress pressure case (G) prevents the fluid pressure from being applied to the spline end of the bolt; otherwise, most of the axial load from the fluid pressure would be assumed by the bolt and not by the specimen. The resultant stress state in the specimen is twice the hoop compressive stress to the axial compressive stress ($\sigma_{\theta\theta} = 2\sigma_{zz}$ from the external pressurization) plus the additional axial

compressive stress from the preload tension of the bolt. As the pressure is applied, some of the axial compressive prestress in the specimen, produced by the tension in the bolt, is lost because of the longitudinal elastic shortening of the specimen. The bolt and loading sleeve are designed to be elastically soft as compared to the specimen in order to minimize this reduction in preload on pressurization. Calculations,[24] show that this relaxation is 11.5%, i.e., 11.5% of the preload is lost on pressurization to the level expected to cause failure in the 1:1 stress state. Depending on the amount of axial preload introduced, any biaxial compressive stress state from 1:0.5 to 1:1 can be obtained.

Because of the great strength of the alumina material in compressive stress states, very careful design was required to make the fixture work. The axial load necessary to fail the specimen in a 1:1 compressive stress state was near 500,000 lbs. Over half this load must be carried by the prestressing bolt. Due to the space considerations in the bore of the pressure vessel, the wall of the prestress pressure case can only be one inch thick, yet it must support 60 ksi fluid pressure without collapse. In light of these design criteria, 18% Ni maraging steel was chosen as the material from which to fabricate the device. This steel can be heat treated to a tensile yield strength of 270,000 psi and exhibits exceptional ductility at this strength level.

Large amounts of energy are stored in the elastically strained parts of the device during the test. When the specimen fractures, this energy is released as kinetic energy in the bolt, accelerating it into the surrounding casing. Tensile waves are also created which can

propagate through the device destroying parts and even the pressure vessel. Considerable effort was spent designing a fixture which would absorb this energy and damp out the shock waves. The concept employed was that of squashing rings of lead to absorb the energy. When the specimen breaks, the end load from the pressure on the end cap plus the stored elastic energy in the bolt does not drive the bolt into the end of the prestress case, but the load is taken up by the safety sleeve (L) and the lead and steel washers (M) and (N). The deformation of the lead washers absorbs large amounts of energy and reduces the magnitude of the tensile-compressive shock waves produced.

The two lead washers (M) are in parallel in the load train with the specimen; any load they carry must be subtracted from the preload on the specimen. Because of this, the washers had to be accurately sized such that they subtracted only a small amount of the axial preload from the specimen as they were squeezing down during the preloading operation. On the other hand, the washers also had to be geometrically proportioned to allow them to absorb the large quantities of energy released and have great resistance to deformation when the specimen broke during the test under full load. This was accomplished by designing the washers to deform in a "thin film" condition where the loads required to decrease the washer thickness increases exponentially as the washer becomes thinner. The width to thickness proportion of the washers was chosen such that the initial deformation necessary in the washers to permit the application of the preload to the specimen required only a small percent of the preload. Under the conditions of specimen fracture, the loads required to further deform the washers increase 100 fold.

Since the lead washers are in parallel with the specimen in the load train; an experiment was conducted to establish exactly how much load the washers' deformation would subtract from the preload being applied to the specimen. The lead washers, steel washers and safety sleeve assembly were placed in an MTS testing machine in the configuration they are using in the 1:1 stress state device. The entire assembly required 20,000 lbs. to compress down 0.075" (twice the required deformation for preloading) in ten minutes. The crosshead was moving at a linear rate. The displacement was then held fixed and the decrease in load was monitored to ascertain the creep characteristics of the lead washers. In 60 minutes, the load had decreased to 9,000 lbs. This information indicated that during the 1:1 biaxial compressive strength test the lead washers would be assuming approximately 2-1/2% of the axial preload and pressure load so long as the loading is sufficiently slow to allow the lead to creep.

A design problem encountered during initial tests with the device was that of a stick-slip friction between the rotating loading sleeve (H) and the spline end nut (D). Various "relieved" configurations of the nut bearing face were attempted but none were successful. The stick-slip friction problems continued to give large variations in the torque required to wind the nut and popping would send acoustic shock waves through the specimen, which could cause premature specimen failure. The problem was finally solved by adding a thrust washer (X) between the nut and loading sleeve. It had a thickness contour which compensated for the elastic displacement of the nut face under load. First the washer was machined accurately with a constant thickness. The two faces

of the thrust washer were flat and parallel to ± 0.0002 inch, then one face was contoured.

Six-hundred grit lapped surfaces were used for the surfaces that rotate against each other under high load. Polished surfaces were initially used but this did not allow the lubricant to imbed into the surface to ensure a constant supply as the surfaces rotated. The rationale behind the thrust washer approach was (i) because of the relief contour, the stresses would be uniformly distributed over the bearing area as the load increased and (ii) two sliding surfaces were present instead of one; thus the test could proceed even if the friction increased on one of the two surfaces. This approach worked well. The thrust washer actually contoured itself by slight galling during use. By lightly repolishing the surfaces after each test, the surface contour improved with use and the torque required to apply the preload decreased over the series of tests from the drop in friction between the rotating surfaces.

The level of axial preload stress is determined by monitoring longitudinal strain gages mounted on the outside diameter of the test section. As for the other tests, the stresses arising from the external fluid pressure are calculated by using the thick wall pressure vessel equations. When calculating the axial stresses from the pressure load the loss of preload from the elastic shortening of the specimen must be considered. A derivation of the equations for determining the stress state in the specimen at failure is given in Appendix B.

v. Uniaxial tension test device

The uniaxial tension test is designed to stress the material in a state of hoop tension where $\sigma_{\theta\theta}$ is the maximum principal stress. This is important since a valid comparison of the tensile and compressive strengths of this material can only be made when the possibility of measuring differences in strengths due to anisotropic specimen properties is eliminated.

The hoop tension stress state was produced by expanding a bladder with fluid pressure against the inside bore of the test specimen. The design of the device to accomplish this is shown in Figure 8. A hand-operated pump was used to deliver hydraulic fluid through a surge valve to the internal side of the rubber bladder. The bladder was bonded to the mandrel on its ends with rubber cement to set the initial seal. The specimen tube was slid over the bladder-mandrel assembly with an interference fit slightly compressing the rubber bladder. The pump was operated until fluid exited from the bleed plug hole then the bleed plug was tightened. The protection shield was installed and pumping continued until the specimen failed. The fluid pressure seated the rubber bladder against the mandrel and specimen bore creating the high pressure seal. The accumulator was a large I.D. tube filled with air which compressed as the fluid pressure was raised creating a cushion which facilitated control by allowing small changes in pressure to be made smoothly. A ball-seating surge valve was placed in the pressure line just ahead of the mandrel to prevent all but a tiny amount of fluid from releasing energy into the specimen during fracture. The hoop stress at failure was measured by circumferential strain gages mounted on the O.D. of the

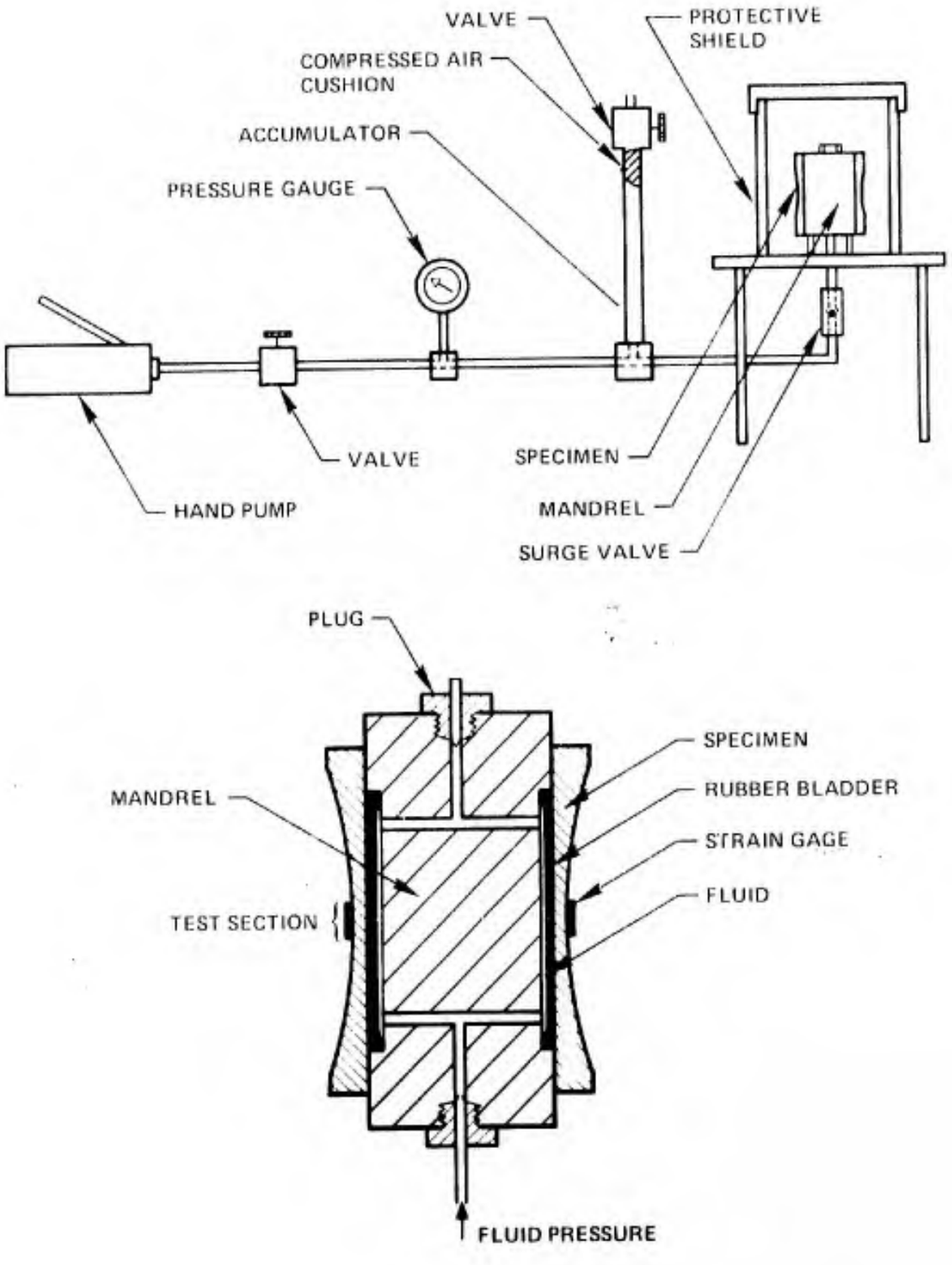

Figure 8. Tension Test Device.

test section. For the test section geometry, the maximum hoop stress at failure, which occurs on the inside diameter of the test section, is related to the circumferential strain measured on the outside diameter by the following equation:

$$\sigma_{\theta\theta}(\max) = (1.133)\ \varepsilon_{\theta\theta}^{O.D.}\ E = (6.0725 \times 10^{7})\ \varepsilon_{\theta\theta}^{O.D.} \quad \ldots \qquad (10)$$

σ_{rr} is a maximum on the inside diameter and decreases to zero on the outside diameter as shown in Equation (8). Since the axial extension of the specimen is not constrained σ_{zz} is zero.

CHAPTER III

MECHANICAL TESTING

A. Test Facility

The external fluid pressure was applied to the test devices inside a pressure vessel which was a converted isostatic press capable of pressurizing a 5 inch diameter by 60 inches long volume to a pressure of 100,000 psi. The vessel was constructed from an 8 inch naval gun made in 1945 by the Crucible Steel Company which had been cut, sleeved down to 5 inches diameter, and plugged to make a chamber 60 inches long. The pumping system was of conventional design utilizing electric and pneumatic pumps to supply the high pressure intensifier with pressurizing fluid. Control of the high pressure was accomplished by means of a by-pass throttle valve which controlled the primary pressure drive of the intensifier. The vessel was instrumented for precision pressure measurement by a recording Foxboro bulk modulus cell, a Heise precision Bourdon tube gage, and an electric resistance strain gage installed in the circumferential direction on the exterior of the cylindrical vessel. These three independent pressure measurements were monitored continuously during the tests and all gave the same pressure indications within their range of accuracy. The vessel was operated remotely from a bunker constructed of sand bags, steel I-beams and thick hardwood sheets. All automatic controls were replaced by manual ones for higher reliability.

The pressurizing fluid was a mixture of water and water soluble oil. Because of the fine particles of abrasive alumina which were released into the pressurizing fluid when the specimen failed, fresh

fluid was used for each test. Calculations of the stored energy in the fluid under pressure indicated that for safer operation and to minimize the damage done to test devices during fluid redistribution at specimen failure, the volume of fluid under pressure had to be minimized. This was accomplished by filling all unused portions of the pressurized volume with steel blocks; the total volume of pressure fluid was always less than one quart. Specimen collapse could be detected by the moderately loud zipping sound produced and the drop in fluid pressure. No high pressure accidents occurred during the testing program and neither the pressure vessel nor any test devices were ever damaged. A photograph of the pressure vessel facility appears in Figure 9. Additional details of the pressure vessel modification and reconditioning is contained in reference (25).

B. Specimens

The material tested was a high density, high purity commercial alumina manufactured by Western Gold and Platinum (WESGO) of Belmont, California which is designated by them as AL-995. This material was isostatically pressed then sintered in rough form. Machining to final dimensions was done by diamond grinding. Straight walled tubes of the sintered material were diamond ground to the final specimen dimensions. The finish was made with a grinding wheel containing #200 grit diamond and the final cut was less than 0.002 inches. Sedlacek[26-30] studied the finishing of alumina and found that no improvement in surface finish or increase in the measured tensile strength is obtained from the use of finer grit and that limiting the cut to 0.002 inches prevents the introduction of machining damage. A photograph of the test

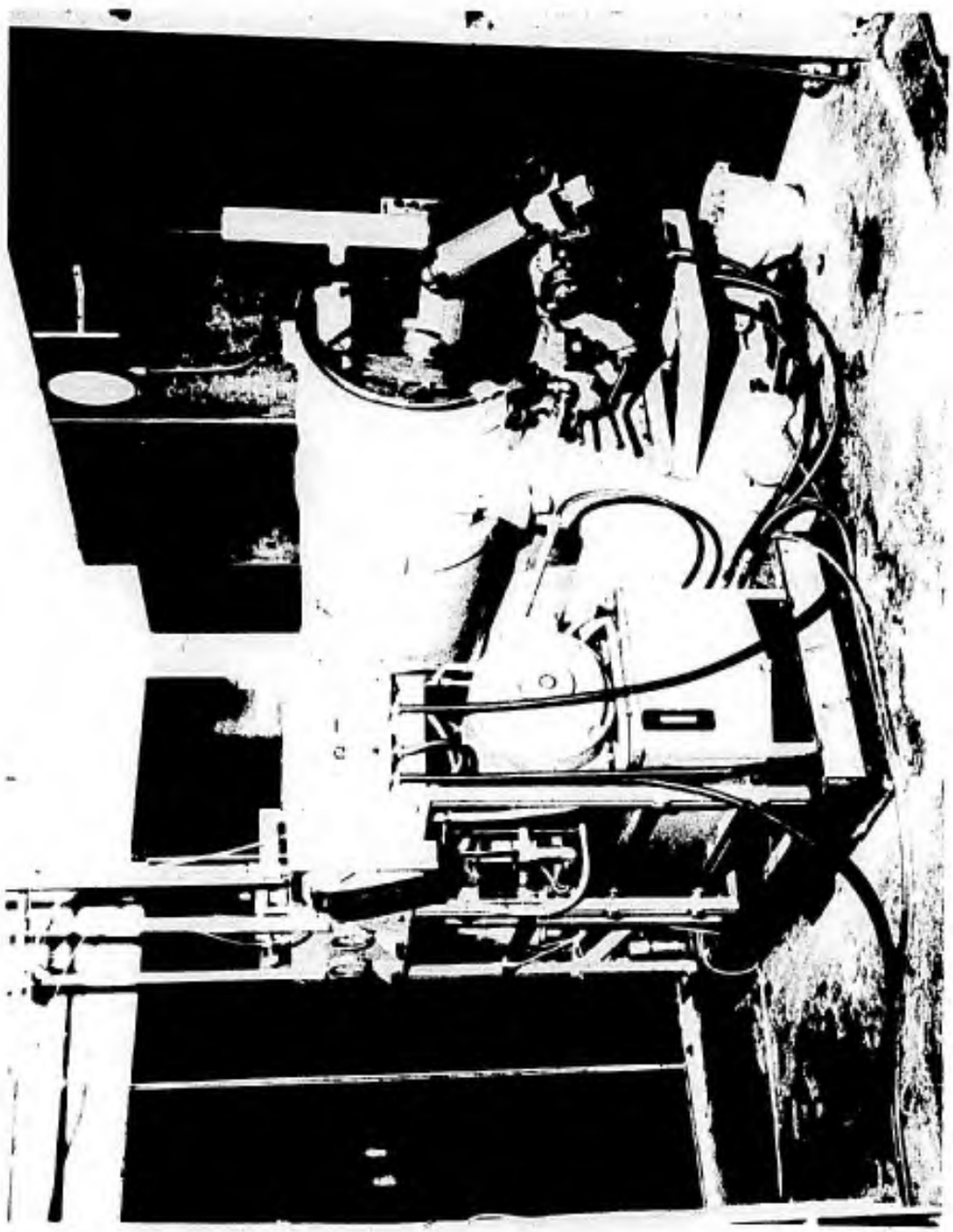

Figure 9. Pressure Vessel Facility.

specimen and compliance tubes appears in Figure 10. The properties of WESGO AL-995 alumina as reported by Sedlacek[19] appear in Table I; the material used in this study was produced to the same specifications as the material Sedlacek evaluated.

TABLE I

Properties of "WESGO" AL-995 Alumina

Young's Modulus (tensile & compressive)	53.6×10^6 psi[1] $\pm 0.3 \times 10^6$ psi
Initial Poisson's Ratio (compression)	0.24
Tensile Strength (@ stress rate of 3000 psi/sec)	31.6×10^3 psi $\pm 1.1 \times 10^3$ psi
Flexural Strength (@ stress rate of 3000 psi/sec)	36.9×10^3 psi $\pm 3.0 \times 10^3$ psi
Uniaxial compressive Strength	448×10^3 psi $\pm 36 \times 10^3$ psi
Density	3.850 gm/cc
Average Grain Size	approximately 20 microns

[1] 1 psi = 7.03×10^{-4} kgm/mm^2

Two batches of specimens were produced for this study. The first batch had a one inch test section and was tested only in 1:0.5 biaxial compression. The second batch was made with a 1/2 inch test section and these were tested in all stress states investigated in the study. All specimens for each batch were fabricated at the same time from the same lot of material. In addition all machining was done by the same machinist. Since the same geometry was used for every stress state, this meant a direct comparison of strengths measured in different stress

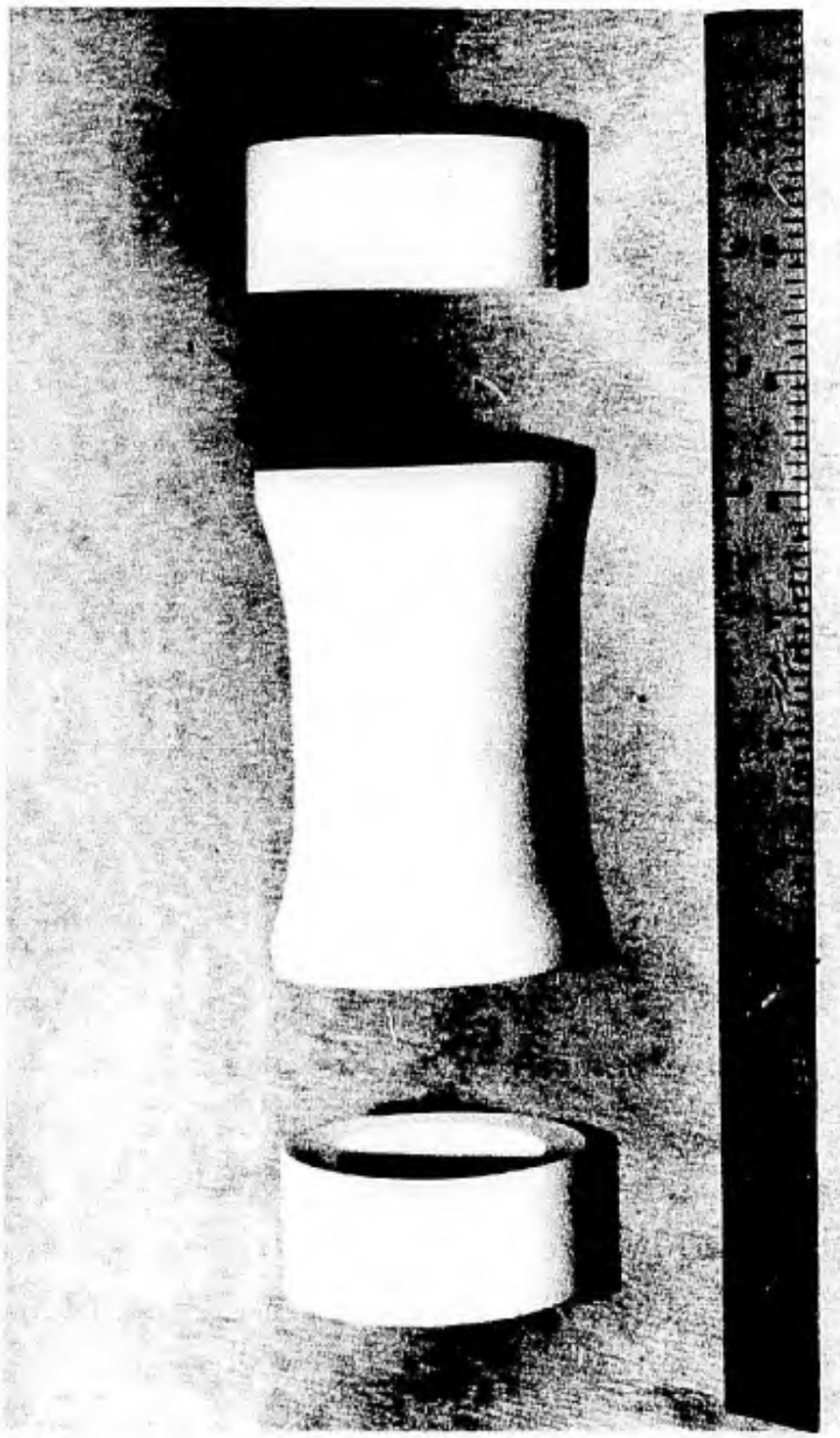

Figure 10. Test Specimen with Compliance Tubes.

states could be made without the possibility of an influence of specimen geometry, size, or processing history.

Small amounts of ellipticity (out of roundness) in the specimen diameters or a lack of concentricity of the inside and outside diameters can induce large bending moments in the loaded test specimen. These bending moments will cause failure from the tensile stress they induce before the actual compressive strength of the material is reached. The machining tolerances specified for concentricity and ellipticity of diameters was 0.0005 inches. These tolerances were verified for each specimen tested by a thorough dimensional inspection of all important dimensions and tolerances. Eccentricity or ellipticity of the specimen diameters never exceeded 0.0003 inches. The inside and outside diameters of the test section did not vary from the dimensions shown on Figure 2, by more than ± 0.0005 inches.

C. Testing Procedures and Results

1. 1:0.5 biaxial compression tests

Before assembly of the 1:0.5 test device the critical mating surfaces of the specimen tube, compliance tubes and the end caps were carefully lapped together to assure that no disparities were present between the contacting surfaces which could cause localized concentrations of stress. First, the hardened steel end caps were lapped smooth on a machinist's lapping flat with #600 silicon carbide powder. Next, the ceramic compliance tube surface which mates with the end cap was lapped to the cap using medium grade, levigated alumina powder. Finally, the contacting conical surfaces between the compliance tubes and the specimen were hand lapped together using a series of diamond

lapping compounds beginning with 15 micron diamond size and progressively reducing the particle size through 6 micron, 3 micron, and finally one micron. Some attempts were made to final lap with 0.25 micron diamond compound to attain an optical quality finish but this resulted in an uneven figure of the surface finish. Some areas would be optically smooth and others would have a matte appearance. Uneven distribution of the lapping compound on the conical angle was the cause. Since no increase in the measured strength was observed with the 0.25 micron lapped specimens, the laborious task of lapping with the fine compound was not used. Also it was suspected that an uneven surface finish might lead to variations in the coefficient of friction between the faces which could result in stress concentrations developing. Final lapping with the 1 micron compound yielded a very uniform, fine matte finish. During this lapping, the tubes and specimen were placed on a 2 inch diameter steel mandrel, and rotated against each other so that the conical surfaces would remain conical and concentric with the test section. The amount of contact between the two mating surfaces in each of these steps was determined by applying radial lines with a 6H hard lead pencil to each of the surfaces before lapping; then observing how the lines disappeared as the lapping proceeded. Lapping was continued with each grade of compound until the lines drawn on both surfaces were removed uniformly. Unsuccessful initial tests indicated the quality of figure of the contacting surfaces was extremely critical for successful testing.

After lapping, all device parts were carefully cleaned and the device was assembled. A heat-shrunk polyethylene tube was applied to

the outside of the specimen to eliminate the possibility of pressurizing fluid contacting the specimen. The edges of the plastic tube were feathered to the specimen surface smoothly and adhesive backed polyvinyl tape was used to seal them. There was no evidence of pressurizing fluid contacting the specimen during any of the tests.

Alignment of the end caps, compliance tubes and specimen tube was done manually. Because of the accurate machining, simply by running a fingernail back and forth across the part line of the two mating surfaces around their circumference, a misalignment of only ±0.0005 inch could be detected. As the end cap was tightened on the threaded tie rod, the alignment at all four critical interfaces of the assembly was checked. When the end cap was finally tightened sufficiently to hold the three ceramic tubes in place, the alignment was checked once more. Then the plastic sleeve was heat-shrunk into place using a heat gun. Lastly, a neoprene girdle was taped around the test section of the specimen to prevent alumina particles of the fractured specimen from escaping.

The specimen assembly was inserted into the chamber of the pressure vessel and the pressure was raised over a 10 to 15 minute period until fracture occurred. The pressure increases were made in steps of 5 or 10 ksi with cross calibration checks on pressure measuring instruments made between each increase. The pressure increases were made at a rate of approximately 200-500 psi/sec. Fracture was indicated by a small sharp noise and by a sudden drop in measured pressure. Preservation of the failed specimen was quite good owing primarily to the center mandrel and plasticine in the specimen bore. A series of photos

showing a typical failed specimen appear in Figure 11. The compliance tubes were usually intact except for a few longitudinal-radial cracks through the wall thickness and/or circumferential cracks. In the region of the test section pulverization of the alumina occurred only in the immediate area where structural collapse originated.

Four successful tests were performed with one inch test section specimens and with half-inch test section specimens in this stress state. The strengths measured for these specimens are given in Table II and Table III. The two specimen types were fabricated from two different batches of material.

TABLE II

1:0.5 Biaxial Compression Test Results with One Inch Test Sections

Test	Fluid Pressure at Failure (ksi)	Calculated Failure Stress $\sigma_{\theta\theta}$ (ksi)
1	61.8	585
2	59.9	567
3	60.3	572
4	59.5	566
	Average Failure Stress $\bar{\sigma}_{\theta\theta}$ =	572 ksi
	Standard Deviation S =	8.7 ksi

A comparison of the test results in Table III obtained from specimens containing a 1/2 inch test section with the results of the tests performed on specimens with a 1 inch test section in Table II is strong experimental evidence that the 1 inch test section specimens did not fail by buckling. The 1 inch test section specimens failed at consistently greater loads than the 1/2 inch test section specimens.

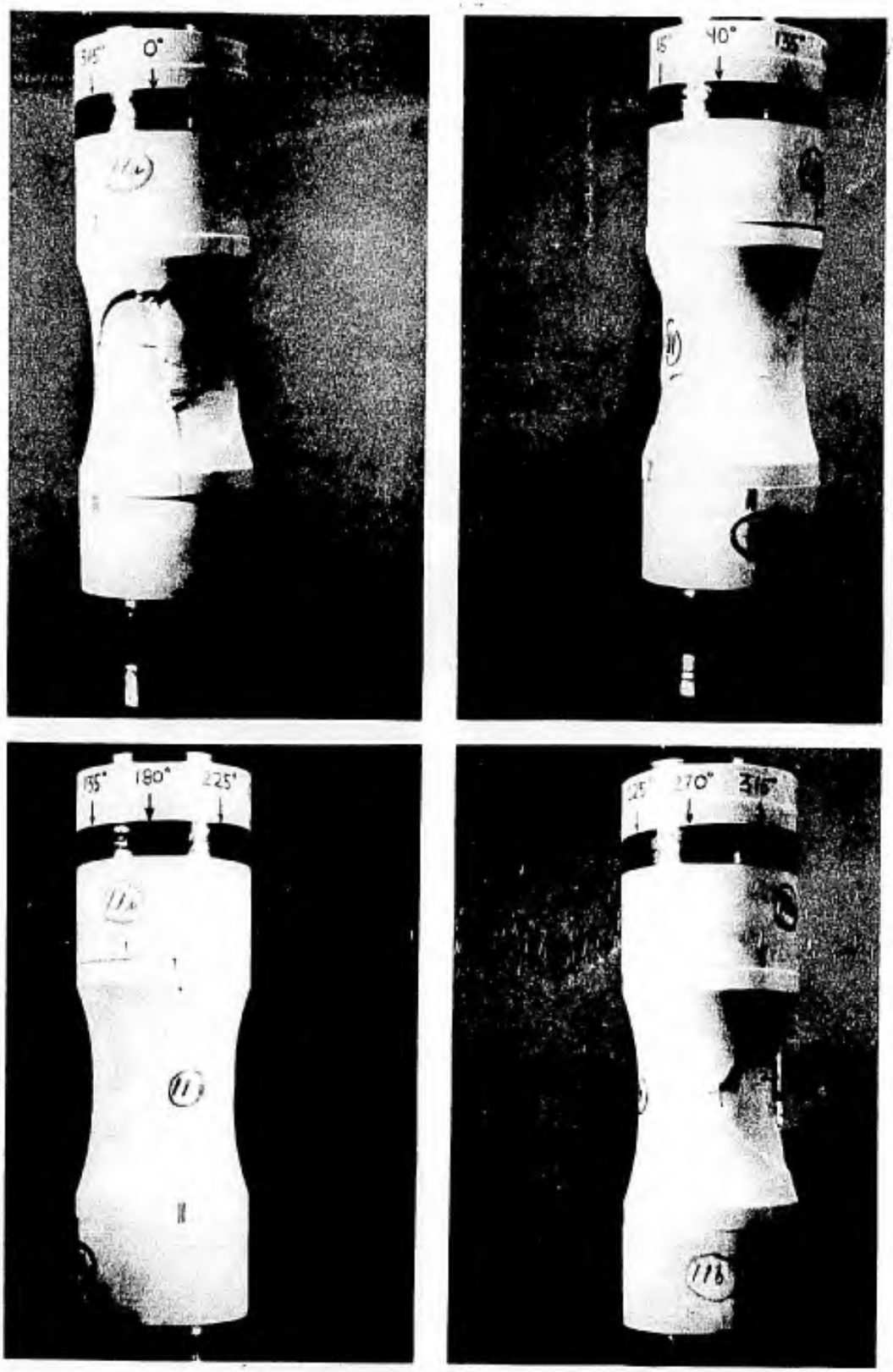

Figure 11. Failed 1:0.5 Biaxial Compression Specimen.

TABLE III

1:0.5 Biaxial Compression Test Results with One-Half Inch Test Section

Test	Fluid Pressure at Failure (ksi)	Calculated Failure Stress $\sigma_{\theta\theta}$ (ksi)
1	55.5	529
2	55.0	524
3	55.2	526
4	50.0	477
	Average Failure Stress $\bar{\sigma}_{\theta\theta}$ =	514 ksi
	Standard Deviation S =	22 ksi

If failure by buckling was occuring in the 1 inch test section specimens, the shorter 1/2 inch test section specimens would have higher failure loads since buckling would be more difficult in these specimens (i.e., require greater loads). The shorter test section would result in a greater wall thickness in the area where buckling would occur and this increased wall thickness would give greater resistance to "out of the round" deformation. The average strength of the 1 inch test section specimens was 11% greater than the 1/2 inch test section specimens; thus, failure by buckling did not occur. The lower strength measured for the 1/2 inch test section specimens was most likely due to batch variation in the alumina material.

ii. 1:0.1 biaxial compression tests

Before assembly of the test device the squared ends of the specimen were lapped on an internal diameter mandrel with 15 micron diamond lapping compound to assure flatness of the seal surface and to create

circumferential scratches on the surface to prevent extrusion of the rubber seal element out of the seal area at high pressures. The steel seal elements were also roughened with circumferential scratches on their surfaces which interfaced with the rubber seal elements. Problems were encountered in effecting both the initial low pressure seal and the high pressure seal with this device. The above treatment solved the high pressure seal problem. The low pressure seal problem was solved by applying a bead of RTV-116 silicone rubber around the seal area after the device was assembled. After assembly of the device the specimen was wrapped with polyvinyl adhesive tape to prevent pressurizing fluid contact. However, there was evidence this technique did not prevent pressurized fluid from contacting the specimen in the overlap area of the tape. The pressurization procedure was as described for the 1:0.5 tests. The measures strengths of the four half-inch test section specimens tested is presented in Table IV.

TABLE IV

1:0.1 Biaxial Compression Test Results

Test	Fluid Pressure at Failure (ksi)	Circumferential Stress at Failure ($\sigma_{\theta\theta}$)
1	56.2	536
2	55.7	531
3	58.0	553
4	58.2	555
	Average Failure Stress $\bar{\sigma}_{\theta\theta}$ =	543 ksi
	Standard Deviation S =	12.2 ksi

iii. 1:0.01 compression tests

Specimen preparation, device assembly, and pressurization procedures used in the 1:0.01 compression tests were similar to those described above for the 1:0.1 compression tests. Again, initial seal problems were encountered but were solved by accurate sizing and surface preparation of the seal elements.

1:0.01 compression tests were performed on four 1/2 inch gage length specimens. The measured strengths are reported in Table V. Tests #1 and #2 were performed on specimens which were damaged during preliminary tests in which attempts were made to produce a 1:0 uniaxial compression stress state at failure, since there were no specimens remaining for additional tests. The damage produced in these two specimens during the attempted 1:0 test is shown in Figure 12. Two circumferential cracks were produced near each end at some stress level during the 1:0 compression test attempts. These cracks extended completely around the circumference and penetrated completely through the wall thickness. Each set of two cracks had identical longitudinal spacings on each end and were coplaner with the tube diameters. On the inside diameter these cracks had an onion peel appearance and on the outside diameter the normal to their plane was parallel to the specimen axis. Further discussion of the origins of this crack damage appears in Chapter V.

On retesting in the 1:0.01 compression stress state, heat-shrinkable polyethylene tubing sealed at the ends with RTV-116 silicone rubber was used to prevent fluid from entering the cracks and filling the inside bore of the specimen with fluid pressure. Specimen #3 and

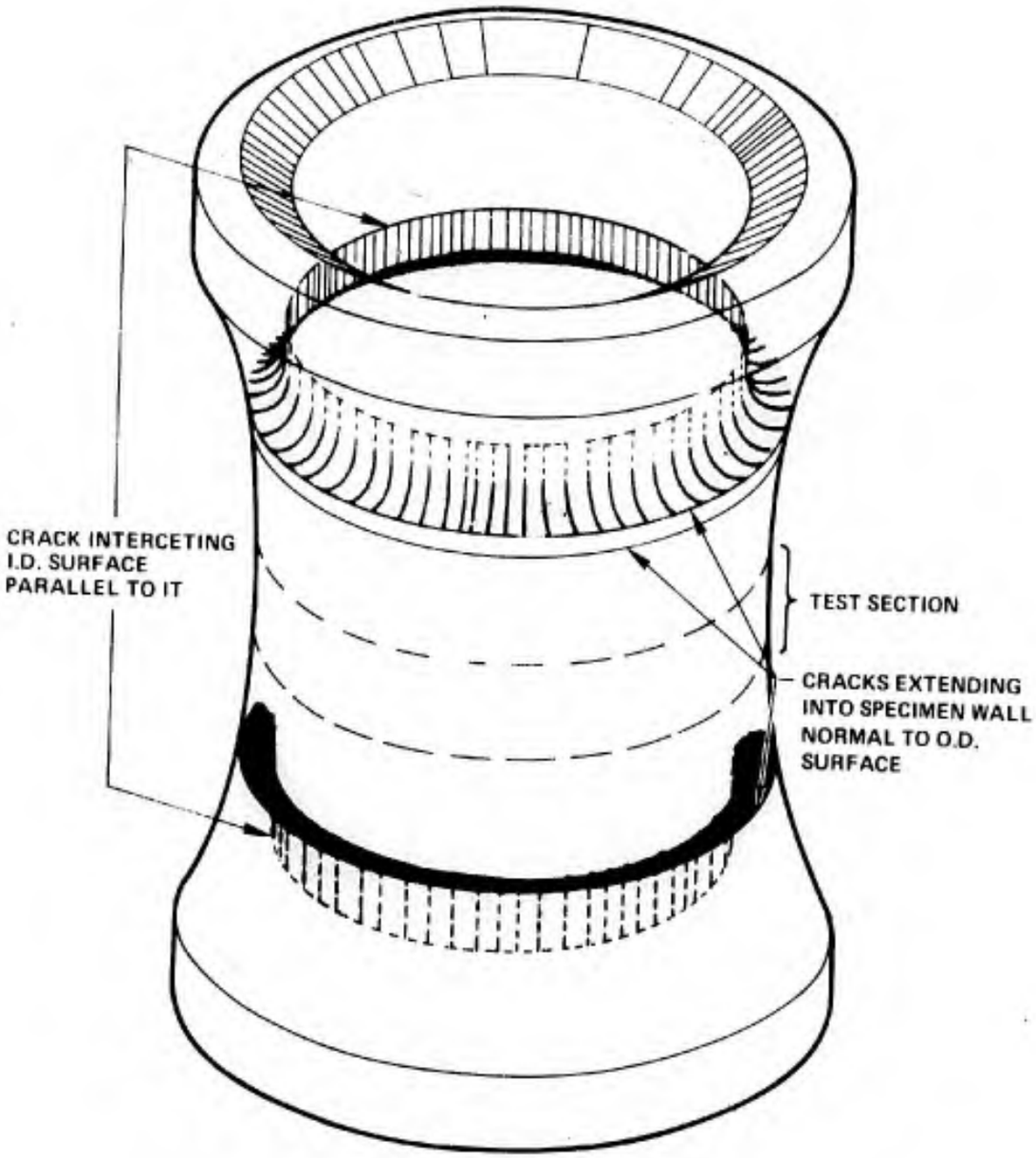

Figure 12. Specimen Damage During Attempted 1:0 Uniaxial Compression Test.

#4 were tested without the formation of these cracks. All four specimens failed in the test section with macroscopic failure characteristics very similar to the 1:0.5 tests. The presence of the cracks did not appear to significantly affect the strength or to change the mode of specimen collapse.

TABLE V

1:0.01 Compression Test Results

Test	Fluid Pressure at Failure (ksi)	Failure Stress (ksi)
1	48.6	463
2	52.5	500
3	53.3	508
4	52.7	502
	Average Failure Stress $\overline{\sigma}_{\theta\theta}$ =	493 ksi
	Standard Deviation S =	20.5 ksi

iv. 1:1 and 1:0.8 biaxial compression tests

Preparation of the mating surfaces of specimens and compliance tubes tested in the 1:1 and 1:0.8 stress states was the same as that used in the 1:0.5 tests. The square ends of the compliance tubes were lapped to the loading washer (J) and loading ring (I) (see Figure 7). Because strain gages were mounted on the external surface of the specimen to measure the preload, the specimen could not be protected effectively from contact with the fluid pressure. The specimen surface was wet in some areas by the pressurizing fluid. The pressurization of this device was accomplished more slowly to allow the lead safety

rings to creep under load, minimizing the amount of axial load they assumed. Pauses of at least eight minutes were used between incremental increases in pressure. Near the failure pressure the increments of pressure increase were reduced to only a few ksi.

During the preloading operation of the 1:1 test device in the lathe, the manual cranking was stopped every five turns to allow the keyways to straighten and the keys to slide. Readings of the three circumferential strain gages and the nut wrench load cell were made every 50 turns. (Between 300 and 400 turns of the lathe were required to preload specimens in the 1:1 and 1:0.8 tests.) The uniformity of the σ_{zz} stress around the test section was constantly verified by comparing these readings. The non-uniformity never exceeded 2% and was always less than 1% at the preload stress level. The torque of the nut wrench used to hold the nut stationary as the device was wound up, was reacted on a 3000 lbs. load cell positioned 24 inches from the centerline of the bolt. In this manner, the torque applied by the lathe to turn the nut on the bolt was measured. Maximum torques required to apply the preload varied from 5,000 to 5,500 ft. - lbs. Strain readings were made with the various strain gages mounted on the specimen with a BLH SR-4 strain indicator using a strain gage switching box with multiple contacts. Readings were taken by manually balancing the half bridge circuit. This was more time consuming than an automatic recorder but was felt to be less prone to errors. Additional details of the problems encountered with the testing device and the procedures used during testing are presented in References 31 and 32.

A difficulty was encountered in the 1:1 compression tests; during the application of the axial preload, the ceramic compliance tubes cracked at a value of approximately 90% of the desired preload. A study was made of this cracking problem,[32] and it was concluded that the cracking was probably induced by the tensile hoop stresses caused by slippage of the conical faying surface of the compliance tube over the specimen tube as the axial load was increased. The ceramic compliance tubes were replaced by hardened steel ones, but this resulted in splitting of the specimen as shown in Figure 13. Nevertheless, the tests using the split specimen tubes were completed and, in spite of the splitting, had an average biaxial strength of 465 ksi. (See Table VI). All tests were performed on the one-half inch test section specimens.

TABLE VI

1:1 Biaxial Compression Test Results

Test	Preload Force (lbs)	Failure Pressure (ksi)	Calculated Axial Failure Stress σ_{zz} (ksi)	Calculated Hoop Failure Stress $\sigma_{\theta\theta}$ (ksi)	$\sigma_{zz}/\sigma_{\theta\theta}$
1	234,000	44.8	472	427	1/0.90
2	223,000	50.1	482	477	1/0.99
3	218,000	42.0	440	400	1/0.91

One of these measured strengths was within the scatter-band of the 1:0.5 tests. It is thought that if a smaller conical angle had been used with the ceramic compliance tubes the splitting would have been avoided but not enough specimens remained to duplicate the test.

By reducing the preload stress level in the 1:1 test device to yield a stress state at failure of 1:0.8, the compliance tube cracking

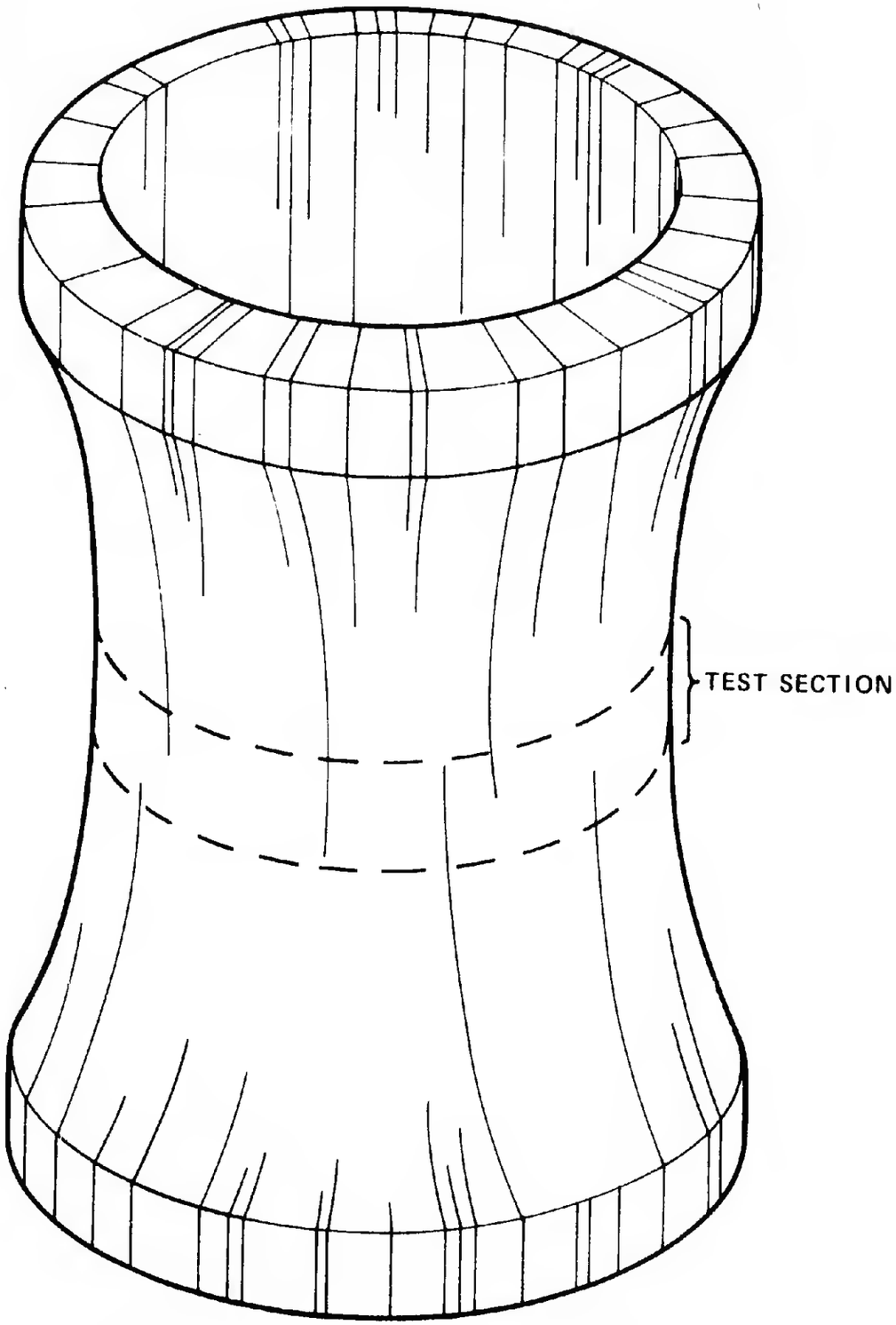

Figure 13. Specimen Damage During 1:1 Preloading.

problem was eliminated. Four successful 1:0.8 biaxial compressive tests were performed with the 1:1 stress state device on 1/2 inch test section specimens using the ceramic compliance tubes. The data from these tests are presented in Table VII. There was no damage produced in the specimens or the compliance tubes during the preloading. A sample calculation of the data reduction for this test is given in Appendix A.

TABLE VII

1:0.8 Biaxial Compression Test Results

Test	Preload Force (lbs)	Failure Pressure (ksi)	Calculated Axial Failure Stress σ_{zz} (ksi)	Calculated Hoop Failure Stress $\sigma_{\theta\theta}$ (ksi)
1	145,000	56.3	423	536
2	147,000	56.8	427	541
3	148,000	53.2	412	507
4	149,000	55.2	422	526
			Average Axial Stress at Failure $\bar{\sigma}_{zz}$ =	421 ksi
			Average Hoop Stress at Failure $\bar{\sigma}_{\theta\theta}$ =	528 ksi
			Standard Deviation S =	13.5 ksi

When tests are made with the 1:1 stress state device, the internal cavity of the specimens cannot be filled with plasticine as in the 1:0.5 tests; consequently, the damage done to the specimen on fracture is considerably greater (See Figure 14).

v. Uniaxial tension tests

No special preparation was required for the specimens tested in this stress state. A photo of the testing apparatus is shown in

Figure 14. Failed 1:0.8 Biaxial Compression Test Specimen.

Figure 15. The hoop stress at failure and its uniformity were determined by strain gages mounted on the specimen which were monitored continuously during the pressurization. Three circumferential strain gages were mounted on the outside diameter of the gage section 120° apart. The three strain readings obtained always remained in agreement within the accuracy of measurement of the strain gages. The fluid pressure was measured with an ASHCROFT Bourdon tube pressure gage which allowed a crude check on the stress as calculated by the thick wall pressure vessel equation. The measured strengths of the four half-inch test section specimens tested, as calculated from the strain measurements at fracture, are reported in Table VIII. A photograph of a failed specimen is shown in Figure 16. The fracture in this specimen seems to have originated in the area of one of the strain gages but this was not typical of the other failures.

TABLE VIII

Uniaxial Tension Test Results

Test	Strain at Failure o.d. $\varepsilon_{\theta\theta}$ (μ-in/in)	(Failure)
1	477	29.0
2	425	25.8
3	425	25.8
4	505	30.7
Average Failure Stress $\bar{\sigma}_{\theta\theta}$ =		27.8 ksi
Standard Deviation S =		2.4 ksi

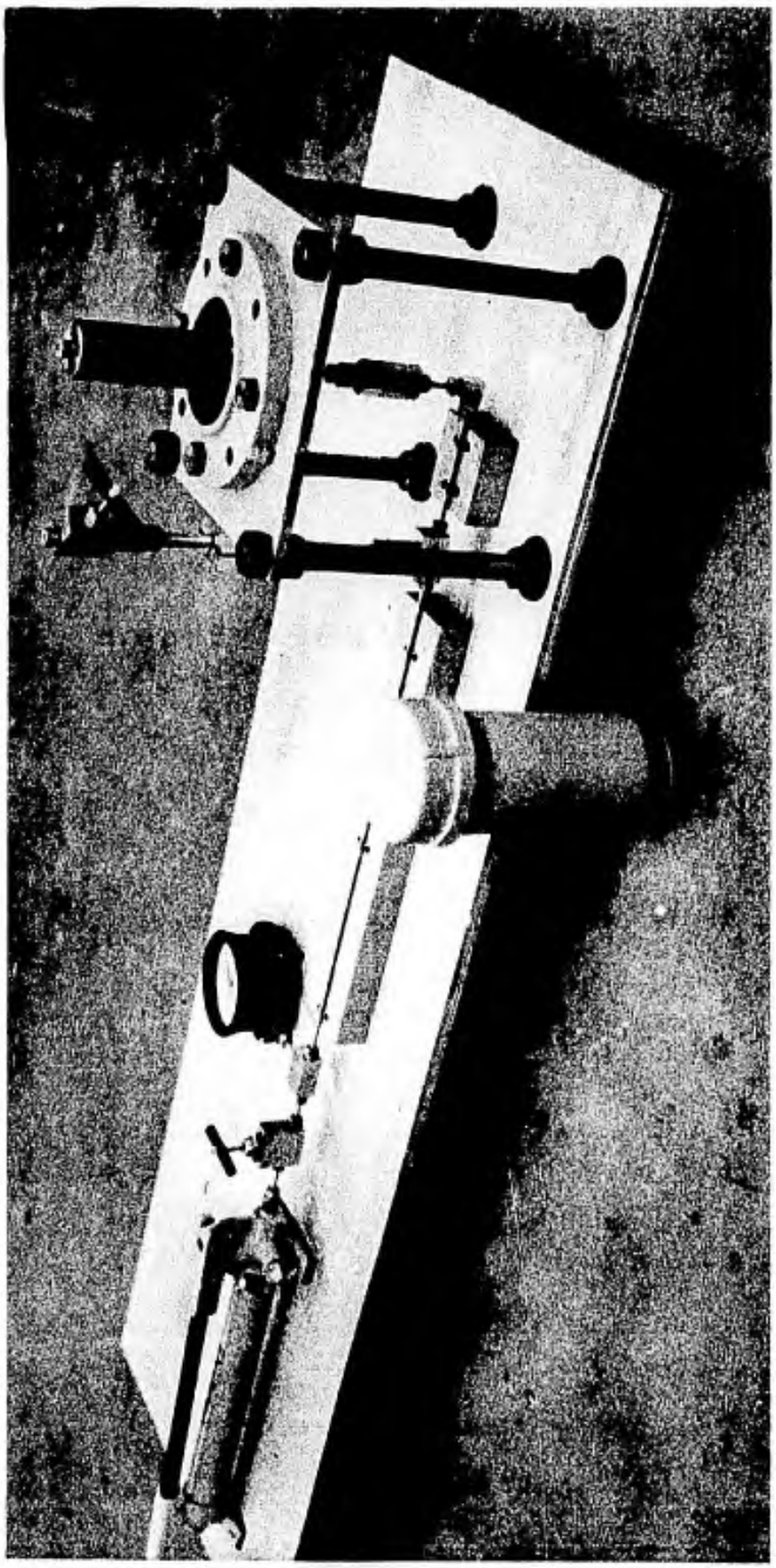

Figure 15. Tension Test Apparatus.

Figure 16. Failed Tensile Test Specimen.

The rate of application of the stress during these tests was approximately 3-5 psi/sec. The pressure increases were made in increments and the strain gages were read during the pause between increases except near fialure when the gages were monitored continuously.

Part of scatter in measured values is probably attributable to the variation in "time at high stress" between different tests due to the discontinuous nature of the incremental stress increases. Undoubtedly, static fatigue is occurring at stress levels near failure in the slow, discontinuous loading rate test. The pressurizing fluid did not appear to be penetrating the rubber bladder and wetting the specimen, but the tests were run in ambient air with a relative humidity of 30-50%.

One specimen was instrumented with two circumferential and two longitudinal strain gages in order to determine Poisson's ratio in tension. Poisson's ratio at 30% of the failure stress was 0.22 and decreased monotonically to 0.20 at a stress 90% of failure. Since only one specimen was measured, it is uncertain whether any significance may be attached to this observed decrease. Perhaps stable crack extension, perpendicular to $\sigma_{\theta\theta}$ direction at stresses less than failure, increases the $\varepsilon_{\theta\theta}$ strain without affecting the ε_{zz} strain.

D. The Experimentally Determined Failure Envelope in Biaxial Stress Space

1. Failure envelope in the compression-compression stress quadrant

A summary of the strengths measured in the various stress states investigated in this study appear in Table IX. Figure 17 is a plot of the average strength values in biaxial stress space. A solid line is

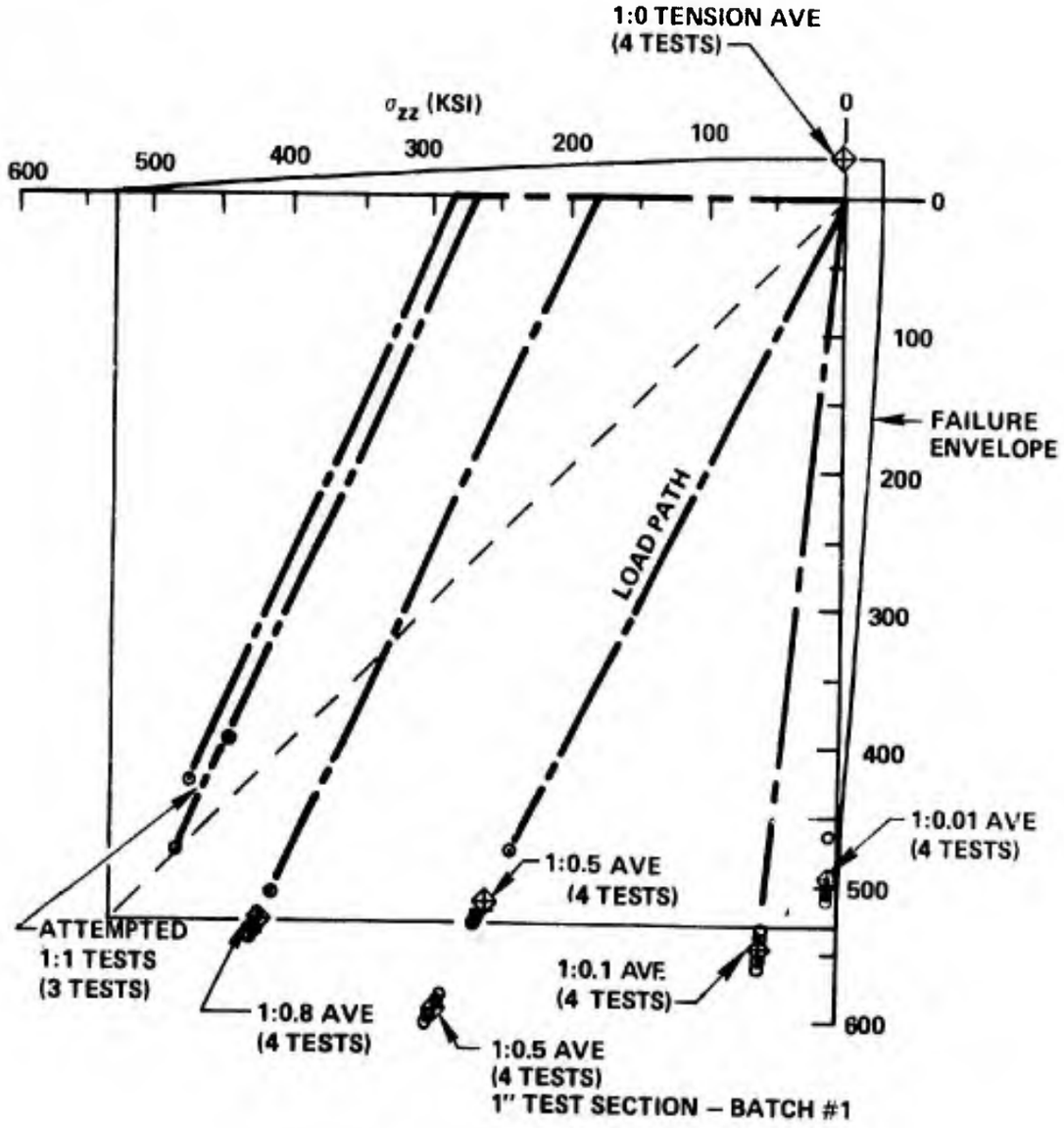

Figure 17. Biaxial Compressive Strength Data.

drawn through the data representing the failure envelope. Load paths are shown which indicate the stress states developed in the specimen test section as the load was increased.

The most striking aspect of the data is that the measured values plot almost horizontally across the biaxial compression quadrant. Varying the magnitude of the second principal compressive stress has only a very slight effect on the strength. This is in contrast to experimental data on concrete,[33] mortar,[34] granite rock,[35] to experimental data on alumina,[36] and recently proposed theories.[37-38] All of the above show or predict the 1:0.01 or 1:0 compressive strength to be much less than the 1:0.5 compressive strength. The present data shows that the 1:0.1 strength is almost equal to, being slightly greater than, the 1:0.5 strength. The point in this quadrant where the failure curve makes an abrupt upturn, i.e., where the compressive strength begins to decrease, is in the vicinity of the intersection of the failure curve with the uniaxial compression axis as shown by the solid line in Figure 17.

The average strength in the 1:0.01 stress state of 493 ksi is 7% lower than the best fit horizontal straight line through the 1:0.8, 1:0.5, and 1:0.1 average values which shows a strength of 528 ksi with a standard deviation of the mean values of 14.5 ksi. However, any eccentricity or misalignment in the test specimen producing a tensile bending stress of only 2 ksi would lower the observed 1:0.01 compressive strength to the 493 ksi value from the 528 ksi horizontal line strength. It is possible that an inadvertent tensile stress of such magnitude could have been produced during the 1:0.01 tests. Careful design,

TABLE IX

Test Results for AL-995 Alumina

TEST RESULTS ON BATCH #2 (1/2 inch long test section)

Test ($\sigma_{\theta\theta}$:σ_{zz})	No. of Specimens	$\sigma_{\theta\theta}$ Average Strength (ksi)[1]	Standard Deviation (ksi)
Compression 1:1	3	465*	22
Compression 1:0.8	4	528	13.5 (on load path)
Compression 1:0.5	4	514	22
Compression 1:0.1	4	543	12.2
Compression 1:0.01	4	493	20.5
Tension 1:0	4	27.8	2.4

*cracked in preloading but test continued.

TEST RESULTS ON BATCH #1 (1-inch long test section)

Compression 1:0.5	4	572	8.7

[1] 1 ksi = 0.703 kgm/mm^2

fabrication and assembly procedures were used to avoid these inadvertent stresses, but the exactitude with which such tests must be performed leaves some doubt. It is also possible that some reduction in compressive strength does occur very near the uniaxial compression axis. A theoretical discussion of such a possibility will be presented in Chapter VI. The testing techniques employed in this study are not capable of resolving this question.

The ratio of the measured compressive strength to the measured uniaxial tensile strength is seen to be approximately 18. The significance of this value and its interpretation in terms of failure mechanisms will be discussed in Chapters V and VI.

ii. Comparison of measured strength values

Broutman and Cornish[36] and Sedlacek[19] have measured the uniaxial compressive strength of WESGO AL-995 alumina. Broutman and Cornish measured an average value of 215 ksi with a standard deviation of 33 ksi on straight-walled tubes with dimensions similar to the present study. This value is approximately one half the strength measured on the 1:0.01 test specimens. Sedlacek measured the uniaxial compressive strength on rings subjected to external fluid pressure with dimensions i.d. = 2.000 inches, height = 0.450 inches, and wall thickness = 0.075 inches. His average value of measured strength on twelve specimens was 448 ksi with a standard deviation of 36 ksi. Broutman and Cornish[36] also measured the 1:0.5 biaxial compressive strength of this alumina to be 591 ksi with a standard deviation for five specimens of 49 ksi.

Imperfect testing techniques always yield lower values of measured compressive strength as will be discussed in the following section. The measured value of compressive strength must always be considered as the lower bounds of the true strength. There is no way to demonstrate unequivacally that the measured value is, in fact, the true strength of the material tested. There does appear to be a variation in compressive strength between different batches of the AL-995 alumina which may account for some of the discrepancy in the various measured

values. The 1:0.5 biaxial compression tests on two separate batches of material tested in this study showed a difference of 11% in the average measured strengths.

Sedlacek measured the tensile strength of AL-995 alumina under several different stressing rates. He observed that the strength decreased with decreasing loading rate. This is consistent with the known static fatigue behavior of this material. The loading rate used in this study was $\frac{1}{20}$ of the slowest stress rate (100 psi/sec) employed by Sedlacek in which he measured a tensile strength of 28.7 ksi. Our measured value of 27.8 ksi is in reasonable agreement with Sedlacek's measurements considering the "time at stress" dependency for tensile failure in these materials. Our data also supports Sedlacek's findings that the strength decreases with decreasing loading rate, since our 3-5 psi/sec measured strength was lower than his 100 psi/sec strength measurements.

iii. Testing problems

It can be seen from the general shape of the failure envelope in Figure 17 that in the tension-compression quadrant the compressive stress required for failure is very sensitive to the amount of transverse tension. In any mechanical test where the property of high compressive strength is to be measured, the stress state imposed must be free of any tensile stresses since small amounts of tension will greatly decrease the observed compressive stress at failure. This is particularly true for a brittle, high strength, material such as AL-995 alumina where the compressive strength is 18 times the tensile strength. Uniaxial compression tests are very difficult to perform. Small

amounts of transverse tension, arising from ellipticity of diameters, lack of concentricity of diameters, lack of squareness on loaded ends, or misalignment of the loading fixture, will produce a tension-compression stress state in which the applied compression necessary for failure is considerably less than the uniaxial compressive strength.[3] In compressive biaxial or triaxial stress states the minor applied compressive stresses can cancel the inadvertant tensile stresses developed and the specimen will fail in a wholly compressive stress state.

Another source of stresses in compression testing which can cause premature failure is the mismatch of transverse compliance between the specimen and the test device parts which apply the compressive load to the specimen. The problem of the hardened steel compliance tubes splitting the alumina test specimen tube under axial load in the 1:1 biaxial compression test is an example of a general design problem which will be encountered when trying to measure or use the compressive strength of brittle ceramics. When the steel device element which applies the compressive load to the brittle ceramic has a lateral stiffness different from the ceramic element, high local stresses can be produced because of the mismatch in the lateral displacements under load. The static coefficient of friction between alumina and steel under high normal forces is quite large because the much harder alumina surface will tend to imbed in the steel and produce mechanical interlocking of the surfaces. For this reason the alumina and steel will tend to attain the same displacements at their interface. If the transverse stiffnesses of the two elements are not matched, the steel will put the alumina into tension or compression in the vicinity of the interface, depending on whether the

stiffness of the steel part is less than or greater than the alumina part, respectively. A simple model was used to develop the equation of the transverse stresses which can occur from the differences in Young's modulus and Poisson's ratio when the two elements have the same cross-sectional areas and are long (See Figure 18). The equation is developed as follows:

assuming:

$$\varepsilon_{xx}^{(s)} = \varepsilon_{xx}^{(c)} = \varepsilon_{yy}^{(s)} = \varepsilon_{yy}^{(c)} \quad \text{i.e. no sliding between surfaces}$$

where $\varepsilon^{(s)}$ = strain in steel element, $\varepsilon^{(c)}$ = strain in ceramic element, then from $\varepsilon_{xx}^{(s)} = \varepsilon_{xx}^{(c)}$ we get:

$$\frac{\sigma_{xx}^{(s)}}{E_s} - \frac{\nu_s \sigma_{yy}^{(s)}}{E_s} - \frac{\nu_s \sigma_{zz}^{(s)}}{E_s} = \frac{\sigma_{xx}^{(c)}}{E_c} - \frac{\nu_c \sigma_{yy}^{(c)}}{E_c} - \frac{\nu_c \sigma_{zz}^{(c)}}{E_c} \tag{11}$$

observing that:

$$\sigma_{zz}^{(s)} = \sigma_{zz}^{(c)} = \sigma_{zz}$$

for equilibrium of a free body cut across the interface:

$$\sigma_{xx}^{(s)} = \sigma_{yy}^{(s)} = -\sigma_{xx}^{(c)} = -\sigma_{yy}^{(c)}$$

substituting the identities from above into Equation (11) and simplifying:

$$\sigma_{xx}^{(c)} = \sigma_{yy}^{(c)} = -\sigma_{zz} \frac{E_c \nu_s - E_s \nu_c}{E_c - E_c \nu_s + E_s - E_s \nu_c} \tag{12}$$

where: E_c = modulus of cermic

E_s = modulus of steel

ν_c = Poisson's ratio for ceramic

ν_s = Poisson's ratio for steel

σ_{zz} = normal stress across interface

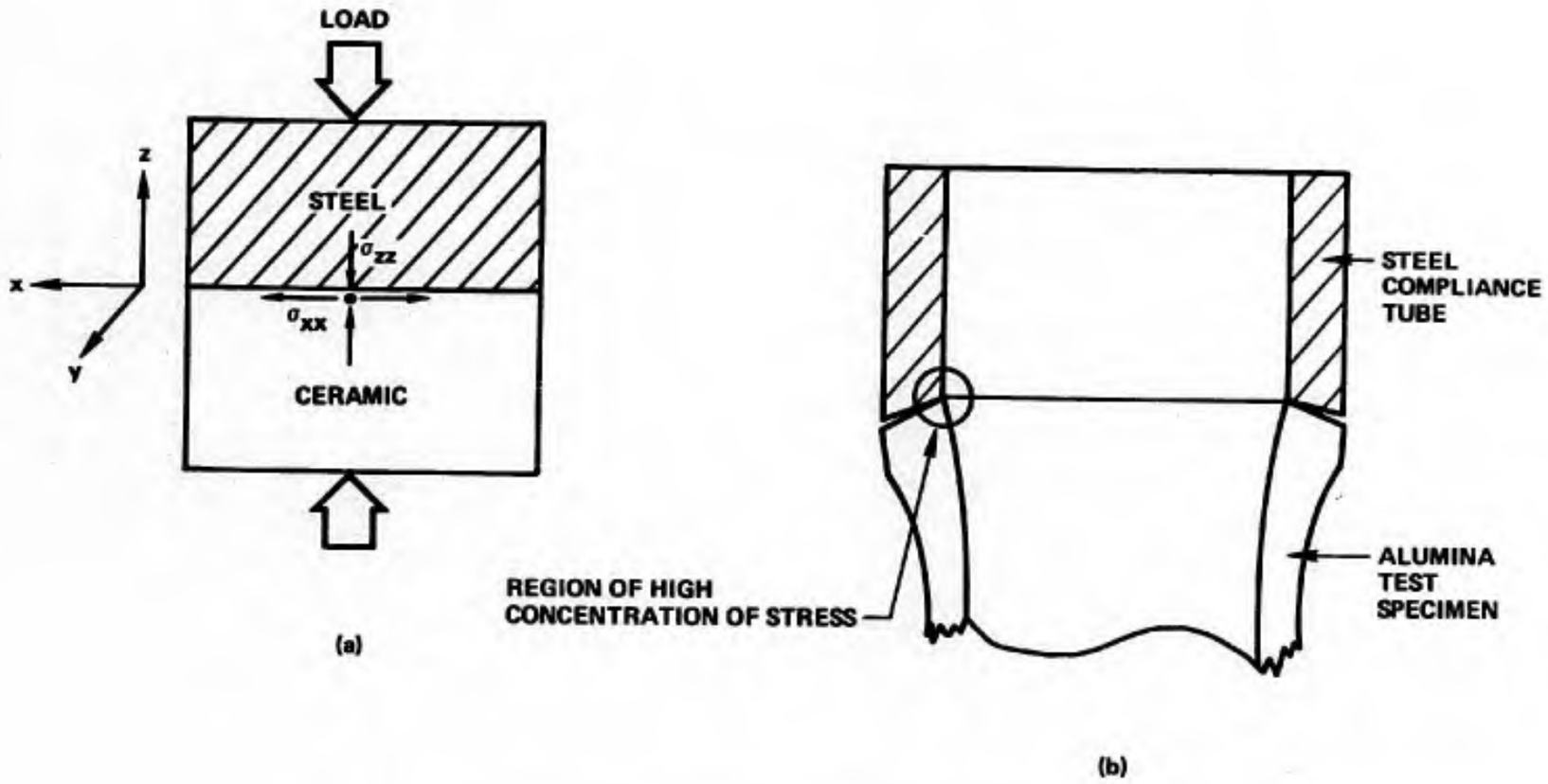

Figure18. 1:1 Biaxial Compression Testing Problems.

Even though the magnitude of these $\sigma_{xx}^{(c)}$ and $\sigma_{yy}^{(c)}$ transverse tensile stresses in the 1:1 compression test were only 1/3 to 1/2 the tensile strength of Aℓ-995, the specimen tube cracked. A second phenomenon which induced this cracking was probably occurring. Because of the geometry and stress condition, rotations were being produced in the alumina caused by the displacements necessary to match the steel tube displacements. This rotation produced high concentrations of stress in the alumina in the regions indicated in Figure 18. Cracks were produced in the alumina tube in the orientations shown in Figure 13.

A mismatch in the transverse stiffness between a brittle ceramic element and the element which loads it can produce high local stresses in the ceramic. This is so because of the necessity to accomodate displacements in the ceramic and because of possible rotations occurring in the ceramic element which produce very high, local concentrations of stress. In general, a stiffness mismatch which is the result of the steel loading element being either more stiff than the ceramic element or less stiff can produce concentrations of stress (Figure 19). The 1:1 compression strength measurements may be low because of cracks caused in this manner in the preloading, and several other reported values of compressive strengths for brittle ceramics may be too low for similar reasons. The use of finite element analysis in the design of the loading elements could be employed to avoid such situations.

If a transverse compression is applied parallel to the interface between the loading element and the ceramic element, as in the 1:0.5 test where external fluid pressure creates compressive σ_{rr} and $\sigma_{\theta\theta}$ stresses, the mismatch in transverse stiffness is not nearly so severe

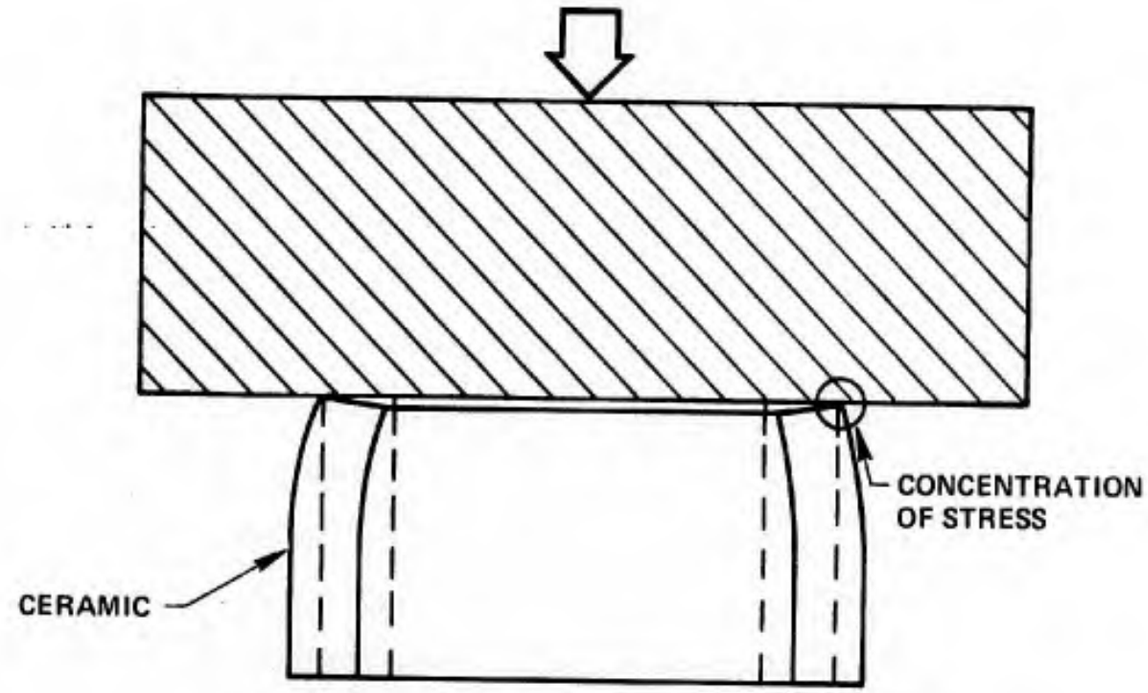

(a) LOADING PLATE MORE STIFF THAN CERAMIC

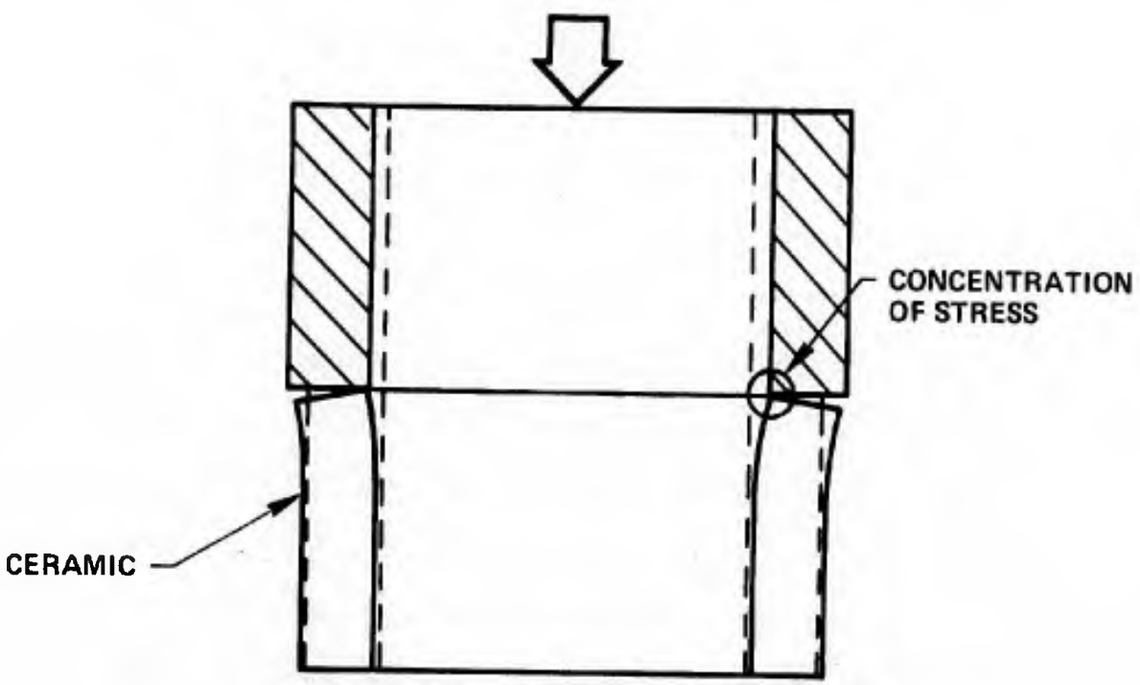

(b) LOADING PLATE LESS STIFF THAN CERAMIC

Figure 19. Rotations Produced by Mismatch in Transverse Stiffness of Loading Elements.

a problem because the magnitudes of the transverse displacements in the two elements are much less. Under most loading conditions where a surrounding external pressure is present, all three principal stresses in both elements will remain compressive. The magnitude of the transverse displacements, which induce the rotations, will be smaller and the ε_{xx} and ε_{yy} strains will approach zero or become negative. This is undoubtedly one of the reasons why the highest compressive strength values are measured in test utilizing external pressure acting on a closed-end tube. One of the major causes of lower strength values measured in uniaxial compression, as compared to biaxial compression, is that the uniaxial compression strengths were measured by applying an axial load with no provision for eliminating the loading platten-specimen stiffness mismatch.

The sequence of application of the loads to a biaxial compression test specimen (the load path) may have some effect on the measured strength. As will be discussed in detail in subsequent chapters, compressive failure is the result of the accumulation of crack damage produced in the specimen under increasing loads. The nature of this crack damage is dependent on the magnitudes of the principal stress and the ratios of their magnitudes. Two specimens which have been brought to the same failure stress state via different load paths may contain different geometries of crack extension. This would result in each having a different resistance to structural collapse.

CHAPTER IV

INVESTIGATION OF SPECIMEN DAMAGE UNDER COMPRESSIVE LOADS

A. Spalling Studies

During the disassembly of some tests in which the specimen had been subjected to stress levels insufficient to cause failure, it was observed that spalling (chipping off of small pieces of alumina) had occurred on the inside diameter of the test section. Sedlacek had also noticed this phenomenon in the course of his testing program[19] in which he measured the compressive strength of AL-995 alumina with thin walled tubes. A literature study revealed that such spalling had been observed by F. Adams[39] while testing thick walled tubes of rock in compressive stress states in 1913. Mr. Adams made a general speculation that such phenomenon might be related to the mechanism of failure. A study was carried out to establish the nature of the alumina spalling and its relationship to the applied stresses.

1. Experimental techniques

The 1:0.5 biaxial compression test was used to study the spalling because of its ease of repetition on the same specimen and its low cost. The technique was to:

(1) Pressurize the specimen to a predetermined stress level.

(2) Remove the load and disassemble the test device.

(3) Observe the spalling

(4) Reassemble the test device and repressurize the specimen to a higher stress level.

This procedure was continued until the specimen failed which was after 12 cycles. Once the intended stress level was reached for each

pressurization cycle, the pressure was decreased very slowly to prevent the creation of any damage in the specimen from dynamic effects which can occur during rapid pressure decreases. The rise time of the pressure was approximately equal to the decrease time being very short at low stress levels and approaching three minutes at the highest stress levels.

The technique devised to observe the spalling was by surface replication of the inside bore of the specimen, utilizing centrifugally cast polyvinyl chloride (PVC) material as the replication medium. Several materials were investigated before the PVC material was found. The replicating material had to make an accurate, detailed impression of the surface and exhibit some adhesion to the alumina without developing excessive adhesion. The inside bore area to be replicated was quite large which eliminated the standard techniques for replication such as those using cellulose acetate-acetone solvent system employed by electron microscopits. Cellulose acetate does not work well over large areas because of the formation of bubbles. Also, cellulose acetate becomes brittle when hardened and shows no tendency to adhere to alumina. Several varieties of rubber which cure at room temperature were tried. These were very successful in all respects except they would either bond with high adhesion to the alumina or not at all. No intermediate bond strengths could be obtained. Either no adhesive bond was formed or the strength of the adhesive bond would be greater than the cohesive strength of the material and it could not be removed without tearing.

The PVC material which ultimately gave success was supplied by Hastings Plastic Company, Santa Monica, CA which was designated by them

as MOLDKOTE SEALER #1906. This material is applied as an organic solvent solution of low molecular weight vinyl chloride polymer. On evaporation of the solvent vehicle, the vinyl chloride polymerizes out of solution as a solid sheet of polyvinyl chloride. The material was obtained in a clear, unpigmented form and in a form with a dark green pigment which rendered the material opaque. An important property of the clear, unpigmented material was that it polymerized into a glassy molecular structure which resulted in it being inactive in polarized light. The polymerized PVC was stiff, yet flexible enough for easy handling. It exhibited very little tendency to take on permanent set if slightly stretched during handling. This dimensional stability allowed accurate position and dimension measurements to be made on the replica.

The centrifugal casting of the PVC into the bore of the specimen was accomplished by holding the specimen in the chuck of a lathe and applying the PVC to the inside bore of the specimen with a hypodermic syringe. A suction chamber was installed around the specimen to accelerate removal of the vapors of the organic vehicle. With the specimen rotating at 600 rpm, 15 ml of vinyl chloride solution was applied to the bore. The rotation speed was then increased to 1600 rpm and the suction chamber was installed. After 2 1/2 hours the specimen was removed and allowed to cure in ambient for a minimum of 6 hours before removal of the replica. The fully cured PVC replica had a thickness of 0.004 inches. The centrifugal force helped push the vinyl chloride solution into intimate contact with the details of the alumina surface.

The replicating ability of the PVC was exceptional, being equal to that obtained with the cellulose acetate technique. The adhesive bond strength of the cured PVC to the alumina was such that it took approximately 40 oz. of force to peel a one inch wide strip off at an angle of 90° to the surface. This was considered a sufficient bond strength to remove spalled particles from the surface. After several replication cycles a small deposit of residual material (probably plasticizer) was left on the surface. This could be removed by rinsing in solvent. Attempts to replicate areas using the PVC without centrifugal casting were unsuccessful.

To study the outside surface of the specimen, a clear, cellulose acetate backed adhesive tape (SCOTCH ELECTRICAL ADHESIVE TAPE #7) was applied. The tape was simply pressed into place at room temperature. Its acrylic adhesive bonded very well to the alumina surface. (90° peel force for the one inch wide tape was ~3-5 lbs.). This tape could remove spalled particles but did not replicate the surface.

Two kinds of PVC replicas were made. Clear replicas were in place during the pressurization cycle. After depressurization the clear replica was removed; it contained the spalled particles on its surface which were tightly attached thereby preserving their positions and orientations. A second green replica was made to record the new surface features created under the stress. This process was repeated for 12 progressively higher pressurization cycles on a single 1:0.5 test specimen from zero stress to the stress at which it failed. Table X shows the stress levels to which the specimen was subjected and the replicas which were made at each stress level.

TABLE X

Stress Levels Studied in the 1:0.5 Compression Test

Pressurization Cycle	Maximum Pressure Applied to Specimen (ksi)	Maximum Stress in Specimen $\sigma_{\theta\theta}$ (ksi)	Percent of Failure Stress $\frac{\sigma_{\theta\theta}}{\sigma_f} \times 100$	Designation of Replica Sets Taken: Clear (during pressurization)	Designation of Replica Sets Taken: Green (after pressurization)
	0	0	0		A
1	7.8	74.0	15	B	C
2	13.5	129.0	26	D	E
3	18.9	180.0	36	F	G
4	27.3	260.0	52	H	I
5	35.1	334.0	67	J	K
6	43.7	416.0	83	L	M
7	46.1	439.0	88	N	O
8	48.8	465.0	93	P	Q
9	50.8	484.0	97	R	S
10	51.5	491.0	98	T	U
11	52.5	500.0	100	V	W
12	52.3	498.0	Actual Failure	Y	-

Before each replica was taken, a grid of fiducial marks was applied to the inside bore of the test specimen with a 6H lead pencil. The appearance of the grid is shown in Figure 20. The grid was applied by sliding a stencil template tube, containing a rectangular grid pattern of dots as 0.040 inch holes drilled through its wall, into the specimen

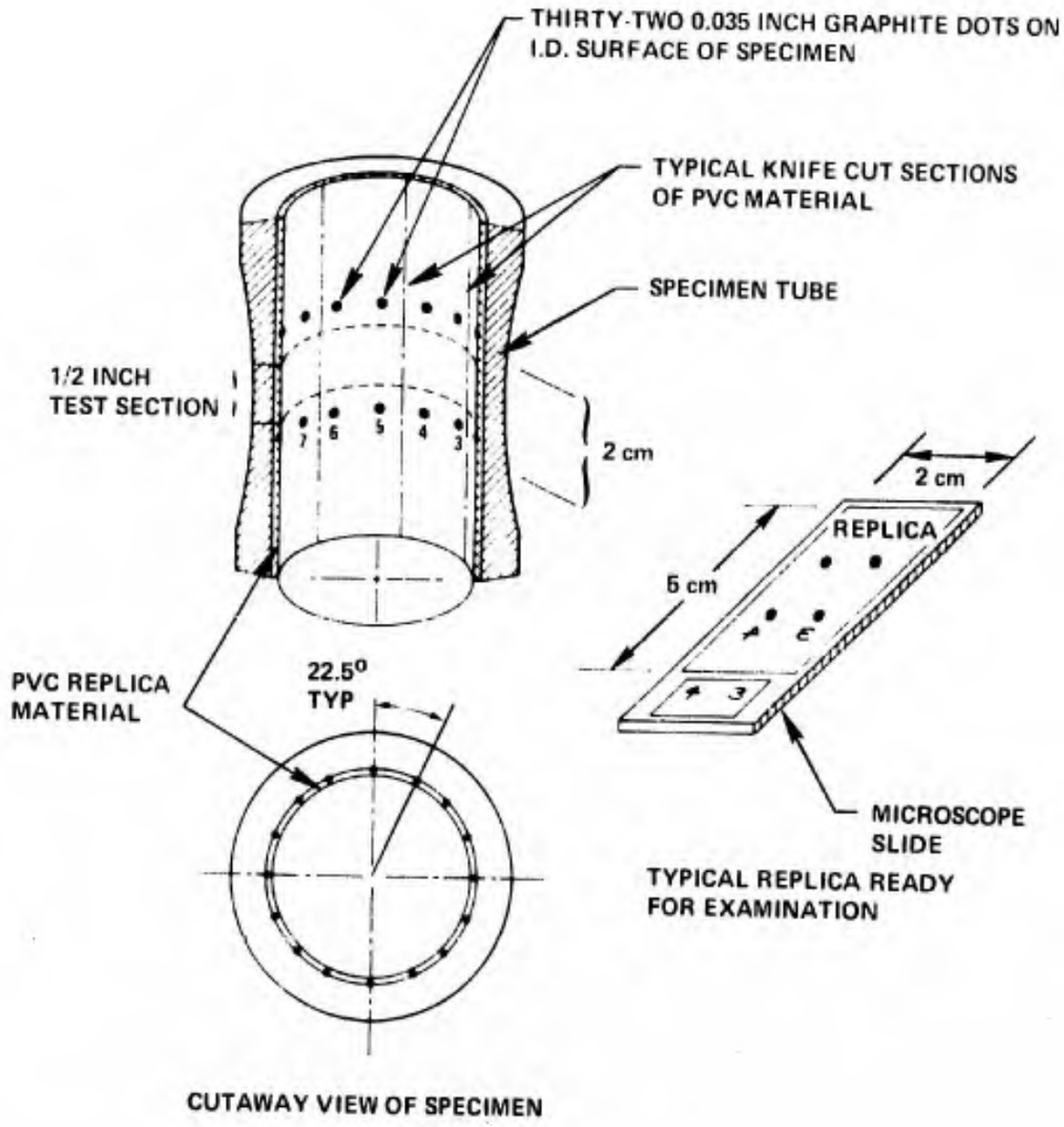

Figure 20. Orientation of Replicas.

bore. The template was aligned each time to a permanent fiducial mark on the specimen. By marking through the template a precise pattern of identically positioned dots could be obtained each time. When the replica was removed, the graphite transferred to the PVC creating a grid which could be used to locate identical positions on replicas taken at different stress levels. This enabled the recording and comparison of the progressive damage occurring to the specimen in any microscopic area of the surface over the entire range of stress levels.

The replica was removed from the specimen by sectioning the film into eight 2 cm. wide strips with a razor knife blade and carefully peeling off each strip. A very light cutting force was used to prevent knife blade damage to the alumina. The replicas were only handled on the ends which were subsequently cut off and not used for the study. The orientations of the sections and the dimensions of the replica strips used for the study are shown in Figure 20. The replicas were placed on glass slides for ease of handling and numbered as to stress level and position on the specimen surface.

ii. Examination and analysis of replicas

Measurements were made on the replicas to establish the nature and amount of damage produced on the inside diameter of the specimen at successively higher stress levels. The percent area spalled off at each stress level and histograms of the sizes of the spalled particles were determined. This was done by scanning the replicas with a Leitz-Ortholux microscope using special illumination techniques. The X-Y stage of the Leitz microscope was fitted with a slow speed synchronous motor drive which moved the stage at a constant 10 microns/sec. A 20x

dry objective in combination with a 10x cross-hair eyepiece was used to view the 200x magnified field. The stage was set at the starting position of the scan and the motor drive was started. As the alumina particles on the replica passed under the cross hairs a push button was depressed which applied a voltage to offset the pen on a Sanborn 299 recorder. As the particle passed from under the cross hairs, the push button was again depressed which removed the recorder pen voltage. The recorder paper was driven at 5 mm/sec. and the pen offsets recorded particle size and information on spacing between particles. By recording the length of time spent traversing particles and comparing this to the total scan time, a "percent area covered by spalled particles" value could be obtained. A schematic of the instrumentation for making these measurements is shown in Figure 21.

The time consuming manual search over the replicas was used because distinguishing alumina particles from the detailed replica background would have been extremely difficult for an automatic, electronic sensor. Automatic techniques are available for more precise analysis of particle distributions but none were capable of meeting the total requirements of the investigation. It is felt the simple techniques employed yielded information with sufficient statistical accuracy to demonstrate the general trends.

The alumina crystal (α-alumina) is optically uniaxial.[79] This permitted the identification of most particles by viewing them under crossed polars. Some particles, however, would have their optic axes oriented so that they would not appear bright in crossed polars and would be unobservable. To assure that these particles were counted, a

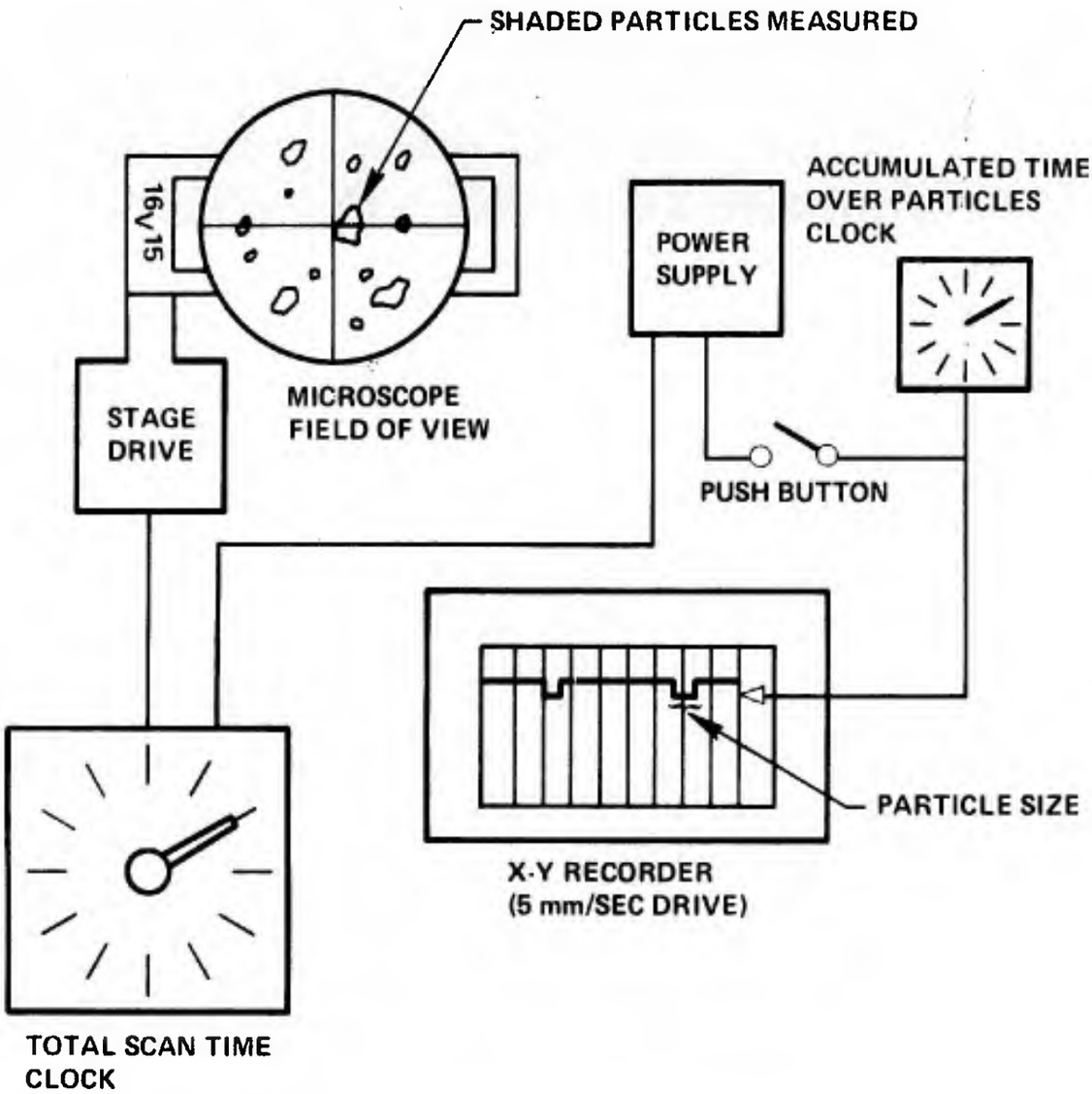

Figure 21. Particle Distribution Measurement Apparatus.

low level reflected illumination was used in conjunction with the polarized, transmitted illumination. The direction, intensity and angle of polarization of both illuminators was constantly varied by the operator to inspect each piece of the replica as it traversed the field of view. With these techniques all alumina particles could be identified.

Large enough pieces of the replicated test specimen survived the fracture process to permit the determination of the major fracture path. The major longitudinal fracture path occurred in the vicinity of the 15-16 replicas; hence, these 15-16 replicas were chosen for the spalled particle analysis. Six scans were made on each of the ten clear replicas which had been on the specimen during the pressurization cycles at stress levels between 15% and 100% of the failure stress. The scans were each 1 cm. long and were made in the grid pattern shown in Fig. 22. Three scans were made in the $\hat{\Theta}$ direction of the specimen and three in the $\hat{Z}$ direction. The results of these scans are shown in Table XI and Figures 23, 24, and 25.

Before replica set A was made the alumina specimen was thoroughly cleaned with detergent and solvents in an ultrasonic cleaner. Careful inspection of the A replica set revealed that no particles of alumina were removed by these replicas. Nor were any particles found on the B replicas which were in place during the 15% σ_f stress level pressurization. Examination of the D replicas, in place during the 26% σ_f pressurization cycle (pressurization to a stress level 26% of the stress which caused failure), showed that alumina particles were beginning to spall off at this stress level; however, the percent of the test section area

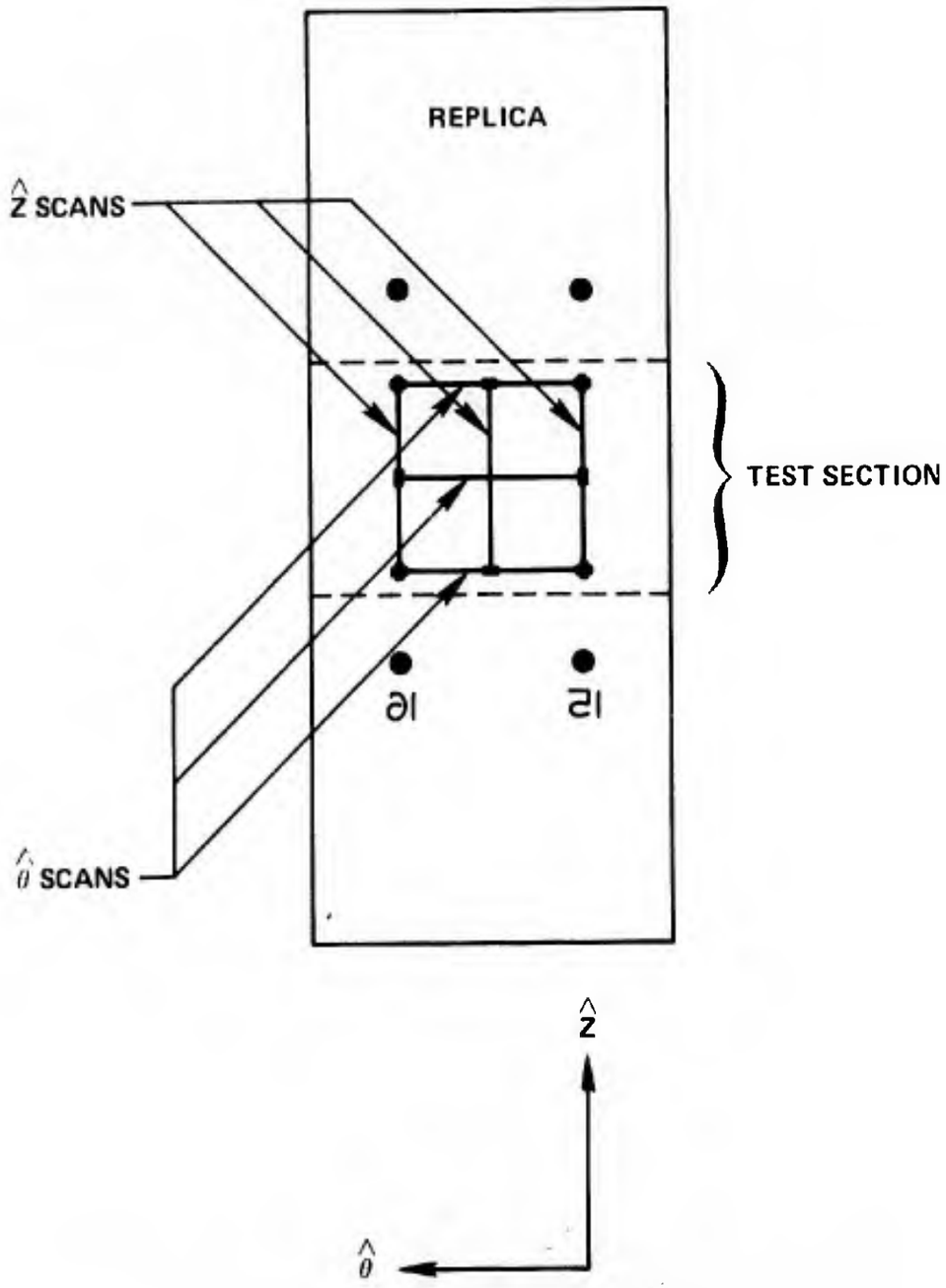

Figure 22. Replica Scan Pattern.

TABLE XI

Percent Area Spalled During Pressurization Cycles

Replica Scanned	Maximum Stress in Specimen as % σ_f	Percent of Test Section, Inside Bore Area Spalled in Pressurization Cycle: Percent Area Spalled $\hat{\Theta}$ Scans	Std. Dev. $\hat{\Theta}$ Scan Values	Percent Area Spalled $\hat{z}$ Scans	Std. Dev. $\hat{z}$ Scan Values	Percent Area Spalled $\hat{\Theta}$ and $\hat{z}$ Scans	Std. Dev. $\hat{\Theta}$ and $\hat{z}$ Scan Values
A	0	-	-	-	-	-	-
B	15%	0.0%	0.0%	0.0%	0.0%	0.0%	0.0%
D	26	0.0	0.0	0.0	0.0	0.0	0.0
F	36	0.7	0.3	0.3	0.1	0.5	0.3
H	52	1.5	0.5	2.7	0.5	2.1	0.8
J	67	4.4	1.2	4.1	0.6	4.3	0.8
L	83	8.1	0.3	7.1	0.3	7.6	0.6
N	88	8.8	1.7	8.6	1.3	8.7	1.4
P	93	9.4	3.77	12.7	1.4	11.1	3.1
R	97	16.5	1.4	12.6	2.8	14.6	2.9
T	98	15.6	3.0	16.8	1.5	16.2	2.2
V	~100	21.5	3.2	31.5	11.2	26.5	9.2

covered with spalled particles was much less than 1%. Only one or two particles per cm^2 were present.

The percent of total area covered by spalled particles was determined from the clock which recorded the time the cross hair was over particles. The percent of the linear scan line which overlay particles is equal to the percent area covered by particles. Table XI shows the

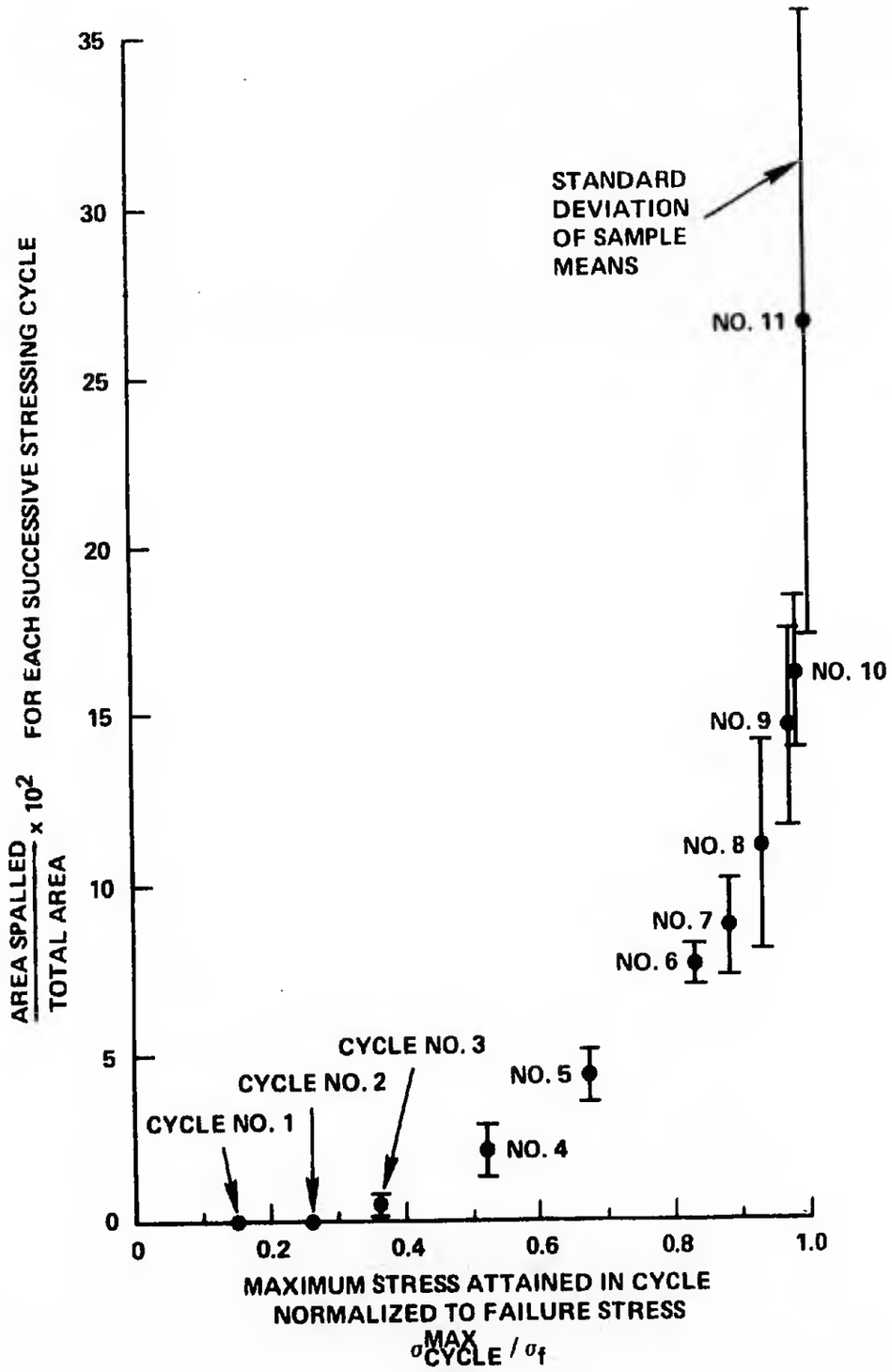

Figure 23. Percent Area Spalled During Each Pressurization Cycle.

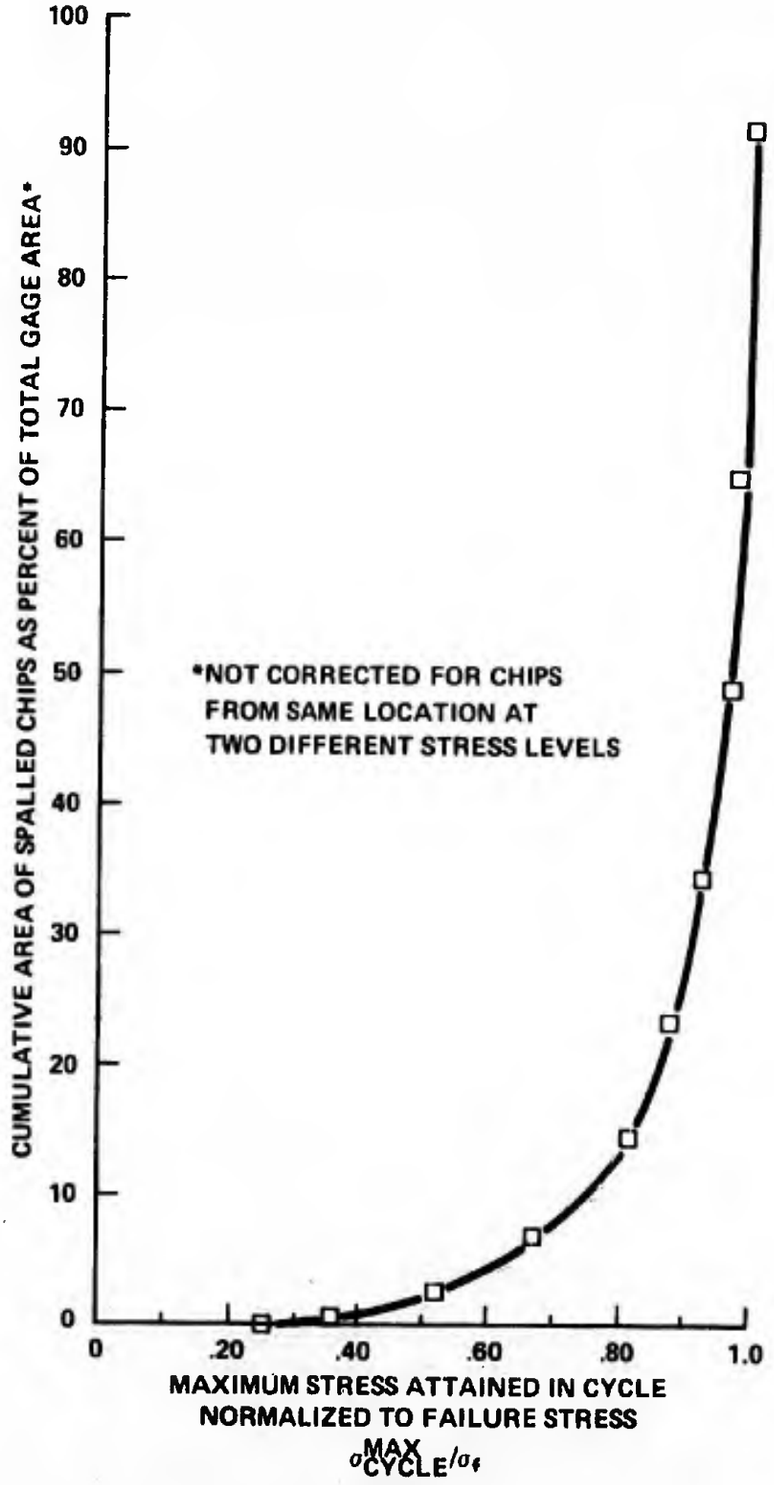

Figure 24. Cumulative Percent Area Spalled at a Given Stress Level.

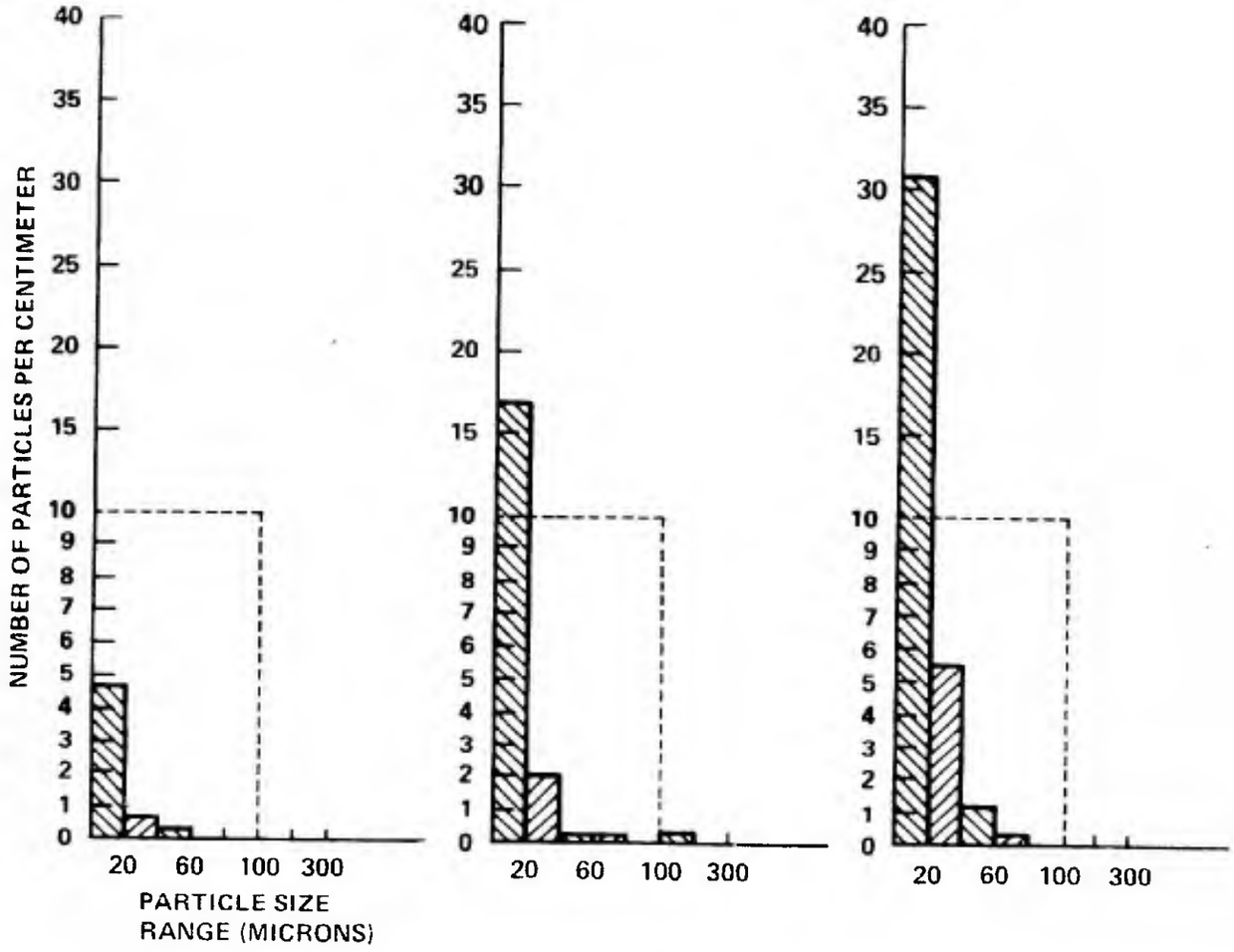

Figure 25. Histograms of Spalled Particle Size Distributions.

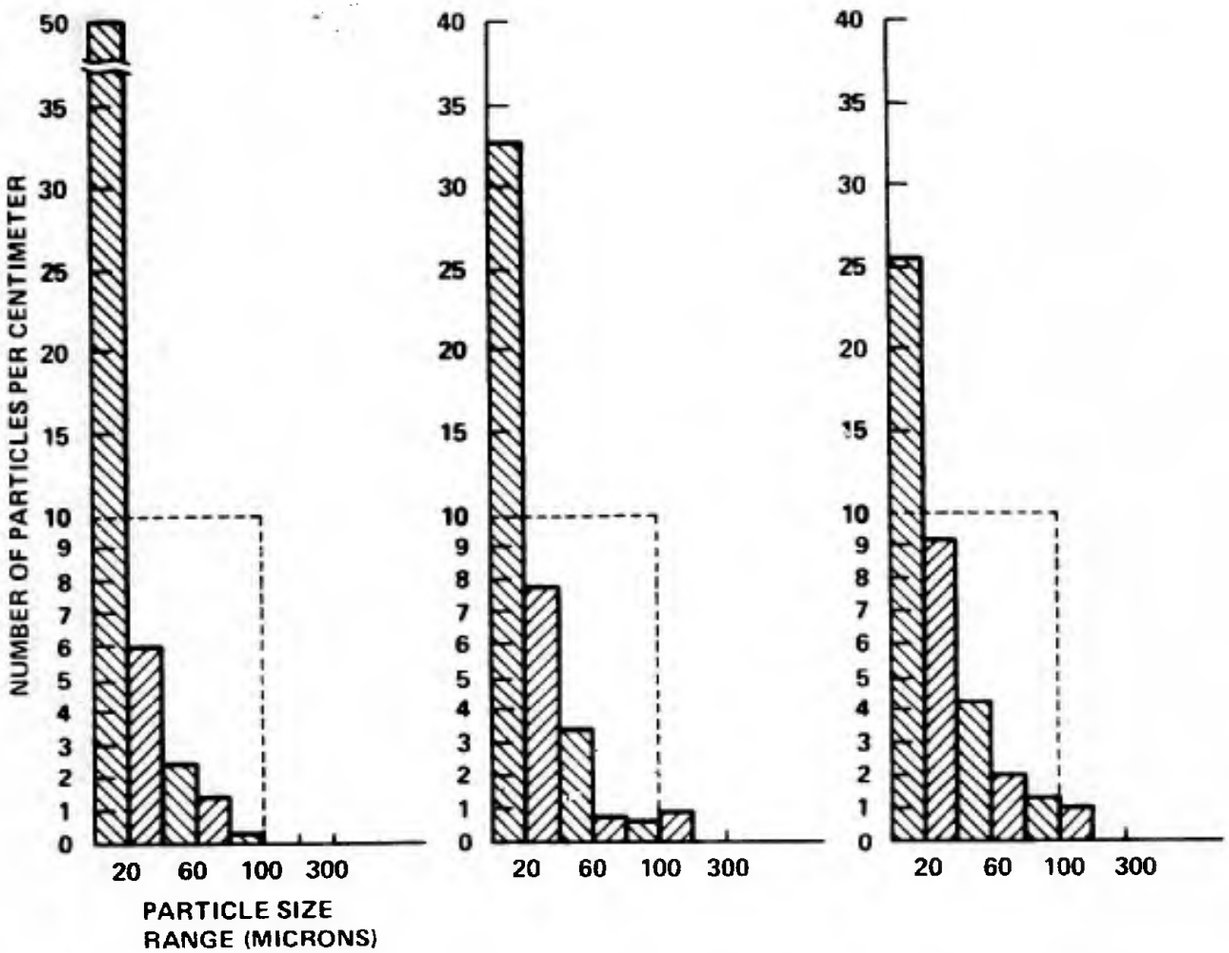

(d) REPLICA L (0.82 σ_f)

(e) REPLICA N(0.88σ_f)

(f) REPLICA P (0.93 σ_f)

Figure 25. (Continued)

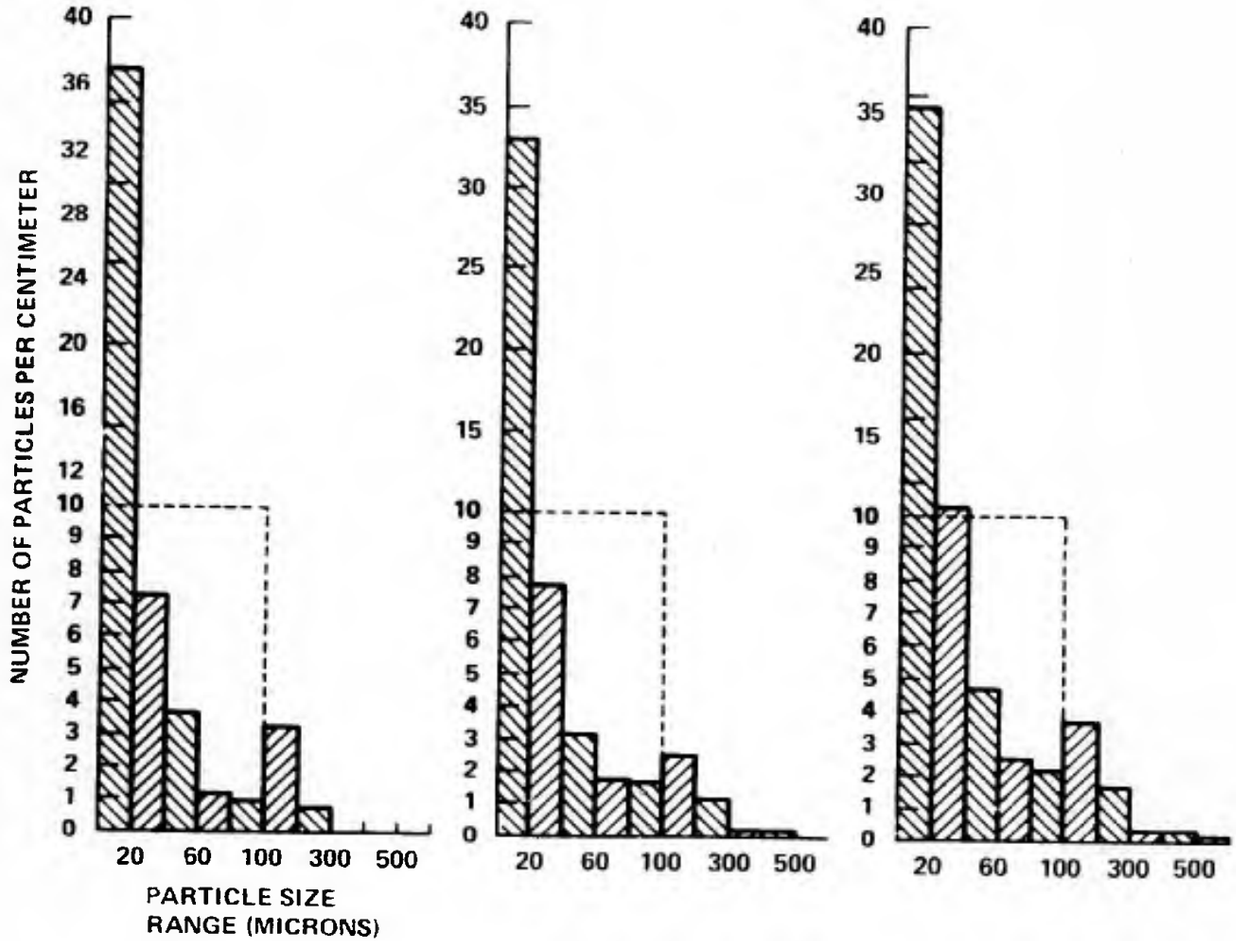

Figure 25. (Continued)

results of the measurements as average values of the percent area spalled off during the indicated stress level pressurization cycle. The average values for the three $\hat{\Theta}$-direction scans, the three $\hat{Z}$-direction scans, and an overall value averaging all six scans together is given along with the standard deviations for each average. The overall average values are plotted in Figure 23 as a function of the applied stress, which is normalized to the failure stress. The rapid increase in the amount of spalling at stress levels near failure is very apparent. This figure shows the percent area spalled during each pressurization cycle. Figure 24 plots the cumulative percent area spalled up to any specified stress level. This again is plotted as a function of the stress level normalized to the failure stress. This figure gives an indication of the cumulative damage which has occurred on the specimen's surface. It should be noted; however, that the construction of this curve ignores the fact that some spalling at higher stress levels occurs in the same location on the inside surface of the specimen during subsequent pressurization cycles. The spalling extends more deeply into the wall thickness as higher stress levels are attained. Spalling occurs from the same inside surface area more than once before structural collapse of the specimen. This phenomenon is believed to be part of the mechanism of structural collapse in the specimen.

Histograms of the particle size distributions were made from the X-Y recorder data for each replica surveyed. The length of the scan path which was superimposed over a particle was considered to be the size of that particle. This yielded a histogram of "scanned particle sizes" which is an approximation to the real distribution of particle

sizes. It should be noted that the histogram of scanned particle sizes approaches the real particle size distribution only when the distribution of particle shapes and orientations meet certain requirements.[80] It is felt that these requirements were sufficiently satisfied to allow general observations to be made about the behavior of the particle size distribution. The histograms appear in Figure 25, as number of particles per cm. (or cm^2) per size range (note scale factor changes on these graphs).

Some general trends in the behavior of the spalled particle size distributions with increasing stress level are apparent. The particles which spall off at the lowest stresses are small. As the stress level increases both the density of each particle size and the maximum size of particles increases. The 0-20 micron particle density exhibits a curious behavior between the L replica at 0.82 σ_f and the N replica at 0.88 σ_f. This small particle density increases to a maximum at 0.82 σ_f then decreases considerably and remains fairly constant up to failure. It is possible that the 0.88 σ_f stress level is the point at which interaction between flaws and extended cracks begins to occur. Such interaction would tend to decrease the number of small particles spalled and increase the number of larger ones because cracks branching between flaws would tend to produce larger spalled particles. Beyond the 0.88 σ_f stress level the densities of larger particles and the maximum size of the particles continues to increase until failure. Examination of the particle size distribution on replica V made at a stress level within 0.5% of the failure stress, shows that the largest spalled particles are approaching millimeter dimensions. Some particles on the

V replicas are 1-2mm in diameter. Photos of the replicas made in the last four stress states studied (0.93 σ_f, 0.97 σ_f, 0.98 σ_f and 1.00 σ_f) appear in Figure 26.

Some portions of the replica which was in place on the specimen during the failure pressurization cycle were found intact during disassembly of the test device. They were of insufficient quality to permit measurement of the area spalled, but they did show that very large pieces of alumina had been spalled off (see Figure 27). The locations of these replicas were not in the area where structural collapse originated, but one was near it. The sizes of the largest alumina particles on these replicas are larger than the particles on the V replica.

In an attempt to determine whether spalling was localized in certain areas of the specimen (perhaps just in the area where failure would originate at higher stresses) a photographic study was carried out on the entire set of replicas made at each stress level. A Bausch and Lomb macrocamera was used with a magnification of 4X. A flat black background with oblique light illumination from both sides was used to eliminate shadowing an increase particle-background contrast. This technique allowed the identification of particles down to 50 microns in size. Visual comparison between replicas taken in any area of the test section at a given stress level showed that the percent area spalled and the spalled particle size distributions were very similar in all areas of the test section. This uniformity of spalled particle distribution was as consistent on the V replica taken at $\sim 1.00\ \sigma_f$ as the ones at lower stresses.

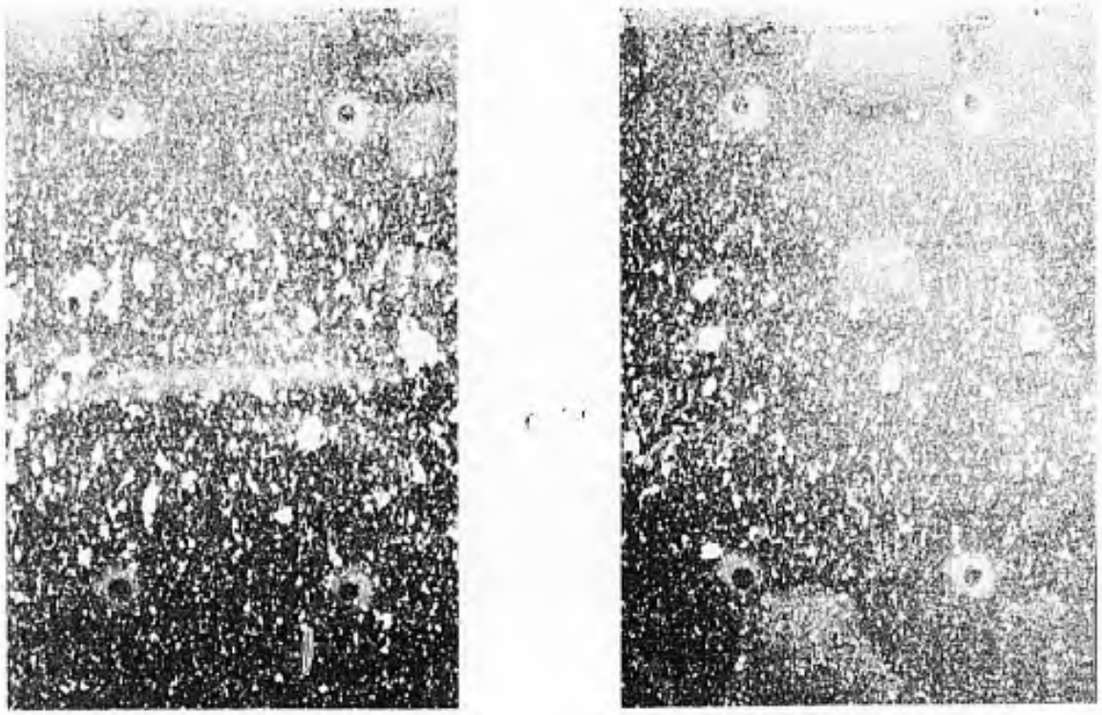

(a) REPLICA V (1.00 σ_f)

(b) REPLICA T (0.98 σ_f)

(c) REPLICA R (0.97 σ_f)

(d) REPLICA P (0.93 σ_f)

Figure 26. 1:0.5 Compression Test Replicas Made at Stress Levels Near Failure. (Horizontal Spacing Between Dots 1 cm)

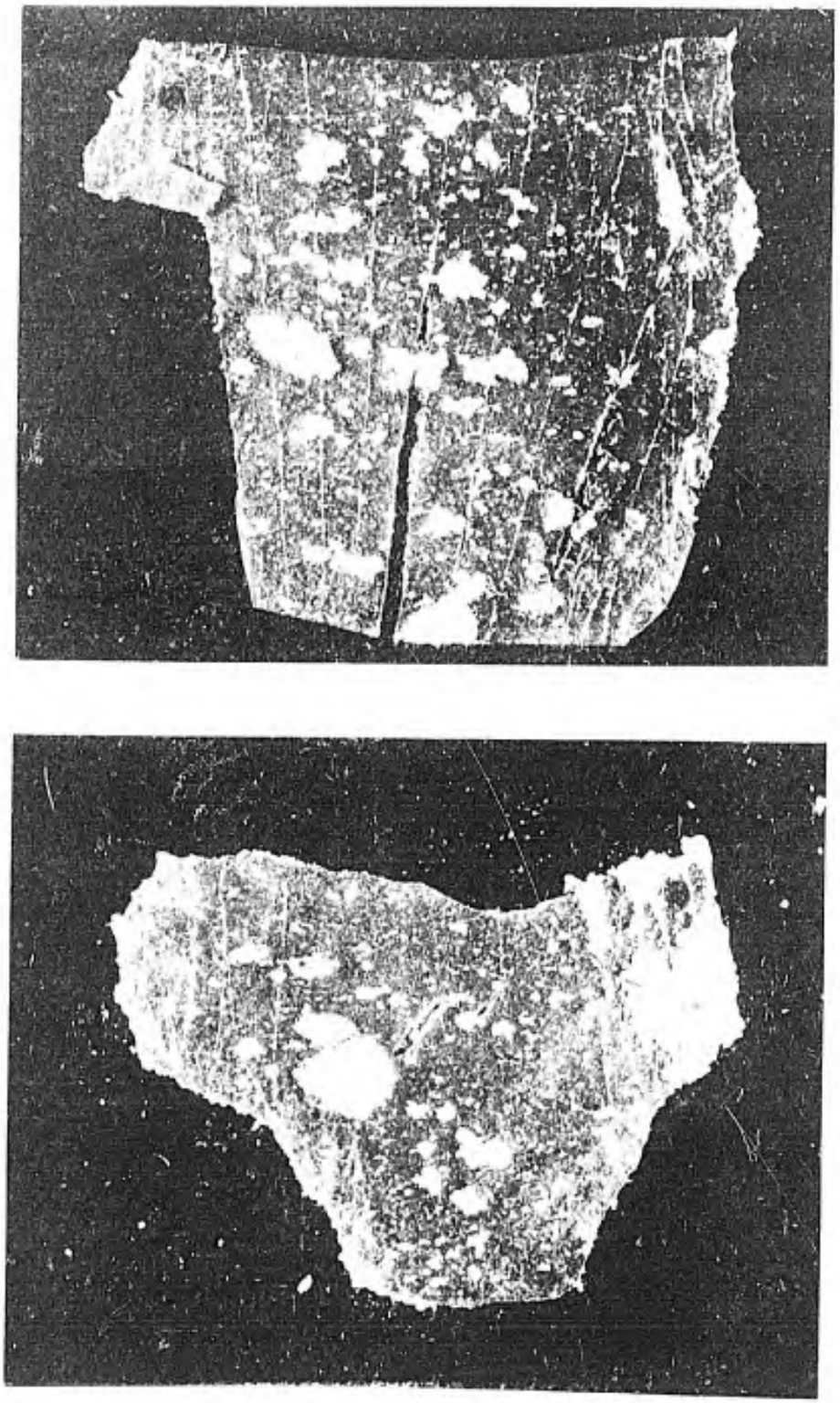

Figure 27. Particles on Portion of Replica from Failed Specimen. (Magnification 4X)

The three-dimensional nature of the spalling phenomenon is of importance to a determination of the structural collapse mechanism of the specimen. To examine this aspect, photos made of the replicas taken from the region of the test section where failure originated were printed on film as 8X enlargements. The spalled particles appeared dark and the background clear. By overlaying the negatives made of the failure region replicas at each stress level, the relationship between the positions of spalling at successively higher stress levels could be studied. Some interesting aspects of the relative locations of the spalling activity at different stress levels were revealed. At lower stress levels ($\sigma < 0.9\ \sigma_f$) the spalled particle positions concentrated to some extent around grinding marks left on the surface from the final surface finishing operation. Some tendency for spalled particles to come from the same or immediately adjacent positions was observed; however, the small size of the particles made the distinction between superimposed or adjacent particle positions difficult. One property of two superimposed replica photos taken at different stress levels was the formation of patterns similar to Moire' patterns if the fiducial marks on each negative were not exactly superimposed. To obtain such patterns, a relationship between the particle positions on each replica would be required. This relationship between the arrays of spalled particle positions is believed to be the result of such particles being spalled from the same or adjacent positions on the specimen's surface. Although some concentration of the spalling activity was observed at the lines of surface damage produced by final grinding, the reminder of

the particle positions appeared to be randomly distributed at stress levels less than 0.9 σ_f.

The particle patterns for stress levels above 0.9 σ_f showed less tendency for the larger particles to concentrate at the lines of machining damage. Moiré-like patterns could still be seen developing for the smaller particles. A very obvious property of these high stress patterns was the clustering of large particle spalling at successively higher stress levels. Large particles on each replica showed a strong tendency to occur in positions where large particles had previously spalled. In some instances the positions were superimposed; in others they were adjacent. The positions of the clusters of large particle spalling appeared to have a random distribution over the replica. To summarize, the spalling of large particles at stress levels above 0.9 σ_f occurs in clusters which appear to be randomly distributed on the surface of the specimen.

To complete a description of the spalling, the shapes of the spalled particles must be characterized. The planar shape of the particles can be seen from the photos (See Figure 26.). They are equant, i.e., they are not predominantly elongated in one principal direction of the specimen [the horizontal and vertical directions on the photographs (Figures 26 and 27) were the $\hat{\sigma}_{\theta\theta}$ and $\hat{\sigma}_{zz}$ principal stress directions, respectively]. The thicknesses of the particles were measured with an optical microscope. The thickness of the smaller particles ranged from 10 to 50 microns and the larger particles ranged in thickness from 50 to 200 microns. The smallest particles (0-50 micron planar dimensions) were chunky being composed of one to a few grains or crystallites. For the

larger particles the ratio of thickness to planar dimension was quite constant, being approximately 1:10 to 1:30. The larger particles could be described as thin plates, one to a few grains thick, and containing many grains in their planar areas. The large particles on the portions of the replica recovered after specimen failure also had values of the same ratio of ~1:20.

The adhesive tape placed around the outside diameter surface of the test section showed that no alumina particles spalled off at any stress level except that slightly less than the failure stress. Considerably less than 1% of the surface had spalled chips at this stress level. The particles found were small (10-50 microns) and resembled closely those seen on replicas of the inside surface made at the 0.26 σ stress level.

Spalled particles are created when cracks extend from inherent flaws in the material under the action of the applied stresses. A study was made to characterize the flaws and the behavior of the cracks which extended from them. The first particles to spall off are associated with the most severe flaws. These particles were small, being composed of one or at most a few grains. The causes of spalling of the first particles were found to be foreign material in grain boundaries and large grain cleavage (larger than 50 micron diameter) which was associated with large (~5 micron) voids adjacent to the grain. The reason for the spalling of other particles at low stress levels was not obvious and was attributed to preexisting cracks introduced during machining. It was not possible to identify the cause of spalling of larger particles consisting of tens of grains. The appearance of the fracture surface

of such particles is shown in Figure 28. Cracks may have originated from flaws at more than one location and intersected to create some of these particles. The fracture paths observed were a mixture of transgranular and intergranular fracture. The path of transgranular cracking was affected by the small (1-3 micron) spherical porosity within the grains. The fracture path would bend from the cleavage plane of the grain to intersect the pores (see Figure 29).

iii. Conclusions of replica study

The relationship between the distributions of spalled particles and the amount of internal damage through the wall thickness of the specimen will be discussed in Chapter VI. It can be seen from Figure 1(a) that the maximum value of the largest principal stress ($\sigma_{\theta\theta}$) occurs on the inside diameter of the specimen and, further, that the radial stress (σ_{rr}) is zero at this position. As will be discussed in Chapter V, the smallest principal stress (σ_{rr}) inhibits crack extension from flaws in triaxial compressive stress states. It is clear that the most highly stressed material is that adjacent to the inside surface which is in a state of biaxial compression. One would expect the maximum damage created by the applied stresses to occur here. Thus, the replica studies are a measure of the most highly damaged regions in the specimen at any stress level. Structural collapse of the specimen originates here by a mechanism to be described in Chapter VI.

Several conclusions concerning the failure process may be drawn from the replica study:

1) Only small particles spall off at low stresses. As the stress level is increased a larger number of particles of each size

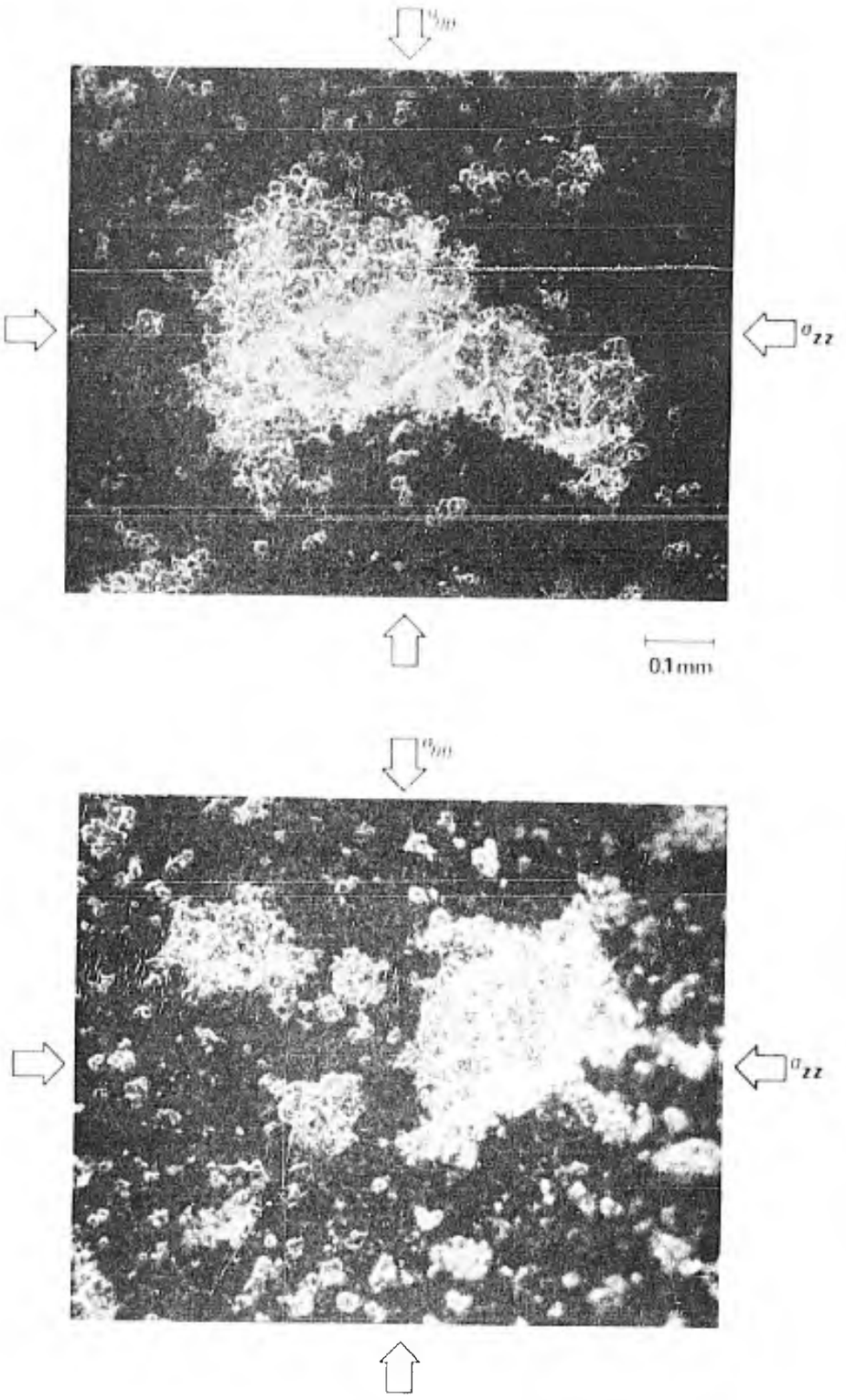

Figure 28. Interior Surface of Large Spalled Particles.

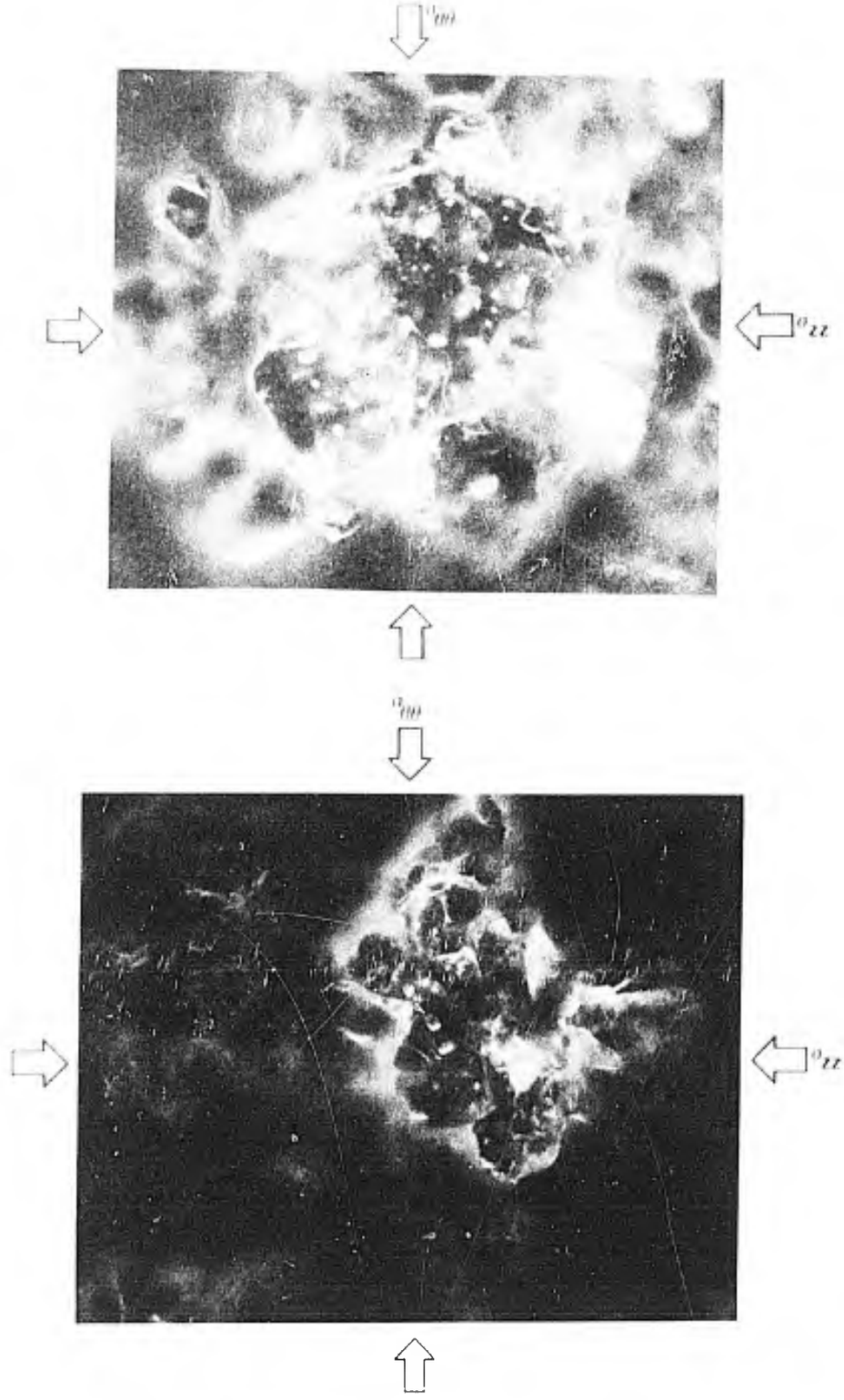

Figure 29. Fracture Path Through a Grain Containing Pores. (Magnification 500X)

spall off, and the maximum size of the spalled particles increases.

2) Particles which spall off at low stress levels relate, at least in part, to machining damage because the pattern of spalled particles is related to the cuts of the diamond grinding wheel.

3) At higher stress levels the spalling of larger particles does not seem to have a direct relationship to the machining damage.

4) The density of spalling is very uniform over the entire test section for any given stress level.

5) The positions of large spalled particles have a direct relationship to the positions of previously spalled large particles. Large particle spalling appears to be clustered with a random distribution of the cluster positions on the test section surface.

6) The density of spalled particles decreases very rapidly as one moves away from the test section area. This is in agreement with the percent area spalled studies which shows this percent to be a very sensitive function of the stress level.

7) The amount of spalling increases tremendously as the failure stress is approached.

8) The particle size distribution displays a peculiar maximum for small particles at the 0.82 σ_f stress level which may be evidence of the onset of crack-crack interaction.

9) The spalling phenomenon results from the action of the applied stresses causing cracks to extend from inherent flaws in the material which separate small particles of the material from the body. The most severe flaws extend cracks first; hence, a careful analysis of the flaws which cause the first spalled particles would reveal the nature of the worst flaws near the surface of the body. In applied stress states containing tensile stresses these worst surface flaws will limit the strength. Such a study can reveal the nature of the worst flaws which limit the strength in tensile stress states; however, the most severe flaws in compression are not necessarily the most severe flaws in tension.

10) A cursory examination of the first spalls and the areas where they occurred revealed the worst flaws to be foreign matter in the grain boundaries and large grains (> 50 microns) which cleaved close to large (~ 5 micron) voids between grains.

11) Examination of the fracture paths on the spalled particles indicated that both transgranular and intergranular fracture was occurring. The fracture path through a grain was affected by the small porosity (1-3 micron dia.) contained within the grains. This effect was to bend the path of fracture from its cleavage plane to intersect the pore.

12) The first particles spalled off at a stress level of 0.25 σ_f i.e., at a compressive stress between 4 and 5 times the magnitude of the measured tensile strength.

B. Additional Observations of Damage Produced in the Specimens

The macroscopic appearance of a failed 1:0.5 biaxial compression specimen is shown in Figure 11. The characteristics of this failed specimen are typical of all specimens failed in the 1:0.5, 1:0.1, and 1:0.01 stress states. The central, axial fracture line in the first view (0° view) is the only region of the specimen in which the alumina material was extensively powdered. This line was formed in each specimen. The circular segment which imploded towards the center of the specimen was formed with virtually identical shape and size in all stress state tests. This segment was laced with cracks and would usually crumble into small pieces when the specimen was removed from the test device. The opposite side of the specimen (180° view) always contained a single circumferential fracture line. The remaining volume of the specimen was fairly well intact. Because energy absorbing techniques could not be used in the 1:0.8 and 1:1 biaxial compression tests, these specimens were badly shattered on failure. (See Figure 14.) Not much information could be obtained from the pieces. Examination of the undisturbed pieces, before the test device was disassembled, indicated the characteristics of structural collapse remained similar to the 1:0.5 specimens. The remarkable similarity and reproducibility of the fracture appearance of all specimens tested in compression is evidence that the same mechanism of structural collapse was operating in each stress state.

The axial line fracture is believed to be the origin of structural collapse in all stress states. The sequence of events of microscopic crack extension which result in the formation of this fracture feature

are discussed in Chapter VI. A more detailed view of this fracture line may be seen in Figure 30(a) and (b) which was made from the surviving test section of a failed 1:0.01 test specimen. Figure 30(a) shows a view looking at the inside surface of the test section in the region of the line. Figure 30(b) shows the alumina material which came from this area and was imbedded in the center post during the fracture process. The portion of the area where the line originated can be seen as a squarish, wider area of the alumina imbedded in the center post.

Between the various pressurization cycles of the replica study the inside bore of the specimen was examined, with a stereomicroscope using an arrangement of mirrors and illuminators. The faces of imbedded cracks near the surface of the specimen would scatter light rendering them darker than the surrounding material. Examination of the inside bore by this technique revealed the subsurface, extending cracks which were forming the spalled particles. The resolving ability of the optical system was not sufficient to allow observation of crack interactions; however, the density and size of subsurface cracks were observed to be similar to the spalled particles. No very large cracks (greater than $\sim$ 1mm) were detected in the test section at any stress level. Also, no cracks were observed to form near the outside surface of the specimen.

Because the technique of optical examination used on the intact specimen could not reveal cracks which were more than a few grains below the surface, portions of failed specimens were mounted and carefully polished to determine the amount of crack damage through the entire wall thickness of the specimen. These pieces were gently lapped for extended periods of time in an automatic lapping device to obtain sections of

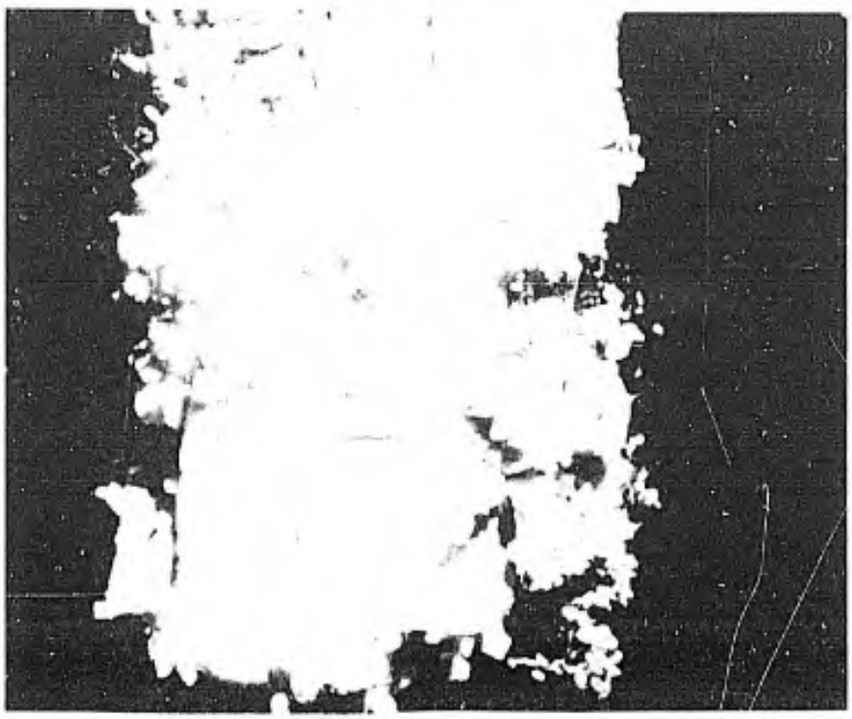

(a) INSIDE DIAMETER SURFACE OF TEST SECTION (MAGNIFICATION 3X)

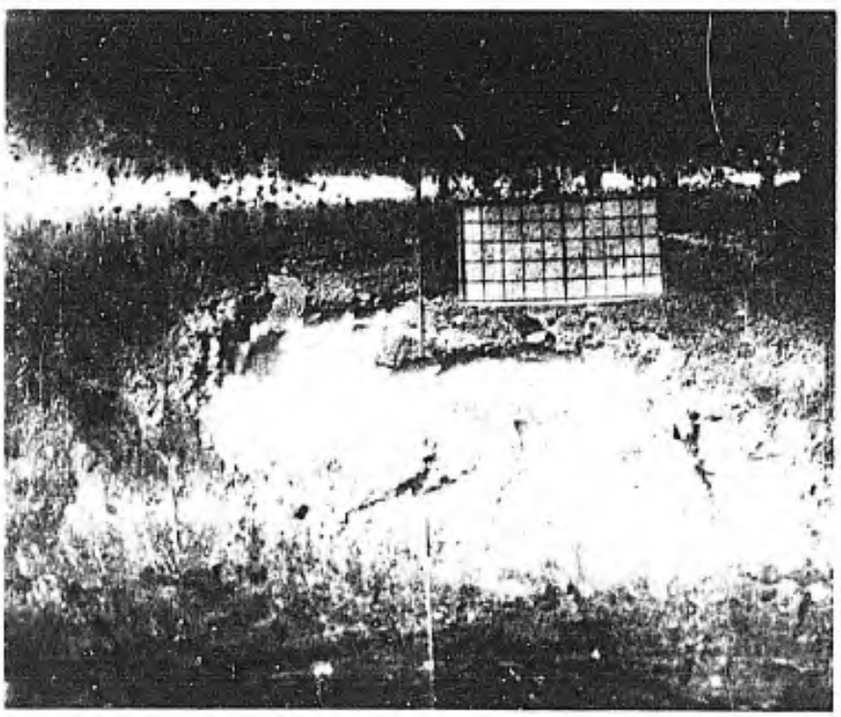

(b) CENTER POST (MAGNIFICATION 3X)

Figure 30. Axial Fracture Line on Failed 1:0.01 Test Specimen.

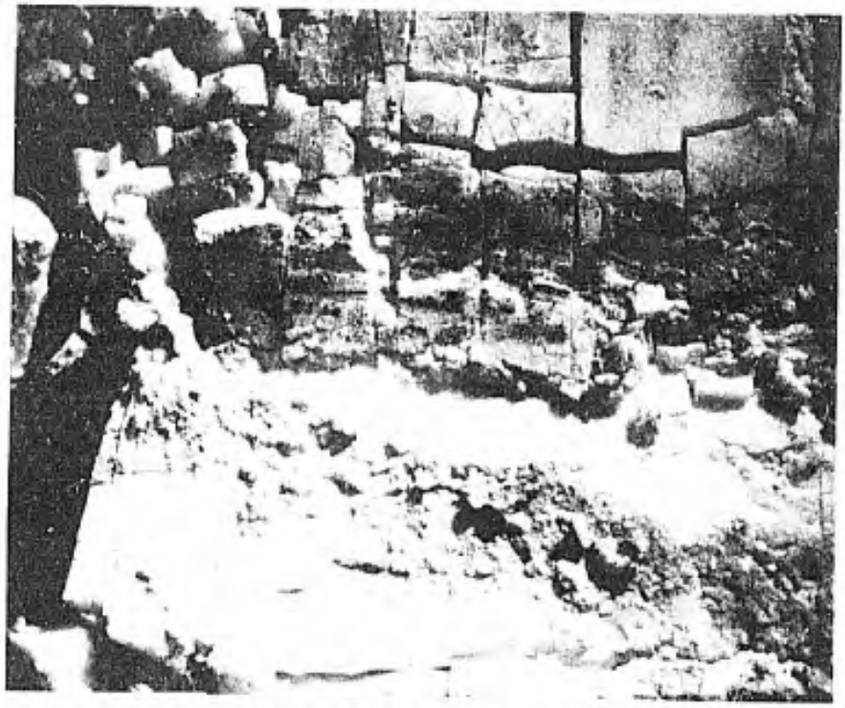

(c) INSIDE DIAMETER TEST SECTION (MAGNIFICATION 8X)

Figure 30. (continued)

relatively undisturbed material. Optical examination of these pieces revealed that no extensive or dense crack network was formed throughout the wall thickness of the test section. Several orientations of sections were made and all indicated that only the material near the inside surface had developed a dense network of cracks.

The Origins of the Specimen Damage in the Attempted Uniaxial Compression Tests

The nature of the cracks produced in the attempted 1:0 compression tests as described in Chapter 3, Section Ciii is shown in Figure 12. These cracks resulted from an inadvertent tensile stress which was produced during the test. The sizing of the specimen tube end diameters was incorrect; the diameters were slightly too large. This meant the application of the pressure load on the specimen ends was external to the inside diameter of the test section. (See Figure 31.) This produced an unbalanced force from the pressure on the outside surface of the specimen that created an axial tensile stress in the region where the crack started. The tensile stresses developed in this way are localized to an area near the outside surface of the specimen. As the propagating crack moved from the outside surface toward the inside surface it encountered the axial compressive stress and turned to become parallel to the direction of the compressive stress.

As will be discussed in the next chapter, cracks extending in a tensile stress field do so in a manner such that the crack plane is perpendicular to the direction of the tensile stress. Cracks extending in a compressive stress field tend to align themselves with the direction of the compression. Examination of these crack surfaces after

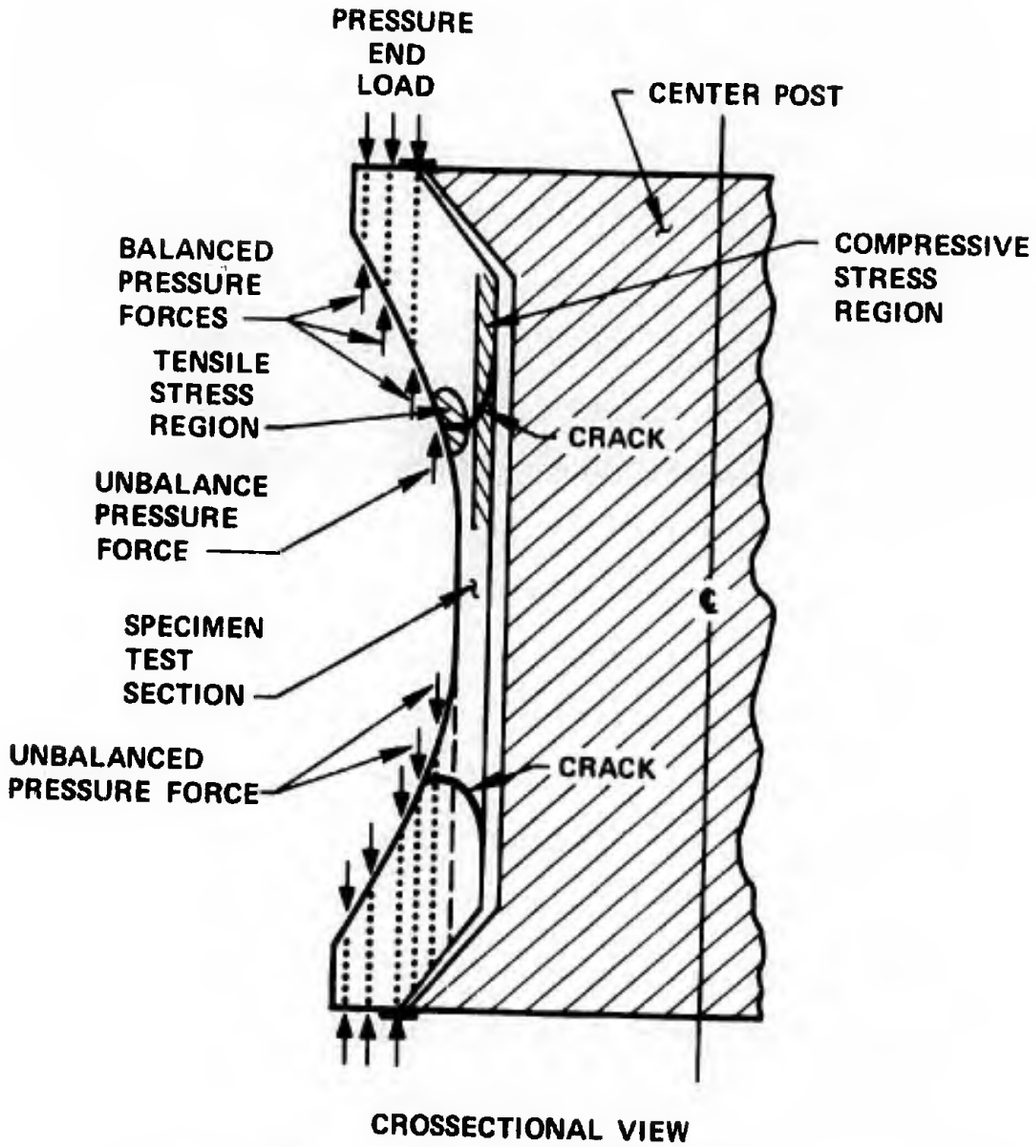

Figure 31. Formation of Cracks During Attempted Uniaxial Compression Test.

specimen failure revealed the transition of the crack plane from being normal to the specimen axis to that of being parallel was a smooth continuous curve down to virtually the scale of the grain size. This is direct evidence that the direction of macroscopic, extending cracks responds to the local stress state in a manner similar to the model studies which will be discussed in Chapter V.

CHAPTER V

CRACK EXTENSION FROM FLAWS IN COMPRESSIVE STRESS STATES

A. The Nature of Two-Dimensional Flaws which May Extend Cracks

A categorization of the types of flaws which may extend cracks and the mechanisms by which the cracks extend under compressive stress fields is given here. The models, by necessity, are idealized to simplify the analysis. The expressions for stresses around the flaws are based on the flaws being contained in a homogeneous, isotropic, elastic medium. Anisotropic elastic constants and the fact that high strength ceramics are composed of a bonded aggregate of crystallites certainly will have some influence on these considerations. It is suggested; however, that these effects will only be significant on a scale of single crystallites. If the cracks extend over tens of grains, then the continuum elastic predictions should be quite accurate. Whether the cracking occurs in the grain boundaries or through the grains should have little influence on the results of this discussion other than to establish the stress level at which these events occur.

The categorization of flaws which can extend cracks are divided into three types to facilitate discussion of the cracking mechanisms. A fourth type of flaw can be envisioned. It is that of an inclusion which has elastic properties different from the matrix in which is imbedded. A consideration of this type of flaw would be important in dealing with multiphase materials. Koide[40] has presented an analysis of crack initiation from heterogeneous inclusions which have elastic properties that differ from the matrix. In general, the greater the difference in elastic properties between the inclusion and the matrix,

the larger is the intensification of stresses around the inclusion. The stress intensification around inclusions is analogous to that around a crack or pore of equivalent geometry but the stresses around the inclusion are less. Since we are considering only high strength, high purity, single phase materials, the behavior of this type flaw will not be pertinent to the discussion.

The quantities of each flaw type occur in various proportions and densities in different materials. It is probable that the types of flaws which predominate in any given material will have an influence on the nature of the crack damage created in the material subjected to stresses less than those required to cause structural failure. This will in turn influence the mechanism of final structural collapse and the measured strength. This is not to say the inherent flaw densities do not have an effect but rather the type and density of flaws present are two primary factors influencing the material strength. The effects of the flaw density and density of extended cracks will be discussed in Section C of this chapter.

Crack initiation and extension at flaws subjected to compressive stress states is more complex and varied than that observed when tensile stresses are present. Several mechanisms of crack initiation and extension are possible in compression. Crack extension in three dimensions and/or under triaxial stress states is more difficult to treat and will be touched upon in Sections B and C. For the present, two-dimensional flaws subjected to biaxial compressive stresses which act in the plane of the flaws and extend a crack only in the two-dimensional plane of the these stresses, will be considered. This model of flaws utilizes only

two-dimensional elastic theory to obtain solutions for the stresses around the flaw. As a matter of definition, a flaw is any microscopic area or feature in a stressed body which concentrates the stresses in the body above their nominal values. Flaws can include cleaved grains, unbonded or weakly bonded grain boundaries, pores, inclusions, and a host of other microstructural features inherent in the body as fabricated. Cracks (fractures in the continuous material surrounding the flaw) extend from flaws in the body under the action of applied stresses which are intensified at the flaws. It will be shown that inherent flaws, the ones that exist in the body after fabrication and before any load is applied, may not be the only flaws acting to extend cracks at high levels of stress. There are several possible mechanisms for increasing the density of flaws which can extend cracks.

i. Type I - open flaws

These are the kind of flaws first proposed as being responsible for the reduction of the measured strengths of brittle bodies from their theoretical or intrinsic strengths of 1×10^6 to 10×10^6 psi to observed values $\frac{1}{100}$ to $\frac{1}{1000}$ as large. Griffith in 1920[41] proposed this flaw type as being responsible for the reduction in the strength of glass. Solutions for the stress fields around various geometries of open flaws and arrays of open flaws are available. Since a large variety of these kinds of flaws have been extensively treated in the literature, only the fundamental ideas will be presented here.

The two-dimensional, Type I flaw can be considered in one extreme as a circular hole and the other extreme as an infinitely sharp crack. The ellipse formed by the perimeter of the flaw has semi-major axis (c)

and semi-minor axis (a). (See Figure 32(a).) The condition for defining this type of flaw is that the flaw remains open under all stresses imposed. The faces of open flaws never come into contact to allow transmittal of normal or shear stresses across the faces. Inglis[42] first obtained the stress distribution in the vicinity of such flaws. If the open flaw is modeled as an ellipse, the ratio of semi-major to semi-minor axis (c/a) determines the severity of the stress concentration near the free surface of the flaw. The severity of the stress concentration increases as the c/a ratio increases. (See Figure 32(b).) For very large ratios of c/a, i.e., as flaws approach infinite sharpness, a more convenient parameter is the radius of curvature at the tip (ρ) and crack length (c). (See Figure 32(c).) Inglis showed that the maximum tensile stress (σ_{max}) occurs near the flaw tip and could be described by:

$$\sigma_{max} = \sigma\left(1 + \frac{c}{a}\right) \quad \ldots\ldots\ldots \quad (13)$$

where: $\sigma \equiv$ traction applied to an infinite body containing the flaw in a direction perpendicular to major axis of flaw.

For an elliptical shaped flaw: $\rho = \frac{a^2}{c}$

and:

$$\sigma_{max} = \sigma\left[1 + \sqrt{\frac{c}{\rho}}\right] \simeq \sigma\sqrt{\frac{c}{\rho}} \quad (14)$$

for: $c >> \rho$

This open, Type I flaw model may be used to analyze the maximum stresses around any complex shape of two-dimensional, open flaws quite accurately.[43] (See Figure 32(d).)

Much use has been made of these models in the discipline of fracture mechanics where the concentrated stresses in the vicinity of the flaw

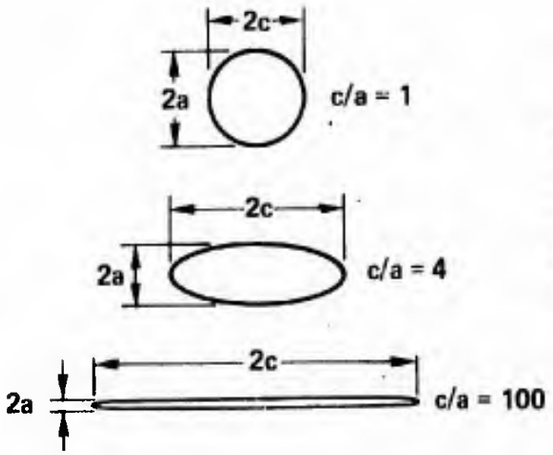

(a) OPEN FLAWS

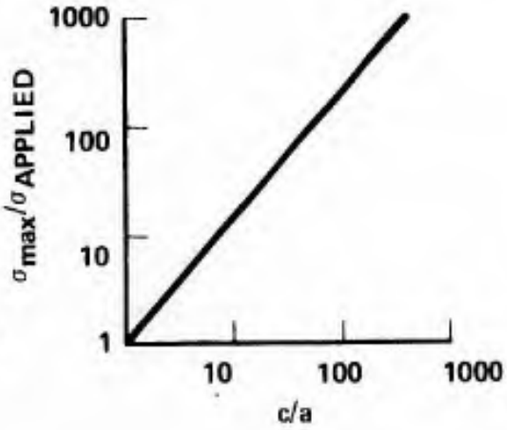

(b) STRESS CONCENTRATION AROUND OPEN FLAWS

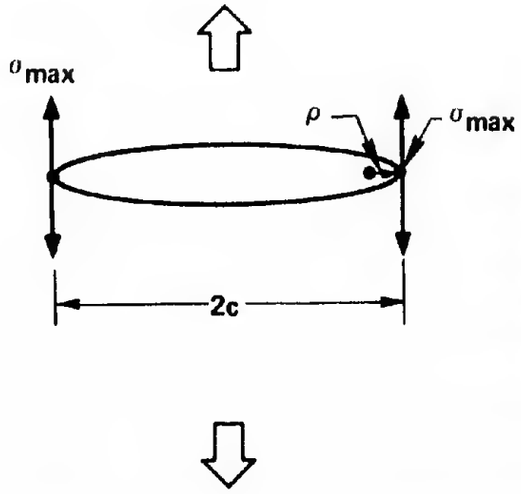

(c) TENSILE STRESS CONCENTRATION AROUND SHARP, OPEN FLAW.

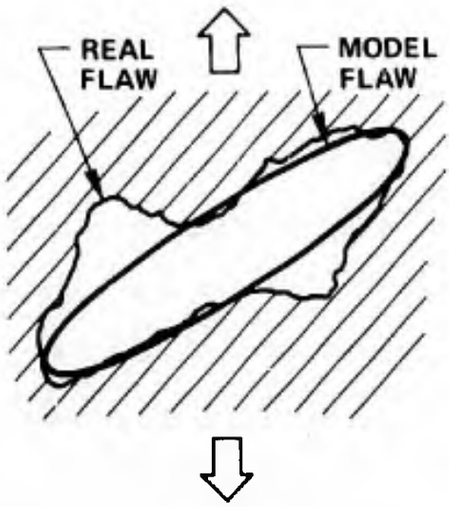

(d) MODELLING OF REAL OPEN FLAW WITH MATHEMATICAL ELLIPSE.

Figure 32. The Modelling of Open Flaws in a Material.

cause local plastic deformation in materials which exhibit ductility. The plastic flow mechanisms control the stress level at which a crack nucleates at the flaw and the manner in which it extends. For perfectly brittle materials (ones which exhibit linearly elastic behavior to failure even in microscopic areas around the crack tip) crack initiation and extension is controlled by the magnitude of the concentrated tensile stress in the vicinity of the flaw tips. When the concentrated tensile stress equals the intrinsic or theoretical strength of the flaw free material, a crack is initiated.

The expression for the tensile stresses in the vicinity of the surface of an elliptical hole, subjected to applied stresses in the plane of the flaw as derived by Inglis, may be used to calculate the applied load necessary to create tensile stresses at the tips of a flaw which are equal to the intrinsic material strength. Using this approach, Griffith[44] proposed a maximum stress criterion for crack extension from infinitely sharp, open, elliptical flaws in 1924. He calculated the concentrated stresses in the vicinity of the flaw which arise from applied biaxial tractions by superimposing the stress fields created by the action of the normal and shear stresses acting on the plane of the flaw. Babel and Sines[13] generalized this criterion to treat crack extension from flaws of any c/a ratio. Their results are particularly applicable to materials such as porous zirconia which is known to contain a high density of open flaws. Both the Griffith theory and its generalization by Babel and Sines have been successful in explaining strength values measured in tension-tension and tension-compression stress states. The Griffith theory has also been somewhat less

successful at explaining strengths of rock measured in triaxial compression stress states.

The generalized, two-dimensional, Griffith stress criterion for the initiation of cracks at open flaws subjected to biaxial stresses has been plotted by Kobayashi.[45] (See Figure 33.) These curves show the necessary values of the variables σ_1, σ_3 and ξ for crack initiation or failure, where σ_1 and σ_3 are the major and minor applied stresses respectively and where (ξ) is the angle between the flaw plane and the direction of σ_1. These computations were made for a flaw of aspect ratio c/a = 10,000, which is a realistically sharp flaw; e.g. 10Å grain boundary separation over a length of 10 microns. The applied stress (σ_1) is normalized to the uniaxial tensile strength (σ_t). The theory predicts a ratio of uniaxial compressive strength to uniaxial tensile strength of 8. In compression-compression stress states the strength of the body (σ_1) increases with increasing minor compression σ_3. This stress state is analogous to stress states developed in the triaxial compression tests used by geologists ($\sigma_1 > \sigma_2 = \sigma_3 = -p$; where p is the confining pressure). The parabolic increase in the strength with σ_3 is observed in such tests.

An interesting aspect of the behavior of open flaws subjected to purely compressive stresses is apparent from the curves of Figure 33. If compressive stresses much greater than 8 times the tensile strength are imposed before the body fails in compression, then all flaws in such a material will initiate cracks whose orientations are included in a large angular range ($\Delta\xi$). In a material such as AL-995 alumina where the compressive strength $\sigma_c = 18\ \sigma_t$, some of the first flaws which

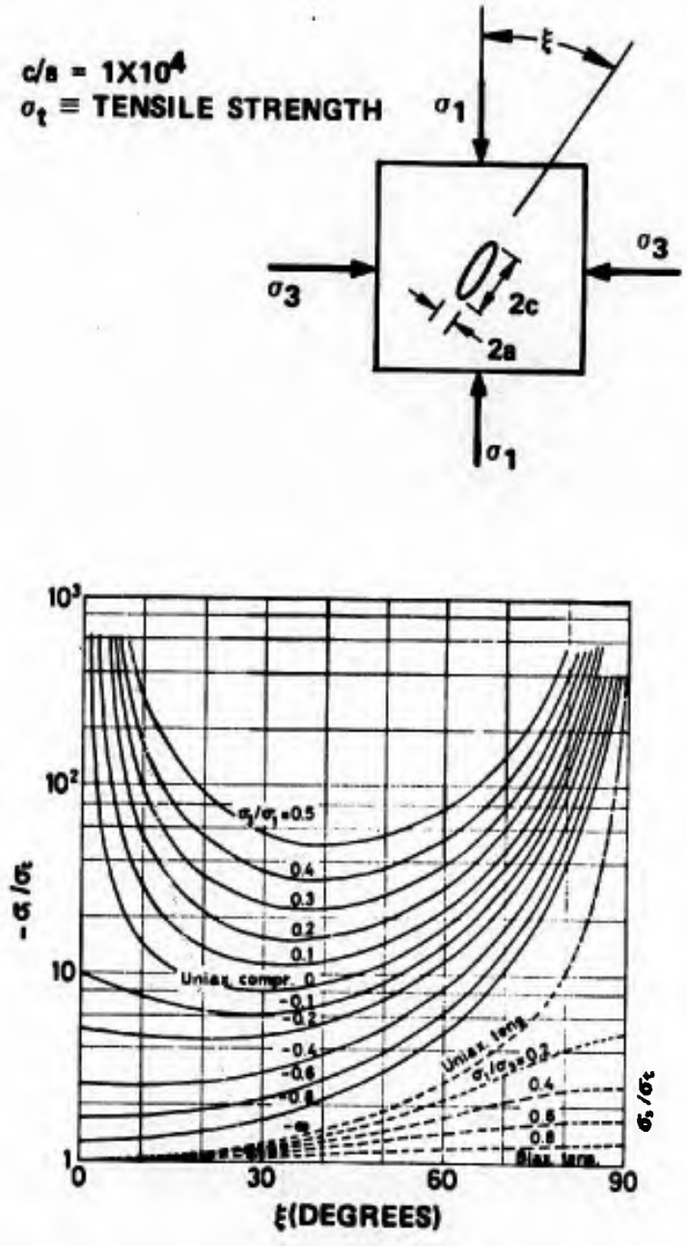

Figure 33. Griffith Criterion for Crack Initiation at Open Flaws.

initiate cracks will be subjected to applied stresses of more than twice the applied stress at which they first initiated the cracks before structural collapse of the material occurs. As the applied load increases beyond 8 σ_t, by this model, the angular range ($\Delta\xi$) of flaws which initiate cracks increases. Applying a second principal compression does not totally inhibit crack initiation from flaws but does increase the value of maximum principal compression necessary to initiate them and also reduces the angular range ($\Delta\xi$) of flaws which will extend cracks.

The number of flaws in a body which initiate cracks increases with increasing applied load for two reasons. First, the higher the load, the smaller the flaw (one which creates a lesser stress concentration) which can attain the critical tensile stress concentration at its tip. Secondly, as the applied load increases, $\Delta\xi$ increases for any given size flaw. The increase in the density of flaws which have initiated cracks as a function of $\Delta\xi$ may be determined from Figure 33. The increase in the density as a function of size c depends on the flaw size distribution in the material. Knowing these two parameters, a function could be described giving the density of flaws which have initiated cracks vs. applied load. This relationship will be developed in Chapter VI.

It is important to emphasize that the theory being presented here is for a two-dimensional model. The actions of stresses on the behavior of flaws in the third dimension are not being considered. For some conditions of triaxial loading (e.g. geologist's confining pressure test) this two-dimensional model may be representative of the three-dimensional

behavior but this is only a special case of a more complex, three-dimensional behavior.

By the Griffith theory, flaws will concentrate applied stresses on a body in regions near their tips. When this concentrated tensile stress equals the cohesive strength of the material a crack extends from the flaw. If one of the principal stresses in the region of the flaw is tensile, crack initiation and unstable crack extension coincide or almost coincide.[46] This results in structural failure of the body brought about by unstable crack extension completely through the body from one of the first flaws to initiate a crack. Another way of describing this event, using the language of fracture mechanics,[47] is to say the stress intensity factor (K) for the flaw reached the critical stress intensity (K_c) for the material under the stresses imposed. K is defined in general as $K = \sigma\sqrt{\alpha\pi c}$, a function of applied stress (σ), flaw length (c) and flaw geometry (α). As the crack extends under applied tension, the K for the flaw-extending crack configuration increases while K_c is a material constant. If K remains greater than K_c, the crack extension will be unstable; the load applied when $K = K_c$ continues to be more than sufficient to maintain extension of the crack.

The nature of crack extension is very different when the principal stresses are all compressive. Various experimental studies have shown that cracks which extend from flaws in purely compressive stress states do so stably. A stably extending crack is one whose length (ℓ) is at all times a function of the applied stresses. Further, these extending cracks tend to align themselves with a principal stress direction such that the normal to the crack plane $\hat{c}$ is perpendicular to the direction

of principal compression similar to that shown in Figure 34(a). This behavior has been experimentally observed in such materials as polymethylmethacrylate (PMMA) plastic, glass, rocks, and cement. The stress dependence of crack initiation for an open, two-dimensional slit is well understood and analytical expressions are successful in predicting the applied stress at initiation. Analytic expressions for the stresses in the vicinity of the extended crack tip or the dependence of the extended crack length (ℓ) on the applied stresses have not been formulated. There is a great difficulty in modeling the flaw-crack configuration. Since large numbers of cracks extend in brittle materials subjected to compressive stress states before structural collapse occurs, an analytical understanding of the nature of this crack extension is quite important to theories of strength.

Qualitatively speaking, when a compressive stress is applied to a body containing a flaw, the greatest concentrated tensile stress (σ_t^{max}) occurs near the tip in the area shown. (See Figure 34(b).) Its direction is tangent to the free surface of the flaw. When σ_t^{max} exceeds the cohesive strength of the material a crack extends from the flaw in a direction perpendicular to the direction of maximum tension. As the stress is increased, the extending crack curves toward the direction of principal compression because the least work is required to extend a crack in this direction. The stored energy associated with cracks parallel to the compression is at a minimum. It should be noted that there is also a maximum concentration of compressive stress near each tip. When the extended crack length becomes a sizable fraction of c, the conditions for further extension are not clear. If the extended

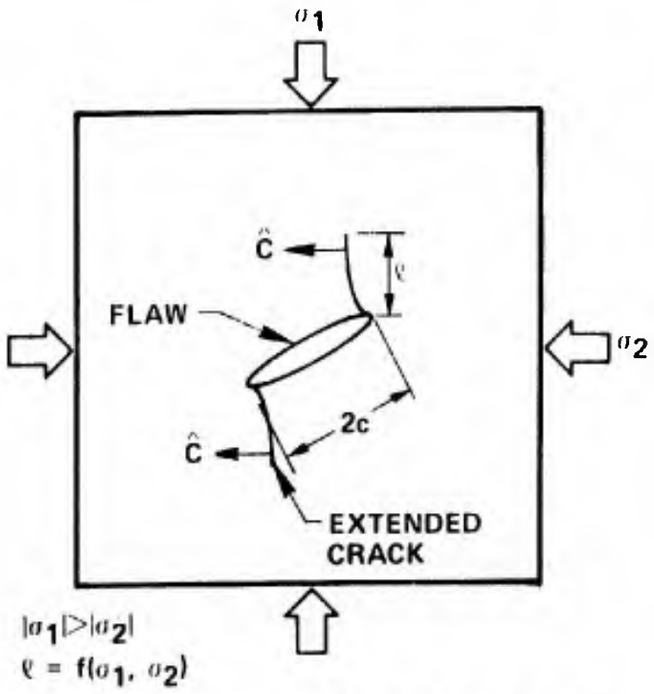

(a) CRACK EXTENSION FROM OPEN FLAW

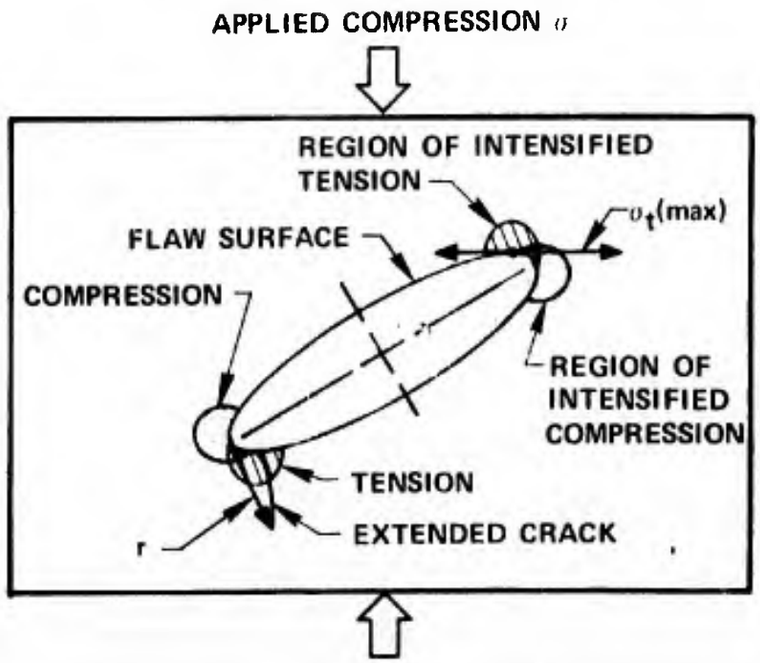

(b) CONCENTRATED STRESSES AROUND OPEN FLAW UNDER COMPRESSION.

Figure 34. The Behavior of Cracks Extending From Two-Dimensional Flaws in Compression.

crack tip is a large distance from the flaw where the crack plane has become parallel to the applied compression, the tensile stress at the tip is equal in magnitude to the applied compression. (See Appendix C.) In a material such as Al_2O_3 where the applied compression can exceed 500 ksi, the tensile stress at the tip of an aligned crack is still considerable. This phenomenon of the further extension of cracks aligned parallel to the compressive stress by loads which are sufficient to produce a tensile stress equal to the tensile strength of the material has been observed by the author in PMMA plastic plates. Unstable crack extension was observed to occur from a long crack, aligned with the applied compressive stress, when the applied compression on the plate equaled the tensile strength of the PMMA material. (See Chapter V, Section B(ii).)

Stable crack extension from a flaw subjected to compressive stress may be discussed in terms of K, the stress intensity factor. When a crack initiates at a flaw, $K = K_c$; but, as the crack extends, K decreases because of the changing geometry of the flaw-crack configuration. If the applied stress is not increased, further crack extension does not occur since $K < K_c$. If the stress is increased again such that $K = K_c$, the crack will extend until K becomes less than K_c. Over at least a limited range of crack extension, the geometric parameter in the K factor is decreasing with further extension. This means an increase in the applied stress (σ) is necessary to maintain the relationship $K = K_c$, the criterion for extension. At higher levels of applied stress and for cracks which have extended to a considerable length, other mechanisms of extension may operate, nullifying the above behavior.

ii. Type II - closed flaws with sliding faces

If an open flaw closes when subjected to the action of applied stresses, the nature of the intensification of applied stresses in the vicinity of the closed flaw differs from that of an open flaw. The definition of a closed flaw is that the stress acting normal to the plane of the flaw is transmitted across the flaw faces and thus is not concentrated at the tips of the flaw. The major concentrated stresses at the tips of a closed flaw arise from the shear stress acting in the flaw plane. For an open flaw both the normal and shear stresses on the flaw plane are concentrated at the tips of the flaw. (See Figure 35.) Using elliptical coordinates α, β for an open, elliptical shaped flaw where, on the free surface:

$$\alpha_o = (\rho/c)^{1/2}$$

$$\frac{dy}{dx} = \alpha_o \cot \beta$$

α_o is related to the sharpness of the flaw and β describes a point on the the flaw edge in terms of the slope of the edge at that point. Inglis[42] gave an expression for the local normal stress ($\sigma_{\beta\beta}$) along the surface of a narrow flaw which can be approximated for a relatively sharp flaw as:

$$\sigma_{\beta\beta} = \sigma \frac{2\alpha_o}{\alpha_o^2+\beta}$$ for an applied stress σ normal to the flaw. (15)

$$\sigma_{\beta\beta} = \tau \frac{2\beta}{\alpha_o^2+\beta^2}$$ for an applied shear stress τ parallel to the flaw. (16)

The concentrated local stress ($\sigma_{\beta\beta}$) at the surface of an open flaw may be found for any combination of applied biaxial stresses by summing the

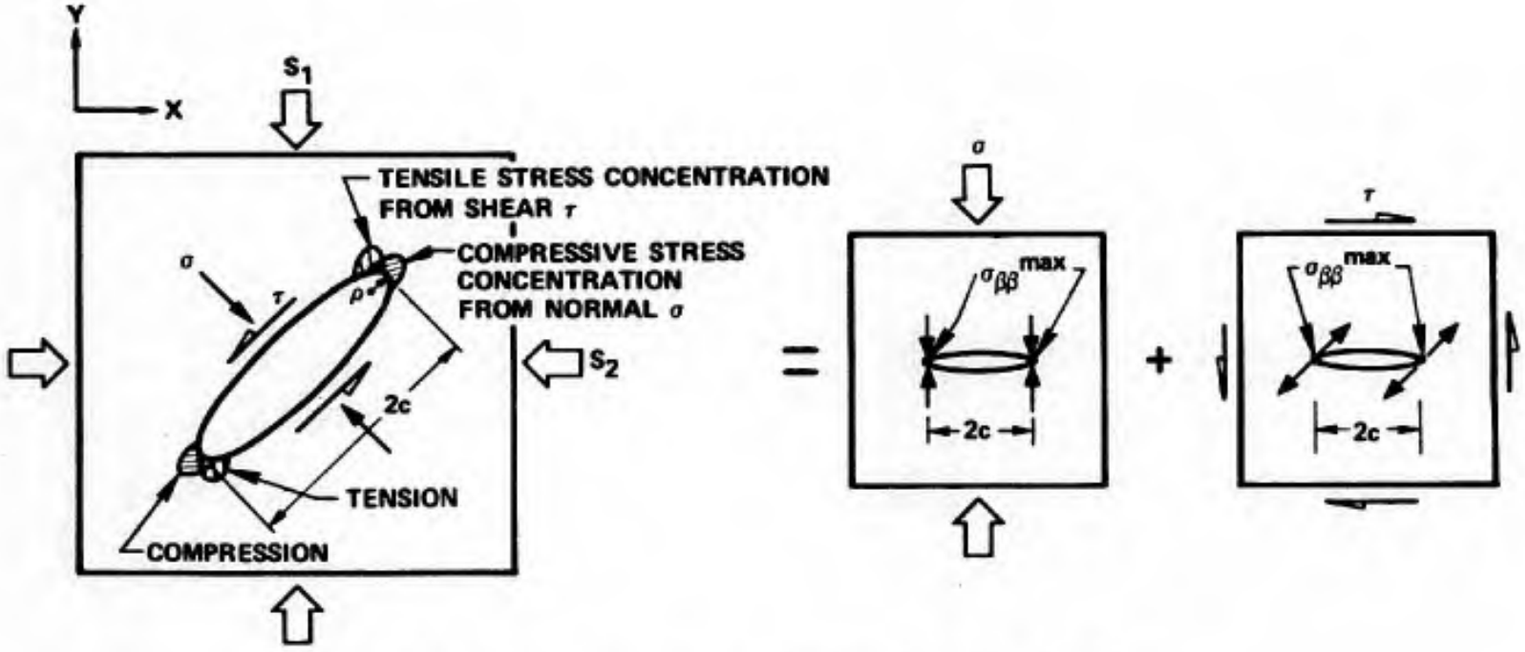

Figure 35. Method of Calculating Intensified Stress Around an Open Flaw.

values of $\sigma_{\beta\beta}$ produced by the normal and shear stresses acting on the flaw plane. After the flaw closes, any additional normal stress applied to the flaw plane is not concentrated by the flaw. Consequently, the value of the concentrated stress ($\sigma_{\beta\beta}$), with further increase of the applied stresses beyond the point of flaw closure, is augmented only by the shear stress (τ) acting on the plane of the flaw. After flaw closure, the magnitude of the shear stress τ is diminished by the frictional resistance to sliding of the flaw faces.

A two-dimensional model for an open flaw that closes under a stress (σ_c) normal to its faces, which subsequently slide under an increasing applied load with a constant coefficient of friction (μ), was proposed by McClintock and Walsh.[48] A theory of strength was developed, based on this model, to explain the tension-compression and triaxial compressive strength of rock materials that are believed to contain such flaws. The theory has been applied primarily to such material, where the strengths were measured using confining pressure (triaxial compression). The theory calculates the value of the maximum local tensile stress $\sigma_{\beta\beta}$ in the vicinity of the flaw by superposition of the stress states developed by the simple loadings σ_{xx}, σ_{zz}, τ_{xz}, σ_n and σ_f. (See Figure 36.) Only the loadings σ_{xx} and τ_{xz} are important in determining $\sigma_{\beta\beta}$. By setting the $\sigma_{\beta\beta}^{crit}$ stress which causes failure under simple tension loading equal to the expression for $\sigma_{\beta\beta}^{max}$ under biaxial loading, a failure envelope for triaxial compressive stresses is obtained with the stress axes normalized to the tensile strength.

The applied stresses on the body containing the flaw are σ_1 and σ_3 where $|\sigma_3| \geq |\sigma_1|$. (See Figure 36.) ξ is the angle between the plane

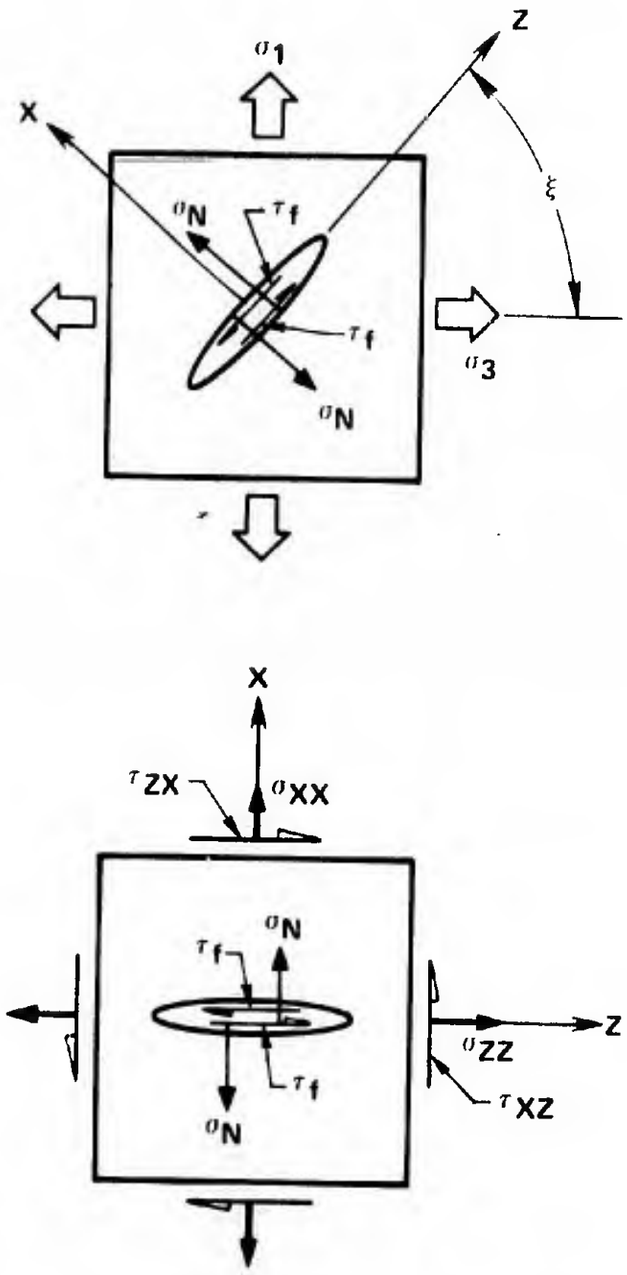

Figure 36. Loading and Stress Components of Closed Cracks Under Biaxial Applied Stresses.

of the flaw and the direction of σ_3. The normal stress (σ_{xx}) and shear stress (τ_{xz}) on the flaw plane may be obtained by using Mohr's circle. The normal stress on the flaw's free surface (σ_N) is a function only of the applied stress normal to the flaw plane (σ_{xx}) i.e.

$$\sigma_N = 0 \quad \text{for} \quad |\sigma_{xx}| < |\sigma_c|$$

$$\sigma_N = \sigma_{xx} - \sigma_c \quad \text{for} \quad |\sigma_{xx}| \geq |\sigma_c| \tag{17}$$

When $\sigma_{xx} = \sigma_c$, the faces of the flaw close. The magnitude of compressive stress required to close the flaw (σ_c) will depend on the geometry of the flaw and the elastic constants of the material. Flaws may be closed under no applied stress ($\sigma_c=0$), may close partially at stresses up to those necessary to cause structural collapse of the body, or may completely close. The normal stress (σ_{xx}) is intensified in the vicinity of the open flaw and, under applied compressive stresses, tends to diminish the tensile magnitude of $\sigma_{\beta\beta}$ arising from the action of the shear (τ_{xz}) on the flaw plane. When $\sigma_{xx} = \sigma_c$ and the flaw closes, any additional increase in σ_{xx} above σ_c is not intensified by the closed flaw since the additional stress (σ_N) is being carried across the faces of the closed flaw.

As the flaw closes, a shear traction (τ_f) arises on the flaw faces from the frictional resistance to the displacement of the faces past each other under the action of the τ_{xz} shear stress. The maximum frictional resistance to flaw face displacement is defined to be:

$$\tau_f = -\mu\sigma_N \tag{18}$$

where μ is a constant coefficient of friction between the flaw faces. The shear stress τ_{xz} is not intensified by the flaw unless the frictional

resistance to sliding (τ_f) is overcome i.e. a displacement of the crack faces in opposite directions is required to produce an intensification of the τ_{xz} stress.

In summary, the intensified stresses at the tip of the flaw ($\sigma_{\beta\beta}$) arise from (i.) an intensification of the shear stress on the plane of the flaw which is diminished by the frictional shear resistance ($\tau_{xz}-\tau_f$) and (ii) from an intensification of the normal stress on the plane of the flaw up to the value of the closure stress (σ_c). $\sigma_{\beta\beta}$ is found then from a superposition of the Inglis solution for the two simple loadings shown in Figure 37. Before the flaw closes, the intensified stress $\sigma_{\beta\beta}$ is calculated from the two simple loadings σ_{xx} and τ_{xz}. Flaws which close under applied stresses may exhibit various kinds of behavior some of which are briefly discussed below:

(1) If the flaw closes under a very small applied stress $\sigma_c \approx 0$ and $\mu = 0$, the applied stress criterion for crack initiation depends solely on a critical value of τ_{xz}. ($\sigma_{\beta\beta}$ arises only from the action of τ_{xz}.) This type of closed, two-dimensional flaw will initiate cracks at lower applied stresses than its open flaw counterpart.

(2) If $\sigma_c \approx 0$ but μ is large i.e. ≥ 1, crack initiation will be controlled by the ($\tau_{xz}-\tau_f$) term and crack initiation will occur at applied stresses greater than those to cause crack initiation with the open flaw.

(3) If the closure stress (σ_c) is sufficiently large that closure does not occur, the flaws will behave as open flaws.

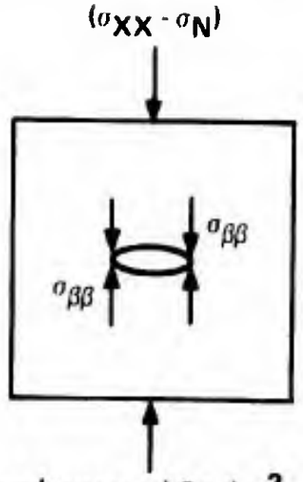

$$\sigma_{\beta\beta} = (\sigma_{XX} - \sigma_N)\, 2\alpha_o/\alpha_o^2 - \beta^2$$

WHERE: $\sigma_N = 0$ FOR $|\sigma_{XX}| < |\sigma_c|$ OPEN FLAW

AND: $\sigma_N = \sigma_{XX} - \sigma_c$ FOR $|\sigma_{XX}| \geq |\sigma_c|$ CLOSED FLAW

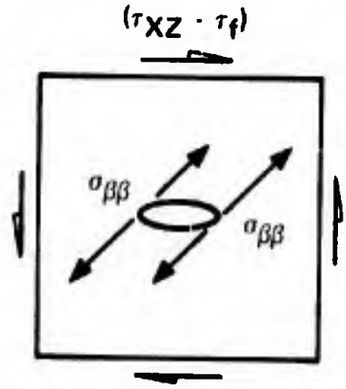

$$\sigma_{\beta\beta} = (\tau_{XZ} - \tau_f)\, 2\beta/\alpha_o^2 + \beta^2$$

WHERE: $\tau_f = 0$ FOR $|\sigma_{XX}| < |\sigma_c|$ OPEN FLAW

AND: $\tau_f = -\mu\sigma_N$ FOR $|\sigma_{XX}| \geq |\sigma_c|$ AND $\tau_{XZ} > \tau_f$ CLOSED SLIDING FLAW

Figure 37. Calculation of Stresses Around Simply Loaded Open or Closed Flaws.

(4) If the cracks close only partially at applied stress levels sufficient to cause crack initiation, it is not entirely clear how to describe $\sigma_{\beta\beta}$ nor is it clear what criterion should be used. Qualitatively, if a flaw is partially closed the open portion can behave quite like an open flaw. The normal stress (σ_{xx}) will be concentrated only at the ends of the open portions and the "effective" flaw size (2c') intensifying this stress will be only the open portion. (See Figure 38.) The shear stress τ_{xz} creates a tensile $\sigma_{\beta\beta}$ which occurs at the tips of the open portion of the flaw (position A) when $\tau_{xz} < \tau_f$ and it is concentrated by the open flaw length (2c'). When $\tau_{xz} \geq \tau_f$, the closed portions of the faces may slide and the tensile $\sigma_{\beta\beta}$ from the shear τ_{xz}, diminished by the frictional shear τ_f, is then concentrated by the flaw length (2c) and occurs at the tips in position B. Crack initiation may occur at either location, A or B, depending on the flaw geometry and the magnitudes of the various quantities. This phenomenon of cracking in the central portions of flaws has been experimentally observed by Hoek and Bieniawski[49] in glass plates with "closed cracks."

It is not entirely clear whether a flaw will close from the center out or from the tips in. For convenience of illustration the flaw in Figure 38 is shown as closing from the tips inward. The geometry of real flaws will control the closing. Flaws which have very large c/a ratios will close down uniformly in the center portion first leaving open segments at each end.

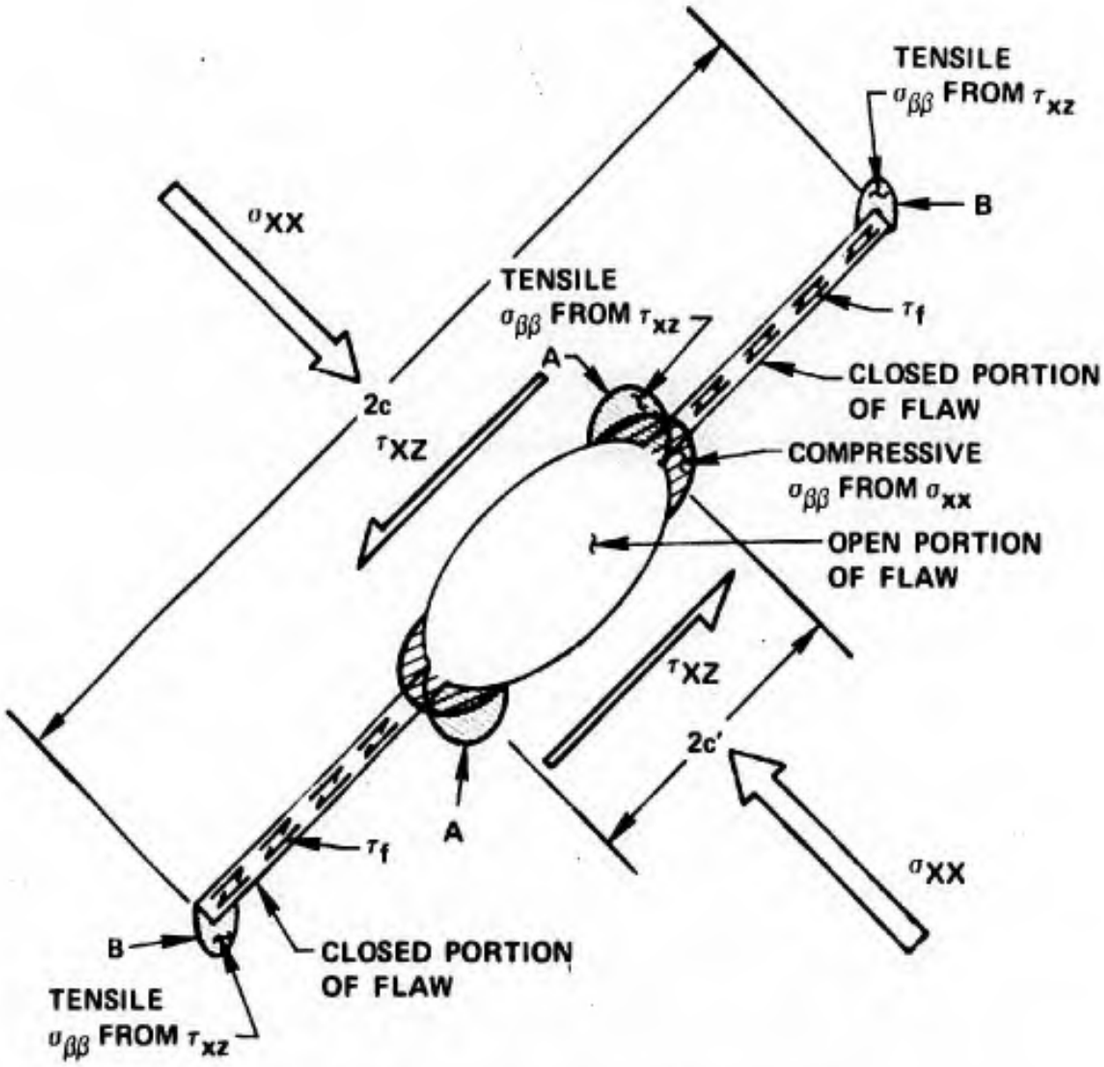

Figure 38. Stresses Around a Partially Closed Flaw.

By setting the expression for the maximum tensile stress developed at the tip of the closed flaw under biaxial stresses equal to the expression for the critical stress at the tip of the same flaw which extends the first crack under an applied uniaxial tension, the condition for crack initiation may be obtained in terms of the tensile strength (σ_t), the applied compressions σ_1 and σ_3, the coefficient of friction (μ), the flaw orientation (ξ), and the stress required to close the crack (σ_c). This condition for crack initiation is as follows:

$$\mu(\sigma_3+\sigma_1-2\sigma_c)+(\sigma_1-\sigma_3)(\sin 2\xi+\mu\cos 2\xi) = 4\sigma_t\sqrt{1-\frac{\sigma_c}{\sigma_t}} \qquad (19)$$

Kobayashi[45] has plotted this equation for $\sigma_c = 0$ as ξ versus $\frac{\sigma_3}{\sigma_t}$ for various μ and σ_1/σ_t values. (See Figure 39.) Examination of this form of the criterion for crack initiation at completely closed flaws shows that the effects of σ_1 and ξ on the maximum compressive stress σ_3 necessary to initiate a crack are similar to that found for the open flaw case. There are differences, however, and the kinds of possible behavior are considerably increased due to the larger number of variables. As σ_1 is increased, the angle of most critical crack orientation (ξ_{crit}) remains constant while for open flaws it becomes greater. The most critical flaw orientation in the closed flaw model is only a function of the coefficient of friction, being:

$$\xi_{crit} = \frac{1}{2}\tan^{-1}\left(\frac{1}{\mu}\right) \qquad (20)$$

As the coefficient of friction across the crack faces increases, the range of flaw orientations ($\Delta\xi$) which can extend cracks at any given stress level is greatly reduced. Also as μ increases, the effect of σ_1 on inhibiting crack initiation is much stronger.

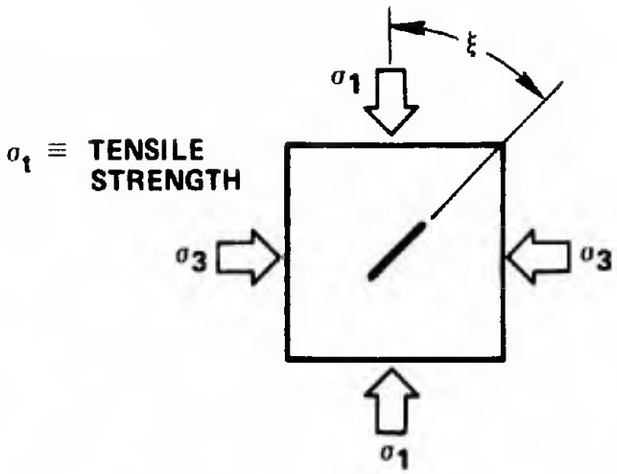

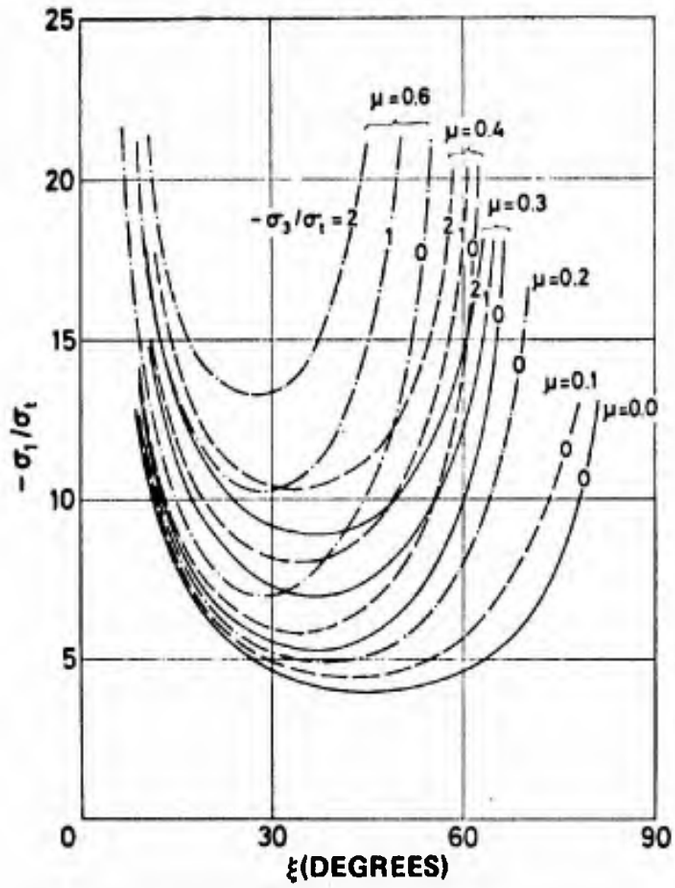

Figure 39. Fracture Initiation Criterion for a Closed Flaw.

The above discussion of closed flaw behavior was concerned only with crack initiation at the flaw tip. The nature and amount of crack extension which occurs from such flaws is not understood. As in the open flaw case, a relationship between the extended crack length (ℓ) and the applied stress is desired. As before, the difficulty in obtaining the relationship $\ell = f(\sigma \text{ applied})$ is involved with modeling the flaw-crack configuration, only in this case the situation is further complicated with additional parameters. Crack extension from closed, sliding flaws will also be stable for the same reasons cited in the open flaw case. As the closed flaw extends a crack, the intensified stresses around the flaw are reduced because of the change in geometry of the free surfaces as the crack extends. As K for the flaw approaches K_c, the crack initiates and $K_{\text{flaw-crack}}$ becomes less than K_c. A further increase in applied stress is needed to satisfy the criterion for additional crack extension i.e.

$$K_{\text{flaw-crack}} = K_c. \tag{21}$$

Qualitatively, the extension of a crack from a two-dimensional, Type II flaw may be represented as in Figure 40. The flaw may be seen as two blocks (upper and lower) sliding past each other under the action of a shear stress (τ). No stress concentration exists at the tips until the flaw faces slide. As the faces slide, they pry open a crack. The displacement of the faces, parallel to the plane of the faces, controls the crack opening displacement (C.O.D.) and the level of the stresses tending to open the crack. The extended length of the crack must be related to the relative displacements of the crack faces. It can be

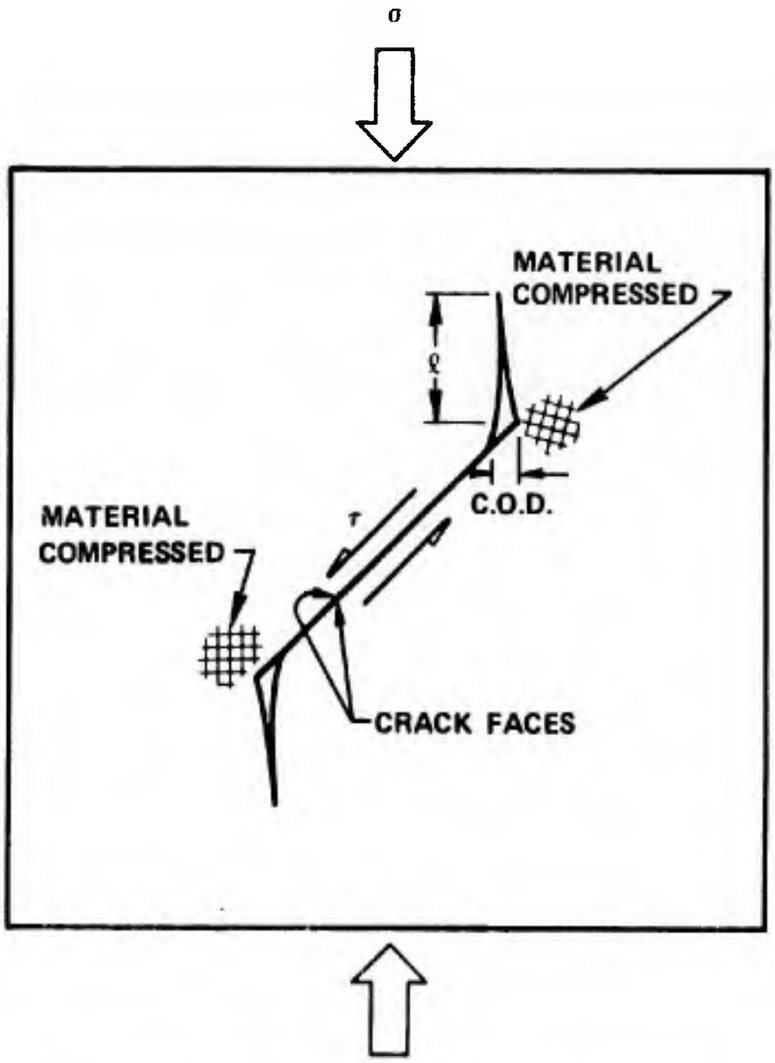

Figure 40. Crack Extending from Closed, Sliding Flaw.

seen that the displacement of the faces and resultant opening of the crack requires material to be compressed at the other end of the face. This steady compression of material under increasing load results in stable crack extension and $\ell = f(\sigma \text{ applied})$.

iii. Type III - closed flaws which are locked

Type III flaws are flaws which have closed faces that transmit normal stress across them and whose faces are locked into a fixed position with respect to each other. The faces are either mechanically interlocked or weakly bonded together. (See Figure 41(a).) A shear stress τ_u must be created on the flaw plane to break the flaw faces free to slide. Once the flaw faces begin to slide the intensified stresses around the flaw may be calculated in a fashion similar to that used for Type II flaws with a characteristic dynamic coefficient of friction μ_D.

Type II flaws may become Type III flaws by locking during the sliding displacements of their faces under increasing applied loads. The segments of the flaw between locking points can act as short Type I or Type II flaws and will have stress concentrations at the ends of the segments which can initiate cracks before $\tau = \tau_u$ (See Figure 41(b).) This is another possible explanation of the cracking observed in the central portions of flaws by Hoek and Bieniawski.[49]

The magnitude of the concentrated stresses at the tips of the "open" or "closed and sliding" portions of pinned flaws can become great enough to break in direct shear the material at the pinning points. In materials in which the measured compressive strength is on the order of one tenth of the theoretical material strength (10^6psi), unflawed material at the pinning points can be sheared apart. Areas in the

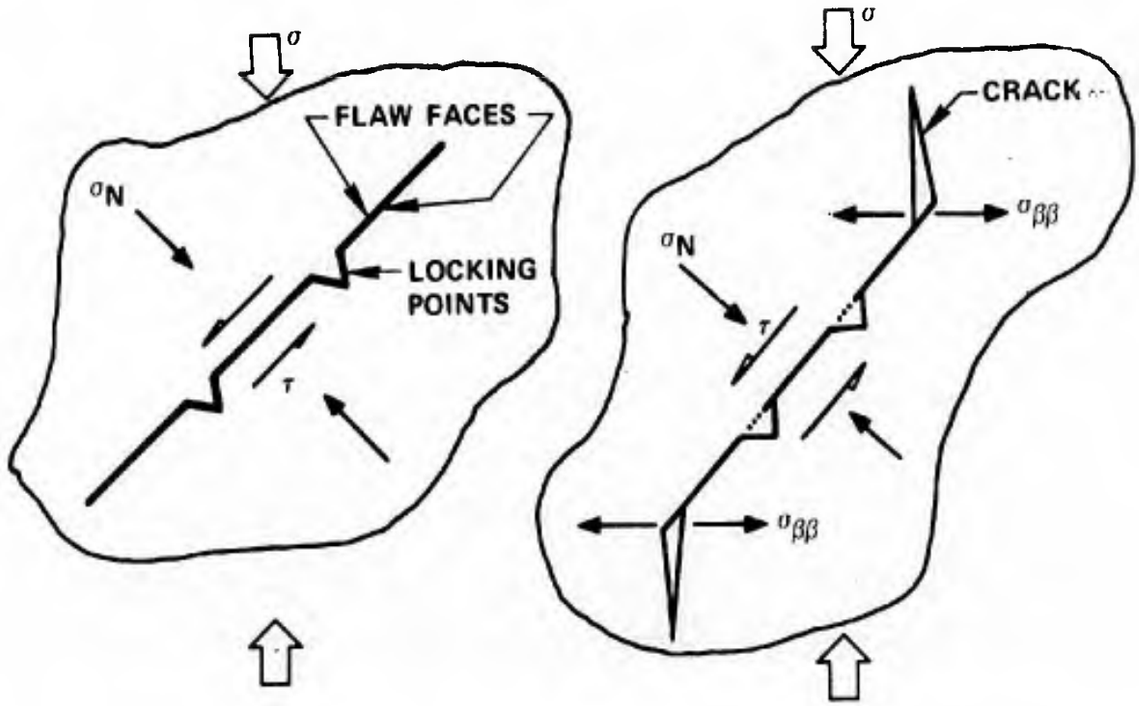

$\tau < \tau_u$ $\tau \geq \tau_u$; $\sigma_{\beta\beta} = (\tau - \tau_f)\ 2\beta/2\alpha_0^2 + \beta^2$; $\tau_f = -\mu_D \sigma_N$

(a) TYPE III FLAW INITIATING CRACKS BY UNLOCKING

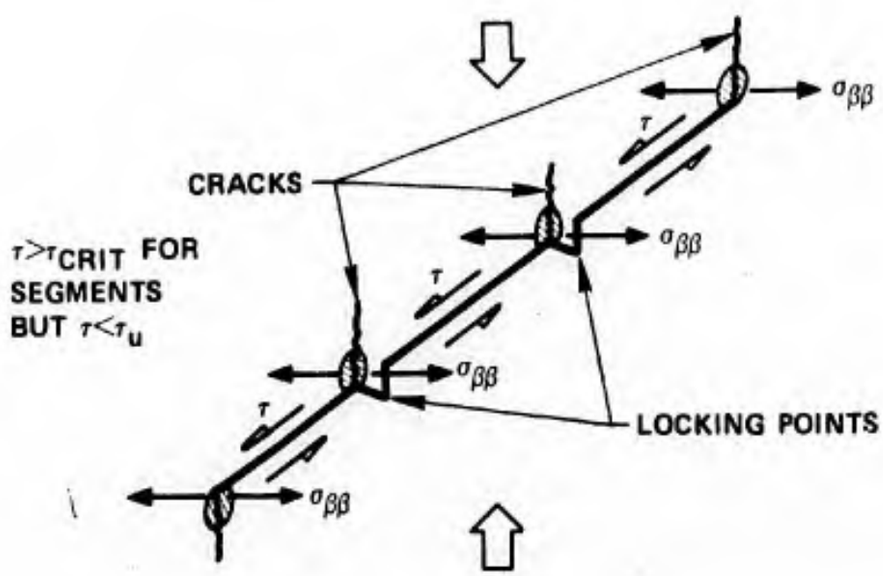

(b) TYPE III FLAW INITIATING CRACKS BEFORE UNLOCKING.

Figure 41. Conceptual Diagram of Type III Flaw Behavior.

material particularly susceptible to this are pinned grain boundaries associated with pores positioned critically at grain triple-points which would allow large unrestricted face displacements. In high strength materials that have low flaw densities, the shear stresses may become great enough to cause weaker, continuous areas of the material to fail. This would produce a crack in unflawed material which could then function as a flaw to extend a crack in a direction similar to Type II flaws. The twinning mechanism of crack formation proposed by Rice[50] would be this form of Type III flaw.

The stress concentrations around a bonded Type III flaw are near to zero until the bond is sheared apart. The stress concentrations around a mechanically-locked, Type III flaw can be quite complex until the flaw faces break free and slide. When $\tau = \tau_u$ and the faces begin to slide, the solution to the stress intensification at the tips is analogous to a Type II flaw; however, as the flaw faces break free, a dynamic effect will occur resulting in a higher level of concentrated stresses at the flaw tips. A first approximation to the dynamic effect shows that the magnitude of the initial stress impulse will be twice the magnitude of stress created by slow loading. Also a dynamic coefficient of friction (μ_D) would have to be used. The relationship between the critical shear stress on the flaw plane necessary to overcome the lock (τ_u) and the critical shear stress necessary to initiate a crack (τ_{crit}) is unrestricted-τ_u may be less than, equal to or greater than τ_{crit}.

Because of the dynamic manner in which the local intensified stresses are created and in light of the various possible relationships

between τ_u and τ_{crit}, Type III flaws may exhibit various kinds of crack initiation and extension behavior.

(1) If $\tau_u << \tau_{crit}$, then crack initiation will occur stably and in a fashion very similar to Type II flaws.

(2) If $\tau_u < \tau_{crit}$, stable crack initiation can occur at lower stresses than those required for the equivalent Type II flaw. The McClintock-Walsh theory predicts that Type II flaws which have a coefficient of friction between the faces near to zero can initiate cracks when the applied compressive stress is four times the magnitude of the applied tension required for crack initiation. If a Type III flaw unlocks ($\tau = \tau_u$) under an applied compressive stress which is twice the magnitude of the tensile stress required for crack initiation, the dynamic effect will raise the shear stress on the flaw plane to be equivalent to the shear stress developed by a static compressive loading four times the tensile stress required for crack initiation. The condition $\tau \geq \tau_{crit}$ will be satisfied and these Type III flaws will initiate cracks at applied compressive stress levels of only twice the magnitude of the tensile strength.

(3) If $\tau \approx \tau_{crit}$, crack initiation will occur at similar stress levels to Type II flaws. Since at the moment of Type III flaw face sliding the dynamic value of τ is at least doubled, the propagation of the initiated crack from this type flaw will initially be unstable since $\tau > \tau_{crit}$. The initiated

crack at this flaw will extend some distance before stopping greater than that under the previously discussed conditions.

(4) If $\tau_u > \tau_{crit}$ but less than the maximum seen at structural collapse of the body, the applied stress level for crack initiation will be controlled solely by τ_u and crack initiation will occur only at stresses greater than for Type II flaws. Since at crack initiation (face sliding) $\tau = \tau_u > \tau_{crit}$, a condition of unstable crack propagation will prevail. The dynamic effects will be very large and the extended crack lengths will be considerably longer at the applied stress level for crack initiation than for the previous cases. Bonded Type III flaws and some mechanically well-interlocked flaws are examples of those which may behave in this manner.

Flaws which have an orientation ξ to the applied stresses that results in a large normal compressive stress on the flaw plane will have a greater tendency to behave as Type III flaws. Large values of the normal stress on the flaw plane would encourage Type III flaw behavior. For a uniaxial applied compression large values of ξ would promote such behavior. In biaxial and triaxial stress states the value of the normal stress would have to be examined for all flaw orientations to determine which would promote such behavior.

As noted in the above discussion, crack propagation from Type III flaws can be unstable at the moment of crack initiation. In the language of fracture mechanics, the K for the flaw at the stress level for unlocking may be much larger than K_c the critical stress intensity necessary to extend a crack from the flaw. Dynamic crack propagation considerations

must be used and K will represent a dynamic stress intensity factor. As the crack propagates away from the flaw, the K for the flaw-crack configuration will decrease as seen before. Eventually K will become less than K_c for any constant applied stress level and crack propagation will cease. The dependence of the length of the extended crack on the applied stresses will thereafter be identical to a Type II flaw, so long as the faces do not lock again. The initial length of the unstably propagated crack may, however, be considerably larger than the total extended crack length possible from Type II flaws at any stress level less than that to cause structural collapse of the body.

iv. Flaw positions within the body

Type I, II, or III flaws may occur at any position with respect to a free surface of the body. At one extreme the flaw is positioned well away from any free surface of the body. These are the kind of flaws considered in the preceding discussions of flaw models. At the other extreme the flaw may intersect a free surface. The stresses around an identical flaw situated in the two extreme position are different. The intensified stresses around a flaw change as the position of the flaw approaches a free surface because the presence of the free surface affects the boundary conditions imposed on the differential equations for equilibrium of the stresses. In general, surface flaws intensify applied stresses to a greater extent than imbedded flaws.

Modes of Flaw Face Displacements

It is useful at this point to invoke a concept developed in fracture mechanics - that of dividing the stress fields near flaw tips

into three basic types, each of which is associated with a local mode of deformation or displacement.[43] (See Figure 42(a).)

In Mode I, the opening mode, the flaw faces move directly apart in a direction parallel to the y-axis, i.e. perpendicular to the faces of the flaw. The displacements are symmetric with respect to the x-z and x-y planes. In Mode II, the edge sliding mode, the flaw faces slide past one another in a direction parallel to the x-axis. The displacements produced by this mode of flaw opening are symmetric with respect to the x-y plane and skew-symmetric with respect to the x-z plane. In Mode III the flaw faces slide past each other in a direction parallel to the z-axis, i.e. the leading edge of the flaw. Displacements in this mode are skew-symmetric with respect to both the x-y and x-z planes. Kassir and Sih[61] state that the most general case of flaw tip deformation and stress fields may be described by superposition of these three displacement modes.

The stress and displacement fields associated with each mode were described by Irwin[51] who used the Westergaard[52] method. Using the coordinates of Figure 42(b) the stresses associated with each mode are as follows:

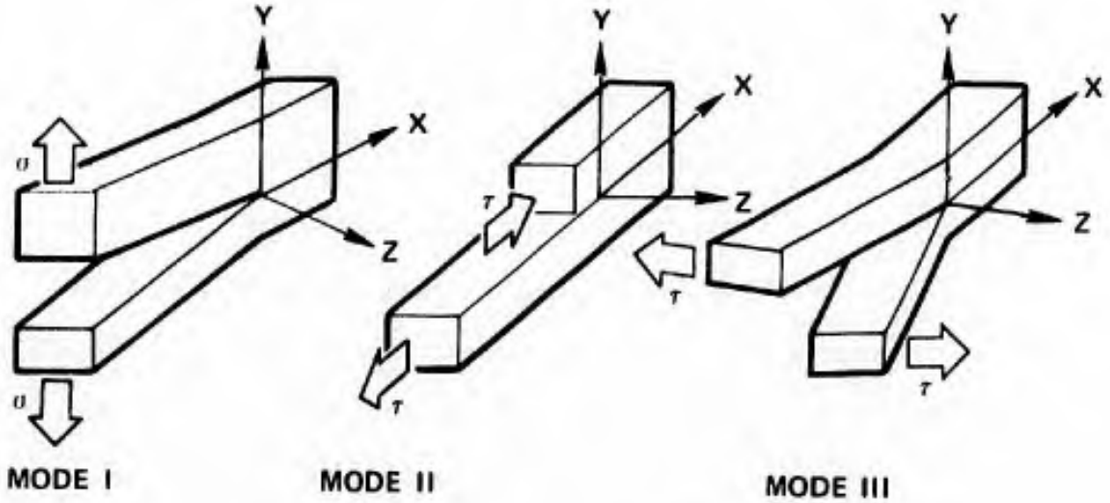

(a) MODES I, II, AND III

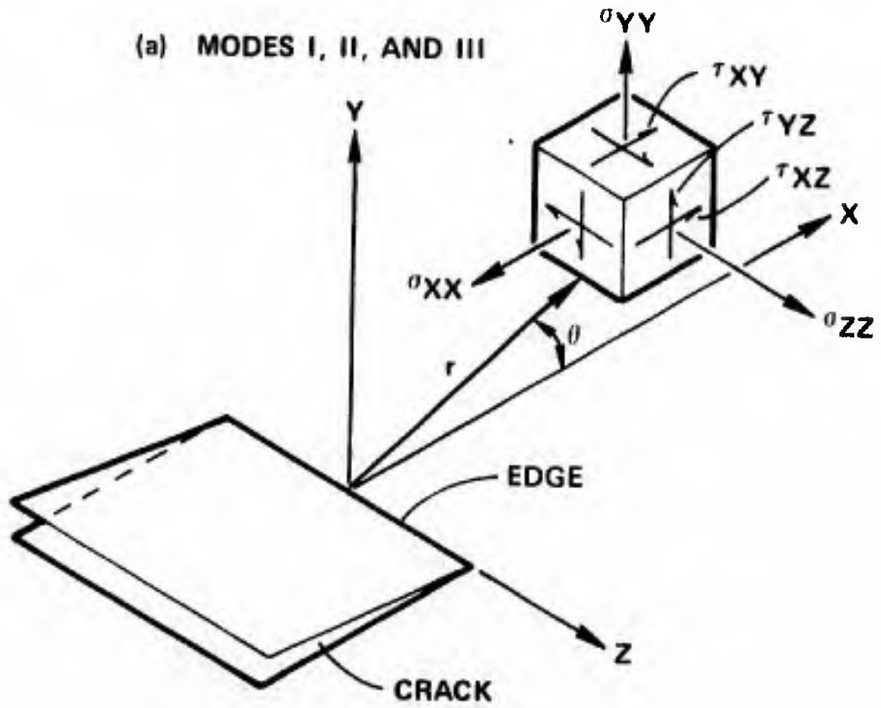

(b) COORDINATES USED TO DESCRIBE STRESS COMPONENTS IN CRACK TIP REGION.

Figure 42. Modes of Crack Face Displacement.

Mode I (plane strain)	Mode II (plane strain)	Mode III
$\sigma_x = \frac{K_I}{(2\pi r)^{1/2}} f(\theta)$	$\sigma_x = -\frac{K_{II}}{(2\pi r)^{1/2}} f(\theta)$	$\sigma_x = \sigma_y = \sigma_z = \tau_{xy} = 0$
$\sigma_y = \frac{K_I}{(2\pi r)^{1/2}} f(\theta)$	$\sigma_y = \frac{K_{II}}{(2\pi r)^{1/2}} f(\theta)$	$\tau_{xz} = -\frac{K_{III}}{(2\pi r)^{1/2}} f(\theta)$
$\sigma_z = \nu(\sigma_x+\sigma_y)$	$\sigma_z = \nu(\sigma_x+\sigma_y)$	$\tau_{yz} = \frac{K_{III}}{(2\pi r)^{1/2}}$ (22)
$\tau_{xy} = \frac{K_I}{(2\pi r)^{1/2}} f(\theta)$	$\tau_{xy} = \frac{K_{II}}{(2\pi r)^{1/2}} f(\theta)$	
$\tau_{xz} = \tau_{yz} = 0$	$\tau_{xz} = \tau_{yz} = 0$	

where: K_I ≡ stress intensity factor for Mode I loading

K_{II} ≡ stress intensity factor for Mode II loading

K_{III} ≡ stress intensity factor for Mode III loading

ν ≡ Poisson's ratio

$f(\theta)$ ≡ various functions of the θ coordinate

These equations are approximations which are good for r small compared to the flaw length but large compared to the tip radius (ρ). The stress intensity factors (K_j) describe the intensity of the stress fields and contain the magnitude of the applied stresses, the stressed body configuration, and the crack or flaw configuration. For simple loadings, the magnitudes of the stress intensity factors may be compared to ascertain the relative values of the intensified stresses with respect to different flaw positions within the body. The local stress intensification around the flaw for different crack displacement modes cannot be compared by the K_j's; for comparison between modes, the stresses σ_i, τ_i around the free surfaces of flaws must be calculated and compared directly.

The following observations may be made concerning two-dimensional flaws: The Mode I stress intensity factors for edge and imbedded flaws of length 2c are as follows: (See Figure 43(a) and (b).)

$$K_I = \sigma(\pi c)^{1/2} \qquad \text{imbedded flaw} \qquad (23)$$

$$K_I = 1.58\sigma(\pi c)^{1/2} \qquad \text{edge flaw} \qquad (24)$$

The stress around an edge crack in Mode I loading is 58% greater than for an imbedded one. The Mode III stress intensity factors for edge and imbedded flaws of length 2c are as follows: (See Figure 43(c),(d).)

$$K_{III} = \tau(\pi c)^{1/2} \qquad \text{imbedded flaw} \qquad (25)$$

$$K_{III} = 1.41\tau(\pi c)^{1/2} \qquad \text{edge flaw} \qquad (26)$$

The stress around the Mode III edge flaw are 41% greater than the imbedded one. The stress intensity factor for a Mode II imbedded flaw are: (See Figure 43(e).)

$$K_{II} = \tau(\pi c)^{1/2} \qquad \text{imbedded flaw} \qquad (27)$$

The solution for the stress intensity factor for the Mode II edge flaw is not available.

The crack extension "mode" of Type I, II and III flaws is not entirely clear. The situation becomes even more complex when three-dimensional flaws are considered. In general, it may be seen that the K factors for edge flaws are greater than for imbedded ones. A K factor criterion ($K_j = K_c$) for crack initiation is not synonymous with a critical tensile stress criterion ($\sigma_{\beta\beta} = \sigma_{crit}$) for flaws subjected to compressive stresses. Once initiation has occurred, a valid criterion for continued propagation is $K_{flaw\text{-}crack} \geqq K_c$ where for complex geometries and stresses this is generalized to:

$$f(K_I, K_{II}, K_{III}) \geq (K_{crit}). \qquad (28)$$

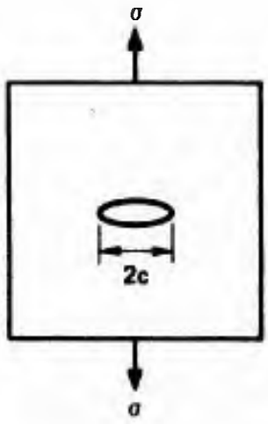

(a) AN INFINITE SHEET CONTAINING FLAW WITH UNIFORM NORMAL STRESS AT INFINITY.

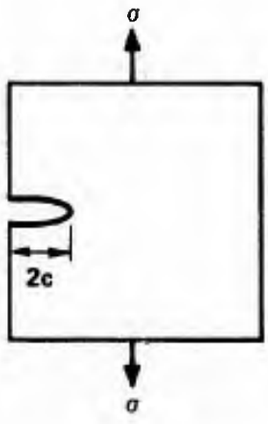

(b) EDGE FLAW IN SEMI-INFINITE SHEET WITH UNIFORM NORMAL STRESS AT INFINITE.

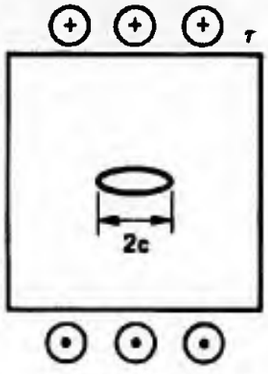

(c) INFINITE BODY WITH "TUNNEL FLAW" SUBJECTED TO OUT OF PLANE SHEAR (τ) AT INFINITY

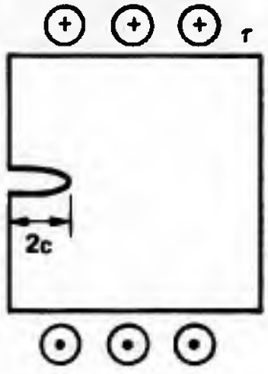

(d) EDGE FLAW IN SEMI-INFINITE BODY SUBJECTED TO OUT OF PLANE SHEAR (τ) AT INFINITY.

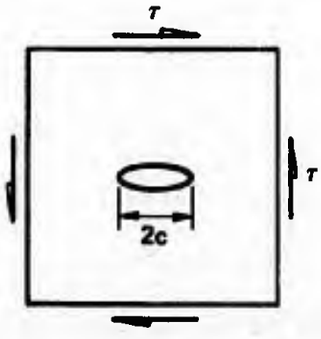

(e) INFINITE BODY WITH "TUNNEL FLAW" SUBJECTED TO UNIFORM IN PLANE SHEAR (τ) AT INFINITY.

Figure 43. Loading of Flaws at Various Positions Within Infinite Bodies.

With this in mind it is seen that flaws intersecting the free edge will behave differently than imbedded flaws.

Persimmon Seed Model

If two open flaws intersect the free edge of a body and are oriented as shown in Figure 44(a), both flaws will have concentrated tensile stresses at their tips ($\sigma_{\beta\beta}$) and these concentrated stress fields will overlap if the flaws are in sufficient proximity. Cracks extending from each flaw will tend to link up between the flaws. This can be thought of as a compressive stress "squeezing out" the particle of material between them. Because of the superposition of the two concentrated tensile stress fields of the two flaws and since the stress concentrations are greater for edge flaws, a crack will extend between them and produce a free chip before imbedded flaws in the body extend cracks. If the open flaw faces close and slide with a stick-slip action, the two flaws will extend cracks independently of each other, behaving as single, isolated Type III flaws. Single edge flaws will also extend cracks stably in a direction to intersect the free edge producing a free chip. This occurs because cracks extending near a free surface will tend to intersect the surface to lower the stored elastic strain energy around the crack. Cracks extending from edge flaws curve to become parallel to the applied compression but if a free surface is near they also extend to intersect the free surface since this results in a greater reduction in stored energy. A mathematical analysis of these two competing trends is not yet available. (See Figure 44(b).) If a single edge flaw has closed and locked, then when sufficient shear stress is present to overcome the lock, a crack will initiate and extend

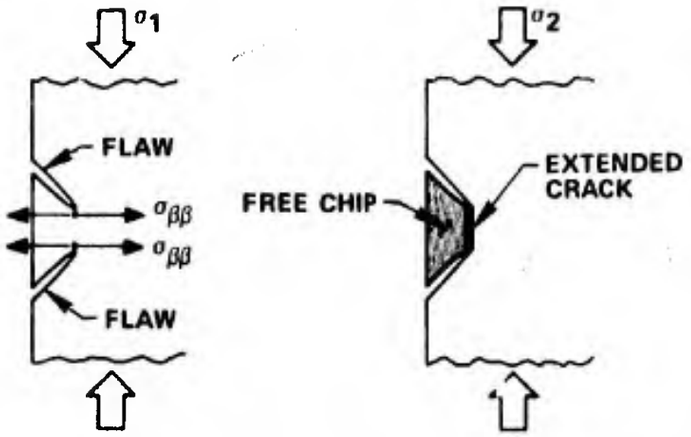

(a) PERSIMMON SEED CHIP FORMATION FROM TYPE I FLAWS ($\sigma_1 < \sigma_2$).

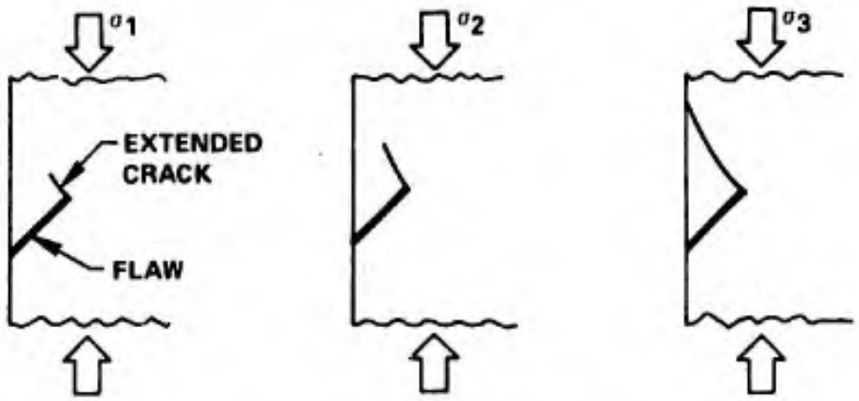

(b) STABLE CRACK EXTENSION FROM TYPE II SURFACE FLAW ($\sigma_1 < \sigma_2 < \sigma_3$).

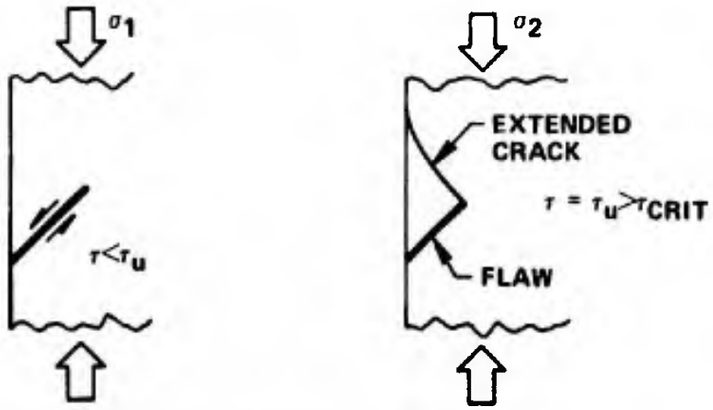

(c) UNSTABLE CRACK EXTENSION FROM TYPE III SURFACE FLAW ($\sigma_1 < \sigma_2$).

Figure 44. The Nature of Crack Extension from Edge Flaws.

unstably to the free edge, instantly producing a chip. (See Figure 44(c).)

Flaw-Crack Interactions

In materials which contain high densities of inherent flaws and in materials which contain high densities of extended cracks at stress levels near structural collapse, interaction between the stress fields of flaws and cracks may become prevalent throughout the body. These interactions will not be considered here other than to suggest that at the point of extensive interaction, structural collapse of the body is imminent.

"Flea-on-a-flea Flaws"

Very small flaws in the vicinity of large flaws may extend cracks at applied stress levels comparable to that at which the larger flaw extends cracks. This can occur even though the ability of the small flaw to concentrate the applied stresses is less than that of the larger flaw. The "effective applied stress" on the small flaw can, under certain geometries, be almost the full magnitude of the intensified stress around the larger flaw. An example of this would be a small Type II flaw at the tip of a large open flaw which is located in the area of maximum intensified compressive stress. (See Figure 45.) The applied stress level on the body containing these flaws is σ. The intensified compressive stress near the surface of the large flaw is $\sigma_{\beta\beta}$ which is calculated by the Inglis equations for the applied stresses acting on the large flaw. The direction of $\sigma_{\beta\beta}$ is tangent to the surface of the large flaw and the magnitude of $\sigma_{\beta\beta}$ decreases as the inverse root of the distance from the large flaw surface. This $\sigma_{\beta\beta}$ is effectively

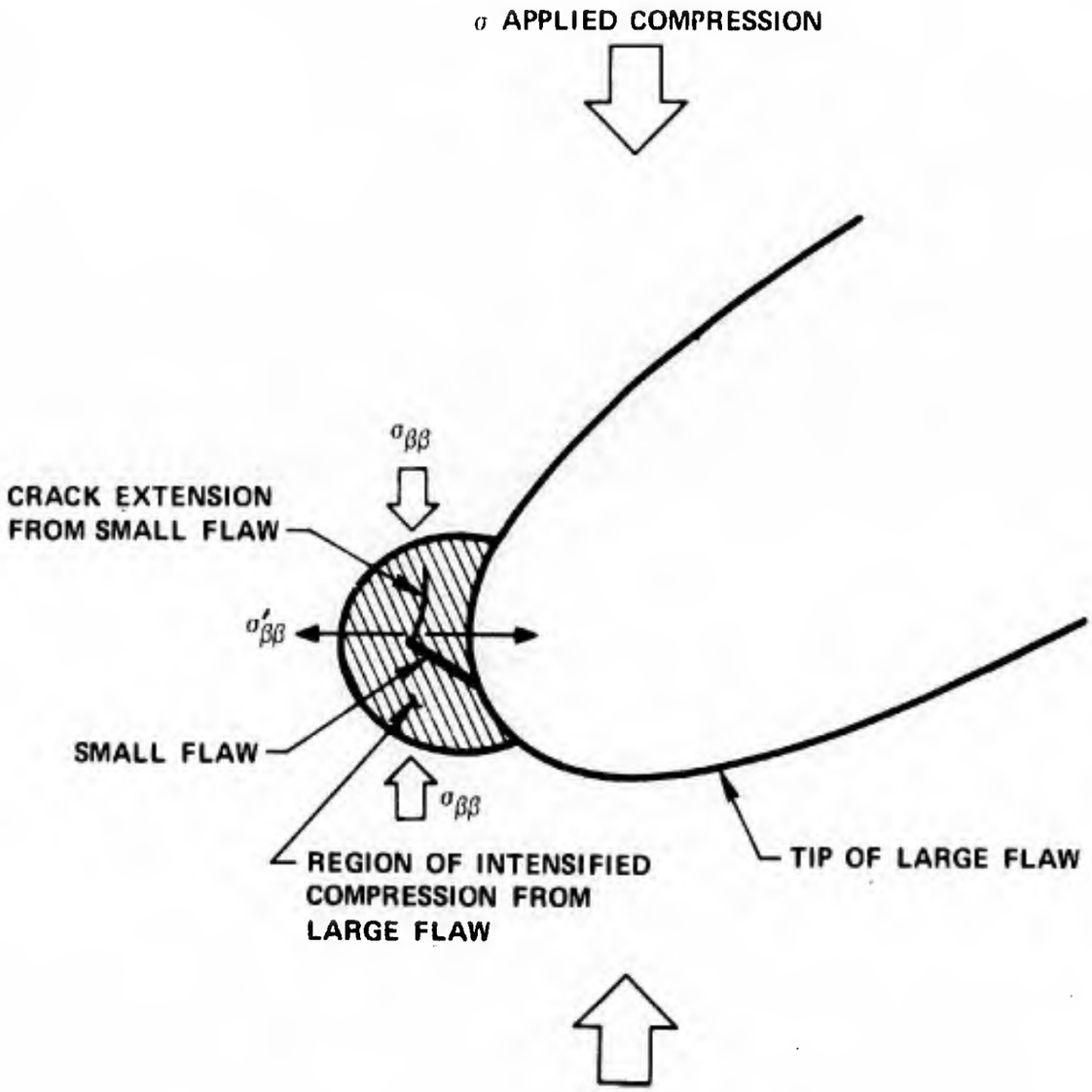

Figure 45. Flea-on-a-flea Flaw Crack Extension.

the "applied stress" on the small flaw. A calculation of the intensified stress at the tip of the small flaw ($\sigma'_{\beta\beta}$) is accomplished by applying the Inglis equations to the small flaw and assuming $\sigma_{\beta\beta}$ to be the applied stress. Such a small flaw in the intensified stress regions of the large flaw can initiate and extend cracks because of the intensified tension $\sigma'_{\beta\beta}$ at its tip. Such extended cracks will be of shorter length than the cracks extended from the large flaw. This kind of crack extension has been observed to occur from very small flaws at the tips of machined, three-dimensional slits introduced into blocks of polymethylmethacrylate plastic and loaded in compression. The small flaws were the result of machining damage created by the saw at the tip of the penny-shaped slits. If the small flaw was located in the intensified tensile stress region of the large flaw, it would serve to "sharpen" the large flaw tip but its behavior would not be distinguishable from the event of crack extension from the large flaw.

B. Experimental Studies of Crack Extension from Flaws

1. Recent experiments on crack extension from flaws in compression

Brace and Bombolakis[53] first demonstrated that the growth of cracks from flaws subjected to uniaxial compression proceeded on a curved path which becomes parallel with the direction of compression. They observed, when the extending crack is aligned with the direction of applied compression, growth stops and further extension does not occur unless the applied compression is increased considerably. These studies were made on slits introduced into plates of glass and photo-elastic material. Slow stable crack growth was observed to occur under increasing compressive loads. They also examined the behavior of en échelon crack arrays

to see if interaction between the stress fields of cracks occurred to produce crack linking and/or lowering of the stress required to initiate cracks. They found the cracks behaved independently as single, isolated cracks except perhaps for very special orientations of the array.

Hoek and Bieniawski[49] studied crack initiation and propagation behavior from two-dimensional flaws in glass plates subjected to biaxial compression. An important conclusion of the study was that the Griffith theory reliably predicted the applied stress required to initiate crack extension for the open flaws introduced into the plates. They also determined that the length of stably propagated cracks was related to the magnitudes and ratio of the applied principal stresses. The length of a stably propagated crack in uniaxial compression was found to be linear with the applied stress. Under biaxial compression the stably extended length of the crack decreased greatly when the transverse applied compression was only a small fraction of the longitudinal compression. Under applied biaxial compressive stresses with $\sigma_1 = 0.05\sigma_3$ the total extended length of the crack was limited to less than 0.2 of the originating flaw size. A small amount of transverse compression on a flaw significantly raises the stress to initiate cracks and limits the extended crack length to a fraction of the originating flaw size.

They also briefly investigated crack propagation from closed flaws and found that the crack tip plays a minor role in initiating the first cracks at such flaws. The factor responsible for crack initiation was the relative movement of the flaw faces. Irregular crack surfaces resulted in an uneven stress distribution along the faces and crack extension was found to initiate in regions where the tensile stresses

were high. Bieniawski[54] did further work on crack extension from closed flaws in glass and showed that large cracks do extend from the tips of such flaws when the stress is great enough to slide the entire flaw face. He demonstrated that the behavior of closed flaws in glass agrees with the predictions of the McClintock-Walsh theory (Type II flaws) if a coefficient of friction of $\mu = 0.7$ is assumed to exist between the crack faces.

Kobayashi[45] recently conducted more compressive experiments on the propagation of cracks from two-dimensional flaws introduced into a variety of brittle materials. Plates were loaded on their edged in biaxial compression and the flaw types studied were open, closed and inclusions. Some of the results of Kobayashi's open flaw study done in polymethylmethacrylate may be particularly important to the behavior of flaws in alumina. At flaw orientation angles of $\xi = 30\text{-}70°$ to the maximum applied compression the slits closed in the center at low loads and did not close on the ends until crack extension began. For flaw orientations with ξ small, little change occurred in the stresses around the flaw at crack initiation. But when ξ was large, the stress field around the flaw changed abruptly at the onset of crack extension, decreasing suddenly as the crack extended. The increase in crack length was observed to be roughly proportional to the applied load but extension was intermittent, not continuous. Crack initiation at the open flaws which closed under the applied compression was found to agree with the McClintock-Walsh theory. The lengths of the extended cracks were found to be limited under both uniaxial and biaxial compression. Cracks extended the furthest under uniaxial compression and almost no extension

was observed under biaxial compression if the minor applied compression was greater than 4% of the larger applied compression. The flaw orientation (ξ) also affected the extended length. The lengths of stably propagated cracks was found to be limited to less than two times the length of the originating flaw.

The experimental work described above showed that crack extension from flaws in compression is stable and of limited length at least for applied stresses less than several times the stress required to initiate the cracks. The theories concerning crack initiation at open and at closed flaws are fairly successful at predicting the stress levels for initiation. The extended crack length in uniaxial compression appears to be roughly proportional to the applied stress and is limited to two times the originating flaw size. Under biaxial stresses in the plane of the plate, crack initiation and the extended crack length are greatly inhibited by a small magnitude of the second compression. It is unfortunate that the effects of a biaxial stress state with the second compression in the other orthogonal, transverse direction was not investigated. The behavior of flaws subjected to this biaxial stress state is of importance when dealing with failure in biaxial compression. It should be emphasized that in the studies described above, all flaws studied were through-plate slits. It is to be shown that the behavior of cracks originating at three-dimensional flaws is similar in general, but more complex.

ii. Experimental study on the nature of cracks extending from flaws in compression

A comprehensive mathematical description of the extension of cracks from flaws in compression has not yet been formulated. In an effort to obtain some understanding of the relationship between the applied compressive stress and the extended crack length for two-and three-dimensional flaws this study was carried out. The study involved machining slits into plates or blocks of polymethylmethacrylate plastic (PMMA) and loading them in compression to produce crack extension from the introduced "flaws".

The plates used for the two-dimensional study were $3\frac{1}{2} \times 3\frac{1}{2} \times \frac{1}{2}$ inches with 3/4 inch long by 0.010 thick, through-cut slits introduced with a jeweler's saw. (See Figure 46.) The three-dimensional studies were performed on blocks $3\frac{1}{4} \times 2 \times 1$ inch thick. (See Figure 47.) Circular "penny-shaped" flaws were machined into the blocks using a 3/4" diameter by 0.006 inch thick circular saw. A 0.200 inch radius relief cut had to be made with an end mill to allow the circular saw to move a sufficient distance into the block such that a semicircular slit could be produced. By welding two blocks together containing 3/8 radius, 0.006 thick semicircular slits a full 3/4 inch diameter, penny-shaped flaw could be produced. These were loaded in uniaxial and biaxial compression as shown in Figure 47.

A 100,000 lbs. capacity Riehle beam machine with self aligning loading platents was used to apply the uniaxial compressive loads. The biaxial compression test was performed by using a machinists vise to constraint the transverse displacement of the specimen. A focused light

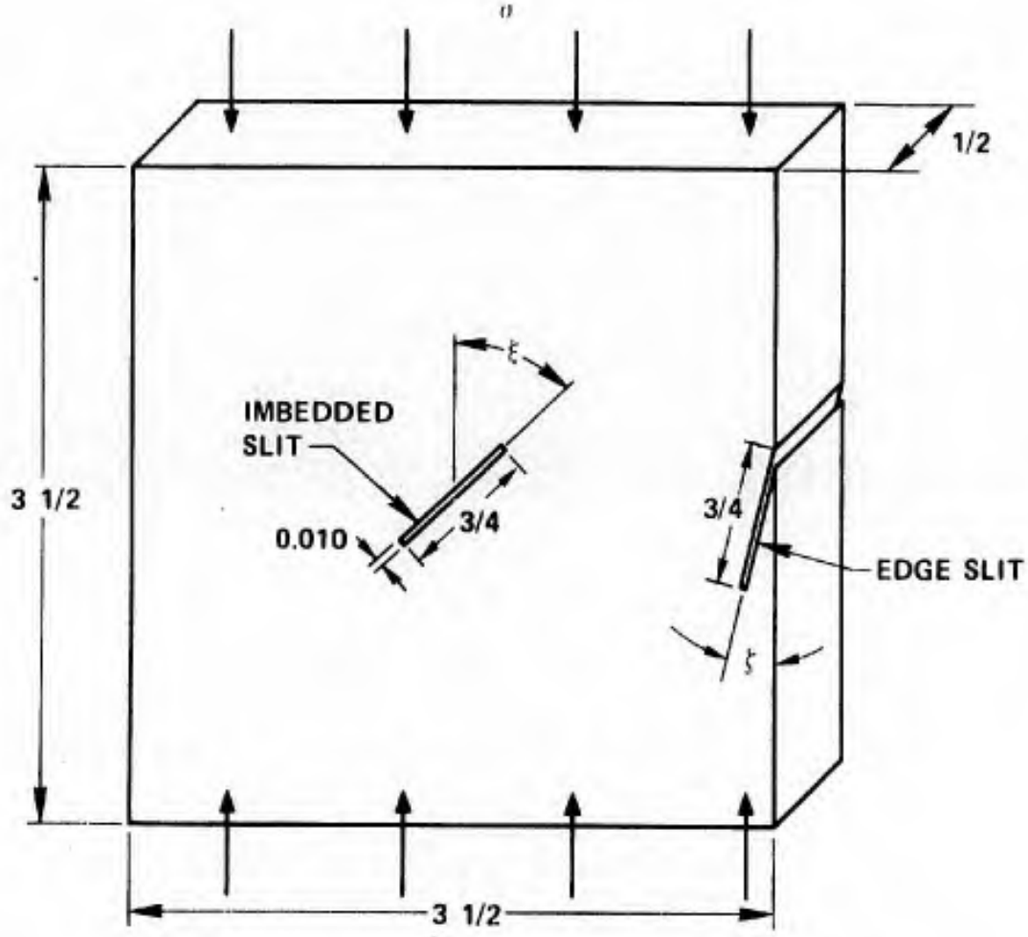

Figure 46. Two-Dimensional Slit Specimen Plate (One Slit per Plate).

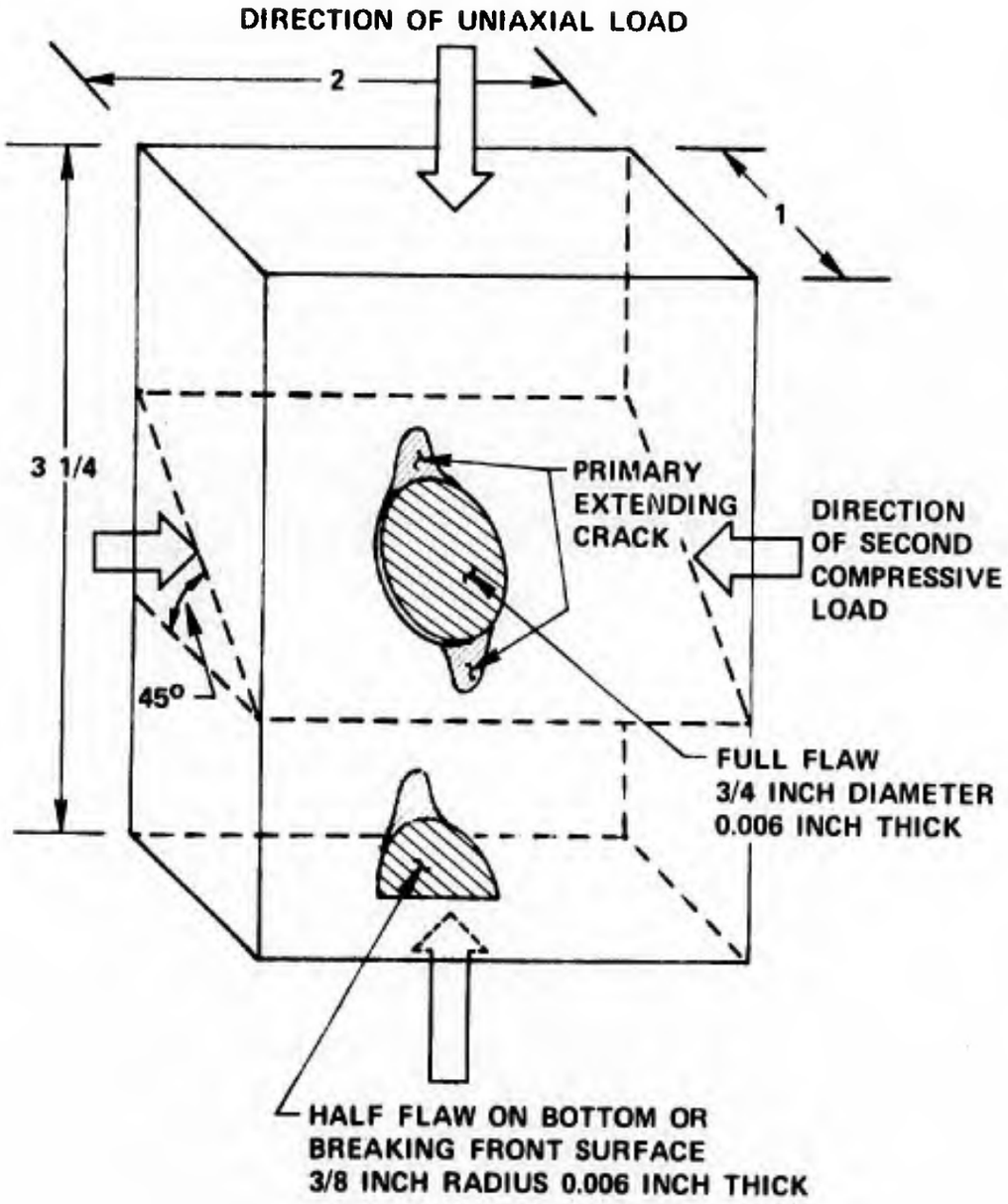

Figure 47. Penny-shaped Flaw in PMMA Plastic Test Block.

source was positioned to project the outline of the flaw and extending crack onto tracing paper mounted on the back of the specimen. By this technique the crack extension during various incremental stress increases was recorded by tracing the perimeter of the extended crack shadow. PMMA is a viscoelastic material and will approximate the behavior of a brittle material if loaded very rapidly then quickly unloaded. The specimens were loaded to a predetermined stress level at a rate of 2 kips (two thousand pounds) per second then immediately unloaded when the desired maximum load was reached. Crack extension was recorded and the specimen was reloaded to a higher stress.

The results of the two-dimensional studies are shown in Figure 48. The numbers shown on the figures indicate the load in kips applied to the plate to form a crack of the extended length indicated. In agreement with the predictions and experiments of other investigators with closed flaws, the stress required for crack initiation at imbedded flaws is at a minimum in the neighborhood of $\xi = 45°$ and increases as ξ approaches 0° or 90°. Crack initiation stresses at edge flaws exhibited a similar behavior. The crack initiation stress for edge flaws did not appear to be significantly different than that for imbedded flaws. There was a difference in the extended length vs. stress. Edge flaws generally extended longer cracks at a given stress level and these cracks did not become parallel to the applied load but propagated to the edge of the plate forming a detached chip.

The behavior of crack extension from the slit-flaws used in this study is complicated by the fact that the slit faces close and lock under load. Crack extension does not always vary directly with the

applied stress. If the crack faces close but slide, slow stable extension of the crack is observed. If the faces of the flaw lock as they close, no crack extension is observed until the faces break free and slide, then crack extension is rapid over some length after which the crack again stops. Either one type of behavior or the other smooth, stable extension or no extension followed by rapid extension, can be observed at any time during loading of the plate. As an extreme example of the stick-slip sliding phenomenon occurring between the flaw faces, the plate containing the $\xi = 70°$ imbedded flaw was loaded to 26 kips with practically no crack extension. When reloaded again from zero, the large extension shown in Figure 48(c) was observed to occur instantaneously at 14 kips. No further extension occurred until the load reached 25 kips at which point the second extension occurred. The nucleation point of the large extension at 14 kips during the second loading was at a different position on the slit than the very small extension observed during the first loading. The crack extension at 25 kips appears to initiate from the 14 kip extended crack as though the 14 kip extended crack were behaving as an originating flaw in the material. (See Figure 49.) Perhaps the machined slit locked after the 14 kips extension and never unlocked leaving the 14 kip extension of the crack to function as the only "flaw" in the material. The stick-slip behavior of the flaw faces with the accompanying rapid crack propagation was particularly prevalent for flaws which were oriented with ξ large. This is reasonable since for these flaws the normal stress closing the faces is large; this would facilitate locking. The $\xi = 70°$ edge flaw

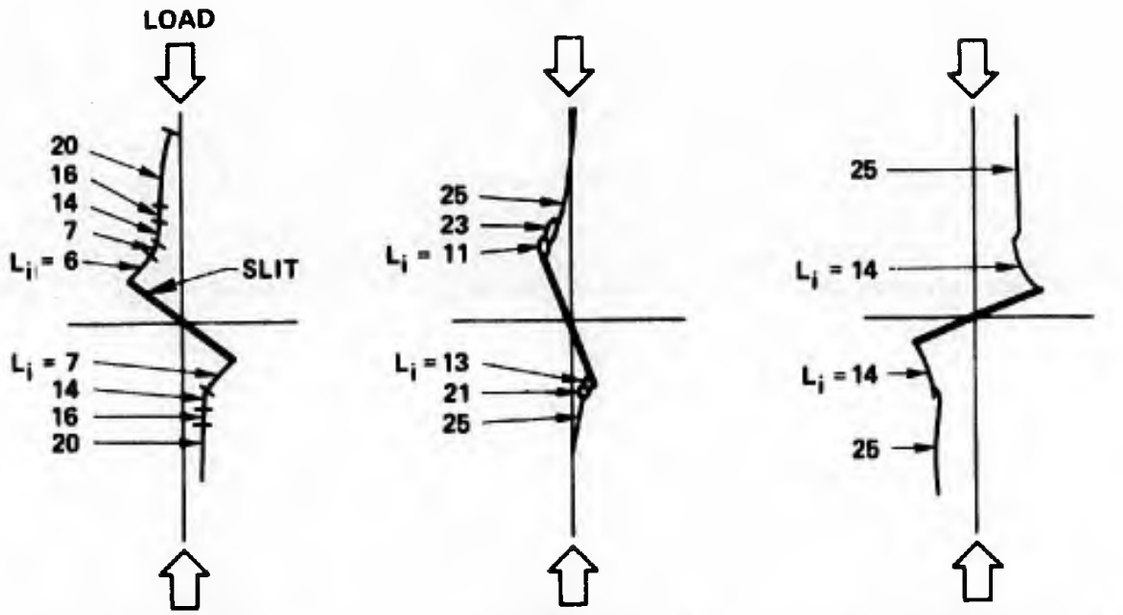

(a) IMBEDDED FLAW $\xi = 45^o$

(b) IMBEDDED FLAW $\xi = 20^o$

(c) IMBEDDED FLAW $\xi = 70^o$

*NUMBERS INDICATE VALUE OF APPLIED LOAD (KIPS) AT LIMIT OF CRACK EXTENSION INDICATED.
*FLAW LENGTH IS 3/4 INCH EXCEPT FOR (h) AND (i) WHERE IT IS 1/2 INCH

Figure 48. Two - Dimensional Crack Extension from Thin Slits in PMMA Plastic.

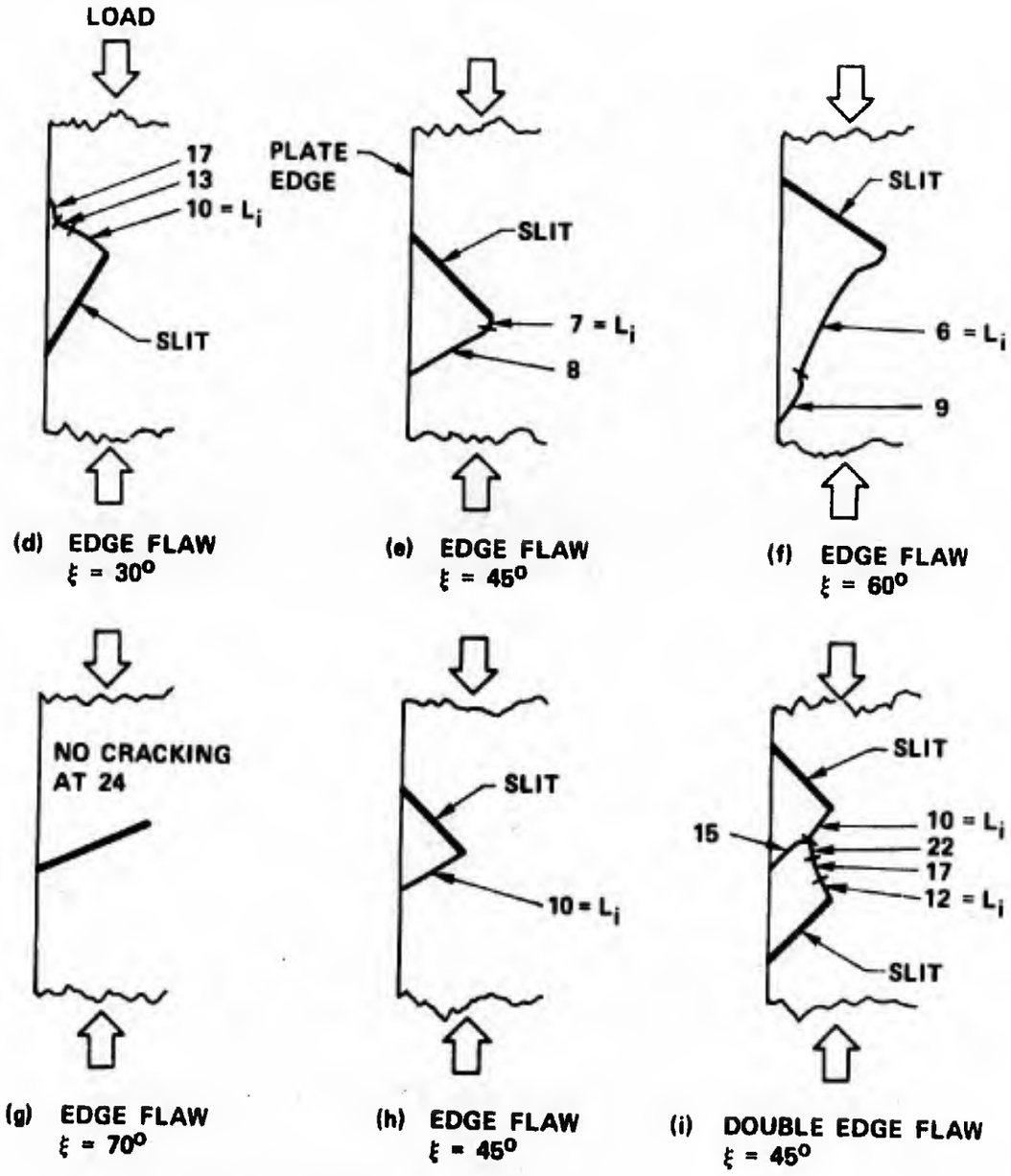

*NUMBERS INDICATE VALUE OF APPLIED LOAD (KIPS) AT LIMIT OF CRACK EXTENSION INDICATED.
*L_i = LOAD AT WHICH CRACK INITIATED IN POSITION INDICATED.

Figure 48. Two - Dimensional Crack Extension from Thin Slits in PMMA Plastic. (Continued)

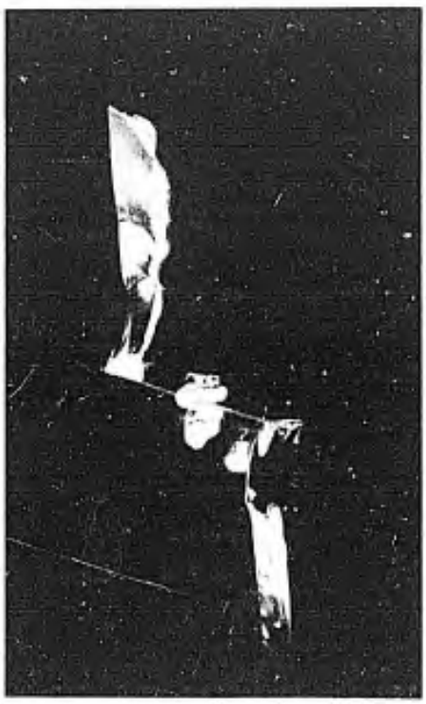

Figure 49. Two Step Crack Extension from $\xi = 70^{o}$ Two Dimensional Flaw Under Uniaxial Compression.

is the most extreme example of this, where it may be assumed that the faces never unlocked and no crack was initiated at loads up to 26 kips during the first loading.

The surface roughness of the machined flaw faces is undoubtedly important to the stick-slip behavior. The surface roughness of the two-dimensional slits was greater than that for the three-dimensional slits being approximately 5000 micro-inches RMS versus 32 micro-inches RMS, respectively. Even so, some reduced level of stick-slip behavior was observed during the loading of some three-dimensional slits. In all cases the sliding of the flaw faces just prior to the point of crack extension was accompanied by loud noises.

The $\xi = 45°$, double edge-flaw (see Figure 48(i)) did not extend a crack between the two slits. Cracks extended from the upper and lower slits independently. This was attributed to each slit intermittently locking and extending cracks. Double slit tests in which ξ was less than 45° did extend a crack between the two slits.

At an applied load of approximately 25 kips, the cracks which had extended from all orientations of flaws suddenly extended to a position near the ends of the test plate in a direction parallel to the applied compression. This phenomenon appeared to be independent of the extended length of the crack at the onset of this rapid extension and independent of the initiating flaw orientation. At applied loads above 25 kips the extended lengths of such cracks were no longer a function of the applied stress level, the extended crack orientation or the initiating flaw orientation. An explanation of this phenomenon is presented in Appendix C.

Figure 50 and 51 show the crack extension behavior of three-dimensional slits under uniaxial and biaxial compressive loads. Figure 50 shows the front face, projected limits of the extended cracks observed under increasing loads. These tracings show the extent of the primary cracks which initiate at the tips of the flaws closest to the applied compressions. Comparing the crack initiation loads for the fully imbedded flaw at 9 kips with the half imbedded flaw at 14 kips (Figure 50(a) and (b)), one can see that the inverse square root of flaw size dependence of the initiating stress agrees with the experiment where $C_{\text{full flaw}} = 1$; $C_{\text{half flaw}} = \frac{1}{2}$. Comparing the crack initiation stresses for the half imbedded flaw with the half surface flaw (Figure 50(b) and (d)), it is apparent the initiating stress does not differ by much. The extended crack length for the half surface flaw is about 50% larger than that of the imbedded half-flaw at any load above that to initiate cracking. The extending crack from the half surface flaw intersects the surface to form a free chip. (See Figure 50(d).)

A comparison of the behavior of the fully imbedded flaw with the imbedded flaw which intersects the surface at one tip shows the behavior of the latter is more complex. The flaw intersecting the surface initiated cracks on its perimeter at slightly lower stresses than the fully imbedded flaw. These cracks initiated near the free surface. (See Figure 50(c).) The extent of cracking at the opposite tip of the surface-intersecting flaw is comparable to that of the fully imbedded flaw; although, higher stress levels are needed for equivalent extension.

Comparing the behavior of the crack extension for the fully imbedded flaw under uniaxial and biaxial compression (Figure 50(a) and (e)), it

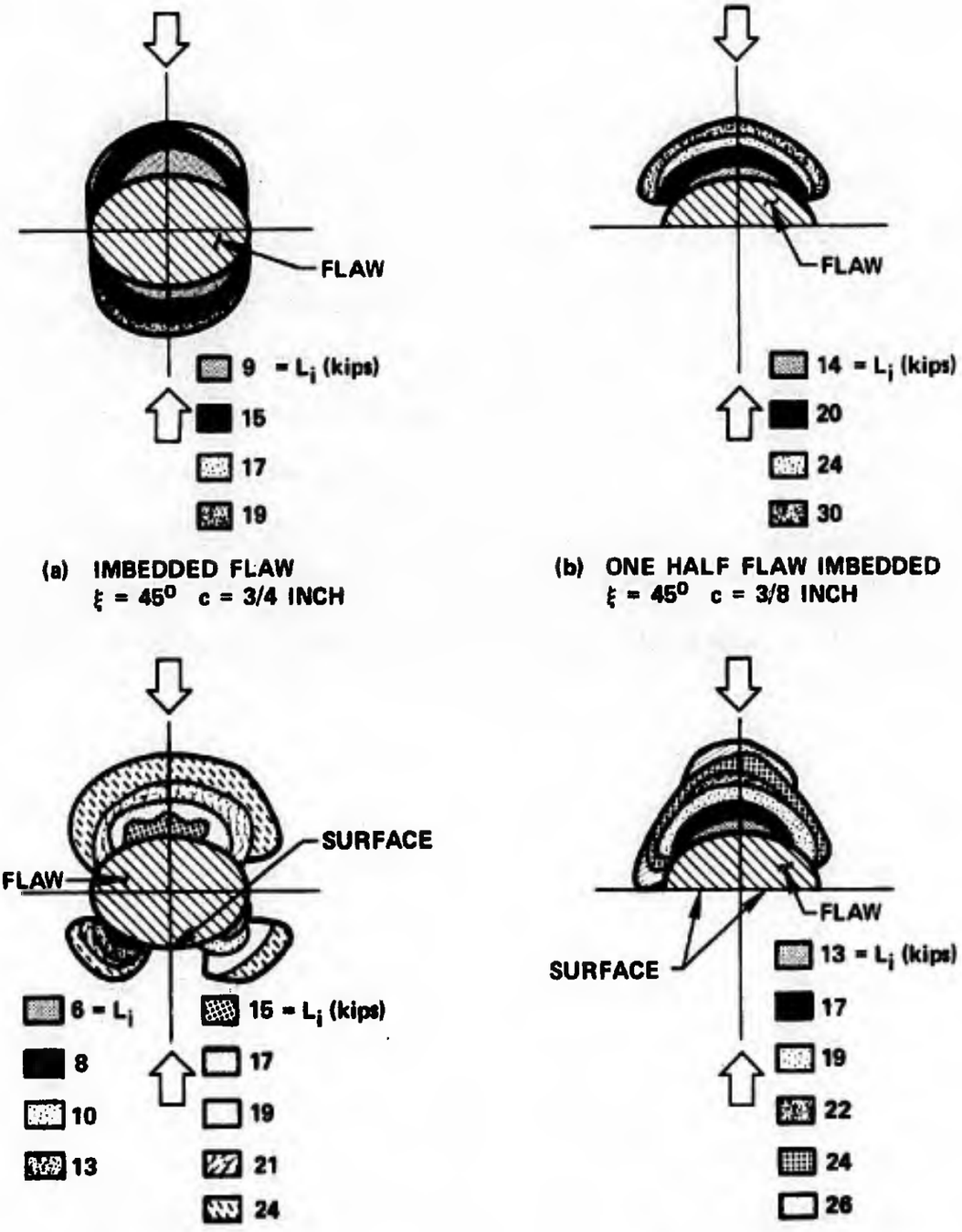

(a) IMBEDDED FLAW
$\xi = 45^0$ c = 3/4 INCH

(b) ONE HALF FLAW IMBEDDED
$\xi = 45^0$ c = 3/8 INCH

(c) IMBEDDED FLAW
INTERSECTING SURFACE
$\xi = 45^0$ c = 3/4 INCH

(d) ONE HALF FLAW
INTERSECTING SURFACE
$\xi = 45^0$ c = 3/8 INCH

*NUMBERS INDICATE VALUE OF APPLIED LOAD (KIPS) AT LIMIT OF CRACK EXTENSION INDICATED.
*L_i = LOAD AT WHICH FIRST CRACK INITIATED IN POSITION INDICATED

Figure 50. Crack Extension from Three - Dimensional Flaws.

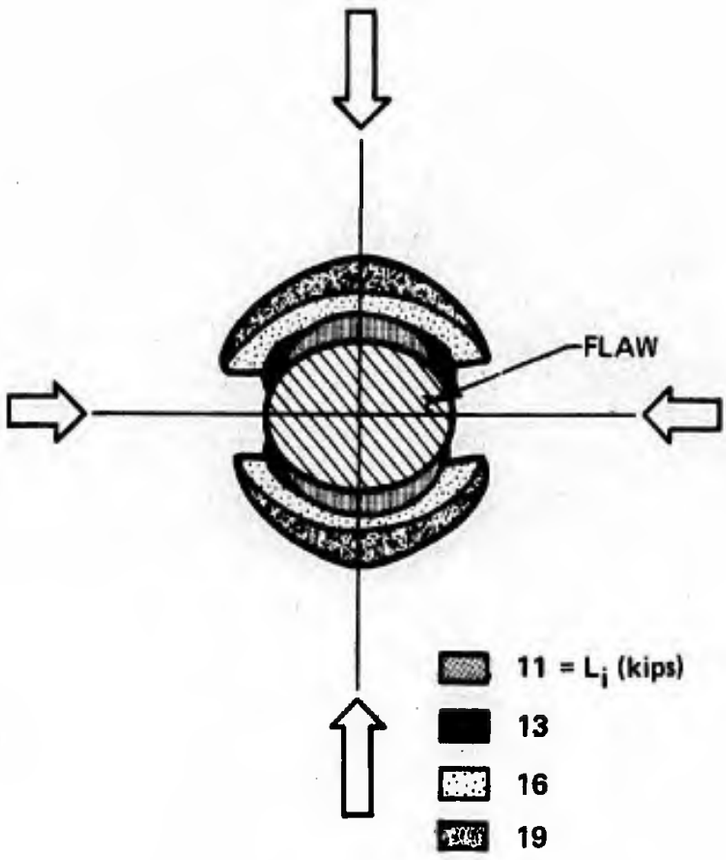

(e) IMBEDDED FLAW
$\xi = 45^o$ c = 3/4 INCH
BIAXIAL COMPRESSION

Figure 50. Crack Extension from Three-Dimensional Flaws. (Continued)

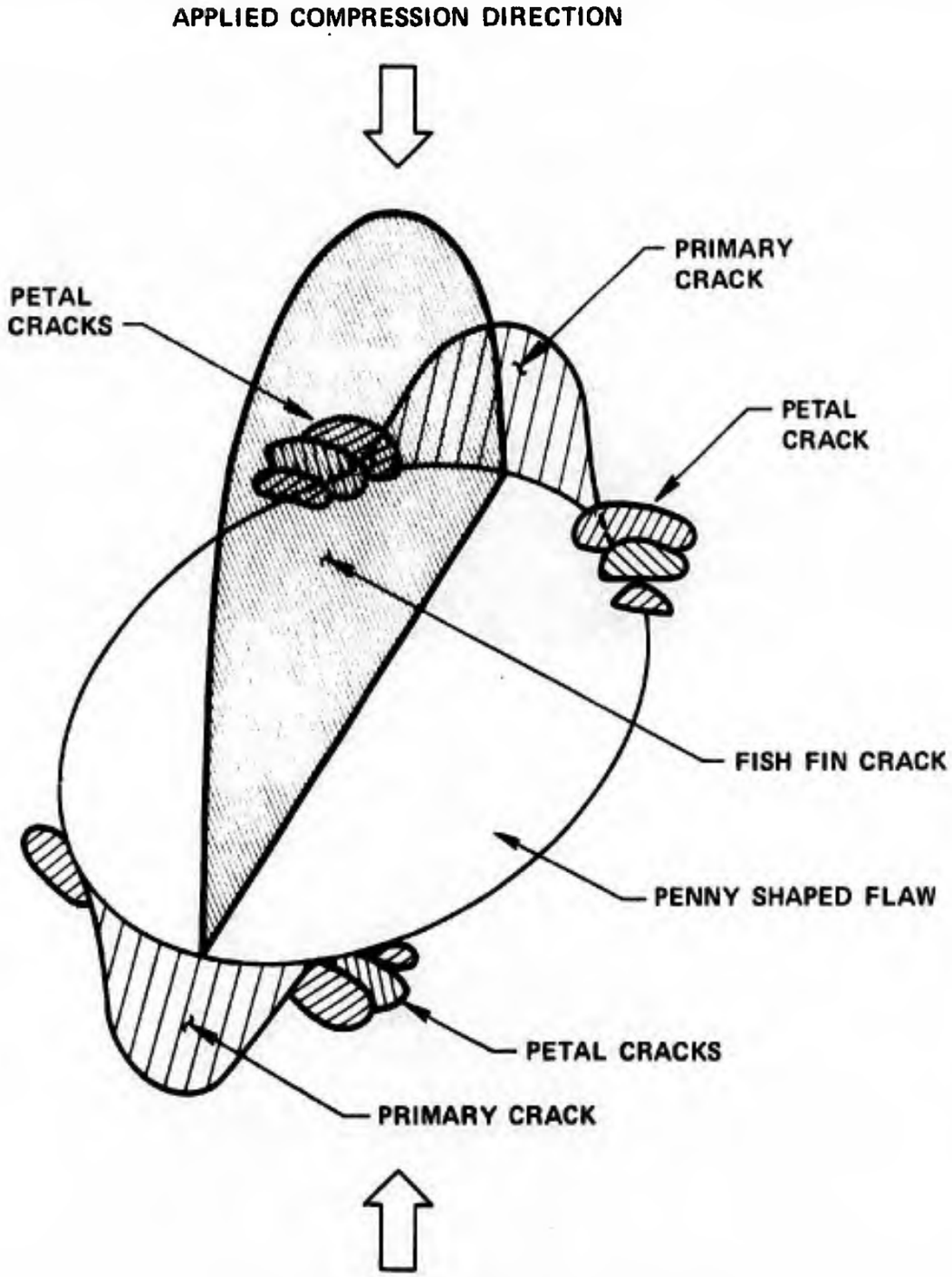

Figure 50f. Three-dimensional Sketch of Kinds of Cracks Which Extend from Penny Shaped Flaw.

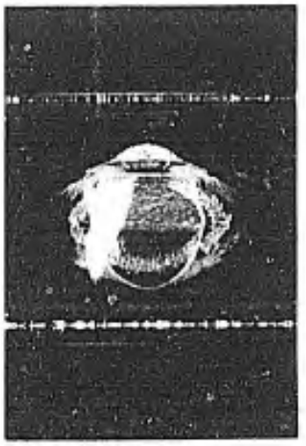

TOP

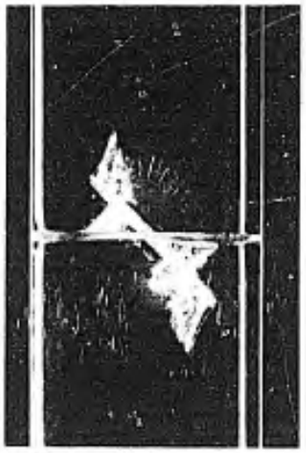

SIDE

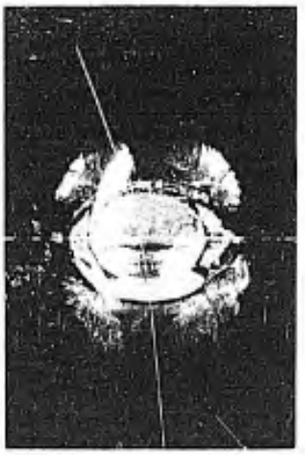

FRONT

(a) FULL IMBEDDED FLAW

Figure 51. Photos of Three Dimensional Flaws with Extended Cracks.

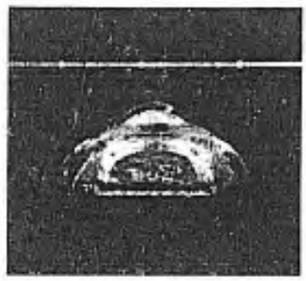

TOP

SIDE

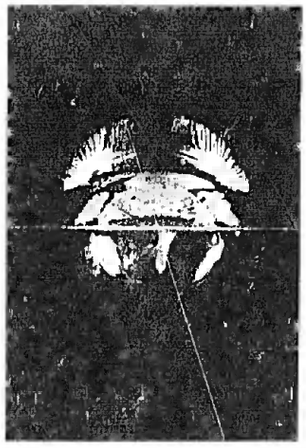

FRONT

(b) ONE HALF IMBEDDED FLAW

Figure 51. (Continued)

TOP

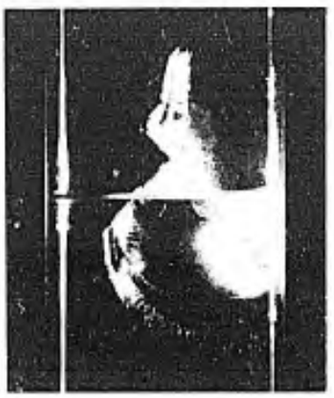

SIDE

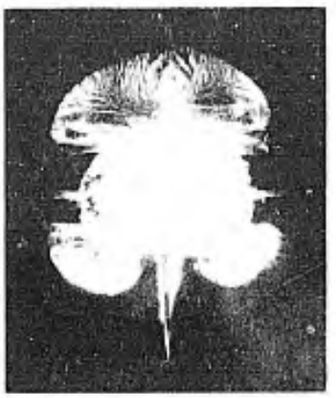

FRONT

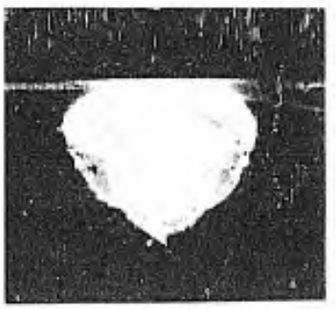

BOTTOM

(c) IMBEDDED FLAW INTERSECTING FRONT SURFACE

Figure 51. (Continued)

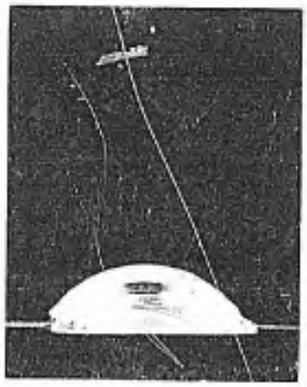

TOP

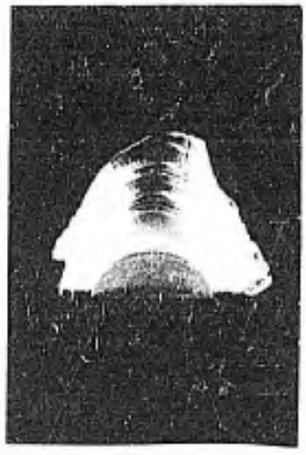

BACK

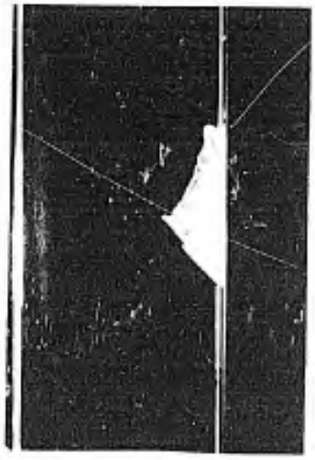

SIDE

(d) ONE HALF FLAW INTERSECTING SURFACE

Figure 51. (Continued)

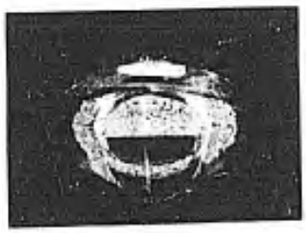

TOP

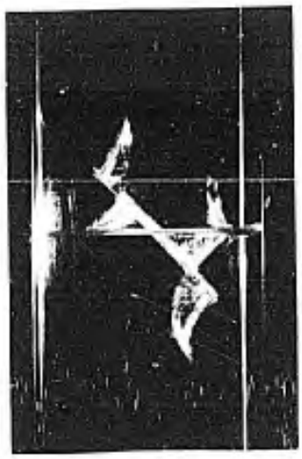

SIDE

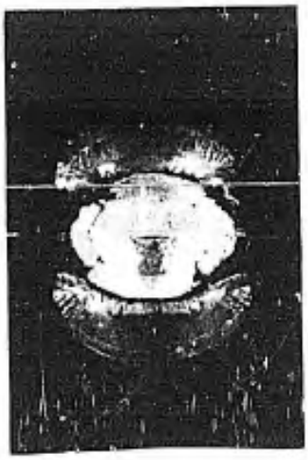

FRONT

(e) FULL IMBEDDED FLAW, BIAXIAL COMPRESSION

Figure 51. (Continued)

is seen that the uniaxially loaded flaw initiates cracks at lower stresses than the biaxially loaded one. The length of the extended crack in the direction of the uniaxial compression is comparable for each at any given stress level. The most important distinction between the two is the formation of "wings" on the extended crack in the direction of the second compression for the biaxially loaded flaw. These "wings" are formed because crack extension is occurring not only under the action of the uniaxial compression but also from the action of the second applied compression.

Figure 51 shows photographs taken of the various three-dimensional flaws and the cracks which have extended from them under the maximum loads to which they were subjected. These photos show several interesting aspects of the three-dimensional nature of crack extension from penny-shaped flaws in compression. Under the orientation of loading in this study the primary cracks initiate at the tips of the flaws nearest the applied compression. With increasing load, the cracks extend away from the tip of the flaw in a smooth curve to become parallel to the direction of the applied compression and simultaneously extend around the perimeter of the flaw. This general behavior is observed whether the flaw is imbedded or intersects the surface. (If a flaw which intersects the surface has its internal tip sufficiently close to the surface, e.g. half surface flaw, crack extension will not be parallel to the applied compression but will tend to intersect the surface.) The extended length of the crack in the direction of the applied compression for any position on the flaw perimeter varies approximately as the "length" of the flaw at that perimeter position where the "length" is

measured in the cross-sectional plane containing the perimeter position, flaw normal and the direction of applied compression. The maximum extended length occurs at the perimeter position in the center of the flaw. At the side of the flaw no extension occurs.

The primary cracks are not the only cracks which extend from penny-shaped flaws in compression. The maximum extended length occurs at the perimeter position in the center of the flaw. At the side of the flaw no extension occurs.

The primary cracks are not the only cracks which extend from penny-shaped flaws in compression. The photos of Figure 51 show examples of the other kinds of cracks which initiate and grow from various positions on the flaw. These secondary cracks initiate at higher stress levels than that required for primary crack initiation. Similar to the primary cracks, the secondary cracks align themselves with the direction of applied compression as they extend.

Two kinds of secondary cracks have been observed to form. They are called "petal" cracks and "fish fin" cracks. The petal cracks form on the perimeter of the penny-shaped flaws as shown in Figure 50(f). They are believed to be initiated near the flaw tip by the "flea-on-a-flea" flaw mechanism. (See Chapter V, Section A iv.) These petal cracks are formed at the flaw perimeter near the sides of most primary cracks and their extended lengths usually remain a fraction of the extended lengths of the primary cracks. The fish fin cracks form near the center of the flat surface of the penny-shaped flaw. (See Figure 50(f).) These cracks may extend to lengths greater than the length of the primary extended crack. (See Figure 51(c).) The condition for the initiation of fish

fin cracks is somewhat vague because the complete solution to the local stresses around the flaw-extended crack defect is not known. There exists a local tensile stress perpendicular to the plane of the fish fin crack which is described in Appendix C but it is not clear whether such stresses can account for the formation of these cracks.

Under increasing applied stress the primary cracks initiate and extend until they are aligned with the direction of applied compression. After alignment, their extension is arrested because of the reduction in the local tensile stress at the crack tip. As the applied stress level is increased, previously initiated secondary cracks may extend further, even though the primary crack is arrested. By this process a single flaw can create considerably more crack damage than would be predicted by sole consideration of the extension of primary cracks and their arrest.

iii. Conclusions from experimental study on crack extension

Several observations and conclusions may be made from the study on crack extension which bear upon an understanding of the creation of crack damage in a brittle specimen under compressive loadings.

(1) The general trend in the stress to initiate cracks with the orientation (ξ) of two-dimensional flaws is found to agree with theoretical predictions for the PMMA plates. However, this may be complicated by slit-flaws which close and lock, thereby requiring higher stresses to break the flaw faces free and initiate cracks.

(2) Three-dimensional, penny-shaped flaws with maximum dimension equal to that of two-dimensional slits require higher stresses to initiate cracks.

(3) Three-dimensional flaws can initiate secondary cracks in addition to the primary cracks extending from their tips. These secondary cracks may grow to sizable dimensions. Current theories of crack initiation treat only the formation of the primary cracks; yet secondary crack formation may result in considerably more crack damage being produced by a single flaw than that which would be predicted by considering only primary crack extension.

(4) The extension of cracks in two or three dimensions occurs in a direction so as to align the crack plane with the direction of the applied compressive stress.

(5) Under the action of biaxial stresses cracks tend to extend in the direction of both compressive stresses.

(6) The dependence of the extended crack length on the magnitude of the applied compression may be quite complicated. Cracks may extend stably or unstably due to the stick-slip phenomenon occurring at the originating flaw faces. Extending cracks may continue to extend in a smooth fashion or act as originating flaws initiating new cracks from their tips.

(7) The length of single, extended cracks subjected to compressive stress of a magnitude less than the intrinsic tensile strength of the material appears to be limited to dimensions on the order of the originating flaw size. This is no longer true

when the magnitude of the applied compression is equal to the intrinsic tensile strength. At this applied stress the local tensile stress at the tip of a crack, which is aligned with the direction of principal applied stress, equals the intrinsic tensile strength of the flaw free material. (See Appendix C.) At this stress level unstable extension of the aligned crack may occur. This unstable extension was observed to occur from aligned cracks in the PMMA material when the applied compressive stress was $\sim$18 ksi.

(8) Slit or penny-shaped flaws which intersect a free surface extend cracks which intersect the surface. In this way free chips are created.

(9) The action of double-flaws extending a crack between them and forming a free chip depends on whether the flaws are sliding free or intermittently locked and acting independently.

C. The Extension of Cracks from Flaws in Three Dimensions

Real materials are three-dimensional; hence, to adequately describe the failure of real materials, the three-dimensional nature of crack extension must be understood. If one of the principal stresses in a body is tensile, the extending cracks which cause failure always propagate in a direction normal to the principal tensile stress and such extension, once initiated, is generally unstable under the constant applied tension. This aspect of crack behavior in tensile stress states allows two-dimensional theories to predict real material strengths successfully. The behavior of three-dimensional cracks extending in purely compressive stress fields is not well understood but appears to

be considerably more complex than the behavior of cracks under tension. A continuum mechanics model is available for the three-dimensional flaw; it is that of a penny-shaped void in an isotropic, elastic continuum. Solutions for the stresses around such a flaw geometry are only available[55-58] for the open flaw (Type I). Extension of these solutions to the Type II or Type III flaws introduces formidable mathematical complexity.

Sack[59] has shown that for open flaws, Griffith's two-dimensional theory of rupture may be extended into three dimensions (for interior oblate spheroids of the same principal length) in the tension and tension-compression stress quadrants and that the results differ from Griffith's by a factor of 1.57 to 1.81 which depends on the Poisson's ratio of the material. Koide[40] has recently extended the Griffith criterion into three dimensions for purely compressive stress states. This section will present and extend some of the current ideas and observations on crack initiation and extension from three-dimensional flaws.

1. The initiation of cracks at three-dimensional flaws

Crack initiation at the tips of a three-dimensional flaw may be treated in a manner analogous to that used in two dimensions. Koide[40] has obtained solutions for the values of the normal (σ_n) and total shear stress (τ) acting across the equatorial plane of an oblate spheroidal shaped flaw, which are necessary for crack initiation, in terms of the theoretical tensile strength (σ^*) of the material. His approach to the problem is identical with the methods of solution used in the two-dimensional case where the local maximum tensile value of $\sigma_{\beta\beta}$ is set

equal to a critical value, σ^*, and σ_n and τ are determined from this equality. For a very thin, open, penny-shaped flaw he obtains the equation:

$$\tau = \frac{(2-\nu)\pi\sigma^*}{4S} \sqrt{1 - \left(\frac{4S}{\pi\sigma^*}\right)\sigma_n} \tag{29}$$

where ν = Poisson's ratio

S = shape ratio of oblate spheroidal flaw, i.e. ratio of major axis to minor axis length

Combining terms and rearranging:

$$\frac{\tau^2}{A\sigma^*} + B\sigma_n = \sigma^* \tag{30}$$

where:

$$A \equiv \left[\frac{(2-\nu)\pi}{4S}\right]^2$$

$$B \equiv \frac{4S}{\pi}$$

If this equation is stated as an inequality, it then represents the criterion for crack initiation at a flaw of geometry (S) imbedded in a material with Poisson's ratio (ν) expressed in terms of σ_n and τ.

$$\frac{\tau^2}{A\sigma^*} + B\sigma_n \geq \sigma^* \tag{31}$$

For any orientation of flaw plane the values of σ_n and τ may be obtained by resolution of the principal applied stresses onto the flaw plane. Those flaw orientations which satisfy the criterion of equation (31) will initiate, or will have initiated, cracks under the applied stress level considered.

The equation derived by Koide, Equation (29), may be expressed in terms of the principal stresses. If the three principal stresses in the body are σ_1, σ_2 and σ_3, the normal stress on a plane with the direction cosines a_x, a_y, a_z is:

$$\sigma_n = \sigma_1 a_x^2 + \sigma_2 a_y^2 + \sigma_3 a_z^2 \tag{32}$$

where:

$$\hat{x} \equiv \hat{1}$$

$$\hat{y} \equiv \hat{2}$$

$$\hat{z} \equiv \hat{3}$$

The shear stress on this plane is defined by:

$$\tau = (\sigma_1-\sigma_2)a_x a_y + (\sigma_2-\sigma_3)a_y a_z + (\sigma_3-\sigma_1)a_z a_x \tag{33}$$

By substituting these expressions into Equation (31) we obtain the criterion for crack initiation in terms of the applied stress state and the flaw orientation:

$$\frac{(\sigma_1-\sigma_2)^2 a_x^2 a_y^2 + (\sigma_2-\sigma_3)^2 a_y^2 a_z^2 + (\sigma_3-\sigma_1)^2 a_z^2 a_x^2}{A\sigma^*} + B(\sigma_1 a_x^2+\sigma_2 a_y^2+\sigma_3 a_z^2) \geq \sigma^* \tag{34}$$

A graphical solution to this equation is readily obtained by utilizing the method of Mohr's stress circles.[60] The Mohr's circle method is a conformal mapping of the three-dimensional stress state which permits graphical solution of any equation stating a crack initiation criterion when the criterion is expressed in terms of the normal and total shear stresses on the flaw plane. If the stress state is represented on σ_n, τ axes by Mohr's method and the curve of the particular crack initiation criterion under consideration is plotted on these axes, each point within the shaded portion of the area σ_1, σ_2, σ_3 (see

Figure 53) represents the orientation of the normal to a flaw plane which will initiate a crack. (The flaw plane orientation is obtained in terms of the Eulerian angles ξ_1 and ξ_2, see Figure 52.) This is true, since all points lying in the shaded area represent planes on which the normal and total shear stress equal or exceed that necessary to satisfy the crack initiation criterion. Plotting the parabola of Equation (34) for a given size of Type I flaw on the Mohr axes will determine what orientations of flaw planes have initiated cracks as shown in Figure 53(a) for the stress state $\sigma_3 = 10\ \sigma_2$; $\sigma_1 = 0$. The McClintock-Walsh criterion for Type II flaws will yield a straight line curve on the σ_n, τ coordinates (see Figure 53(b)) with slope equal to the coefficient of friction (μ), where $\mu = 0.5$ is used in the example arbitrarily. The Type III flaw criterion for crack initiation can also be represented on such coordinates where τ_u is the value of the shear necessary to unlock the flaw and μ_D is the dynamic coefficient of friction. The graphical solution to this criterion yields the orientations of flaws which initiate cracks as influenced by the additional requirement that $\tau = \tau_u$. (See Figure 53(c).)

Another method of describing crack initiation at three-dimensional flaws is that used in the approach of fracture mechanics introduced in Section A of this Chapter. Kassir and Sih[61] have extended the approach of fracture mechanics to a three-dimensional, flat, ellipsoidal flaw. They have derived the expressions for the Mode I, II and III stress intensity factors around the perimeter of such a flaw for a stress normal to the flaw plane and for all orientations of shear stress on the flaw plane. The results of their calculations are presented as the

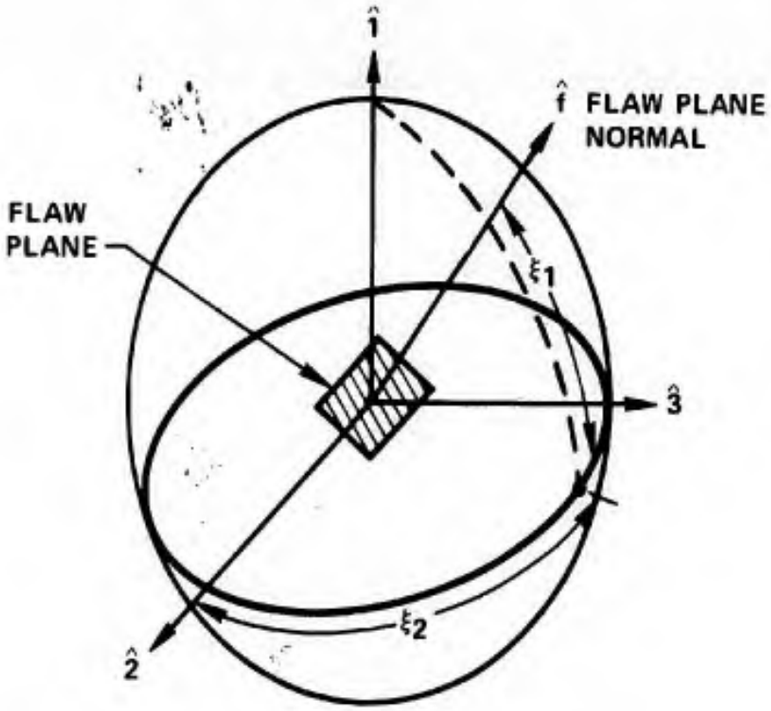

Figure 52. Orientation of Flaw Plane.

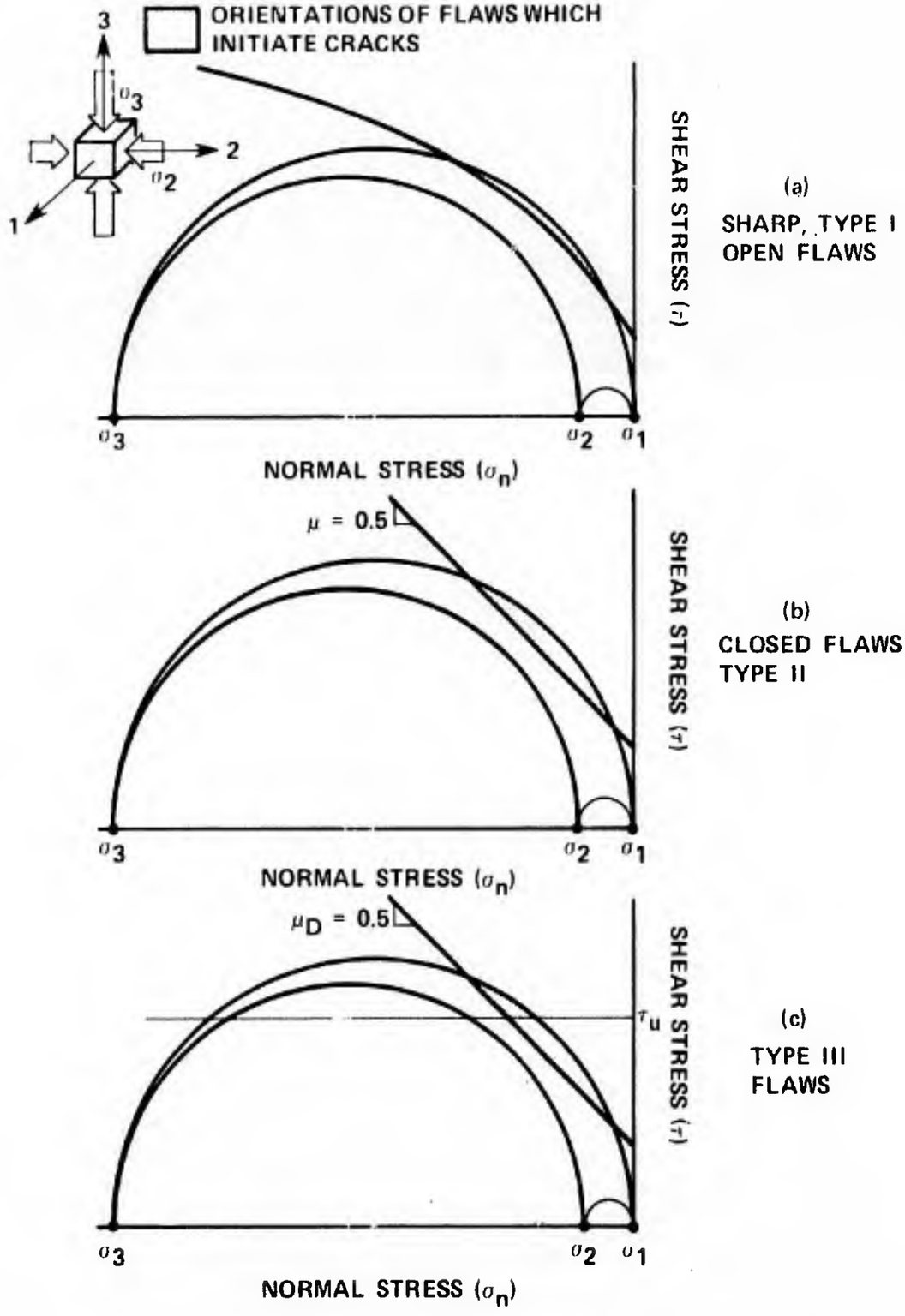

Figure 53. Flaw Orientations which Initiate Cracks Under Biaxial Compressive Stress 1:0.1.

K_I, K_{II} and K_{III} stress intensity factors around the tip perimeter of the flaw. Their predicted variation of the stress intensity factor K_{II} around the perimeter of a flaw loaded in shear agrees very nicely with the observed positions of crack initiation around the perimeter of the three-dimensional slits investigated in this study. As the compressive stress on the slits was increased, the position of crack initiation around the perimeter was adequately described by their K_{II} variation.

A general description of crack initiation at three-dimensional flaws subjected to polyaxial stresses becomes exceedingly complex when the criterion is expressed in terms of stress intensity factors. It is not clear which modes become critical for crack initiation in compression. Under a general compressive stress state, Mode I displacements produce only high concentrations of compressive stress. Modes II and III produce local tensile stress maxima around the flaw at different positions. A general expression for the "critical stress intensity" criterion for crack initiation at a flaw would have to be stated in terms of the relationship.

$$f(K_I, K_{II}, K_{III}) = f_{crit} \tag{35}$$

The critical combination of modes may have to be determined. This appears to be a considerably more complex approach than that of determining when the local tensile stress at the flaw tip equals the intrinsic material strength. This "critical tensile stress" criterion will be used to formulate the general theory of compressive failure because of its ease of physical interpretation.

ii. The description of initiating flaw orientations and the direction of crack extension in three dimensions

To discuss flaws and extended cracks in three dimensions a coordinate system and scheme of notation are needed to describe the orientations of the planes. Any convenient orthogonal coordinate system 1, 2, 3 may be used where $\hat{1}$ is identified with the direction of the minor principal compressive stress, $\hat{2}$ with the intermediate principal compression direction, and $\hat{3}$ with the major or maximum principal compression direction. Since the test specimen was a tube, the cylindrical coordinates $\hat{R}$, $\hat{\theta}$ and $\hat{Z}$ are employed which correspond to the directions of the principal stresses σ_{rr}, $\sigma_{\theta\theta}$, and σ_{zz}, respectively. The notation for describing sets of flaw and crack planes will be similar to that used by crystallographers to describe crystal planes. The orientations of flaw planes and crack planes will be designated by the directions of the normals to such planes, $\hat{f}$ and $\hat{c}$, respectively. The set of flaw planes or crack planes, whose normals are perpendicular to a given direction will be designated as a zone of flaw or crack planes. The three zones of planes corresponding to the principal stress directions are designated as follows: (See Figure 54(a).)

$\hat{R}$ - zone planes $\equiv$ all planes whose normals are perpendicular to the $\hat{R}$ direction.

$\hat{\theta}$ - zone planes $\equiv$ all planes whose normals are perpendicular to the $\hat{\theta}$ direction.

$\hat{Z}$ - zone planes $\equiv$ all planes whose normals are perpendicular to the $\hat{Z}$ direction.

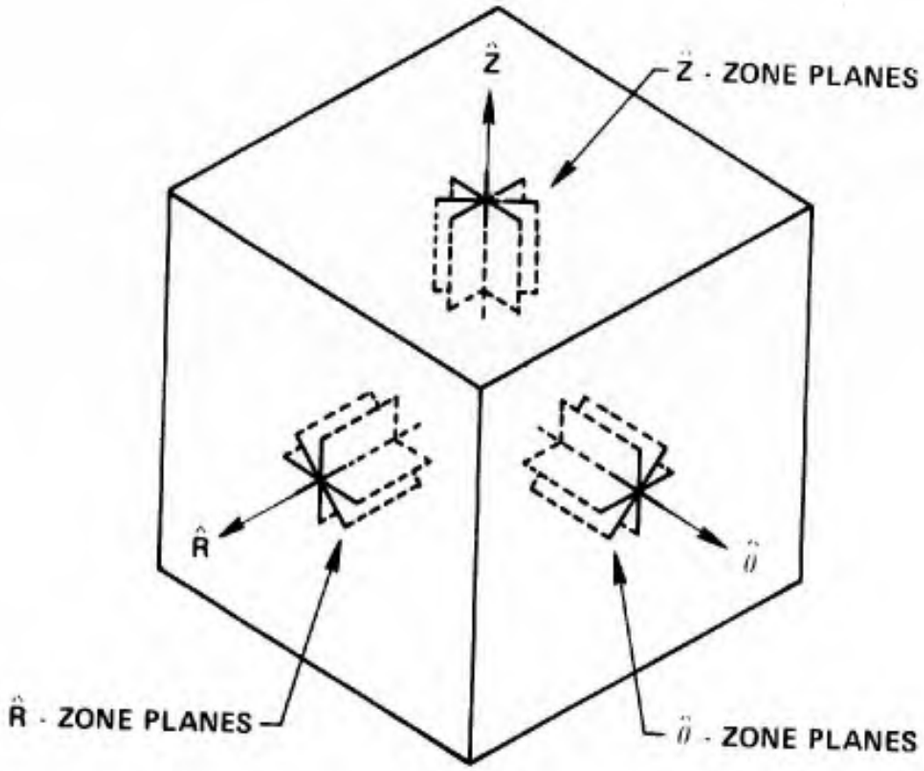

(a) ZONES OF PLANES FOR PRINCIPAL STRESS DIRECTIONS

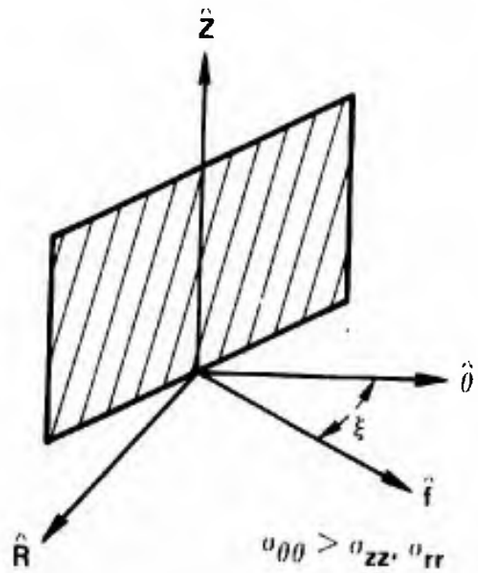

(b) DEFINITION OF ANGLE ξ

Figure 54. Planes of Principal Stress Direction Zones.

From the discussion and experiments of the preceding sections we can make some summary statements about the behavior of flaws on these zones of planes and the orientations of cracks extending from them.

(1) The principal stresses which affect the magnitude and distribution of the local intensified stresses around $\hat{R}$ - zone flaws are $\sigma_{\theta\theta}$ and σ_{zz}; around $\hat{\theta}$ - zone flaws are σ_{rr} and σ_{zz}; around $\hat{Z}$ - zone flaws are σ_{rr} and $\sigma_{\theta\theta}$. The third principal stress, the one acting in the plane of the flaw or crack, is not concentrated by the defect. It thus does not influence the local, intensified stress field.

(2) The angular orientation of the plane (ξ) is given by the angle between the flaw plane normal ($\hat{f}$) or crack plane normal ($\hat{c}$) and the direction of the lasgest compressive stress which is concentrated by the defect. (e.g. for $\hat{Z}$ - zone planes ξ is measured between $\hat{\theta}$ and the flaw plane normal $\hat{f}$, see Figure 54(b).) This definition is different from that used in Section A for two-dimensional flaws by a factor of $90° - \xi$. The redefinition is made at this point because it is easier to deal with the angular relationships of planes in three dimensions by working with their normals. The range of ξ is $0 \leq \xi \leq 90°$.

(3) It has been shown that the direction of crack extension from two-dimensional flaws tends to align the crack parallel to the principal compressive stress direction. This concept may be readily generalized to three dimensions if one considers only cracks extending from flaws included in the three principal

stress zones of planes. If a crack can be initiated at the tip of one of these flaws, its direction of extension will curve to align the extending crack plane with the plane containing the direction of maximum principal compression concentrated by the originating flaw and the zonal principal stress direction. For example, consider crack extension from a $\hat{Z}$ - zone flaw where $|\sigma_{\theta\theta}| > |\sigma_{zz}| > |\sigma_{rr}|$. The two principal stresses concentrated at the flaw are $\sigma_{\theta\theta}$ and σ_{rr}. The plane of the extended crack will become parallel to the $\hat{\theta}$-$\hat{Z}$ plane. (See Figure 55.) Another useful way of looking at this is to say the crack plane normal $\hat{c}$ becomes parallel to the $\hat{R}$ direction.

The foregoing discussion has considered only flaws or cracks on planes whose normals are perpendicular to a principal stress direction. As a first approximation to the description of crack initiation and extension in three dimensions this should be realistic. The stresses which affect the initiation and subsequent extension of cracks from a flaw are the normal (σ_n) and shear (τ) stresses acting on the flaw and crack planes. The extremes of such normal and shear stresses occur in the stressed body on planes included in the three zones of planes considered above.

To have a more complete description of the nature of crack extension from all planes in three dimensions, a more generalized approach must be taken. First, the criteria for crack initiation at all types of flaws spawning cracks in the material (Types I, II, and III) must be expressed in terms of σ_n and τ acting on the flaw plane. σ_n and τ will

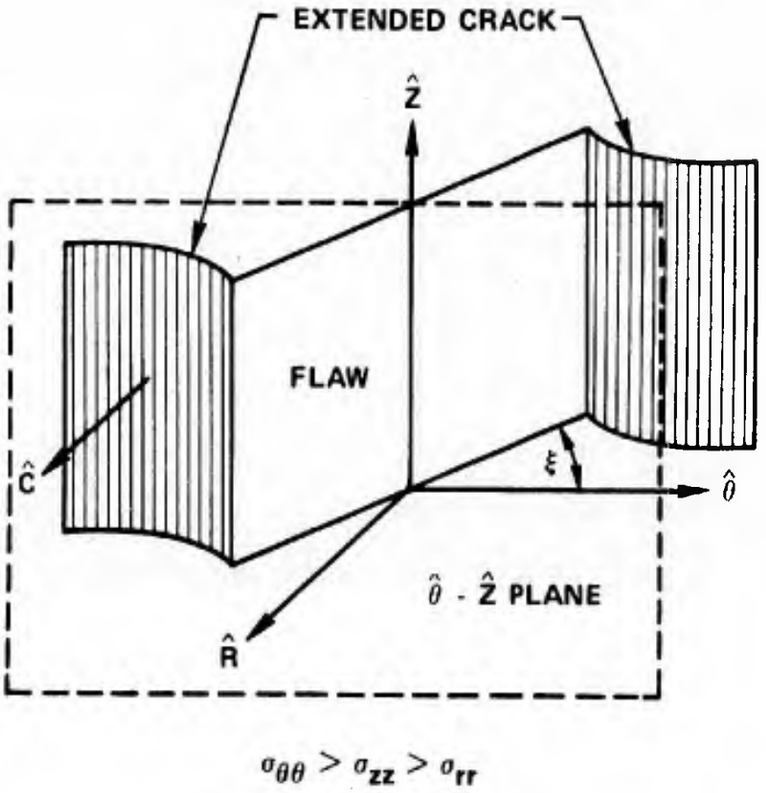

$$\sigma_{\theta\theta} > \sigma_{zz} > \sigma_{rr}$$

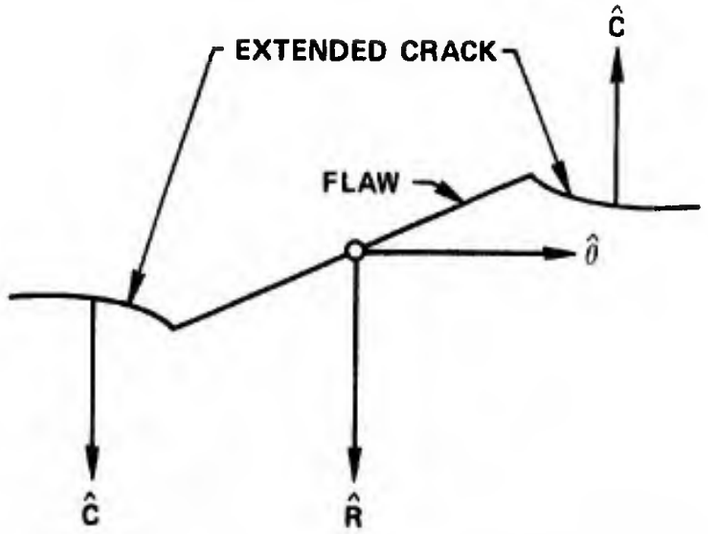

Figure 55. Direction of Crack Extension.

be a function of the applied stresses and the orientation of the flaw plane. (The flaw plane orientation may be defined by ξ_1, ξ_2 (see Figure 52) for graphical solution by Mohr's method or by the direction cosines a_x, a_y, a_z of the plane for analytic solution.) This function will be different for each flaw type and may include additional parameters, e.g. (μ), the coefficient of friction for Type II flaws. If the critical relationship between σ_n and τ is expressed in terms of the direction cosines of the flaw plane normal, for a given ratio of applied stresses (i.e. given stress state), the orientations of flaws planes which will initiate cracks can be determined in terms of the applied stress level by iterative solutions of the equation.

The orientations of flaws which will initiate cracks may be displayed on a stereographic projection, using the Eulerian angles ξ_1 and ξ_2, to give the "figure" of the orientations of flaws which initiate cracks at any given stress level. This "initiated flaw orientation figure" will differ at identical stress levels for the various mechanisms of crack initiation, as can be seen from Figure 53. The flaws which have the orientations ($\hat{f}$) that satisfy the relationship $f(\sigma_n,\tau) = \sigma^*$ will form the boundary of the initiated flaw orientation figure. Flaws for which $f(\sigma_n,\tau) > \sigma^*$ will be inside the boundary lines and flaws for which $f(\sigma_n,\tau) < \sigma^*$ will be outside.

As an example, consider a body containing only sharp, Type I flaws which is loaded in uniaxial compression in the $\hat{\theta}$ direction. This case is simple to treat since the initiating flaw orientations are a function of only the $\sigma_{\theta\theta}$ stress. The flaws are sharp and open so we may use the criterion of Equation (34) which gives:

$$\frac{\sigma_3^2 a_z^2 (a_y^2 + a_x^2)}{A\sigma^*} + B\sigma_3 a_z^2 \geq \sigma^* \qquad (36)$$

The values of a_x, a_y, a_z which satisfy this equation represent the flaw plane orientations (ξ_1, ξ_2) which initiate cracks under the applied stress level $\sigma_3 = \sigma_{\theta\theta}$ for the assumed constant values of A, B and σ^*. When $\sigma_{\theta\theta} = Q$ the first flaw orientation initiates a crack. This orientation is $\xi_1 = 30°$ and is invariant with ξ_2. Figure 56 shows this initiated flaw orientation figure. If the stress level is increased to $\sigma_{\theta\theta} = 1.25\ Q$, $\Delta\xi_1$ increases and the initiated flaw figure is as shown in Figure 56. Further increases in $\sigma_{\theta\theta}$ result in larger values of $\Delta\xi_1$.

Consider now a case of biaxial compression in which $\sigma_{zz} = 0.1\ \sigma_{\theta\theta}$; $\sigma_{rr} = 0$ where the applied stress levels are the same as for the uniaxial case, i.e. $\sigma_{\theta\theta} = Q$ and $\sigma_{\theta\theta} = 1.25\ Q$. By iterative solutions of Equation (34) we may obtain the values of ξ_1, ξ_2 and the initiated flaw orientation figures will be approximately as shown in Figure 57. Comparing the uniaxial and biaxial cases we see that the first flaw to initiate is of the same orientation (ξ_1) in both cases. A smaller range of orientation of flaws initiate cracks at a given stress level in the biaxial case. The second applied compression inhibits crack initiation for flaws over a large range of orientations.

In biaxial compression stress states where the magnitude of σ_{zz} approaches $\sigma_{\theta\theta}$ the range of initiated flaw orientations increases again. When $\sigma_{zz} = \sigma_{\theta\theta}$ the initiated flaw orientation figure is identical in shape to that for uniaxial compression but is centered on the stereographic projection about the $\hat{1}$ direction.

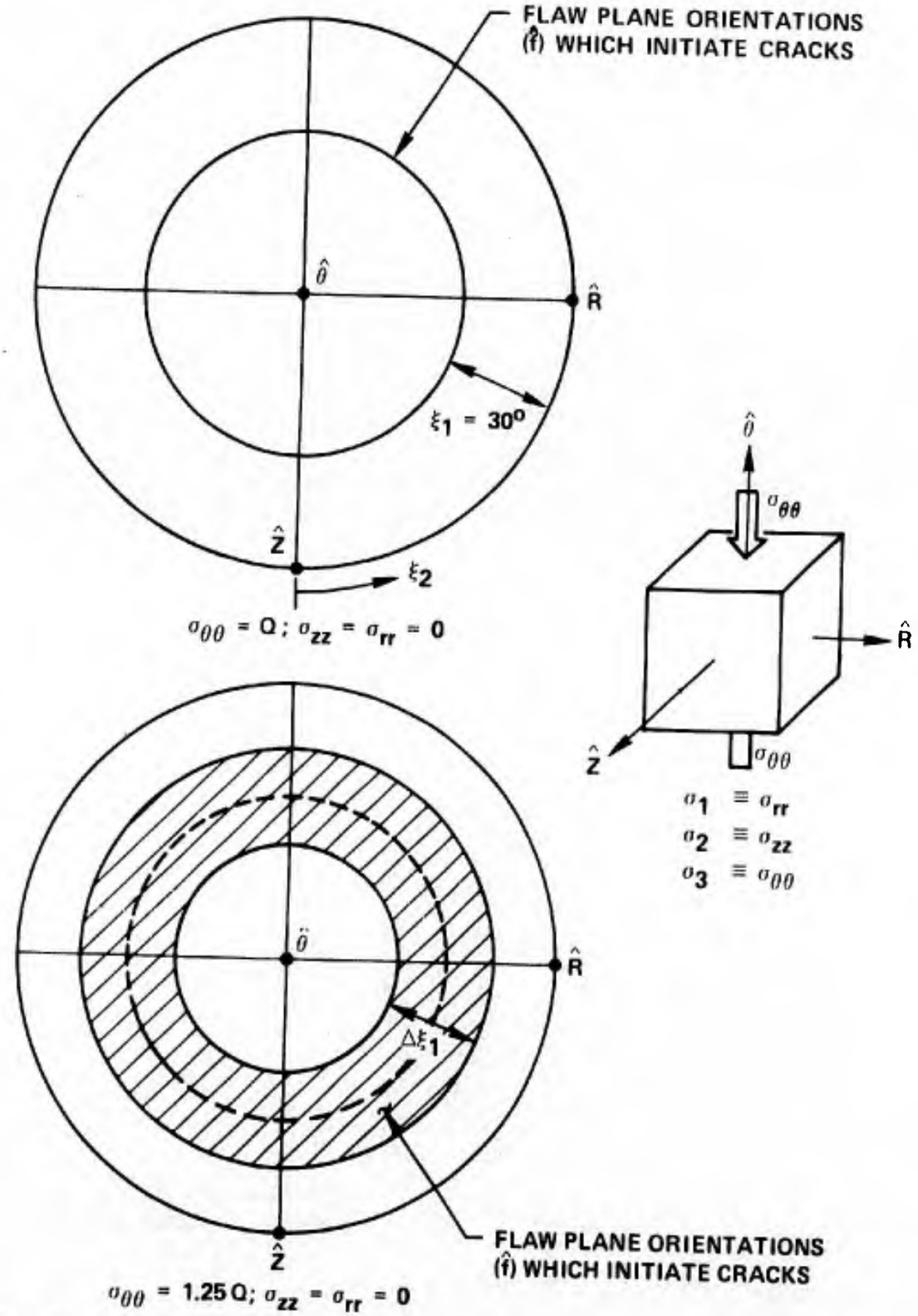

Figure 56. Orientations of Flaws Which Initiate Cracks at Different Stress Levels in Uniaxial Compression.

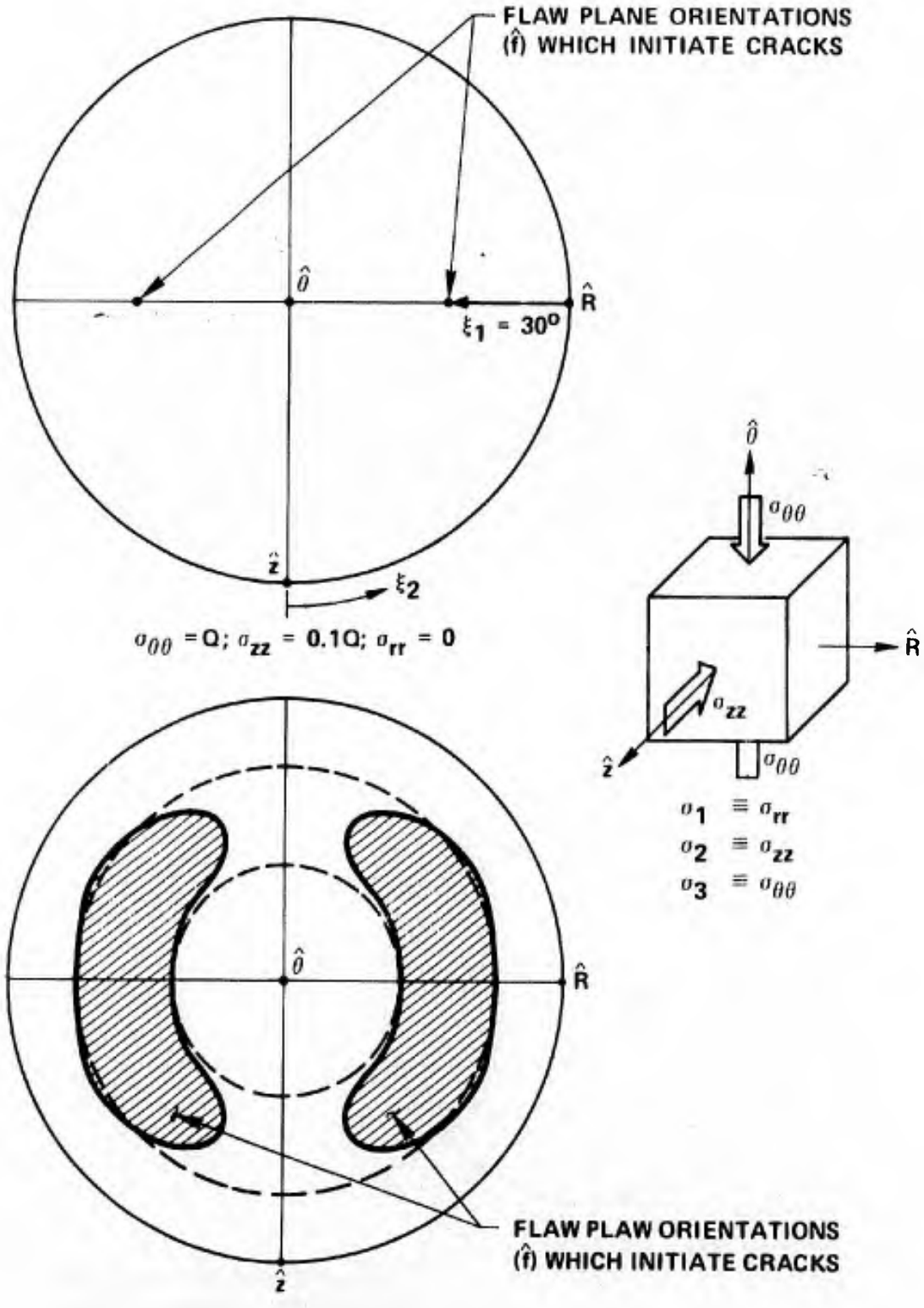

Figure 57. Orientations of Flaws Which Initiate Cracks at Different Stress Levels in Biaxial Compression.

As the stress increases above that necessary to initiate a crack at the flaw, extension of the cracks will occur in directions tending to align the crack normal ($\hat{c}$) perpendicular to either one or two principal stress directions. In uniaxial compression $\hat{c}$ will become perpendicular to the direction of principal compression ($\hat{\sigma}_3$). In triaxial stress states where $|\sigma_3| > |\sigma_2| \simeq |\sigma_1|$ crack extension also will be in a direction such that $\hat{c}$ becomes perpendicular to the direction of the maximum principal compression ($\hat{\sigma}_3$). For other stress states, $|\sigma_3| \geq |\sigma_2| > |\sigma_1|$, which includes the biaxial case when $\sigma_1 = 0$, crack extension will tend to make $\hat{c}$ perpendicular to the plane formed by the directions of the two largest principal compressive stresses acting on the flaw. The orientations which the extending cracks assume, and the final aligned orientations of the cracks, may be displayed on a stereographic projection by rotating the orientation of the principal stresses from that used above. Figure 58 shows examples of the crack orientations for the uniaxial case and biaxial case where $\sigma_3 = 10\ \sigma_2$. In the case of equi-triaxial compression, $\sigma_1 = \sigma_2 = \sigma_3$, crack initiation or extension is not possible by the mechanisms discussed in this paper.

The two examples given above are representative of the two kinds of crack extension behavior which will be observed in any stress state. The aligned orientations of all extended cracks will either form the zone of planes about the maximum principal compression direction, $\hat{\sigma}_3$-zone planes, or will all become parallel to the plane formed by the two largest principal compressive stress directions. As the magnitudes of the intermediate (σ_2) and minor (σ_1) principal stresses approach that of the major principal stress (σ_3), the greater will be the reduction in

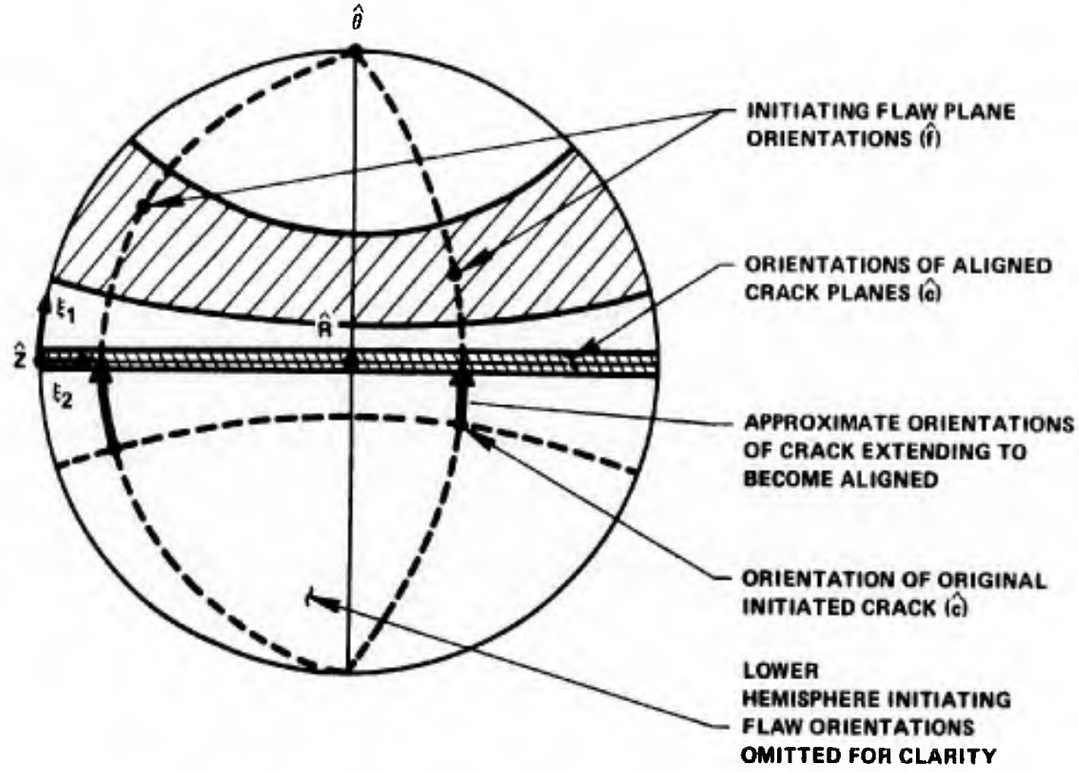

(a) UNIAXIAL CRACK EXTENSION DIRECTIONS

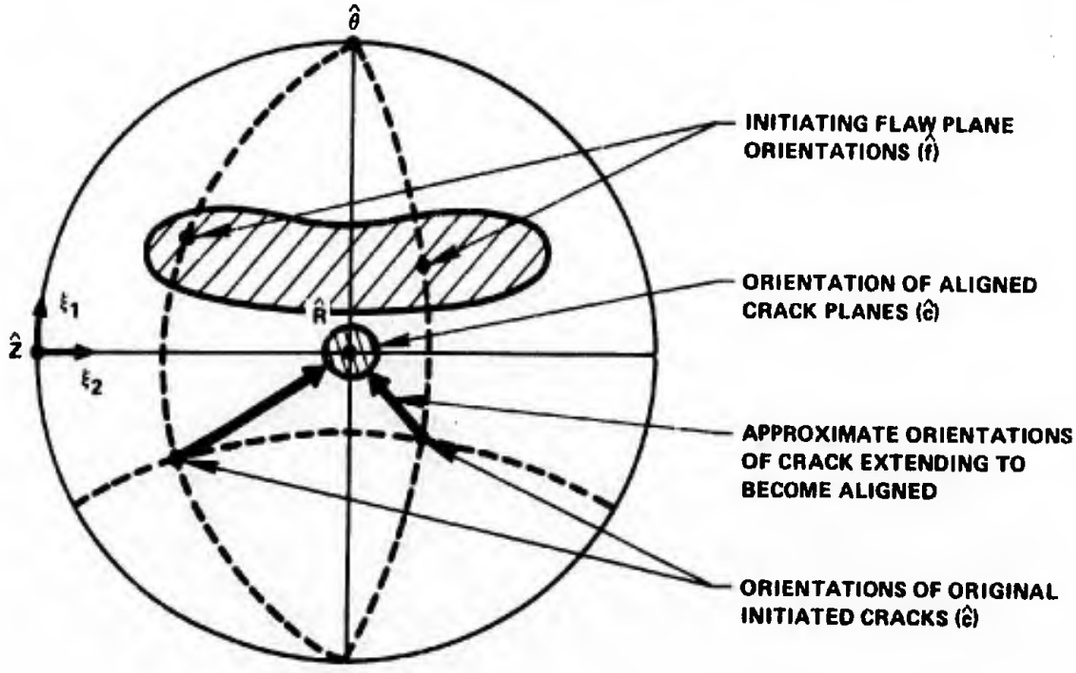

(b) BIAXIAL CRACK EXTENSION DIRECTIONS ($\sigma_{zz} = 0.1\ \sigma_{\theta\theta}$)

Figure 58. Crack Extension Directions.

the range of flaw orientations which may initiate cracks at any given stress level. The orientation of the extended crack normals ($\hat{c}$) to the $\hat{\sigma}_1$ direction in the biaxial compression case is the cause of the "onion peel" spalling observed in the test specimen where $\hat{\sigma}_1$ is identified with the $\hat{R}$ direction.

CHAPTER VI

THE MECHANISM OF FAILURE IN COMPRESSIVE STRESS STATES

To understand how structural collapse occurs in a body subjected to compressive loads, one must understand the nature of the damage created in the body by stably propagating cracks as the compressive loads are increased. The manner in which three-dimensional crack arrays reduce the ability of the body to withstand further increases in load is of importance. At some point, the load carrying capability of the body is reduced to the applied load and structural collapse occurs. (See Figure 59.)

The magnitude of such crack damage has been investigated with various techniques by several experimenters studying the properties of rocks and concretes under compressive loads. Such damage, however, has not previously been studied in high quality, high-strength, ceramic material. The flaw distributions which occur in high-strength ceramic materials differ greatly from those occurring in relatively low strength rock or concrete. The most common method employed to study the crack damage in low strength materials[62-65] is measuring the departure from linearity of the volumetric ($\Delta V/V$) or linear (ε) strains under increasing applied stresses. A theoretical relationship between the crack and/or pore density and the measured strains has been developed by Walsh.[66,67] Peng and Johnson[68] characterized the orientations and lengths of cracks propagated in uniaxially compressed cylinders of Chelmsford granite by sectioning cylinders subjected to various loads and optically observing the large cracks. Some of the most interesting results are those of Scholz[69] who studied acoustic emission as a function of applied

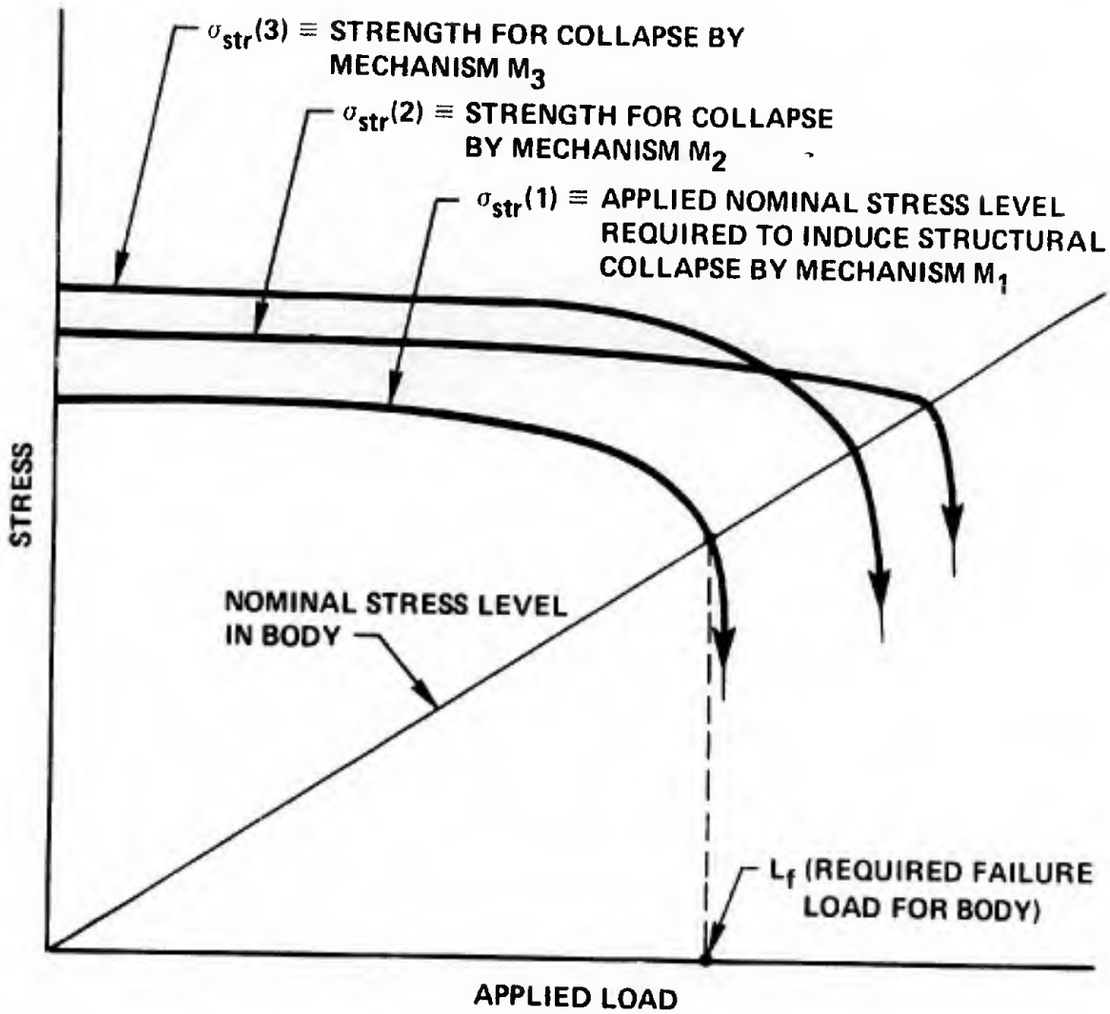

Figure 59. Load Required to Induce Structural Collapse of Body.

compressive stress for several rock materials. The study presumed that the individual acoustic emission events corresponded to micro-cracking events. The relationship between the accumulated frequency of acoustic events and the applied stress, expressed as a fraction of the failure stress, is similar to the accumulated spalling versus applied stress relationship obtained in this study. (See Figure 24.)

The strength reduction with increasing applied load depends on several factors including: material microstructure, the characteristics and distributions of inherent flaws, geometry of the body, and the stress states imposed. The mechanism of final structural collapse will depend on all the above factors. Some structural collapse mechanisms are:

(1) Catastrophic, sequential buckling of microplates or of columns in a localized region.

(2) General reduction of load carrying cross section of material to the point of gross, macroscopic elastic instability (e.g. circumferential buckling of "thinned down" wall of externally pressurized tube).

(3) Development of a network of cracks with sufficient density to permit direct shear failure through lack of cohesive strength between crystallites in the body.

The mechanism which requires the lowest load to operate will be strength-limiting. (See Figure 59.)

It is possible that two compressive strength measurements which used different specimen geometries and loading conditions, could measure different strengths for a material due to different mechanisms of

structural collapse occurring, even though the damage levels in the material for each test were the same at identical stress levels. Below will be presented an analysis of the damage developed in the test specimen used in this study and a description of the mechanism of structural collapse.

A. Failure of the Test Specimen

i. The nature of the crack damage in the specimen

To discuss the nature of the crack damage produced by the applied loads, one must have in mind the stress state in the test section. This is shown in Figure 1 for each stress state test. The hoop stress ($\sigma_{\theta\theta}$) is the largest principal stress. It is at a maximum on the inside surface and decreases to 0.9 $\sigma_{\theta\theta}^{max}$ at the outside surface. The axial stress σ_{zz} is constant through the wall thickness and is a fixed fraction of $\sigma_{\theta\theta}$. The radial stress σ_{rr} is a maximum on the outside surface (being equal to the applied pressure which is $\sim 0.1\ \sigma_{\theta\theta}$) and decreases to zero on the inside surface; thus, the inside surface is the only region having a biaxial stress state.

The results of petrographic sections made on portions of failed specimens (Chapter IV, Section B) indicate that the inside surface is the only region where extensive crack damage occurs before structural collapse. Several conditions favor this kind of behavior. First, the density of extending cracks is extremely sensitive to the applied stress level near failure. Referring to Figure 23, an increase of 3% in the applied stress level from 97% to 100% σ_f produces a twofold increase in the spalled particle density. This 3% decrease in the $\sigma_{\theta\theta}$ stress occurs at a position 30% through the wall thickness. Secondly,

surface and near-surface flaws have higher stress concentrations around them and will extend cracks at lower applied stresses than imbedded flaws. Thirdly, two-dimensional crack studies (See Chapter V, Section A.) show that the effect of σ_{rr} through the wall thickness is to raise the required stress level for crack initiation and to limit the length to which the cracks may extend. This effect on initiation stress for open (Type I) and closed (Type II) flaws may be seen in Figures 33 and 39 respectively. The effect on crack extension is discussed in Chapter V, Section B. Thus, for the geometry of the test specimen and loading conditions used in this study, we need only to consider the crack damage in the region near the inside surface to describe the failure mechanism.

The Griffith theory predicts crack initiation in uniaxial compression to begin at open flaws when the compressive stress is eight times the magnitude of the uniaxial tensile strength. From the spalling studies (See Figure 25) it can be seen that crack initiation and extension begin in the alumina test specimens at a compressive stress 4-5 times the tensile strength. This is not unreasonable, however, when one considers the behavior of Type II flaws and surface flaws. An alternative explanation of this discrepancy, which involves a consideration of residual, thermal stresses in the material, is discussed in Appendix D. The value of eight in the Griffith theory has no real significance since this value only predicts when the worst, sharp, open flaw initiates a crack. Compressive failure in polycrystalline materials is typically the result of very large numbers (10^4-10^6) of flaws of decreasing severity extending cracks. As the stresses are increased, this phenomenon produces increasing amounts of structural damage in the material.

The evidence of the crack damage produced in the specimen by the applied loads is the spalling. The increase in the density of this damage with increasing applied stresses is seen in curves showing the percent of the area spalled. An exponential curve fitted to the data of Figure 24 shows that up to the 0.9 σ_f stress level the function % Area Spalled = $\exp\left(\frac{1.3\sigma}{\sigma_f}\right)$ fits the data and above 0.9 σ_f the function $\exp\left(\frac{3\sigma}{\sigma_f}\right)$ is a good fit. This increase in the coefficient of the stress exponent may be evidence of the operation of additional mechanisms of crack extension at stress levels near failure.

The shape of the spalled particles indicates that extension from flaws is restricted to very specific directions as discussed in Chapter V. Referring to Figure 60, all cracks extend from flaws, when $\sigma_{\theta\theta}$ and σ_{zz} are the greatest compressive stresses, in a manner such that the crack plane becomes parallel to the R plane. This causes the spalled particles to come off as thin, "onion peel" plates. The stereographic projection of the poles of flaw planes which are within $\Delta\xi_1$(crit) and $\Delta\xi_2$(crit) is similar to that shown in Figure 53. As the stress is raised the range of flaw orientations which may extend cracks increases. Regardless of the orientation of the originating flaw, the plane of the extending crack becomes parallel to the inside surface of the specimen or intersects it. By this action of extending cracks, the material adjacent to the inside surface of the specimen is carved into small, thin plates held fixed to the alumina by their edges which remain attached to the body. The sizes of the plates and their planar shapes will depend on the extended crack length and the amount of flaw-crack interaction. The damage created in the specimen by the extended cracks

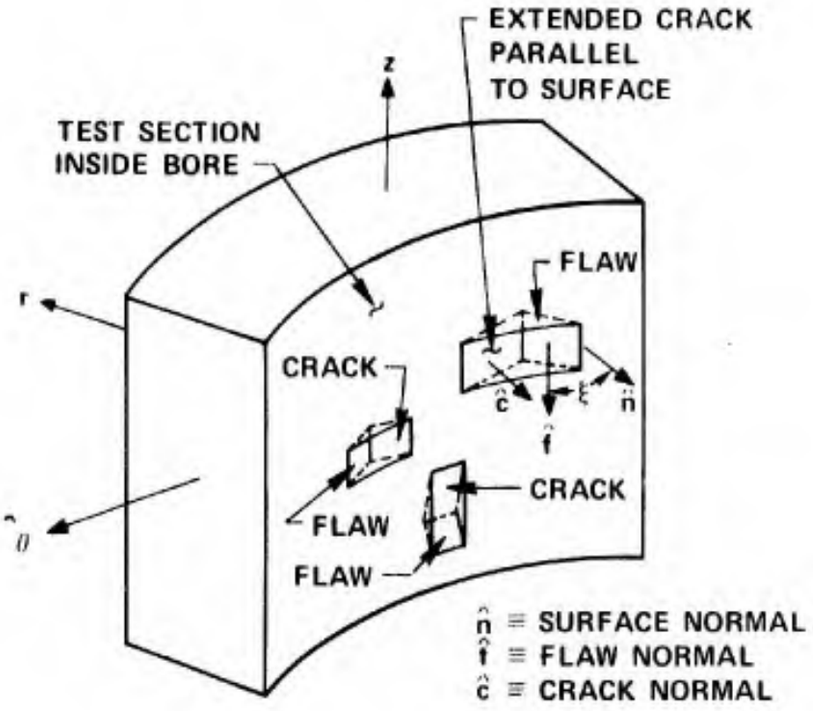

(a) CRACKS EXTENDING FROM SURFACE AND NEAR SURFACE FLAWS

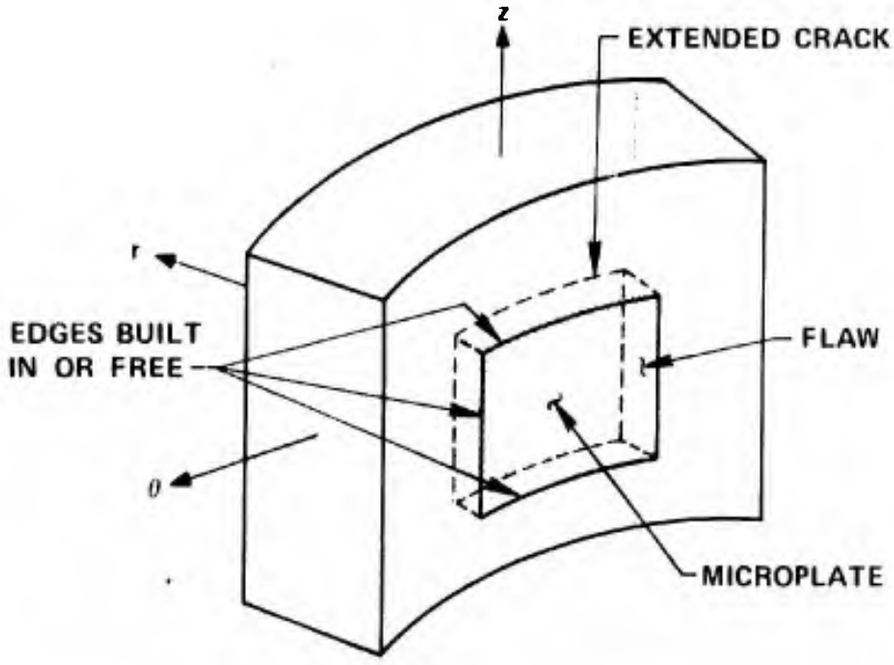

(b) FORMATION OF MICROPLATE

Figure 60. Near Surface Crack Extension in the Specimen.

may vary from slender columns to square plates. From the discussion in Chapter V, Section Cii it is seen that in stress states where $\sigma_{\theta\theta}$ and σ_{zz} are larger than σ_{rr}, the formation of rectangular plates rather than columns is favored because the crack extension directions are parallel to the R plane.

An explanation of the formation of larger spalled particles with increasing applied stress requires an understanding of the nature of crack extension from inherent flaws. The length of a crack extending from a flaw is a function of the stress state and stress level; however, no theory is available to explain this relationship. Further, there exists no good experimental data to indicate what this relationship may be for glass or ceramic materials. The present study on crack extension from flaws in PMMA plastic was limited to investigating the extended crack length for compressive stresses which were less than three times the stress at crack initiation because of the low tensile strength of the plastic. These studies did indicate that extended cracks may act as originating flaws to extend secondary cracks from them which can result in a large total length of extended crack.

Other potential mechanisms for the formation of large plates at stress levels near failure are the unstable extension of cracks from Type III flaws and the creation of a sufficient density of extended cracks to allow link-up of the extending cracks. Since the most severe Type I or II flaws initiate cracks at 1/4 σ_f, Type III flaws which "break free" and operate at stress levels near failure may suddenly be subjected to applied stresses four times those required to induce stable crack extension if the flaw had not been locked. Because of the dynamic

nature of the loading, the effective stress levels may reach eight times that required for stable extension. The length of cracks initiated in this manner may be many times the flaw length.

Above the 0.9 σ_f stress level, the stress fields around flaws and extended cracks in regions near to the free surface may no longer be independent of one another. From Inglis' equation it can be seen that the critical flaw size (c) for crack initiation decreases as the inverse square of the applied stress, from Equation (14):

$$\sigma_{max} \propto \sigma_{applied} \sqrt{\frac{c}{\rho}}$$

if: $\sigma_{max} \equiv \sigma_{crit} \equiv$ critical tensile stress for crack initiation (a constant)

$\rho \equiv$ constant tip radius

$c =$ critical flaw size

Then:

$$c \propto \left(\frac{\sigma_{crit}}{\sigma_{applied}}\right)^2 \propto \left(\frac{1}{\sigma_{applied}}\right)^2 \qquad (37)$$

This assumes a constant tip radius for all flaws which is a reasonable assumption if one is considering atomically sharp flaws. The most severe flaws in the alumina test speciment initiate cracks at 1/4 of the compressive strength as shown by the first spalling. If the size of such flaws is assumed to be equal to the largest grains in the body, i.e. 50 microns, the above relation suggests that, near failure stress, flaws 1/16 this size will become critical and initiate cracks. Flaws with dimensions of 4 microns will be extending cracks. This flaw size is 1/5 of the average grain size. At stress levels near failure the density of flaws which initiate cracks should increase greatly. This

can result in overlapping of the intensified stress fields around such flaws, causing crack extension between flaws. This linking-up of the extending cracks will result in the formation of larger spalled particles.

If the surfaces of the spalled particles are extremely flat, one would suspect unstable crack extension from Type III flaws. If the plate surfaces were highly stepped, this would support a crack linking mechanism. Both kinds of surfaces are observed on the spalled particles; although, there is a predominance of very flat particle surfaces.

ii. Structural collapse mechanism of the specimen

The majority of the larger particle spalling at the higher stress levels may be brought about by the elastic buckling of the thin plates or columns carved into the body by the extending, interacting cracks as can be seen by the following:

As cracks extend and interact with increasing applied loads, increasingly larger plates are created which have greater length (L) or width (W) to thickness (t) ratios. When the t/L or t/W ratio becomes sufficiently small, the plates become elastically unstable under the applied normal stresses on the ends of the plate, $\sigma_{\theta\theta}$ and σ_{zz}, which results in the plate buckling. The radial stress has no effect on an inside surface plate but inhibits the buckling of outside surface plates.

Several details of the nature of the plates are difficult to characterize. Because the plates are small areas which have been partially separated from a polycrystalline body by crack extension, the manner in which the edges of the plate are supported is unclear; it probably varies between "built-in edges" and "simply supported edges." (See Figure 60 (b).) The plate thickness varies somewhat, at least on the order of the

grain size. Since the plate may be only a few grains thick, the elastic constants for the bulk material may not accurately describe the plate behavior. Finally, the shapes of the plates are irregular as well as having cracks extending into them.

With the above limitations in mind, the buckling of the plates will be analyzed by continuum mechanics. The model is that of a thin plate, subjected to various edge constraints, and loaded in plane on its ends by two compressive stresses, $S_1 \geq S_2$. The expressions for the critical buckling stresses for plates of various geometry with various edge constraints is developed in Appendix E. The results of these calculations show that plates with t/L ratios of less than approximately 1/15 will buckle under the magnitude of the stresses applied at failure of the specimen. This is in agreement with the observed dimensions of the spalled particles. For a constant (t/L) ratio there is a minimum in the magnitude of the stresses required to buckle the plate as W approaches L, i.e. as the planar shape of the plate approaches that of a square. Plates buckle more easily under biaxial stresses than uniaxial; the lowest buckling stresses are found for a plate subjected to equi-biaxial compression - the highest stresses for a plate loaded in uniaxial compression. Finally, plates with built-in edges are more difficult to buckle than plates with free edges.

The instability which is created may be understood by following the sequence of events which happen in an area where multiple spalling occurs. As the first chip buckles off (see Figure 61), the stresses are redistributed through the remaining test section. The principal stresses, $\sigma_{\theta\theta}$ and σ_{zz}, will increase in magnitude in all areas of the

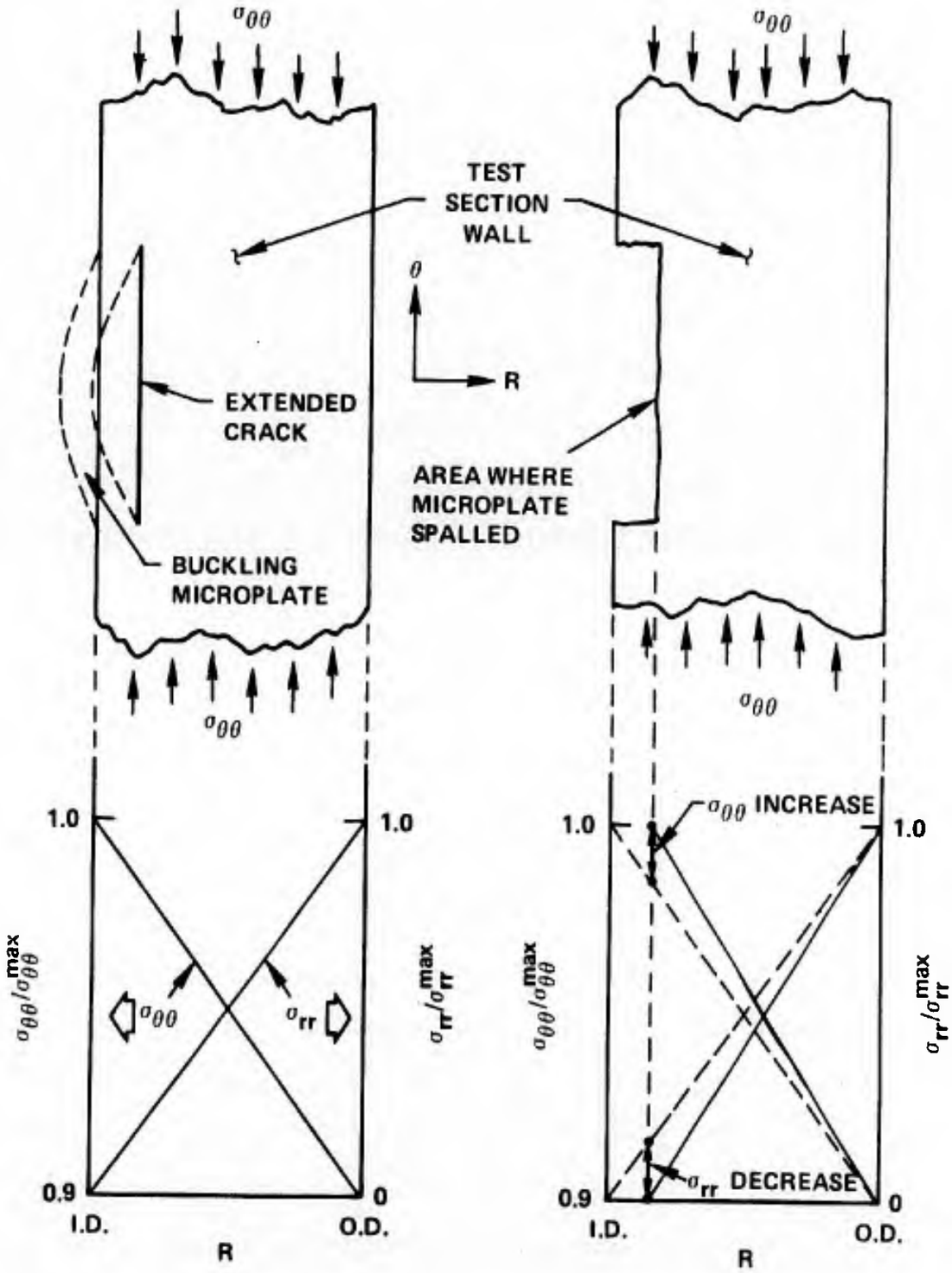

Figure 61. Stress Redistribution from Microplate Spalling.

damaged section because the position of the inside free surface has changed and because the net load-carrying cross section has been reduced. The minor principal stress (σ_{rr}) is reduced in areas near the new inside free surface and remains constant on the outside surface. Since $\sigma_{\theta\theta}$ and σ_{zz} are greater in the remaining wall material and σ_{rr} is reduced in the material adjacent to the inside surface, new cracks will extend from flaws near the spalled area of the inside surface. When these new cracks extend and perhaps interact they will form another microplate which will buckle when $t/L = (t/L)_{crit}$. The entire process will be repeated as the applied stresses are increased. The stress level in the spalled area will become increasingly greater than the nominal stress level with each spall. At some applied stress level the increase in the local stress will be sufficient to cause the process to occur continuously with no further increase in applied stress and rapid collapse of the specimen will result.

The spalling studies indicate the number of stable spalls which occur in a given area before catastrophic spalling sets in is about five. Examination of the failed specimen showed that the depth of spalling at the onset of structural collapse was about 15% through the wall thickness in an area of about 0.5 cm^2. Figure 62 is a photo of the portion of a test section where the spall sequence which initiated structural collapse is thought to have occurred. In the photograph this spalled area is on the extreme right of the inside surface of the test section shown. Other, smaller areas where intensive spalling occurred can be seen on the surface.

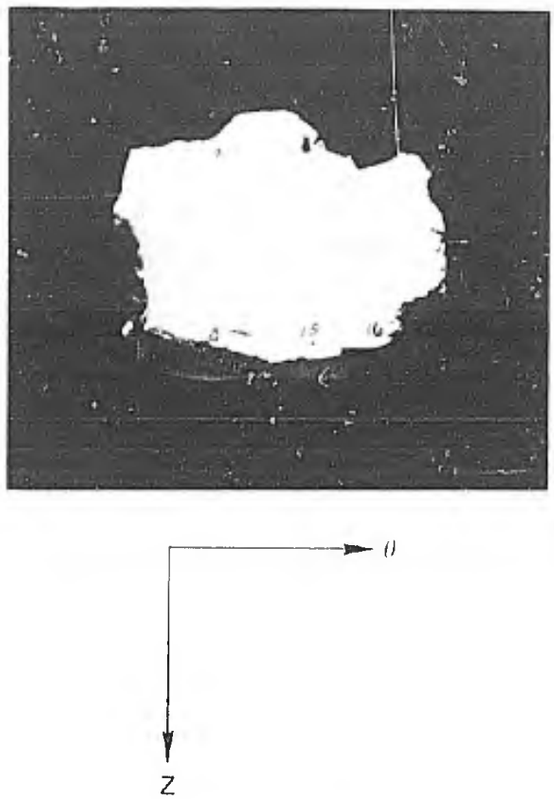

Figure 62. Catastrophic Spalling Area on Failed 1:0.5 Specimen Test Section.

iii. Dependence of strength on state of stress

The biaxial compressive strength of the alumina was found not to depend on the magnitude of the intermediate compressive stress in the range of stress states between 1:0.1 and 1:0.8. Ir stress states near 1:1 the strength may decrease slightly with increasing intermediate stress. Some insight into the influence of the intermediate stress on the strength can be obtained from its influence on crack growth.

It is thought that the appearance of large spalled particles and the change in shape of the spalling-stress curve, Figures 23 and 24, observed when the stress exceeds 0.9 of the strength, signals the onset of extensive crack interaction and/or a large increase in the number of Type III flaws extending long cracks. When the intermediate stress is also more than 0.9 of the strength, it might strongly influence the cracking and the combined effects lower the strength. Thus the failure envelope in 1:1 biaxial compression may be slightly rounded. The data plotted in Figure 17 are consistent with this but the number of tests are insufficient and the cracking under the preload makes them questionable.

Compressive strengths in stress states near 1:0 may decrease because in these stress states not only will a greater number of flaws initiate cracks but also the cracks may grow in a larger variety of directions; therefore, the body may sustain greater crack damage at a given stress level than the biaxially compressed body. As previously discussed, the directions of crack extension are limited by small transverse compressive stresses; thus, a decrease in compressive strength

would occur only in biaxial stress states which are very near uniaxial compression. The data show that a decrease may occur in stress states where σ_{zz} is less than 1/10 $\sigma_{\theta\theta}$ but the decrease is less than 10%.

B. Towards an Analytic Description of General Compressive Failure

A theory which satisfactorily predicts the compressive strength of brittle materials has not been formulated yet. Theories such as the original Griffith theory[44] and its modification by McClintock and Walsh[48] only attempt to treat the initiation of cracks at flaws; but, a criterion for crack initiation at flaws is not synonymous with a failure criterion. Attempts have been made to describe the criterion for compressive failure by assuming failure will occur when a critical quantity of stored elastic energy is present. Such a theory has been proposed by Wiebols and Cook.[38] Their criterion is based on the additional strain energy around Griffith flaws due to the sliding of the flaw faces over each other. They predict that the intermediate principal stress should have a "pronounced and predictable effect" on the compressive strength; however, the present study has determined that the intermediate principal compressive stress has only a very slight effect on the compressive strength. A theory proposed by Priddy[37] predicts a similar large dependence of the compressive strength on the magnitude of the intermediate principal stress. This theory is an extension of the Tsai-Wu[70] theory which is not based on a physical model.

Any satisfactory theory of compressive strength must consider the array of cracks which grow stably from the flaws. At present there is only a crude understanding of the nature of crack extension in compression and almost no quantitative information on the stress fields of the

extended cracks. Bienowski[63] and Brace et al.[62] have shown that changes even in gross elastic properties are appreciable near failure which casts doubt on whether linear elastic stress analysis can be used.

A general description of compressive failure must include a consideration of the following items:

(1) The distributions of shape, size, and orientation of flaws within the body.

(2) The equations describing the stress dependence of crack initiation for the types of flaws present.

(3) The dimensions, shapes and orientations that cracks will have as a function of stress level and stress state.

(4) The interaction behavior of flaws and extended cracks.

(5) The structural collapse mechanism of the body.

i. General theory of compressive failure

An attempt to construct a framework which synthesizes the above elements into a complete description of the failure process in compression will be presented. Very few of the functional relationships are understood in detail. It is hoped that such a discussion will give an overall view of the processes of compressive failure and an appreciation of the important parameters and relationships. A semi-quantitative treatment of crack initiation and some qualitative statements on crack extension will be presented. It will be shown how statistical considerations of the flaw distribution and crack extension may be used to predict failure.

The tensile stress concentrated near the tip of a sharp flaw is proportional to $\sqrt{\frac{c}{\rho}}$ times the shear stress resolved on the plane of the

flaw, where (c) is the major flaw dimension and (ρ) is the radius of curvature at the tip. In compressive stress states this is reduced by the compressive stress resolved on the flaw plane which is also concentrated proportional to $\sqrt{\frac{c}{\rho}}$. For a given flaw orientation and a given stress state the maximum tensile stress near the tip is, therefore, proportional to $\sqrt{\frac{c}{\rho}}$ which is a measure of the flaw severity. Crack initiation occurs when this maximum tensile stress (σ_{max}) equals the cohesive strength of the material. Assuming the flaw to be oriented to the direction of an applied, uniaxial compressive stress such that the tensile stress at the tip is at the maximum (ξ_o), the expression for the applied stress necessary for crack initiation is:

$$\sigma_{max} = \sigma_{coh} = \alpha\ \sigma_a \sqrt{\frac{c}{\rho}} \tag{38}$$

where: $\sigma_{coh} \equiv$ cohesive strength of material

$\sigma_a \equiv$ applied compressive stress

$\alpha \equiv$ geometric constant

Defining the flaw severity to be:

$$\mathbf{C} \equiv \alpha \sqrt{\frac{c}{\rho}} \tag{40}$$

Equation (38) may be written as:

$$\sigma_a = \frac{\sigma_{coh}}{\mathbf{C}} \tag{41}$$

A linear equation is obtained relating the applied stress required for crack initiation to the severity ($\mathbf{C}$) of flaws oriented such that the maximum tensile stress is produced. The general nature of this dependence is shown in Figure 63.

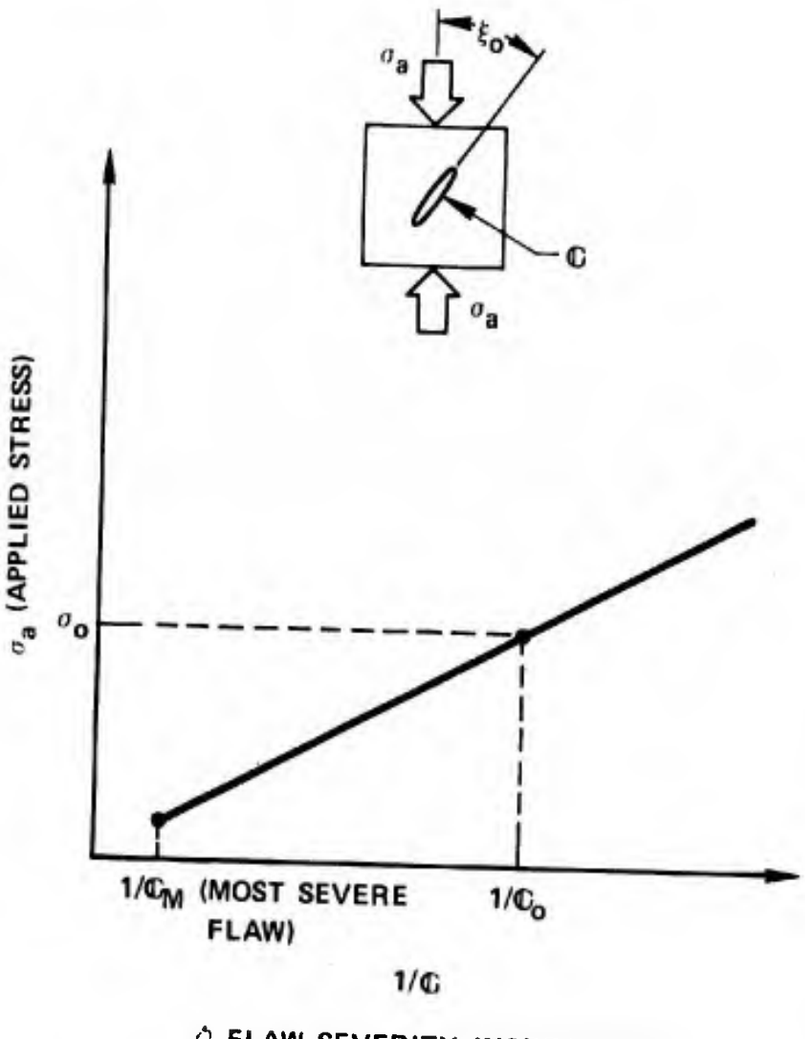

Figure 63. Stress Dependence for Crack Initiation at Flaws of Most Critical Orientation.

If we assume the stressed body contains a distribution of flaws with size-sharpness severity ($\mathbf{C}$) as shown in Figure 64, it can be seen that at any given applied stress level (σ_o) all flaws with $\mathbf{C} > \mathbf{C}_o$, where $\mathbf{C}_o$ is determined from Equation (41), will initiate cracks if all flaws have the most critical orientation (ξ_o) to the applied compression.

The magnitude of the applied stress necessary for crack initiation is a function of not only $\mathbf{C}$ but also of the orientation to the applied stress. This variation is shown in Figure 33 and 39 for the Griffith and McClintock-Walsh theories of crack initiation, respectively. Assuming the body contains only the flaws considered by Griffith (very sharp, Type I flaws), the orientation dependence is as shown in Figure 65 for an applied uniaxial compression. The angular range of flaw orientations which have initiated cracks ($\Delta\xi$) at a given applied stress level (σ_o) may be determined from this relationship for a given flaw severity $\mathbf{C}_i$.

If we now assume the distribution of flaw orientations is continuous and isotropic, i.e. there is an equal number of flaws occurring in each orientation, the fraction of the total number of flaws of severity $\mathbf{C}_i$ which have initiated cracks at a given applied stress level may be determined. Since the range of possible orientations is 0 to $\pi/2$, by dividing $\Delta\xi$ by $\pi/2$ the fraction of initiating flaws $F_{\mathbf{C}}$ is obtained:

$$F_{\mathbf{C}} \equiv \frac{\Delta\xi}{\pi/2} \tag{42}$$

If $F_{\mathbf{C}}$ is plotted as a function of the applied stress level (σ_a) for all values of $\mathbf{C}$ between $\mathbf{C}_m$ (the most severe flaw in the body) and $\mathbf{C}_o$ (the least severe flaw which initiates a crack at an applied stress level σ_o), the set of curves shown in Figure 66 is obtained.

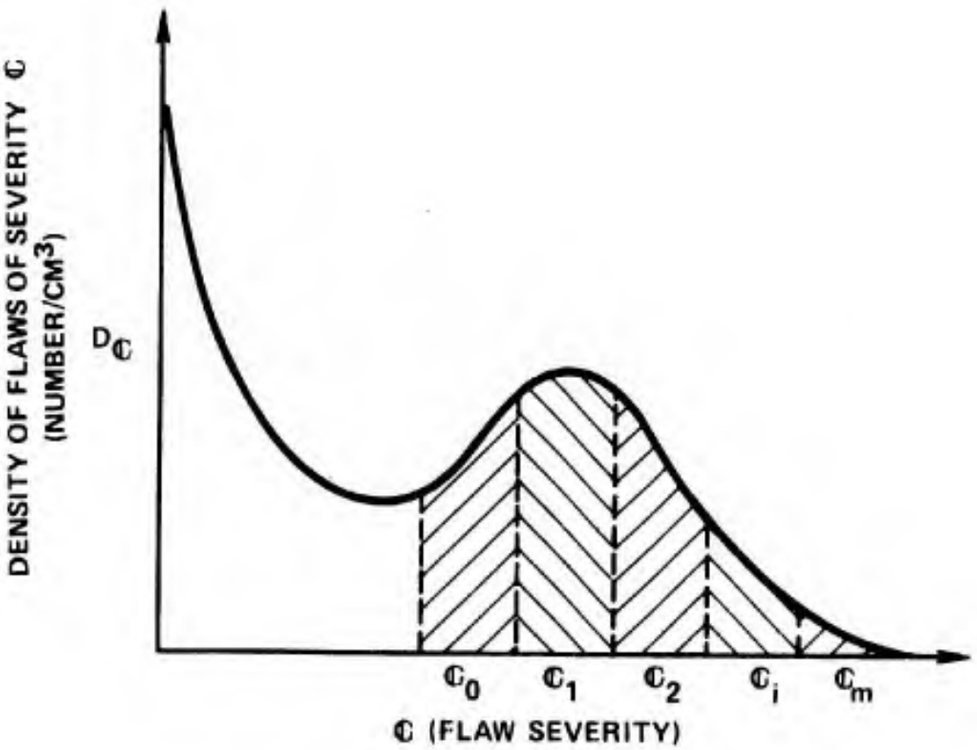

Figure 64. Flaw Density Curve.

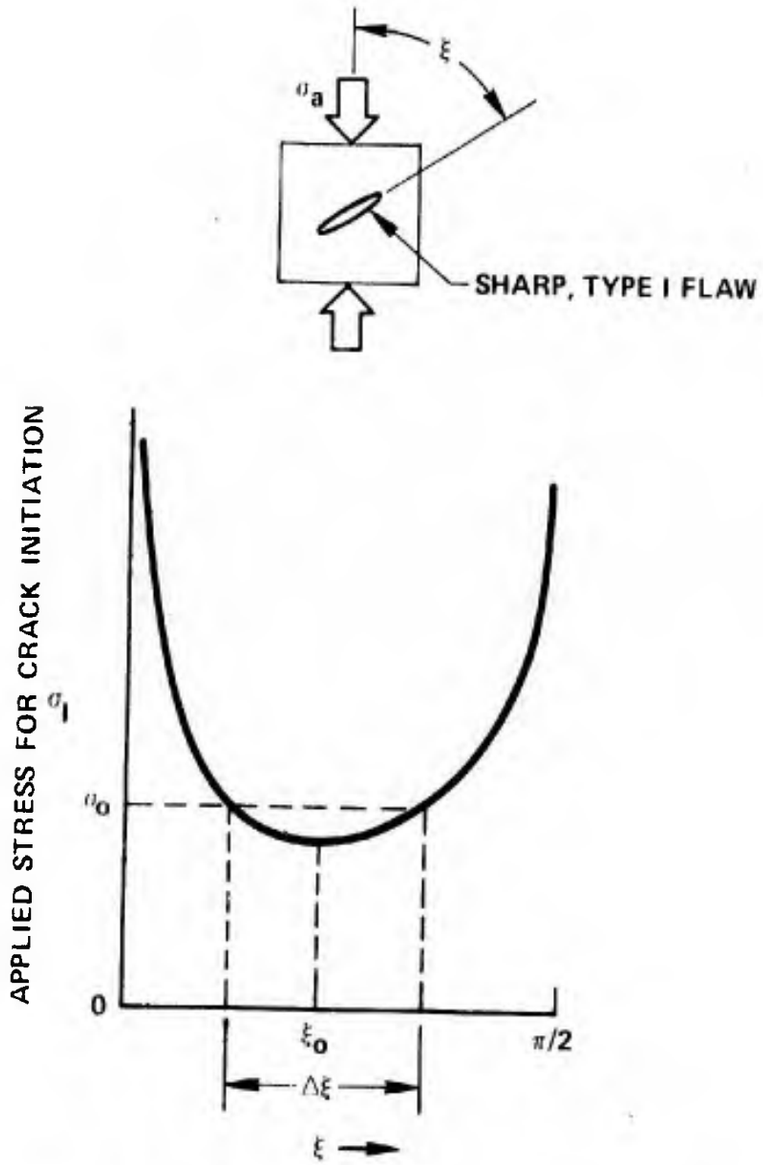

Figure 65. Flaw Orientation Dependence for Crack Initiation.

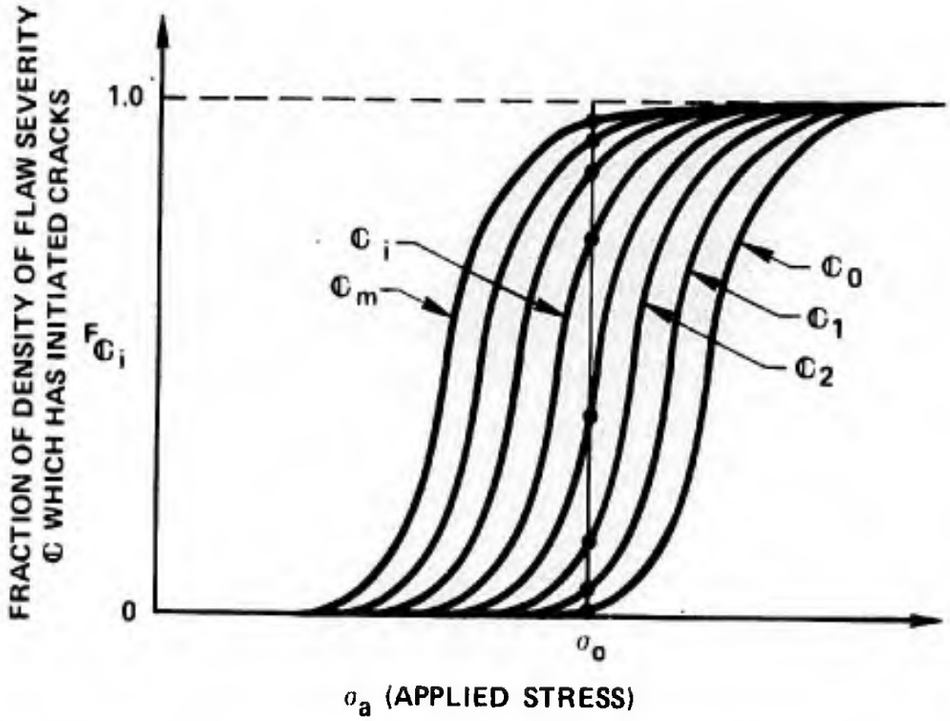

Figure 66. Fraction of Flaw Density Which Initiates Cracks.

If the applied stress is σ_o, the proportion of the density of each flaw severity $\mathbf{C}_i$ which has initiated cracks is given by $F_{\mathbf{C}_i}$. By summing the product of $F_{\mathbf{C}} \times D_{\mathbf{C}}$ for each increment ($\mathbf{C}_i$) of the flaw density curve (Figure 64), the total density of flaws which have initiated cracks ($\mathbb{D}_I$) may be obtained.

$$\mathbb{D}_I = \sum_{\mathbf{C}_i=\mathbf{C}_o}^{\mathbf{C}_i=\mathbf{C}_m} D_{\mathbf{C}_i} F_{\mathbf{C}_i} \tag{43}$$

A plot of the elements of the summation gives the curve describing the density of flaws which have initiated cracks (D_I) as shown in Figure 67. The integral of this curve, D_I, gives the total density of initiated flaws ($\mathbb{D}_I$) at stress σ_o.

Since the flaw severity factor $\mathbf{C}$ is linearly related to the applied stress by Equation (41), the summation of Equation (43) may easily be written in terms of the applied stress state parameter $\mathcal{A}$ using the identity:

$$\mathcal{A}_i \equiv \frac{1}{(\sigma_a)_i} = \frac{\mathbf{C}_i}{\sigma_{coh}} \tag{44}$$

The summation would then be written as:

$$\mathbb{D}_I = \sum_{\mathcal{A}_i=\mathcal{A}_o}^{\mathcal{A}_i=\mathcal{A}_m} D_{\mathcal{A}_i} F_{\mathcal{A}_i} \tag{45}$$

where $D_{\mathcal{A}}$ is obtained from the relationship $D_{\mathbf{C}}$ versus $\mathbf{C}$ in Figure 64 by expressing $D_{\mathcal{A}}$ as a function of $\mathcal{A}$ and $F_{\mathcal{A}}$ is obtained from the relationship $F_{\mathbf{C}}$ versus σ_a in Figure 66 by expressing $F_{\mathcal{A}}$ as a function of $\mathcal{A}$. Equation (45) gives the total density of flaws (i.e. number/cm^3) which have initiated cracks at the applied stress level (σ_o) in terms of the

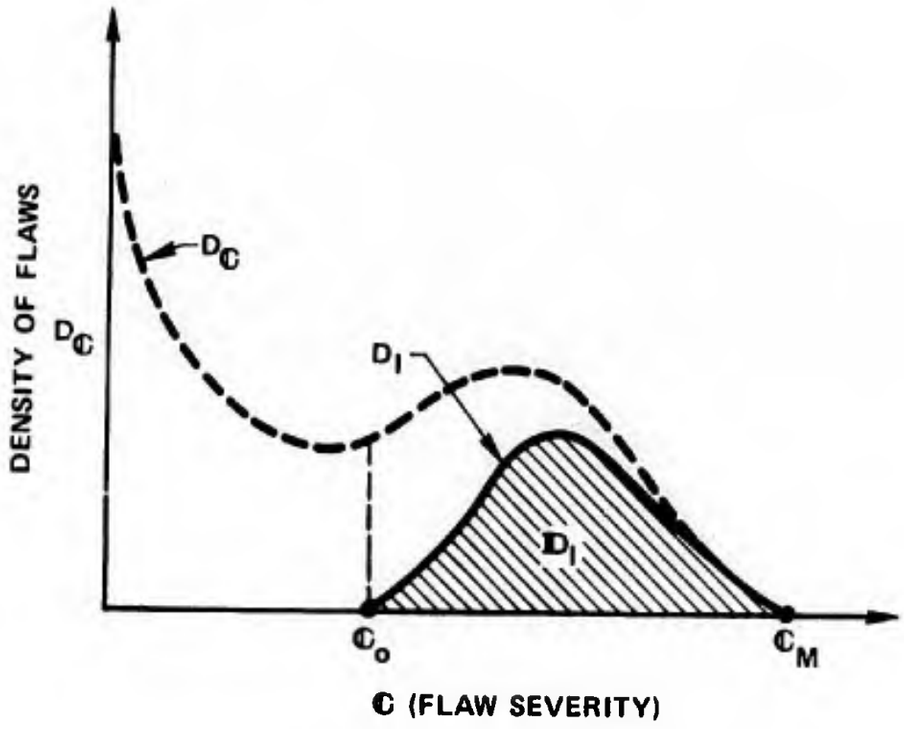

Figure 67. Density of Initiated Flaws Curve.

stress state parameter $\mathcal{A}$. As σ_o is increased, $\mathbb{D}_I$ will increase as shown in Figure 68. As the applied stress level is increased, less severe flaws initiate cracks and a larger proportion of the more severe flaws initiate cracks.

If flaws are initiating cracks by mechanisms other than that proposed by Griffith (e.g. Type II and III flaw mechanisms are operating, see Chapter V, Section A), the relationships between σ_I versus ξ (Figure 65) and $F_{\mathbb{C}}$ versus σ_a (Figure 66) will change. The flaw distribution curve (Figure 64) for Type III flaws will be a function of the applied stress. If more than one crack initiation mechanism is operating, Equation (45) must include a summation over the contribution of each mechanism to $\mathbb{D}_I$.

The foregoing development was in terms of a uniaxial applied compressive stress acting on a two-dimensional flaw. This development may be generalized to three-dimensional flaws and polyaxial compressive stress states by redefinition of the terms in some equations. Under three-dimensional, polyaxial stresses, the relationship in Equation (41) can be rewritten from the definition of Equation (44) as:

$$\mathcal{A} = \frac{\mathbb{C}}{\sigma_{coh}} \tag{41a}$$

where $\mathcal{A}$ is the stress state parameter composed of a function containing the principal stresses on the body and $\mathbb{C}$ may be a more elaborate function of flaw geometry, size and other characteristics:

$\mathbb{C}$ = f (flaw, geometry, size, etc.)

As an example, $\mathbb{C}$ would contain the parameter (S), the shape ratio parameter used by Koide, when treating open, oblate spheroidal flaws. (See

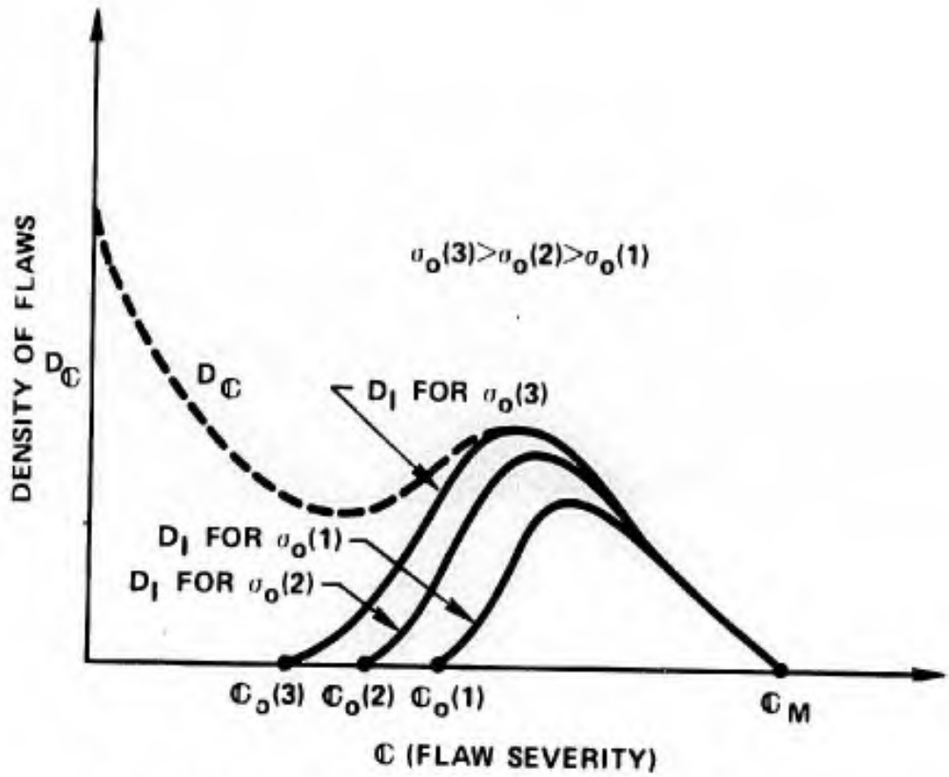

Figure 68. Change in Density of Initiated Flaws with Stress Level.

Chapter V, Section C.) The functions describing $\mathcal{A}$ and $\mathbb{C}$, which will contain the elastic constants of the material and the flaw characteristics, can be determined for any flaw type by an analysis similar to that of Chapter V where the maximum local tension is determined for the given ratio of applied compressions and compared to the critical tension required for crack initiation.

The relationship of $F_{\mathbb{C}}$ versus σ_a would be expressed in terms of $F_{\mathbb{C}}$ versus $\mathcal{A}$. If the normals to the flaw planes ($\hat{f}$), oriented in three dimensions, are identified as points of intersection on a spherical surface surrounding the flawed body, the proportion of flaw orientations which have initiated cracks can be expressed in terms of the proportion of spherical surface area intersected by these normals:

$$F_{\mathbb{C}} \equiv \frac{\text{Spherical Surface Area Intersected (Steradians)}}{4\pi} \qquad (42a)$$

Figure 65 would be replaced by the stereographic projection of this sphere, examples of which are shown in Figures 56 and 57 where σ_1, σ_2 and σ_3 are the principal stresses in the body. The construction of such an "initiated flaw orientation figure" has been described in Chapter V, Section C. The shapes of these figures will, of course, change with different crack initiation mechanisms. The relationship of Figure 64, giving $D_{\mathbb{C}}$ versus $\mathbb{C}$, may be quite complex for three-dimensional flaws in real materials. The nature of this relationship is not at all obvious at the present time. Perhaps by very careful analysis of the flaws which initiate cracks in a material at various stress levels such a relationship could be obtained.

Assuming the functions $\mathbb{C}$, $\mathcal{A}$, $D_{\mathbb{C}}$ and $F_{\mathbb{C}}$ are known, Equation (45) may be used to calculate the total number of flaws per unit volume which have initiated cracks. Simultaneous operation of more than one crack initiation mechanism would be treated as before by summing over the contribution of each mechanism.

To describe the total crack damage produced in a body at any given applied stress level, the term "damage figure" (ψ) is introduced. This damage figure will be a function of the density of flaws which initiate cracks ($\mathbb{D}_I$), the severity of the initiating flaws ($\mathbb{C}$), and the dimensions (ℓ_j) and orientations (ξ_j) of the extending cracks.

$$\psi = f\left[\mathbb{D}_I(\mathcal{A}),\ \mathbb{C},\ \ell_j(\mathcal{A}),\ \xi_j(\mathcal{A})\right] \tag{46}$$

It has been shown how $\mathbb{D}_I = f(\mathcal{A})$ may be calculated from an assumed mechanism of crack initiation. The definition of $\mathbb{C}$ and the distribution of flaw severity ($D_{\mathbb{C}}$) depend, of course, on the flaw types present in the stressed body. The experiments described in Chapter V, Section B indicate that much additional experimental work and elastic stress analysis must be done before the functions $\ell_j = f(\mathcal{A})$ and $\xi_j = f(\mathcal{A})$ are adequately understood.

To successfully describe compressive failure and predict compressive strength, the relationship between the damage figure and the structural collapse mechanism must be known. Structural collapse of the body occurs when the damage figure reaches a critical value ψ^* which allows a specific collapse mechanism, M_1, to operate. This failure criterion may be stated as:

$$\psi \geq \psi^*_{M_1} \tag{47}$$

As discussed at the beginning of this chapter, there are several potential structural collapse mechanisms (M_j). The one which operates to cause structural collapse of the body is the one requiring the minimum value of ψ.

Any one or any combination of the parameters in the expression for ψ may be the primary factor or factors determining when ψ becomes critical. If $\mathbb{D}_I$ becomes large at very small loads, this would be interpreted physically as the body developing a high density of short cracks and the structural collapse mechanism of the body would be similar to that of a soil mass with low cohesion. The other terms in the ψ expression could be neglected and

$$\psi = \psi^*_{\mathbb{D}_I} = \psi^*_{M_1} \text{ where } M_1 \text{ was direct shear}$$

If $\mathbb{D}_I$ was small but (ℓ_j) the extended crack length was large, the structural collapse mechanism might be identified with catastrophic, sequential buckling of plates or columns carved into the material by the extended cracks. The failure of rock, when tested as a solid cylinder in uniaxial compression, occurs, in part, by this mechanism. (See Peng.[68]) It can be seen that the orientation parameter (ξ_j) will also be important in such a collapse mechanism.

The value of ψ may be used to establish at what stress level interaction between the intensified stress fields surrounding flaws and cracks begins to occur. If an interaction volume is associated with each flaw-extended crack configuration and ψ is expressed in terms of this volume, a comparison of ψ with the total volume of the body would enable statistical formulations to be made predicting the magnitude of

the interaction (I). Structural collapse may be brought on by this interaction parameter becoming critical.

$$I(\psi) = I^*; \; M_j \text{ operates} \tag{48}$$

The interaction parameter probably contributes to structural collapse in rocks and in the alumina tested in this program; however, this has not been unequivocally demonstrated.

ii. Some implications of the theory

The alumina tested in this study fails when the maximum principal compressive stress reaches a critical value for stress states between 1:0.1 and 1:0.8. It is theorized that the material behaves in this manner because of the nature of the flaw density curve. (See Figure 64.) Large numbers of flaws of decreasing severity are involved with crack extension as the compressive stresses approach failure. Thus a knowledge of the complete shape of this curve is critical to an understanding of compressive strength. Some information concerning the nature of the flaw density curve may be obtained from the results of the spalling study. Only at applied stresses above 0.9 σ_f did a large amount of spalling occur. This may be interpreted to mean the flaw density curve has a long, shallow tail in the region of high flaw severity. (See Figure 69(a).) At low stress levels there is but a small density of flaws sufficiently severe to initiate cracks. Only for stress levels in excess of 90% σ_f is there a significantly large density of flaws severe enough to initiate cracks and produce extensive damage in the material. Any principal stress which is less than 90% σ_f will not influence the damage level.

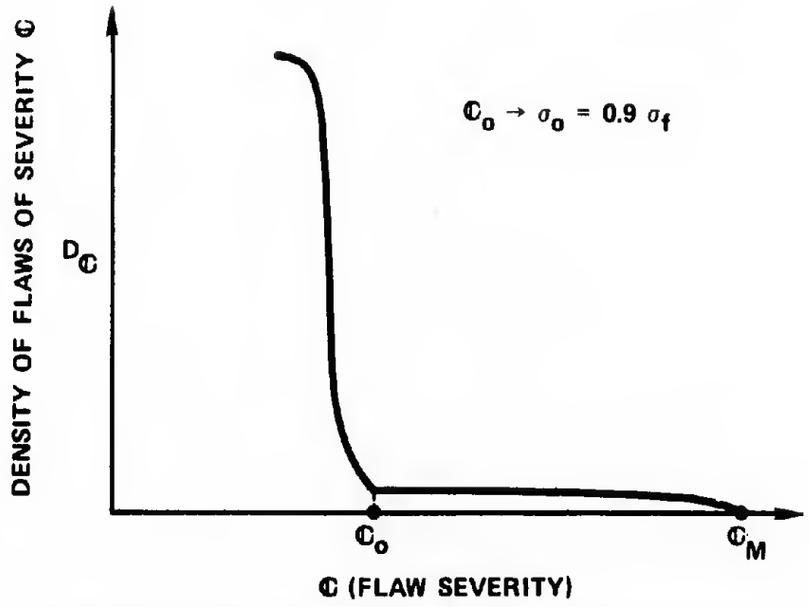

(a) POSSIBLE FLAW DENSITY CURVE FOR HIGH STRENGTH MATERIALS

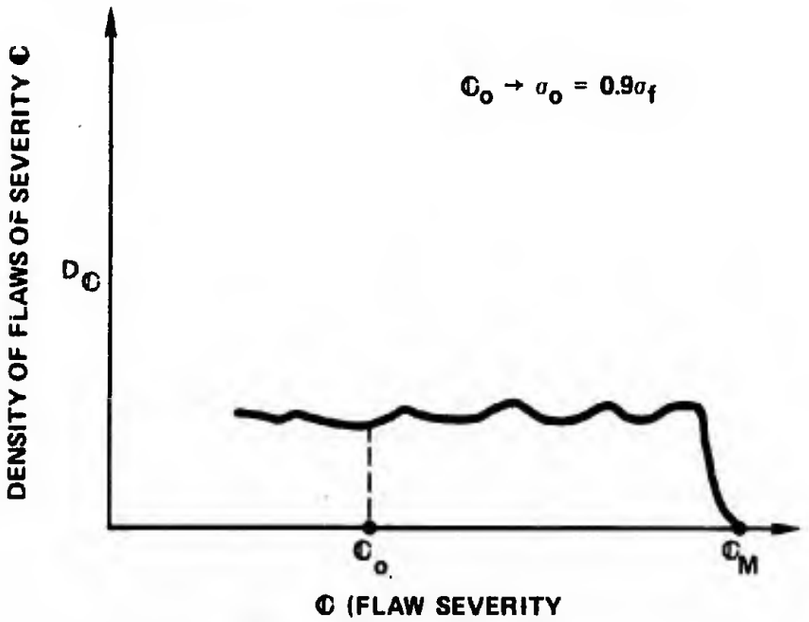

(b) POSSIBLE FLAW DENSITY CURVE FOR LOW STRENGTH MATERIALS

Figure 69. Flaw Density Curves for High and Low Strength Brittle Materials.

The abrupt rise of the flaw density curve shown in Figure 69(a) may be attributed to the attainment of a critical shear stress for unlocking large numbers of Type III flaws. One kind of Type III flaw which may unlock in alumina at such stress levels is the twinning of single grains proposed by Rice.[50] That a peak should occur for Type I or Type II flaws is not obvious but the possibility should not be excluded.

If the above is an accurate description of the distribution of flaw severity in alumina, then the considerations of the process of failure discussed in the previous section become important only at stress levels above 90% σ_f, and any variation in biaxial compressive strength with the intermediate compressive stress will be restricted to stresses within 90% σ_f. The minimum possible value of the uniaxial compressive strength would be within 10% of the biaxial strength. Materials which have low densities of flaws of high severity and a local maximum density of flaws of intermediate severity will behave in this fashion. This category should include the high density, high purity ceramics such as silicon carbide, silicon nitride and alumina.

In contrast to the high strength materials discussed above, low strength materials may have a flaw density curve as shown in Figure 69(b). Significant densities of flaws would initiate cracks at applied stresses much less than 0.9 σ_f and the effects discussed in Section Bi of this Chapter may produce larger variations in the biaxial strength with variations in the magnitude of the intermediate compressive stress. Unfortunately, there is a lack of good biaxial compressive strength data for low strength, brittle materials. The available data[33-35] indicates that such materials do show a greater influence of the intermediate

principal stress on the biaxial compressive strength than that measured for the alumina in this study.

In the bending and direct tensile failure of brittle materials, generally the worst flaw (as determined by size, environment and orientation to the applied stress) propagates to failure on application of the critical stress. Only a few of the less severe flaws extend before the most severe crack has propagated from the worst flaw completely through the material. Crack extension in ceramics in uniform tensile stress fields is unstable; that is, once a crack begins to extend from a flaw, it soon reaches a critical size and further extension of the crack is energetically favorable.

In compressive stress fields, the situation is quite different. First, cracks which extend in compression do not tend to propagate to cause failure of the part but rather tend to curve into the direction of the maximum principal compression stress at which point the tensile stress concentration at their tip is greatly reduced. For all but perhaps the final stage of compressive failure, crack extension is stable and of limited length. When a crack has extended from the worst flaw and stopped, the second worst flaw extends a crack which stops and so forth. This crack extension begins at a compressive stress approximately five times the measured tensile strength for the alumina tested.

One of the important implications of an understanding of this fracture process is that very reproducible strength values, with only a small scatter, should be obtainable with brittle materials such as alumina, in compressive stress states. The worst flaw or tenth worst flaw does not extend to failure. Instead, the 10^5 or 10^6 worst flaw

extends before failure occurs. The small scatter may be explained by using a "weakest link failure statistics" plot (see Figure 70), which shows the number of flaws which have extended cracks as a function of the applied stress. Projecting the intercepts of the "critical crack density" onto the stress axis for the cases of tensile and compressive failure the reduced scatter in compressive strength due to the increased slope of the curve is apparent. In tensile tests the very worst flaws cause failure and the region of considerable probability of failure is spread out over a large stress increment in the tail of the "weakest link curve." Thus, a small variation in the distribution of most severe flaws has a profound effect on the measured strength. In compression, the very large numbers of flaws which are extending cracks at stress levels near failure means that the measured strength is quite insensitive to minor variations in the distribution of inherent flaws. Consistent with this hypothesis, the strengths measured in biaxial compression show very little scatter; the standard deviations of the strength values are only a few percent of the average values.

Note added after final oral examination

The stereographic projections of the "initiated flaw orientation figures" (see Chapter V, Section Cii and Figures 56 and 57) are not constant-area projections of the spherical surface intersected by the normals of the flaws which have initiated cracks. Thus, these figures may not be used directly to determine F_C for the three-dimensional problem. It was suggested by professor J.L. Rosenfeld that a constant-area,

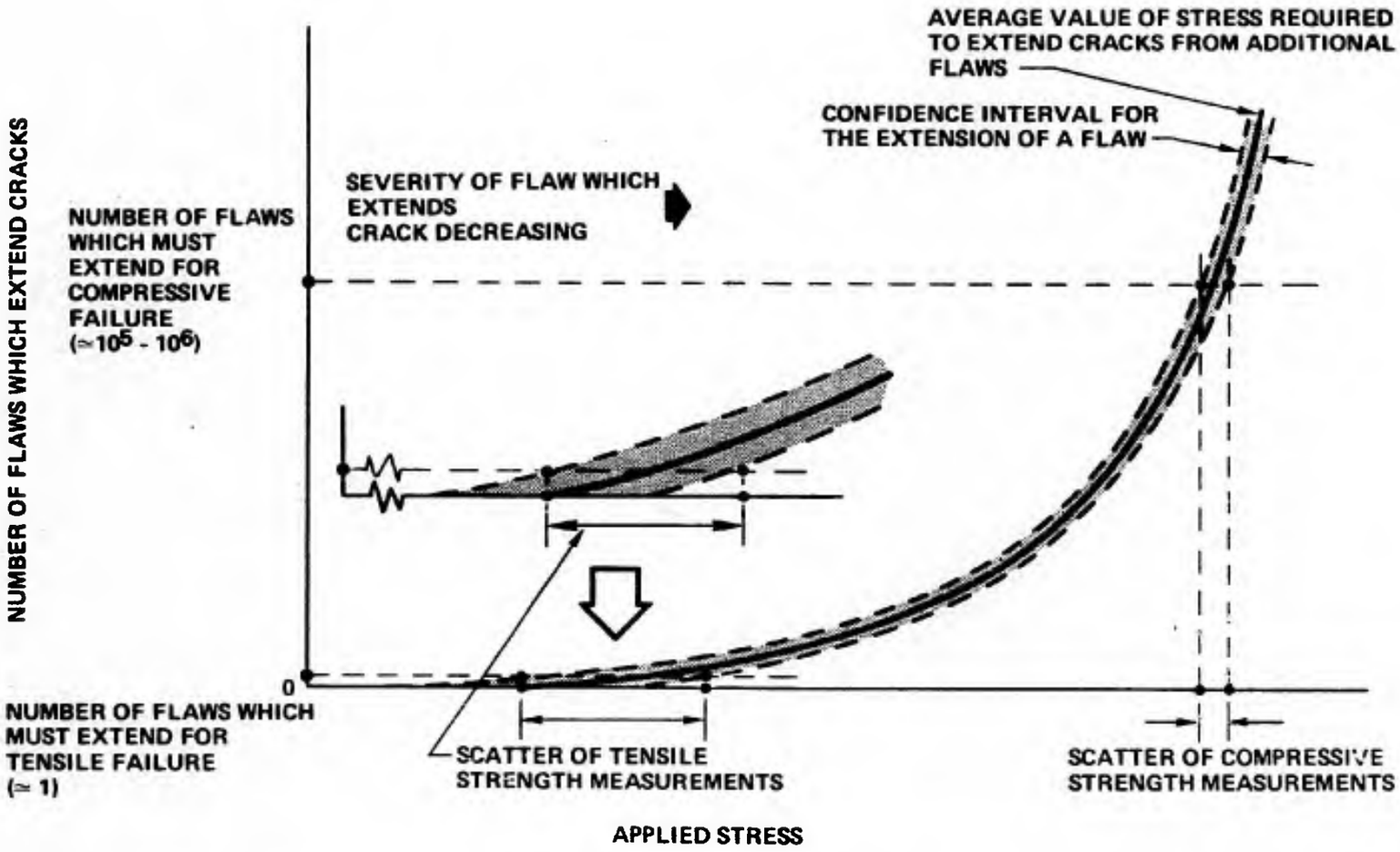

Figure 70. Weakest Link Crack Statistics.

polar mapping of the stereographic projection, developed by the UCLA Geology Department, might be used to obtain the F_C value. This would eliminate the necessity of using computer integration in spherical coordinates.

CHAPTER VII

CONCLUSIONS

Measurement of the compressive strength of brittle materials requires very careful testing techniques because poor techniques may introduce inadvertent stresses which lower the measured strength. Good tests had to be developed which gave data with sufficient accuracy to warrant theoretical consideration before a theory of strength could be proposed. Several mechanical testing techniques were developed which should be applicable to the determination of the compressive strengths of most brittle materials in any biaxial compression stress state. The design of the test devices and the testing procedures developed have been shown to be adequate for materials with high strengths. The approach used in this study was to test carefully a small number of specimens in each stress state. With this approach, the scatter in the measured strengths was minimized and the reported values, hopefully, are near to the true compressive strengths of the material. This study, which determined the biaxial compressive strength of high density alumina, showed that in stress states between 1:0.1 and 1:0.8 the magnitude of the lesser principal stress has little affect on the compressive strength. The average value of the measured compressive strength was 528 ksi; the scatter was only a few percent of this value.

For materials such as this alumina in which the biaxial compressive strength is insensitive to the magnitude of the intermediate compression, a single test may he used to establish the failure envelope in the compression-compression stress quadrant. The problems associated with

uniaxial compression testing indicate that it should not be used to determine the compressive strength. It is recommended that the 1:0.5 biaxial compression test be used.

Compressive failure has been shown to be the result of damage produced in the body by cracks propagating from flaws. The number of extending cracks in a body of alumina subjected to compressive loads was found to be very large, being of the order of 10^6 per cm^3 at loads near failure. This high density of extending cracks at stresses near failure indicates that compressive strength values should be very reproducible and independent of minor variations in the density of flaws in the material.

The spalling studies revealed the nature of crack damage produced in high strength, polycrystalline ceramics. The three-dimensional aspects of this crack damage were characterized. Analysis of the spalling damage showed the nature of the "critical damage figure" and indicated a mechanism of structural collapse which probably caused compressive failure of the test specimen.

Neither the classical Griffith theory of strength nor the modification of it by McClintock and Walsh predicts a ratio of compressive to tensile strength as high as 18, the ratio obtained when the measured compressive strengths are compared to the 1:0 tensile strength of WESGO AL-995 alumina. These theories, however, do not necessarily predict catastrophic failure but predict only when the first crack extension occurs. Micro-spalling on the inside surface of the specimens over the stress range from 25% to 100% of the failure stress

indicates that an explanation of the compressive failure envelope must involve a description of the micromechanical mechanisms of crack extension occurring during the process of failure and the statistics of crack extension from inherent flaws.

A complete description of compressive failure must be based on a three-dimensional model. The mechanisms of crack initiation and extension from three-dimensional flaws are not well understood. Three-dimensional flaws may initiate multiple cracks and extending cracks may function to initiate new cracks. The present studies have shown that such extension is quite complex and that it is not treated completely by present theory.

It is proposed that the kinds of flaws which occur in high-purity, high-strength ceramics may be classified into three types. The behavior of each of these three classifications of flaws has been discussed. A general theory of compressive failure has been presented in functional form which requires knowledge of the distribution of flaw severities for each flaw type present in the material. The key to an understanding of compressive strength is the identification of the critical array of cracks (damage figure, ψ) which induces structural collapse of the body. The damage figure produced in a body at any given stress level depends on the nature of the total distribution of flaws present in the body and the mechanisms by which the flaws extend cracks. Materials which contain different types of flaws and/or different distributions of flaw severity may exhibit different dependencies of the biaxial compressive strength on the ratio of the major to intermediate principal stresses. Unfortunately, the nature of the

total distribution of flaws has not yet been identified for any material. To predict the compressive strength of a material from its intrinsic properties one must know, quantitatively, the nature of the relationships which are, at present, only qualitatively explained.

REFERENCES

(1) Shanley, F.R. and W.J. Knapp. "Ceramics as Structural Materials," J. Structural Div., Proc. Am. Soc. Civil Engrs., Vol. 91, pp. 47-55, 1965.

(2) Knapp, W.J. and F.R. Shanley. "Ceramic Materials — Properties for Structural Applications," Aero/Space Engr., Vol. 17, pp. 34-38, 1958.

(3) Stachiw, J.D. "Glass and Cermaics for Underwater Vehicle Structures," Ceramic Age, Vol. 80, pp. 20-23, 1964.

(4) VanWyk, J.W. "Ceramic Airframe Bearings," Boeing Aerospace Company, Seattle, Washington, Final Report on Contract NASC-N00019-73-C-0230, February 1974.

(5) Burke, J.J., et al. Ceramics for High Performance Applications, Brook Hill, Chestnut Hill, Massachusetts, 1974.

(6) Cornet, I. and R.C. Grassi. "A Study of Theories of Fracture under Combined Stresses," J. Basic Engr. Transactions of ASME, Vol. 83, Series D, No. 1, pp. 39-44, March 1961.

(7) Babel, H.W. "Biaxial-Fracture Strength of Brittle Materials," Douglas Aircraft Company, Santa Monica, California, Technical Report AFML-TR-66-51, March 1966.

(8) Broutman, L.J., et al. "Effects of Combined Stresses on Fracture of Alumina and Graphite," J. Am. Cer. Soc., Vol. 53, No. 12, pp. 649-653, December 1970.

(9) Ely, R.E. "Strength of Titania and Aluminum Silicate under Combined Stresses," J. Am. Cer. Soc., Vol. 55, No. 7, pp. 347-350, July 1972.

REFERENCES (Cont'd)

(10) Dukes, W.H. "Handbook of Brittle Material Design Technology, AGARDograph No. 152," North Atlantic Treaty Organization, AGARD-AG-152-71, February 1971.

(11) Salmassey, O.K., et al. "Behavior of Brittle-State Materials," Battelle Memorial Institute, Columbus, Ohio, WADC Technical Report 50-53, Parts I and II on Contract No. AF-33 (038)-8682, June (1955).

(12) Batdorf, S.B. and J.G. Crose. "A Statistical Theory for the Fracture of Brittle Structures Subjected to Nonuniform Polyaxial Stresses," Aerospace Corp., El Segundo, California, Technical Report on SAMSO Contract No. F04701-72-C-0073, February 1973.

(13) Babel, H.W. and G. Sines. "A Biaxial Fracture Criterion for Porous Brittle Materials," J. Basic Engr. Transactions of ASME, Vol. 90, pp. 285-291, June 1968.

(14) Rudnick, A., et al. "The Evaluation and Interpretation of Mechanical Properties of Brittle Materials," Technical Report AFML-TR-67-316 and DCIC 68-3, April 1968.

(15) Schwaninger, O. "A 2000-Ton Compression Testing Machine," Proc. Inst. Mech. Engrs., Vol. 180, Part 3A, pp. 380-387, 1965-1966.

(16) Pears, C.D. and F.S. Digesu. "Gas-Bearing Facilities for Determining Axial Stress-Strain and Lateral Strain of Brittle Materials to 5500 F," ASTM Proc., Vol. 65, pp. 855-873, 1965.

REFERENCES (Cont'd)

(17) Owen, J.B.B. "Cheap Strength-Testing Machines with Freely Hinged ends and a Known Line of Loading," Proc. Inst. Mech. Engrs., Vol. 180, Part 3A, pp. 411-418, 1965-1966.

(18) Sedlacek, R. and F.A. Halden. "Method for Tensile Testing of Brittle Materials," Rev. Sci. Instruments, Vol. 33, No. 3, pp. 298-300, 1962.

(19) Sedlacek, R. "Investigation of Elasticity and Strength of Ceramics Subjected to Tensile and Compressive Loads," Stanford Research Institute, Menlo Park, California, Technical Report AFML-TR-68-231, August 1968.

(20) Filon, L.N.G. and E.G. Coker. A Treastise on Photoelasticity, Cambridge University Press, London, 1957.

(21) Lambert, J.S. and M.J. Manjoine. "Pressure Tests on Thick-Walled Porcelain Cylinders," unpublished report of Westinghouse Research Laboratories, May 1941 reported in Nadai, A. Theory of Flow and Fracture of Solids, Vol. 1, McGraw Hill, New York, 1950, pp. 343-346.

(22) Babel, H.W. and G. Sines. "An Improved Method for Uniaxial and Biaxial Testing of Brittle Materials," J. of Materials, Vol. 3, No. 1, pp. 134-152, March 1968.

(23) Southwell, R.V. "On the General Theory of Elastic Stability," Philosophical Transactions, Vol. 213A, pp. 187-244, 1913.

(24) Adams, M.A. An Experimental Investigation of the Biaxial Compressive Strength of Ceramics, M.S. in Engineering, Materials Department, University of California, Los Angeles, pp. 46-55, March 1972.

REFERENCES (Cont'd)

(25) ibid., pp. 34-38.

(26) Sedlacek, R. and E.P. Farley. "Processing of Ceramics-Surface Finishing Studies," Stanford Research Institute, Menlo Park, California, Final Technical Report on NASC Contract No. NOw 66-0383-d, May 1967.

(27) Sedlacek, R. "Processing of Ceramics-Surface Finishing Studies," Stanford Research Institute, Menlo Park, California, Final Technical Report on NASC Contract No. N00019-67-C-0494, November 1968.

(28) Sedlacek, R. "Processing of Ceramics-Surface Finishing Studies," Stanford Research Institute, Menlo Park, California, Final Technical Report on NASC Contract No. N00019-68-C-0388, May 1969.

(29) Sedlacek, R. and P.J. Jorgensen. "Processing of Ceramics-Surface Finishing Studies," Stanford Research Institute, Menlo Park, California, Final Technical Report on NASC Contract No. N00019-70-C-0179, September 1971.

(30) Sedlacek, R. "Processing of Ceramics-Surface Finishing Studies," Stanford Research Institute, Menlo Park, California, Final Technical Report on NASC Contract No. N00019-69-C-0229, April 1970.

(31) Adams, M. and G. Sines. "An Experimental Study on the Compressive Biaxial Strength of Ceramics," Materials Department, School of Engineering and Applied Science, University of California,

Los Angeles, Second Annual Report on NASC Contract No. N00019-72-C-0159 (UCLA-ENG-7297), December 1972.

(32) Adams, M. and G. Sines. "An Experimental Study on the Compressive Biaxial Strength of Ceramics," Materials Department, School of Engineering and Applied Science, University of California, Los Angeles, Third Annual Report on NASC Contract No. N00019-73-C-0294 (UCLA-ENG-7395), February 1974.

(33) Vile, G.W.D. Behavior of Concrete under Simple and Combined Stresses, Ph.D. Thesis, Imperial College, University of London, London, September 1965.

(34) Liu, T.C. "Stress-Strain Response and Fracture of Concrete in Biaxial Compression," Department of Engineering, School of Civil Engineering, Cornell University, Ithica, New York, Report No. 339 on NSF Grant GK-10214, February 1971.

(35) Mazanti, B.B. and G.F. Sowers. "Laboratory Testing of Rock Strength," Testing Techniques for Rock Mechanics, American Society for Testing Materials, ASTM STP-402, pp. 207-227, 1966.

(36) Broutman, L.J. and R.H. Cornish. "Effect of Polyaxial Stress States on Failure Strength of Alumina Ceramics," J. Am. Cer. Soc., Vol. 48, pp. 519-524, October 1965.

(37) Priddy, T.B. "A Fracture Theory for Brittle Anisotropic Materials," J. Engr. Materials and Technology, Vol. 96, Series H, No. 2, pp. 91-96, April 1974.

(38) Wiebols, G.A. and G.W. Cook. "An Energy Criterion for the Strength of Rock in Polyaxial Compression," International Journal of Rock Mechanics and Mining Science, Vol. 5, pp. 529-549, February 1968.

(39) Adams, F.D. "An Experimental Contribution to the Question of the Depth of the Zone of Flaw in the Earth's Crust," J. Geology, Vol. 20, pp. 97-118, 1912.

(40) Koide, H. "Fracture Initiation in Brittle Polycrystalline Material such as Rocks," Proceedings of the International Conference on Mechanical Behavior of Materials, Vol. IV, Society of Materials Science, Kyoto, Japan, pp. 455-463, 1972.

(41) Griffith, A.A. "The Phenomena of Rupture and Flow in Solids," Philosophical Transactions of the Royal Society, London, Vol. 221A, pp. 163-198, 1921.

(42) Inglis, C.E. "Stresses in a Plate due to the Presence of Cracks and Sharp Corners," Royal Institute of Naval Architects, Transactions, London, Vol. 55, pp. 219-230, 1913.

(43) Paris, P.C. and G.C. Sih. "Stress Analysis of Cracks," Fracture Toughness Testing and Its Applications, ASTM STP-381, pp. 30-81, April 1965.

(44) Griffith, A.A. "The Theory of Rupture," Proceedings of the First International Congress for Applied Mechanics, Delft, pp. 55-63, 1924.

(45) Kobayashi, S. "Initiation and Propagation of Brittle Fracture in Rock-Like Materials under Compression," J. of Soc. of Materials Science Japan, Vol. 20, No. 209, pp. 164-173, February 1971.

(46) Bieniawski, Z.T. "Mechanisms of the Brittle Fracture of Rock, Part III, Fracture in Tension and Under Long Term Loading," International J. of Rock Mechanics and Mining Science, Vol. 4, No. 4, pp. 425-430, October 1967.

(47) Tetelman, A.S. and A.J. McEvily, Jr. Fracture of Structural Materials, Wiley, New York, 1967.

(48) McClintock, F.A. and J.B. Walsh. "Friction on Griffith Cracks in Rocks under Pressure," Proceedings of the Fourth U.S. National Congress of Applied Mechanics, University of California, Berkeley, pp. 1015-1021, June 1962.

(49) Hoek, E. and Z.T. Bieniawski. "Brittle Fracture Propagation in Rock under Compression," International J. of Fracture Mechanics, Vol. 3, pp. 137-155, 1965.

(50) Rice, R.W. "The Compressive Strength of Ceramics," Materials Science Research, Proceedings of the Sixth University Conference on Ceramic Science, Vol. 5, Plenum Press, New York, pp. 195-229, 1971.

(51) Irwin, G.R. "Fracture Mechanics," Structural Mechanics, Proceedings of the First Symposium on Naval Structural Mechanics, Stanford University, California, Ed. J.N. Goodier and N.J. Hoff, Pergamon Press, Oxford, pp. 557-592, 1960.

(52) Westergaard, H.M. "Bearing Pressures and Cracks," J. Applied Mechanics, Vol. 6, No. 2, pp. 49-53, June 1939.

(53) Brace, W.F. and E.G. Bombolakis. "A Note on Brittle Crack Growth in Compression," J. Geophysical Research, Vol. 68, No. 12, pp. 3709-3713, June 1963.

(54) Bieniawski, Z.T. "Mechanism of Rock Fracture in Compression," Rock Mechanics Division, National Mechanical Engineering Research Institute, Council for Scientific and Industrial Research, Pretoria, South Africa, CSIR Report MEG 459, June 1966.

(55) Sneddon, I.N. "The Distribution of Stresses in the Neighborhood of a Crack in an Elastic Solid," Proceedings of the Royal Society, London, Series A, Vol. 187, pp. 229-260, 1946.

(56) Segedin, C.M. "A Penny Shaped Crack under Shear," Proceedings of the Cambridge Philosophical Society, Vol. 47, pp. 396-400, 1950.

(57) Green, A.E. and I.N. Sneddon. "The Distribution of Stresses in the Neighborhood of a Flat Elliptical Crack in an Elastic Solid," Proceedings of the Cambridge Philosophical Society, Vol. 46, pp. 159-164, 1950.

(58) Sadowsky, M.A. and E. Sternberg. "Stress Concentration around an Ellipsoidal Cavity in an Infinite Body under Arbitrary Plane Stress Perpendicular to the Axis of Revolution of Cavity," J. Applied Mechanics, Vol. 14, pp. 191-201, 1947.

(59) Sack, R.A. "Extension of Griffith's Theory of Rupture to Three Dimensions," Proceedings of the Physical Society, London, Vol. 58, pp. 729-736, 1946.

(60) Nadai, A. Theory of Flow and Fracture of Solids, Vol. 1, McGraw Hill, New York, 1950, p. 96.

(61) Kassir, M.K. and G.C. Sih. "Three Dimensional Stress Distribution around an Elliptical Crack Under Arbitrary Loadings," J. Applied Mechanics, Vol. 33, pp. 601-611, September 1966.

(62) Brace, W.F., et al. "Dilatancy in the Fracture of Crystalline Rocks," J. Geophysical Research, Vol. 71, No. 16, pp. 3939, August 1966.

(63) Bieniawski, Z.T. "Mechanism of Brittle Fracture of Rock," National Mechanical Engineering Research Institute, Council for Scientific and Industrial Research, Pretoria, South Africa, CSIR Report MEG 580, August 1967.

(64) Bieniawski, Z.T. "Mechanism of Brittle Fracture of Rock, Part II Experimental Studies," International J. of Rock Mechanics and Mining Sciences, Vol. 4, No. 4, pp. 407-423, October 1967.

(65) Paulding, B.W., Jr. "Techniques Used in Studying the Fracture Mechanics of Rock," Testing Techniques for Rock Mechanics, ASTM STP-402, Am. Soc. Testing Materials, pp. 73-86, 1966.

(66) Walsh, J.B. "The Effect of Cracks on the Uniaxial Elastic Compression of Rocks," J. Geophysical Research, Vol. 70, No. 2, pp. 399-411, January 1965.

REFERENCES (Cont'd)

(67) Walsh, J.B. "The Effect of Cracks on the Compressibility of Rock," J. Geophysical Research, Vol. 70, No. 2, pp. 381-389, January 1965.

(68) Peng, S. and A.M. Johnson. "Crack Growth and Faulting in Cylindrical Specimens of Chelmsford Granite," International J. Rock Mechanics and Mining Sciences, Vol. 9, pp. 37-86, 1972.

(69) Scholz, C.H. "Microfracturing and the Inelastic Deformation of Rock in Compression," J. Geophysical Research, Vol. 73, No. 4, pp. 1417-1432, February 1968.

(70) Tsai, S.W. and E.M. Wu. "A General Theory of Strength for Anisotropic Materials," J. Composite Materials, Vol. 5, pp. 58-80, January 1971.

(71) Timoshenko, S.P. and J.N. Goodier. Theory of Elasticity, third edition, McGraw-Hill, New York, 1970, p. 70.

(72) Masai, Y., et al. "Handbook of Elastic Stability," NASA, N 69-34689, Washington, D.C. (available from Clearinghouse for Federal Scientific and Technical Information, U.S. Department of Commerce), July 1969.

(73) von Mises, R. "Der Kritische Aussendruck zylindrisher Rohre," Zeits. Vereine deutsher Ing., Vol. 58, 1914.

(74) Flügge, W. "Stability of Circular Cylinders," Ing. Arcv., Vol. 3, No. 5, pp. 463-506, 1932.

(75) Timoshenko, S. Theory of Elastic Stability, McGraw Hill, New York, 1936.

(76) Timoshenko, S.P. and J.N. Goodier. Theory of Elasticity, third edition, McGraw-Hill, New York, 1970, pp. 191-194.

(77) Wachtman, J.B., et al. "Linear Thermal Expansion of Aluminum Oxide and Thorium Oxide from 100° to 1100°K," J. Am. Cer. Soc., Vol. 45, No. 7, pp. 319-323, 1962.

(78) Wachtman, J.B., Jr. "The Influence of Surface Features on the Strength of Polycrystalline Alumina," Mechanical Behavior of Materials, Proceedings of the International Conference on Mechanical Behavior of Materials, Vol. IV, Society of Materials Science, Kyoto, Japan, pp. 432-442, 1972.

(79) Rigby, G.R. and A.T. Green. The Thin-Section Mineralogy of Ceramic Materials, British Ceramic Research Association, London, 1953, p. 89.

(80) Fulrath, R.M. and J.A. Pask. Ceramic Microstructures, Wiley, New York, 1968, pp. 39-49.

APPENDIX A

CALCULATION OF STRESSES PRODUCED AT FAILURE IN THE 1:1 TEST DEVICE

As external fluid pressure is applied to the 1:1 test device after preloading the specimen, the pressure acts on the circumference and the ends of the specimen shortening it as though the specimen were an externally pressurized, closed-end, cylindrical pressure vessel. Because of the design of the 1:1 test device, fluid pressure does not act on the bolt or sleeve; they are unstressed by the pressure. Since the bolt and sleeve are applying a compressive load to the specimen at all times during the small displacements seen in the specimen, they will maintain contact with each other and with the specimen. The change in length of the bolt plus the sleeve during pressurization equals the change in length of the specimen.

The equation for the change in length is:

$$\delta_{specimen} = \delta_{bolt} + \delta_{sleeve} \tag{1A}$$

where: $\delta = CF$

$C = \frac{L}{AE}$ = compliance

F = force

Change in length of the specimen on pressurization:

$$\delta_{specimen} = \Delta F_{bolt}\, C_{bolt} + \Delta F_{sleeve}\, C_{sleeve} \tag{2A}$$

For static equilibrium:

$$\Delta F_{bolt} = \Delta F_{sleeve} = \Delta F_{preload} \tag{3A}$$

Since the bolt and sleeve are in series in the load train their compliances may be combined:

$$C' \equiv C_{bolt} + C_{sleeve}$$

and:

$$\delta_{specimen} = \Delta F_{preload}\, C'$$

The loss in axial preload in the specimen due to the shortening of the specimen under the action of external fluid pressure may be calculated from this equation:

$$\Delta F_{preload} = \frac{\delta_{specimen}}{C'} \qquad (4A)$$

The value of $C' = 59.0 \times 10^{-8}$ in/lb.; this calculation was presented in Reference 24. The expression for δ_p, the axial displacement of the specimen under the fluid pressure is developed as follows:

The change in length of specimen resulting from pressurization of the 1:1 test device is:

$$\delta_p = \int_0^{\ell} \epsilon_{zz}\, d\ell \qquad (5A)$$

where: $\epsilon_{zz} = \frac{\sigma_{zz}}{E} - \frac{\nu}{E}\sigma_{\theta\theta}$; σ_{rr} is assumed negligible

σ_{zz} and $\sigma_{\theta\theta}$ which arise from the fluid pressure are calculated as follows:

$$\sigma_{zz} = \frac{PA_E}{A_W} \qquad (6A)$$

where: A_E = end area of specimen

A_W = cross sectional area of wall at any point

$$A_E = \left(\frac{d_o}{2}\right)^2 \pi = \frac{d_o^2}{4}\pi$$

$$A_w = d_m \pi t$$

$$\sigma_{zz} = \frac{p\left(\frac{d_o^2}{4}\right)\pi}{t\ d_m\ \pi}$$

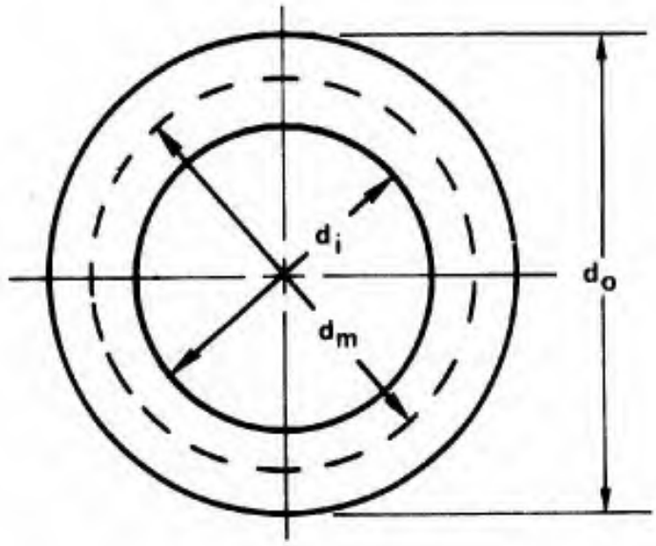

$$\sigma_{zz} = -\frac{p\ d_o^2}{4\ t\ d_m}$$ minus sign because compressive stress (7A)

Using the thick wall pressure vessel equation[71] we obtain:

$$\sigma_{\theta\theta} = -\ a^2\ \frac{b^2(p_o - p_i)}{b^2 - a^2}\ \frac{1}{r^2} + \frac{p_i\ a^2 - p_o b^2}{b^2 - a^2} \tag{8A}$$

where: $r = r_m$ (mean radius)

$p_o = p$ = external fluid pressure (positive)

$p_i = 0$

$b = \frac{d_o}{2}$

$a = \frac{d_i}{2}$

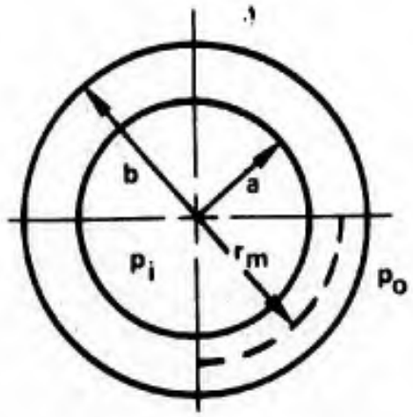

then:

$$\sigma_{\theta\theta} = \left(-\frac{a^2\ b^2 p}{(b^2 - a^2)r^2}\right) - \left(\frac{ph^2}{b^2 - a^2}\right) \tag{9A}$$

and further substitution:

$$\sigma_{\theta\theta} = -\frac{\left(\frac{d_i}{2}\right)^2\left(\frac{d_o}{2}\right)^2 P}{\left[\left(\frac{d_o}{2}\right)^2 - \left(\frac{d_i}{2}\right)^2\right] r^2} - \frac{\left(\frac{d_o}{2}\right)^2 P}{\left(\frac{d_o}{2}\right)^2 - \left(\frac{d_i}{2}\right)^2}$$

$$\sigma_{\theta\theta} = -\left(\frac{P\, d_o^2}{d_o^2 - d_i^2}\right)\left(\frac{d_i^2}{4r^2} + 1\right) \qquad (10A)$$

σ_{rr} is assumed to be neglible and:

$$\varepsilon_{zz} = \frac{\sigma_{zz}}{E} - \frac{\nu}{E}\sigma_{\theta\theta} \qquad (11A)$$

Substituting for σ_{zz} and $\sigma_{\theta\theta}$ from Equation (7A) and (10A):

$$\varepsilon_{zz} = -\left(\frac{P}{4E}\right)\left(\frac{d_o^2}{t\, d_m}\right) + \left(\frac{\nu P}{E}\right)\left(\frac{d_o^2}{d_o^2 - d_i^2}\right)\left(\frac{d_i^2}{4r_m^2} + 1\right) \qquad (12A)$$

Since the specimen is symmetric about its midplane, the change in length of specimen is given by:

$$\delta_p = \int_o^{\ell} \varepsilon_{zz}\, d\ell = 2\int_o^{\ell/2} \varepsilon_{zz}\, d\ell \qquad (13A)$$

The above integral can be approximated by the following summation technique:

$$\delta_p = 2\sum_{n=1}^{n=x}\left[-\left(\frac{P}{4E}\right)\left(\frac{d_o^2}{td_m}\right)_n + \left(\frac{\nu P}{E}\right)\left(\frac{d_o^2}{d_o^2-d_i^2}\right)_n\left(\frac{d_i^2}{4r_m^2} + 1\right)_n\right]\Delta\ell_n \qquad (14A)$$

$$\delta_p = \frac{2P}{E}\sum_{n=1}^{n=x}\left[-\left(\frac{d_o^2}{4t\, d_m}\right)_n + \nu\left(\frac{d_o^2}{d_o^2-d_i^2}\right)_n\left(\frac{d_i^2}{d_m^2} + 1\right)_n\right]\Delta\ell_n$$

$$\delta_p = A\sum_{n=1}^{n=x}\left[-(B)_n + \nu(C)_n\,(D)_n\right]\Delta\ell_n$$

where: $A = \frac{2P}{E}$

$$B = \frac{d_o^2}{4td_m}$$

$$C = \left(\frac{d_o^2}{d_o^2 - 4}\right)$$

$$D = \left(\frac{d_i^2}{d_m^2} + 1\right) = \left(\frac{4}{d_m^2} + 1\right)$$

By making measurements on an enlarged scale drawing of the cross section of the specimen and using 19 elements in the summation the following equation was obtained:

$$\delta_p = \frac{2P}{E} (4.9011) \tag{15A}$$

When steel compliance tubes are used instead of alumina, some of the terms in the summation must be changed since $E_{alumina} \neq E_{steel}$. It is obvious that

$$\delta_p^{total} = \delta_p^{(alumina\ specimen\ tube)} + \delta_p^{(steel\ compliance\ tube)} \tag{16A}$$

changing the proper elements and making the summation we find:

$$\delta_p^{total} = \frac{2P}{E_{alumina}} \ 2.7865 \ + \frac{2P}{E_{steel}} (2.0146) \tag{17A}$$

or:

$$\delta_p^{total} = 2P \ (1.215 \times 10^{-7}) \tag{18A}$$

A sample calculation of the failure stresses in a 1:0.8 biaxial compression specimen from the test data follows.

(i) Preload axial strains measured in test section by three longitudinal strain gages:

$$\begin{array}{r} 3320\ \mu\text{-in/in} \\ 3350 \\ +3375 \\ \hline 10045 \end{array} \qquad \varepsilon_{zz}^{gage} = \frac{10045}{3} = 3348\ \mu\text{-in/in}$$

(ii) Measured pressure at failure was 55,200 psi.

(iii) Change in specimen length due to fluid pressure (p) from Equation (15A) is:

$$\delta_p = \frac{(2)(5.52 \times 10^4)}{(5.36 \times 10^7)}(4.801)$$

$$\delta_p = 9.91 \times 10^{-3}\ \text{in.}$$

(iv) Decrease in axial preload during pressurization from Equation (4A):

$$\Delta F_{preload} = \frac{\delta_{specimen}}{C'} = \frac{9.91 \times 10^{-3}}{5.90 \times 10^{-7}} = 16{,}800\ \text{lbs.}$$

(v) The initial bolt preload was:

$$L_{preload} = \sigma_{zz}(A_{gage}) = \varepsilon_{zz}E(A_{gage})$$

$$L_{preload} = (3.348 \times 10^{-3})(5.36 \times 10^7)(0.832)$$

$$L_{preload} = 149{,}300\ \text{lbs.}$$

(vi) Preload at failure was:

$$F_{preload} = 149{,}300 - 16{,}800 = 132{,}500\ \text{lbs.}$$

(vii) $\sigma_{zz}^{total} = \sigma_{zz}^{preload} + \sigma_{zz}^{pressure}$

where: $\sigma_{zz}^{pressure}$ is from Equation (7A)

$$\sigma_{zz}^{total} = \frac{F_{preload}}{A_{gage}} + \frac{P}{4}\frac{d_o^2}{td_m}$$

$$\sigma_{zz}^{total} = \frac{1.32 \times 10^5}{0.832} + \frac{5.52 \times 10^5}{4} \quad (19.06)$$

$$\sigma_{zz}^{total} = 422,300 \text{ psi}$$

(viii) From Equation (10A):

$$\sigma_{\theta\theta} = \frac{pd_o^2}{d_o^2 - d_i^2} \quad \frac{d_i^2}{4r^2} + 1 \quad = P(9.516)$$

$$\sigma_{\theta\theta} = 526,100 \text{ psi}$$

APPENDIX B

A THEORETICAL CALCULATION OF THE BUCKLING TENDENCIES IN THE SPECIMEN

The circumferential buckling characteristics of the test specimen subjected to external fluid pressure are dependent upon its geometry and the elastic constants of the alumina ceramic. The basic dimensions of the one inch test section specimen are shown in Figure 71. As will be seen below, this one inch test section specimen will buckle at lower pressures than the one half inch test section specimen because it contains a greater length of minimum wall thickness section. The elastic constants of the alumina specimen material as reported by Sedlacek appear in Table I.

For a cylinder of the dimensions shown in Figure 71 little information concerning the circumferential buckling behavior is available in recent literature. Most of the studies are concerned with cylinders where the value of the diameter-thickness ratio $D/t \approx 100$ i.e. for very thin wall pressure vessels. It is necessary to go back to the work of Southwell, von Mises, Flüegge and Timoshenko which are fundamental to the more recent studies. Most of these early results can be found in the Handbook of Elastic Stability.[72]

Most recent investigations are extensions of the work of von Mises[73] which is closely approximated by the more intricate and later results of Flüegge.[74] Their expressions for critical (at the onset of buckling) uniform lateral pressure, with no axial stress, have been discussed by Timoshenko.[75] The successful use of the expressions depends on a correct determination of the buckling mode, i.e. the number of lobes formed

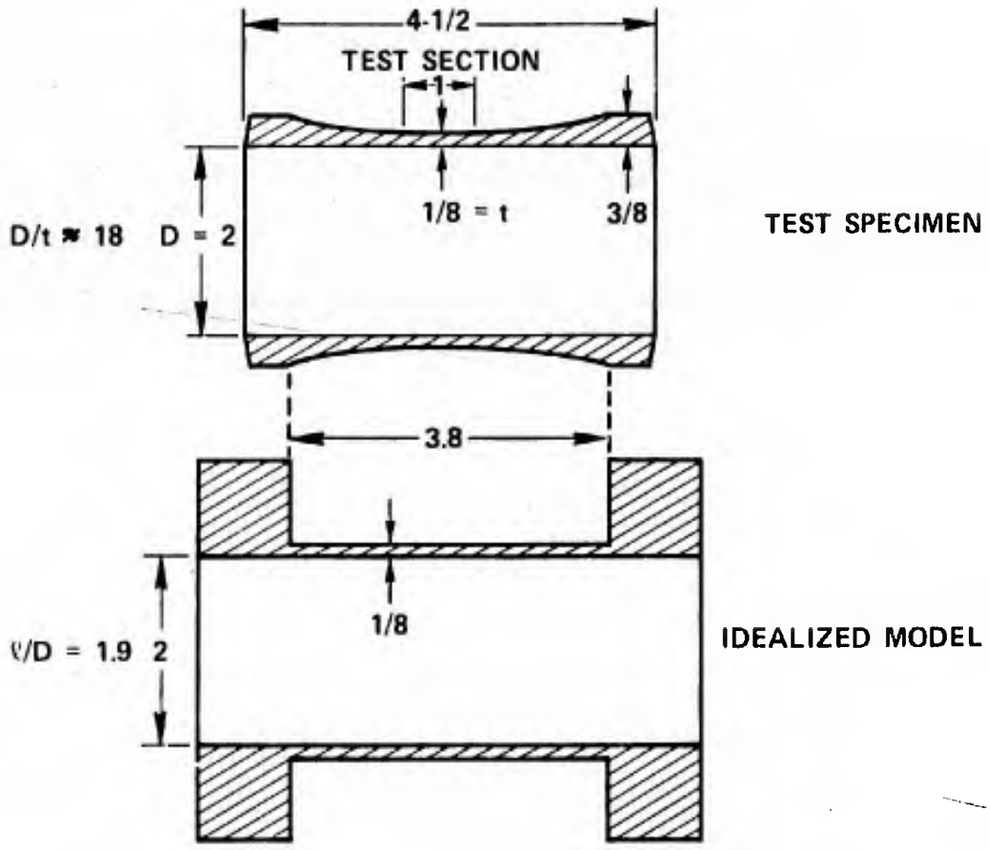

Figure 71. Model for Specimen Buckling.

during buckling deformation. The von Mises results are considered to be invalid for ratios of ℓ/D less than 14, which includes the idealized model of our specimen where ℓ/D 1.9. Southwell[23] describes the external critical buckling pressure in terms of the number of circumferential lobes which are formed prior to failure and assumes a perfectly round end constraint of the tube.

Southwell's equation for the critical external buckling pressure (P_c) for a tube with uniform radial load and no axial load, constrained at the ends to remain perfectly circular, is:

$$P_c = 2E \frac{t}{a} \left[\frac{q^4}{k^4(K^2-1)} + \frac{1}{3} \frac{m^2}{(m^2-1)} (k^2-1) \frac{t^2}{a^2} \right] \qquad (1B)$$

where: P_c = external hydrostatic pressure

$2t$ = wall thickness

a = mean radius

$m = \frac{1}{\nu} = \frac{1}{0.28} = 3.57$

k = number of lobes or nodes in the buckling mode distortion

$q = \frac{\pi a}{\ell}$ where ℓ = length of tube

E = Young's modulus = 53.6×10^6 psi

The difficulty in applying this equation to the analysis of the tapered specimen, which has a gradually reducing wall thickness ending in a minimum wall thickness in the test section, lies in choosing a length (ℓ) for the idealized cylindrical model which represents, in the real specimen, the point at which the diameter is constrained to be perfectly circular by the increased wall thickness. To demonstrate the effect of

the choice of (ℓ) on the critical buckling pressure (P_c) we plot P_c versus ℓ for the above equation, always choosing k to be the value which yields the lowest P_c (see Figure 72).

If we choose an idealized specimen length of 3.0 inches, the critical buckling pressure is seen to be 80,000 psi. This length in the specimen represents the point at which the wall thickness is twice that in the gage section (i.e. 0.250 inches as compared to 0.125 inches). At this wall thickness the moment of inertia (I) of the wall increases 8 times over the (I) in the test section and consequently this portion of the tube is 8 times more resistant to any lateral deformation causing it to go out of round. (See Figure 72.) Probably the force required to constrain the specimen to be round is rather small. The value of 8 times the resistance to out-of-round deformation at the specimen length of 3.0 inches is felt to be a conservative estimate. In addition the idealized model does not include the additional resistance to such deformation arising from the fact that outside the test section the wall thickness is constantly increasing from 0.125 to the value of 0.250 inches at a length of 3.0 inches. It is felt that this value of ℓ = 3.0 inches is a good approximation to perfect end constraint and demonstrates that the specimen did not buckle since all failure pressures were less than 62,000 psi.

The very accurate machining of these specimens and the excellent surface finish, permits the application of this theoretical analysis to the specimens without a "knock-down" factor for geometrical imperfection.

The above discussion has not considered the critical pressure required for buckling under the condition of axial load combined with

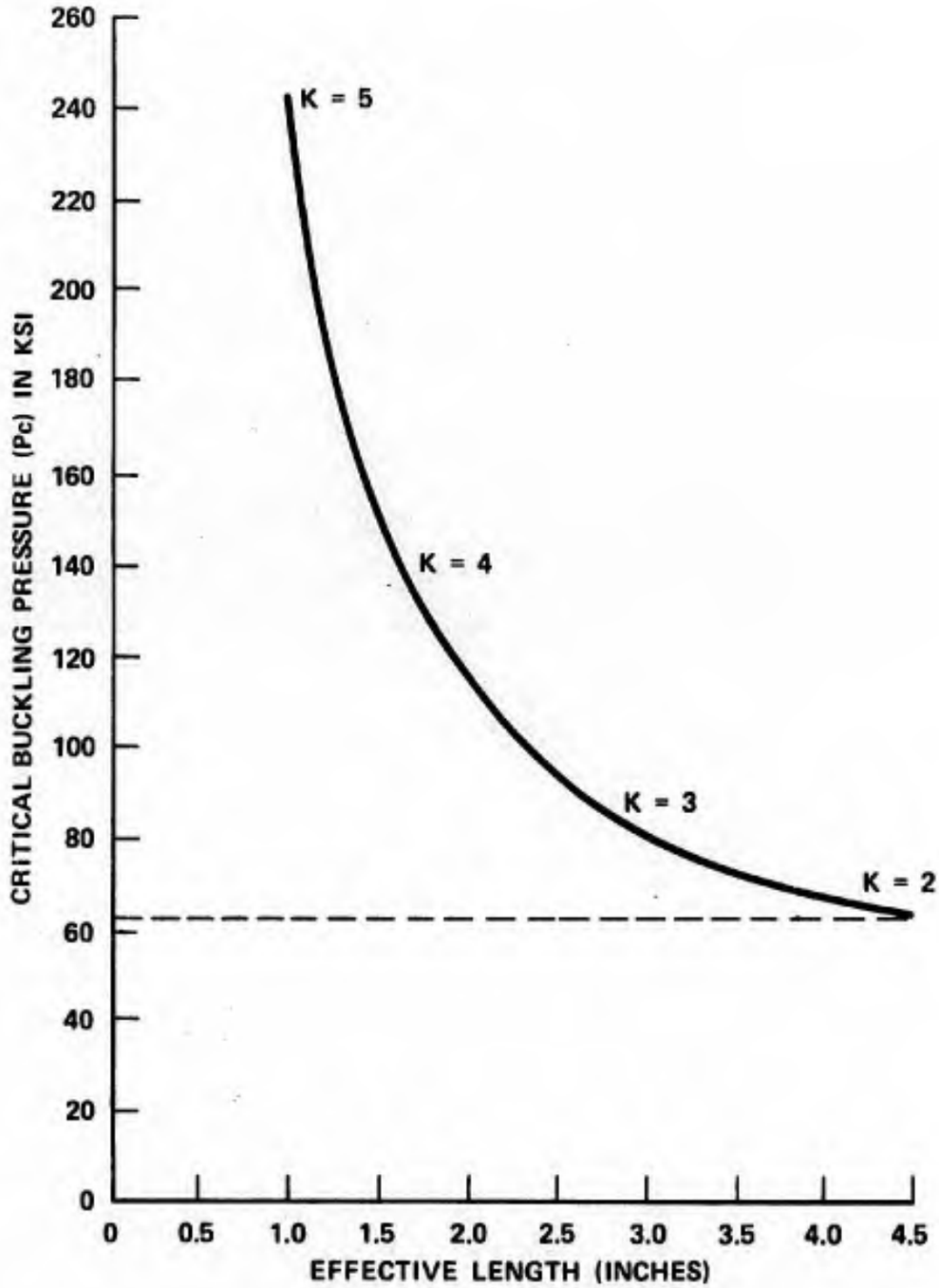

Figure 72. Buckling Pressure versus Effective Specimen Length.

circumferential pressure around the tube. Southwell stated the general relationship between the critical circumferential pressure (P_c) required for buckling and the compressive, axial end load (L) is as follows:

$$P_c = \left[1 - \frac{L}{L_c}\right] P_c^* \qquad (2B)$$

Where P_c^* and L_c are the values of the external surrounding pressure and end load, respectively, each of which would produce collapse of the specimen into the assumed type of buckling distortion if acting alone. L_c is on the order of 4.0×10^6 psi for the specimen tube modelled as containing a 1/8 inch wall over its entire length. The worst case for axial load assisted buckling would occur in the 1:1 biaxial compression test where $L \approx 5.0 \times 10^5$ psi. Remembering that $P_c^* \approx 8.0 \times 10^4$ ksi we may substitute into Equation (2B) the values:

$$P_c^{1:1} = \left[1 - \frac{5.0 \times 10^5}{4.0 \times 10^6}\right] \left[8.0 \times 10^4\right]$$

$$P_c^{1:1} = 7.0 \times 10^4 \text{ psi}$$

It is seen that the critical buckling pressure is reduced 12% to 70,000 psi in the worst case of biaxial loading, the 1:1 test. This means the specimen should not buckle even under the worst conditions of combined axial and circumferential pressure loads.

APPENDIX C

FURTHER EXTENSION OF A CRACK

ALIGNED WITH THE DIRECTION OF APPLIED STRESS

The expression for the stress at the surface of an open, elliptical crack which is tangent to the surface of the crack (see Figure 73(a)) is given by Timoshenko and Goddier[76] for elliptical coordinates ξ, η as:

$$(\sigma_\eta)_{\xi=\xi_o} = S\left[\frac{\sinh 2\xi_o + \cos 2\beta - e^{2\xi_o}\cos 2(\beta-\eta)}{\cosh 2\xi_o - \cos 2\eta}\right] \qquad (1C)$$

If the major axis of the crack is aligned with the direction of applied stress S (see Figure 73(b)) then $\beta = 0$ and the above expression reduces to:

$$(\sigma_\eta)_{\xi=\xi_o} = S\left[\frac{\sinh 2\xi_o + 1 - e^{2\xi_o}\cos(-2\eta)}{\cosh 2\xi_o - \cos 2\eta}\right] \qquad (2C)$$

At the end of the major axis $\cosh \eta = 1$ and the value of (σ_η) here is:

$$(\sigma_\eta)_{\substack{\xi=\xi_o \\ \beta=0 \\ \eta=0}} = S\left[\frac{\sinh 2\xi_o + 1 - e^{2\xi_o}}{\cosh 2\xi_o - 1}\right] \qquad (3C)$$

From the equation of an ellipse it can be seen that:

$$\sinh 2\xi_o = \frac{2ab}{c^2}$$

$$\cosh 2\xi_o = \frac{a^2+b^2}{c^2}$$

$$e^{2\xi_o} = \frac{(a+b)^2}{c^2}$$

Substituting these into expression (3c) one obtains:

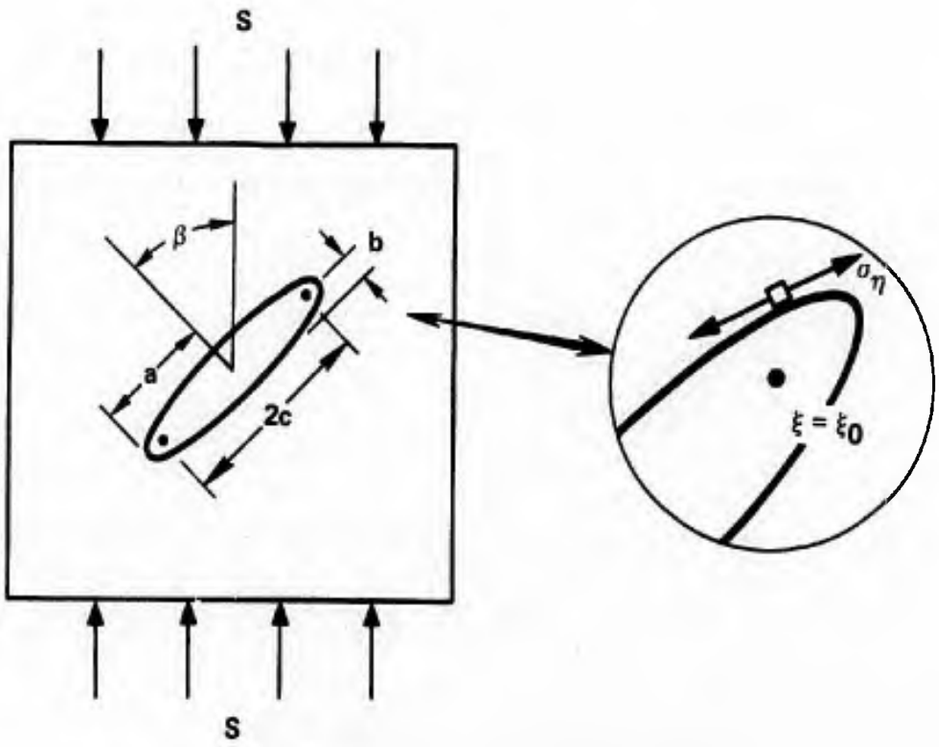

(a) DESCRIPTION OF ELLIPTICAL CRACK

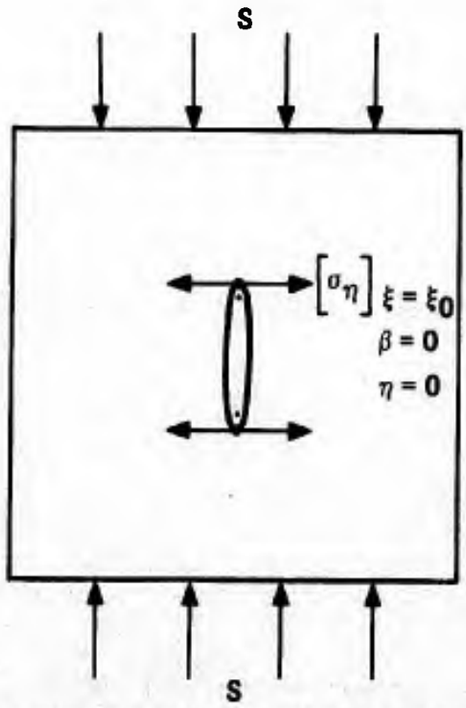

(b) ALIGNED ELLIPTICAL CRACK TIP STRESS

Figure 73. Stress at Tip of Elliptical Crack.

$$\sigma_\eta = S\left[\frac{\frac{2ab}{c^2} + 1 - \frac{(a+b)^2}{c^2}}{\left(\frac{a^2+b^2}{c^2}\right) - 1}\right] \qquad (4C)$$

reducing:

$$\sigma_\eta = S\left[\frac{-a^2-b^2+c^2}{a^2+b^2-c^2}\right] = -S \qquad (5C)$$

For any semi-major and semi-minor axis, a and b, of the ellipse the stress σ_η at the tip of the aligned ellipse is equal to the applied stress S and of opposite sign. As the ratio of a/b becomes very large the extend of the region over which -S acts at the crack tip becomes infinitesimally small.

Regardless of the length or tip radius of a crack or flaw which is aligned with the direction of an applied uniaxial compression, a tensile stress equal in magnitude to the applied compression is present at the tip. In the alumina tested in this study such tensile stresses reached magnitudes in excess of 500 ksi. This value is only one tenth the theoretical tensile strength of the alumina. The very localized nature of the aligned crack tip tensile stress prohibits the concentration of such a stress by any flaws except those in very close proximity to the crack tip. Interaction with such a close by flaw would only extend the aligned crack a short distance. For unstable crack propagation to occur the applied compression would have to equal the theoretical tensile strength; at that level of applied load the crack would continue to extend without the necessity for interaction with any other flaws. Under biaxial or triaxial compressive loading the transverse compressions

which would be concentrated by the aligned crack would easily cancel the tension developed for most orientations of the crack. This would not be the case for an extended crack near the inside surface of the test specimen which was aligned to the plane formed by the $\hat{\theta}$ - $\hat{Z}$ principal stress directions.

APPENDIX D

THE RATIO OF COMPRESSIVE STRENGTH TO TENSILE STRENGTH FOR VERY STRONG BRITTLE MATERIALS

The Griffith theory predicts a ratio of compressive to tensile strength of eight for brittle materials in which the strength controlling mechanism is catastrophic crack propagation from open flaws. The McClintock-Walsh theory predicts a ratio of between four and about ten for closed flaws which have sliding faces. The observed ratios of compressive to tensile strength for high density, high purity brittle materials such as alumina, silicon nitride or silicon carbide range between eight and 18. The data of this study for alumina give a ratio $\sigma_c/\sigma_t \approx 18$. There is great difficulty in determining this ratio exactly since the value of tensile strength is much smaller than the compressive strength and there are many experimental problems in precisely establishing this value. Difficulties in obtaining a pure, uniform stress state in the tension test, static fatigue, and sensitivity to surface damage are some of the factors which complicate tensile strength measurements. It appears that the tensile strength is also sensitive to the method of fabrication of the body which affects the grain size and the residual stresses that are present in the fabricated material.

The value of the residual tensile stresses in the material, if considered to act on a macroscopic scale, will have little effect on the measured compressive strength but can greatly affect the measured tensile strength. Alumina is a trigonal crystal which has a linear thermal expansion coefficient[77] in the plane perpendicular to the c-axis

$\alpha_a = 8.22 \times 10^{-6}\ ^oC^{-1}$ which is smaller than in the direction parallel to the, c-axis $\alpha_c = 9.08 \times 10^{-6}\ ^oC^{-1}$. Wachtman[78] has given results describing the residual stresses which develop around a grain of alumina on cooling from the sintering temperature to room temperature because of the differences in the thermal expansion coefficients. He modeled the grains surrounding the grain under consideration as an isotropic matrix which possesses an average value of thermal expansion with the grain itself considered to be a spherical center of dilation. This model predicts that grains near the surface will develop five times the residual stress of grains deep within the interior. For the alumina considered, surface grains will develop residual tensile stresses of at least 20 to 30 ksi.

Assuming that the residual tensile stresses in the grains of fabricated alumina are 30 ksi, the measured tensile strength will be less than the residual stress free material strength by this amount. If the true tensile strength is 60 ksi which gives a $\sigma_c/\sigma_t \approx 9$, then the measured tensile strength with the residual stresses present will be:

$$\sigma_t(\text{measured}) = \sigma_t(\text{free of residual stresses}) - \sigma_R(\text{residual stress})$$
$$= 60 \text{ ksi} - 30 \text{ ksi} = 30 \text{ ksi}$$

If the residual stress free compressive strength is 560 ksi, the measured compressive strength in a triaxial stress state where $|\sigma_3|$ is greater than $|\sigma_1|$ and $|\sigma_2|$ with residual stress present will be:

$$\sigma_c(\text{measured}) = 560 \text{ ksi} - 30 \text{ ksi} = 530 \text{ ksi}$$

The values of the measured strengths given in the example are approximately those measured in this study where σ_c/σ_t was found to be approximately 18. If the residual stresses were removed from the material

perhaps the σ_c/σ_t ratio would reduce to 9. It can now be appreciated that the statement of when cracks begin to extend from flaws in alumina must be made carefully. The present study shows that crack extension begins in alumina, under compression, at a stress:

$$\sigma_c(\text{crack extension}) \approx 4\ \sigma_t(\text{measured})$$

The above discussion has concerned itself only with a macroscopic continuum approach to a consideration of the effect of residual stresses. This approach has treated the residual stresses as though they produced a hydrostatic tension in the body. On a level of single grain cracking where the stress intensification around flaws of the order of the grain size is being considered, the action of the localized, directed, residual tensile stress in assisting crack initiation and extension is not entire entirely clear.

A residual tensile stress acting in the localized region around a flaw and normal to the flaw plane will be intensified by the flaw. This intensified stress will be additive to the local tension produced by the applied compressive stress acting on the flaw. (See Figure 74.) In this small microscopic region of the flaw the residual stress will act as an applied tension on the flaw, greatly reducing the applied compression necessary for crack initiation. However, when the crack extends out of the local residual tensile stress region, the local intensified tension at its tip will result only from the applied compression and this will be insufficient to continue extension of the crack. If the applied stress is tensile, the short, initial, residual stress assisted extension of the crack may be sufficient to raise the stress concentration factor of the flaw-extended crack configuration sufficiently to

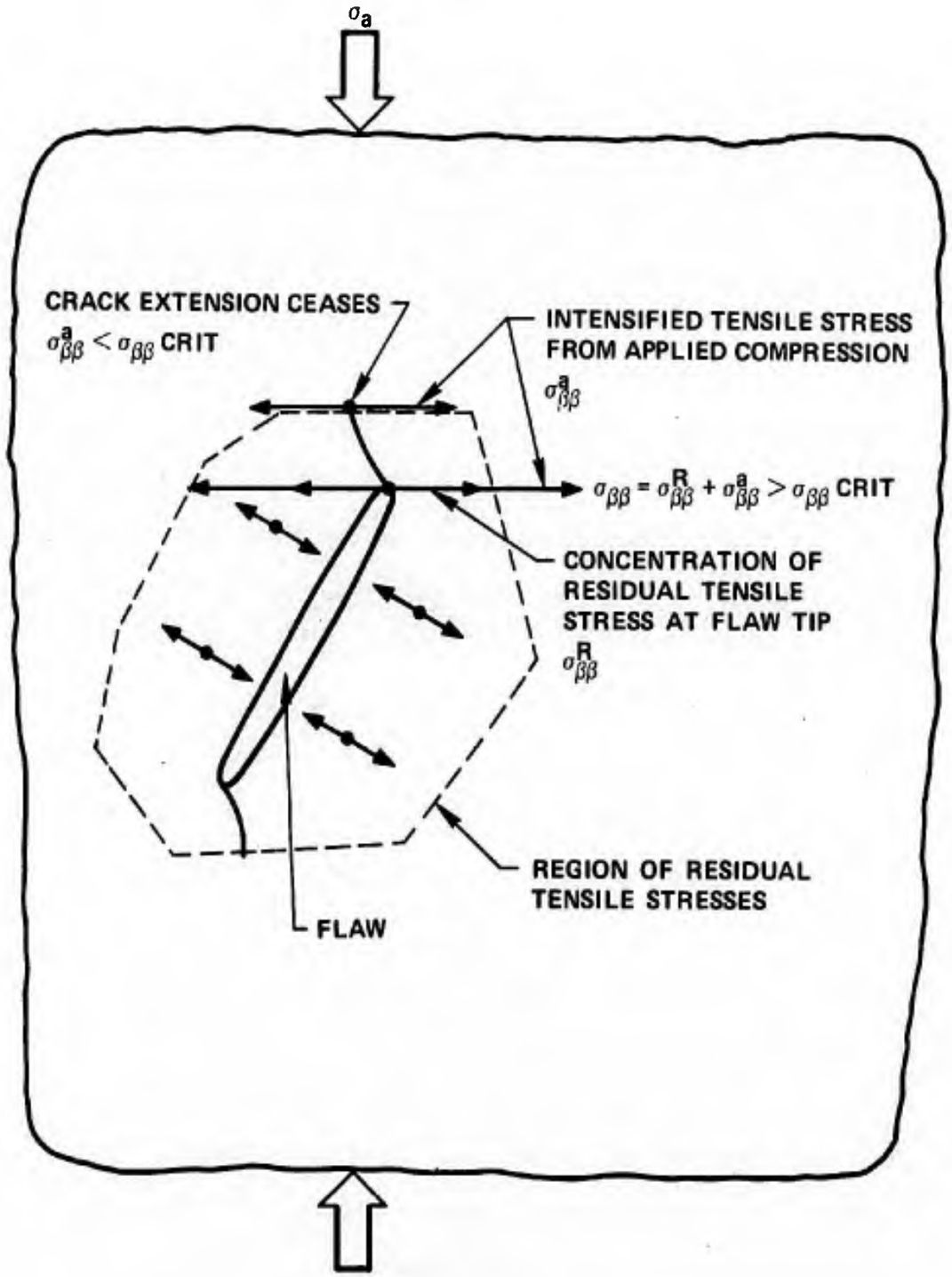

Figure 74. Residual Stress Assisted Crack Extension.

allow the applied tension to cause further unstable extension resulting in failure. Individual flaw-grain configurations must be considered when modeling this process and the anisotropy of the elastic constants of the crystal will be important to such an analysis.

Microscopic residual tensile stresses may result in a direct lowering of the applied tensile stress necessary to unstably extend a crack from a flaw or may produce stable extended cracks in the body if the extended crack length is insufficient to become unstable under the applied tension. Even under this latter condition the body will contain larger flaws which would result in a statistically lower strength. Under applied compressions the relationship is not as simple. The microscopic residual tensile stresses will cause a greater number of flaws to extend cracks since the local tensile stresses will be higher around smaller flaws and flaws of less severe orientation. This crack extension will only be on the order of the grain size. Much greater applied compressions would be needed for further extension. Thus, in compression, residual tensile stresses would result in a greater amount of damage being produced in the body at any applied stress level. The nature of the relationship of this damage level to the stress level required for structural collapse of the body is complex.

APPENDIX E

THE BUCKLING OF THIN PLATES

Timoshenko[75] has treated the buckling of thin plates under the action of several kinds of applied tractions and for several edge constraint conditions. Since the nature and properties of the micro-plate which buckles out of the specimen is variable and can only be approximately defined, a discussion is given here which outlines the range of behavior of plate buckling that includes the types of plates occurring in the specimen. The critical buckling stresses (S_{crit}) are calculated for thin isotropic, elastic plate models. Uniaxial and biaxial applied compressions are considered on plates with simply supported and clamped edges. Plates with simply supported edges are the easiest to buckle and represent the lower limits of S_{crit}. Plates with clamped edges are the most difficult to buckle and represent the upper limits of S_{crit}. The buckling behavior of the plates is examined with respect to the thickness to length ratio (t/L) and the length to width ratio (L/W). The plate being considered is described in Figure 75. Uniform compressions S_1 and S_2 are applied to opposite edges of the plate where S_1 is identified with $\sigma_{\theta\theta}$ in the body of the specimen and S_2 with σ_{zz}.

Case 1: Simply supported rectangular rectangular plate subjected to uniaxial compression, $S_1 = S$ and $S_2 = 0$.

The expression for the critical stress (S_{crit}) to produce elastic instability of the plate is:

$$S_{crit} = \frac{\pi^2 D}{t L^2}\left(m + \frac{1}{m}\frac{L^2}{W^2}\right)^2 \qquad (1E)$$

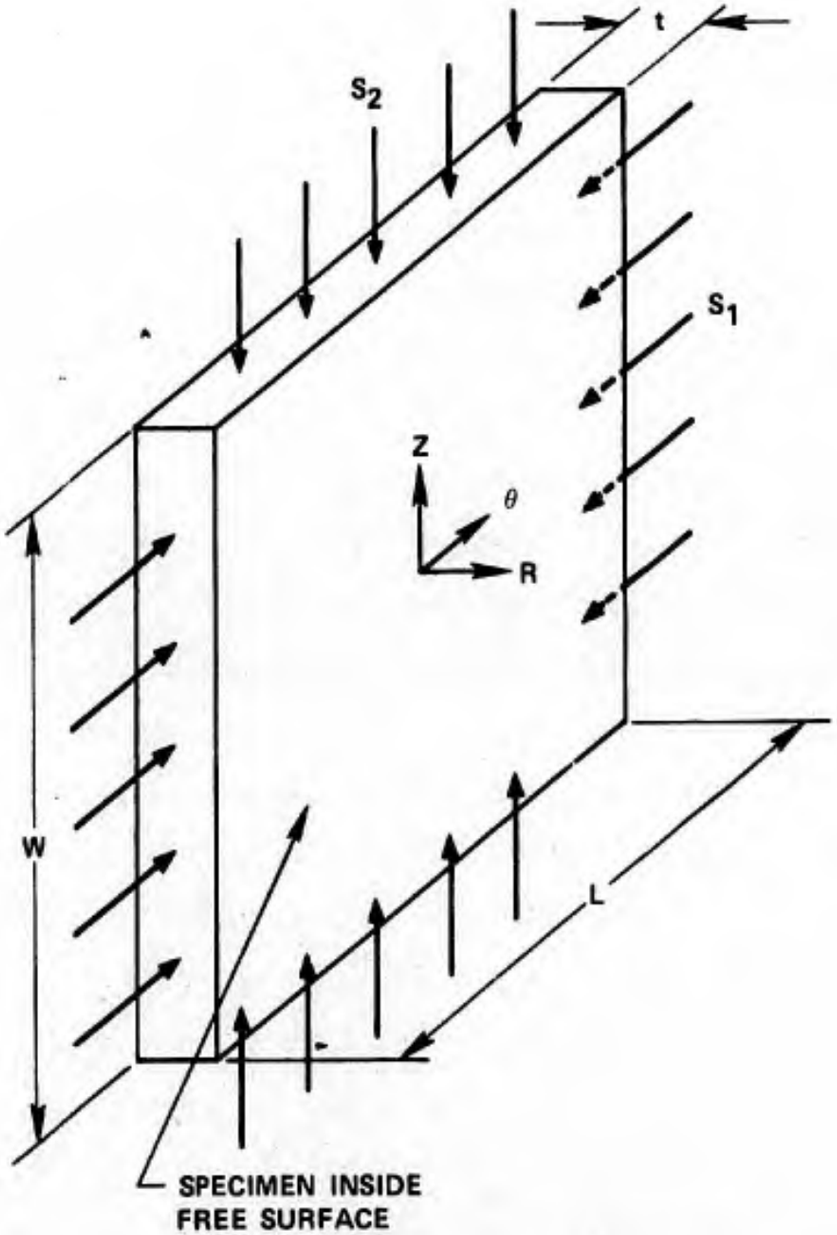

Figure 75. Model Plate for Analysis of Micro-Plate Buckling.

Where:

$$D = \frac{Et^3}{12(1-\nu^2)} \equiv \text{Flexural Rigidity}$$

$E \equiv$ Young's modules = 53.6×10^6 for WESGO AL-995 Alumina

$\nu \equiv$ Poisson's ratio = 0.26 for WESGO AL-995 (average value in compression)

$m \equiv$ Number of half-waves into which the plate buckles along the $\hat{\theta}$ direction

The first factor in Equation (1E) is the critical Euler column stress for a unit width strip of length (L) while the second factor indicates the proportionately greater stability of a continuous plate over the isolated strip. Because the body of the specimen prevents any displacement of the plate into the wall thickness (i.e. - δr displacements of the plate faces are prohibited), only + δr displacements are possible and m must equal one. The plate can only buckle in the one-half wave or first mode. The expression for the critical stress with m = 1 is given by Timoshenko as:

$$S_{crit} = \frac{\pi^2 D}{t W^2}\left(\frac{W}{L} + \frac{L}{W}\right)^2 \qquad (2E)$$

From this expression it may be seen that S_{crit} is at the minimum when the plate is square, L = W. For other proportions of the plate this expression may be generalized as:

$$S_{crit} = K\frac{\pi^2 D}{t W^2} \qquad (3E)$$

in which K is a numerical factor depending on the L/W ratio. A plot of the critical K values for Equation (3E) is given in Figure 76. Since m can only equal one, it is seen that as the proportions of the plate

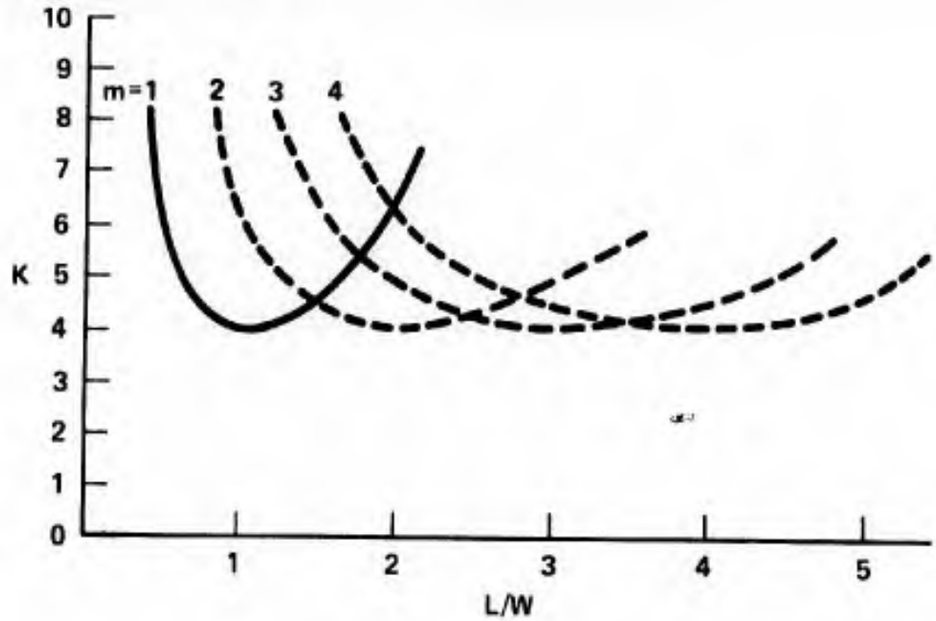

Figure 76. K Factor for Plate Buckling.

change from that of a square, K and hence S_{crit} increase. The two parameters which effect the value of S_{crit} are (L/W) and (L/t); when L/W approaches one and/or L/t becomes larger the value of S_{crit} decreases. The magnitude of the effect of these factors may be seen by inspection of Figures 76 and 77, respectively. Figure 77 is a plot of S_{crit} versus t/L for a square plate using the elastic constants for bulk alumina:

$$S_{crit} = \frac{4\pi^2 D}{t W^2} = 1.89 \times 10^8 \left(\frac{t}{W}\right)^2 \qquad \text{where: } L = W \tag{4E}$$

The combined effect of the two factors may be seen by expressing S_{crit} as a function of both:

$$S_{crit} = \frac{K}{K_{\frac{L}{W}=1}} 1.89 \times 10^8 \left(\frac{t}{W}\right)^2 = 4.73 \times 10^7 K \left(\frac{t}{W}\right)^2 \tag{5E}$$

where K is obtained from Figure 76. A general rule for the buckling mode of a plate is that it subdivides approximately into squares; however, this behavior is not possible in our case for plates with L/W much different than one since m must equal one.

Case 2: Simply supported rectangular plate compressed in two perpendicular directions.

The critical values of the two in-plane compression stresses necessary to cause buckling of the simply supported plate are given by the expression:

$$S_1 m^2 + S_2 n^2 \frac{L^2}{W^2} = S_o \left(m^2 + n^2 \frac{L^2}{W^2}\right)^2 \tag{6E}$$

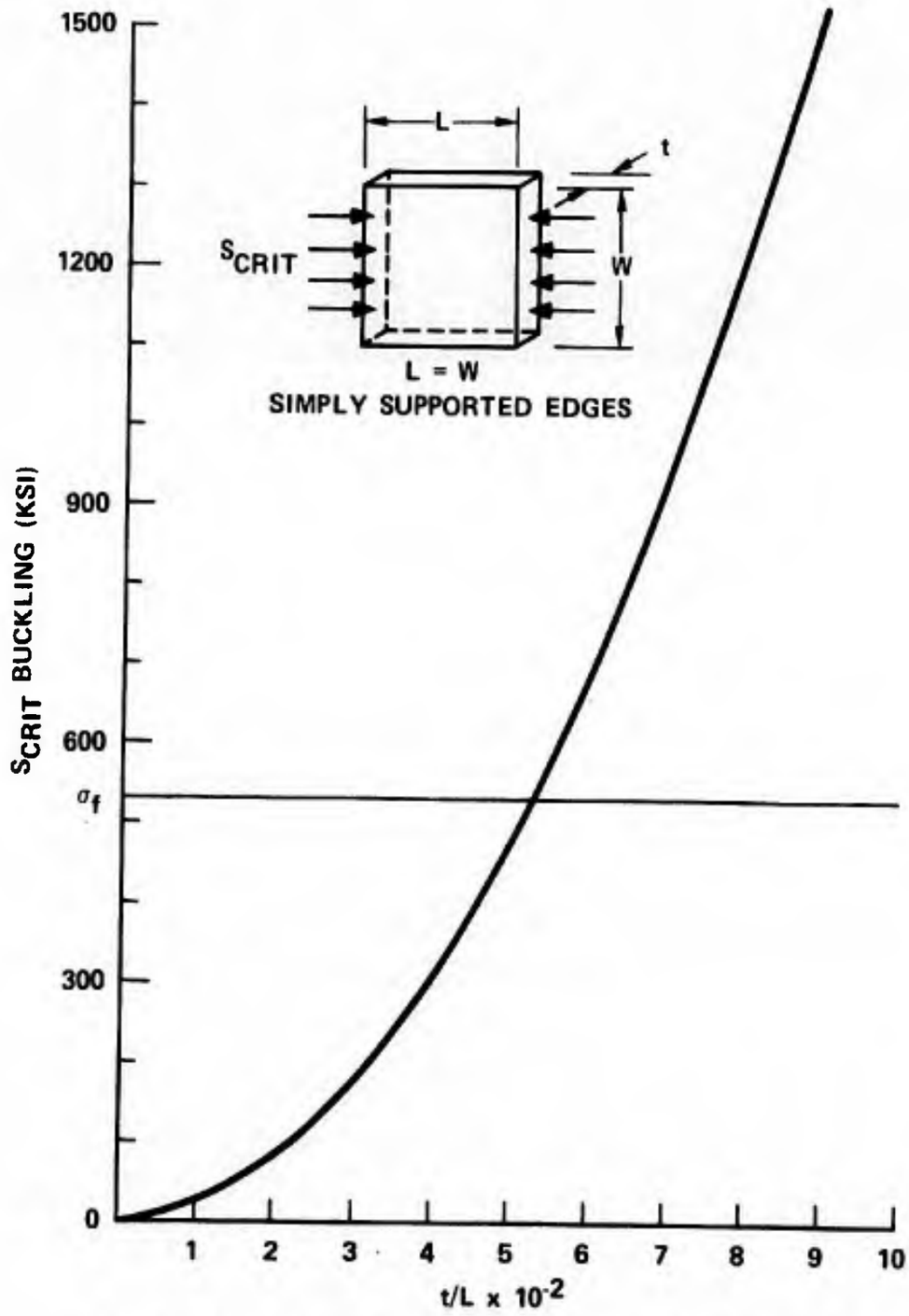

Figure 77. Critical Buckling Stresses for Simply Supported Plate Subjected to Uniaxial Load.

where:

$$S_o \equiv \frac{\pi^2 D}{L^2 t}$$

$m \equiv$ number of half-waves in $\hat{\theta}$ direction.

$n \equiv$ number of half-waves in $\hat{z}$ direction.

As for Case 1, m and n can only equal one because of geometric restriction and Equation (6E) reduces to:

$$S_1 + S_2 \alpha = S_o(1+\alpha)^2 \tag{7E}$$

where:

$$\alpha \equiv \left(\frac{L}{W}\right)^2$$

rearranging:

$$S_2 = \left(-\frac{1}{\alpha}\right) S_1 + S_o \frac{(1+\alpha)^2}{\alpha} \tag{8E}$$

This is the equation of a straight line with slope $\left(-\frac{1}{\alpha}\right)$ and y-intercept $\left[S_o \frac{(1+\alpha)^2}{\alpha}\right]$. For any of the test stress states employed in this study $S_1 \geq S_2$ and the ratio of $S_1:S_2$ was a constant at any stress level during the test. Solutions for the critical buckling stress $S_{crit} = S_1$ in any stress state may be found by solving Equation (8E) for the appropriate values of S_1 and S_2. If Equation (8E) is plotted on S_1, S_2 coordinates with units of S_o, the intersection of constant $S_1:S_2$ lines with the equation lines yield the curves of Figure 78. Figure 78 plots $\left[S_{crit}/S_o = A\right]$ versus $\left[L/W\right]$ from which S_{crit} may be found for a given $S_1:S_2$ and L/W by multiplication of the ordinate (A) of the point by S_o. The expression for S_{crit} is then:

$$S_{crit} = S_o A = \frac{\pi^2 D}{L^2 t} A = 4.72 \left(\frac{t}{L}\right)^2 A \tag{9E}$$

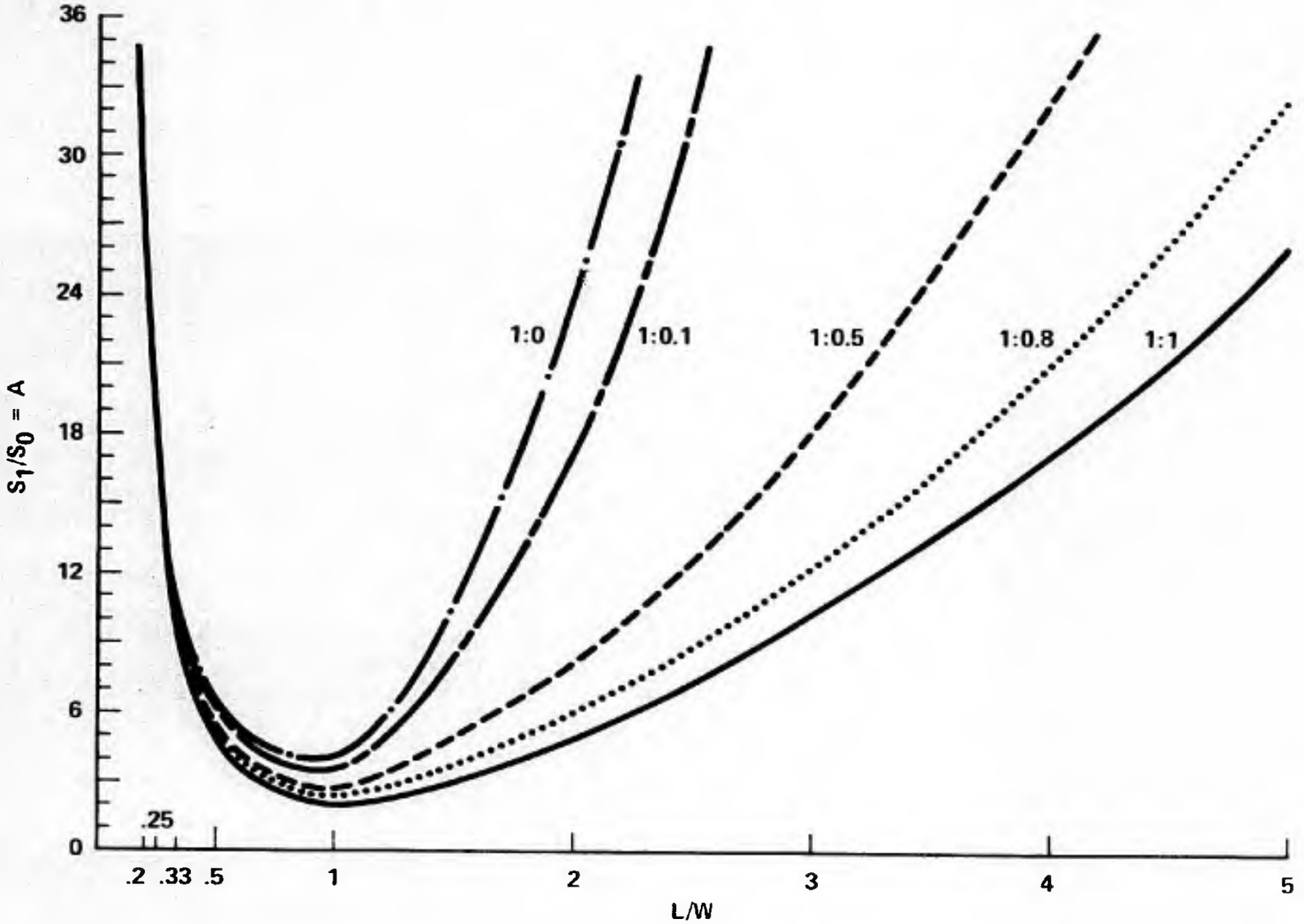

Figure 78. L/W versus A.

The S_{crit} dependence on the shape of the plate (L/W) for various stress states may be seen from Figure 79. In uniaxial compression (1:0) it becomes very difficult to buckle a plate as the plate shape departs from square. It becomes increasingly easier to buckle rectangular plates of any (L/W) as the second applied compression S_2 approaches the magnitude of S_1. For a constant (t/L) plates with a much larger range of (L/W) will buckle in biaxial compression as compared to uniaxial for a given magnitude of applied stress.

Case 3: A rectangular plate with clamped edges subjected to compression in two perpendicular directions.

This solution is only approximate and is most accurate when the plate shape is square and the two applied stresses S_1 and S_2 are equal. This model is a good representation of a plate formed by a totally internal crack surface which does not extend to the free inside specimen surface. The critical values of the applied compressive stresses may be calculated from:

$$\left(S_1 + \frac{L^2}{W^2} S_2\right)_{crit} = \frac{4}{3} \frac{\pi^2 D L^2}{t} \left(\frac{3}{L^4} + \frac{3}{W^4} + \frac{2}{L^2 W^2}\right) \qquad (10E)$$

Because of the approximate nature of this expression, a detailed analysis of plate shape is not warranted; we will look at the effect of (t/L) and various ratios of stress. If L = W and $S_1 = S_2$ the equation reduces to:

$$S_{crit} = 5.33 \frac{\pi^2 D}{L^2 t} = 2.52 \times 10^8 \left(\frac{t}{L}\right)^2 \qquad (11E)$$

For L = W but $S_1 \neq S_2$ equation can be reduced to:

$$(S_1 + S_2)_{crit} = \frac{10.67 \pi^2 D}{L^2 t} = 5.05 \times 10^8 \left(\frac{t}{L}\right)^2 \qquad (12E)$$

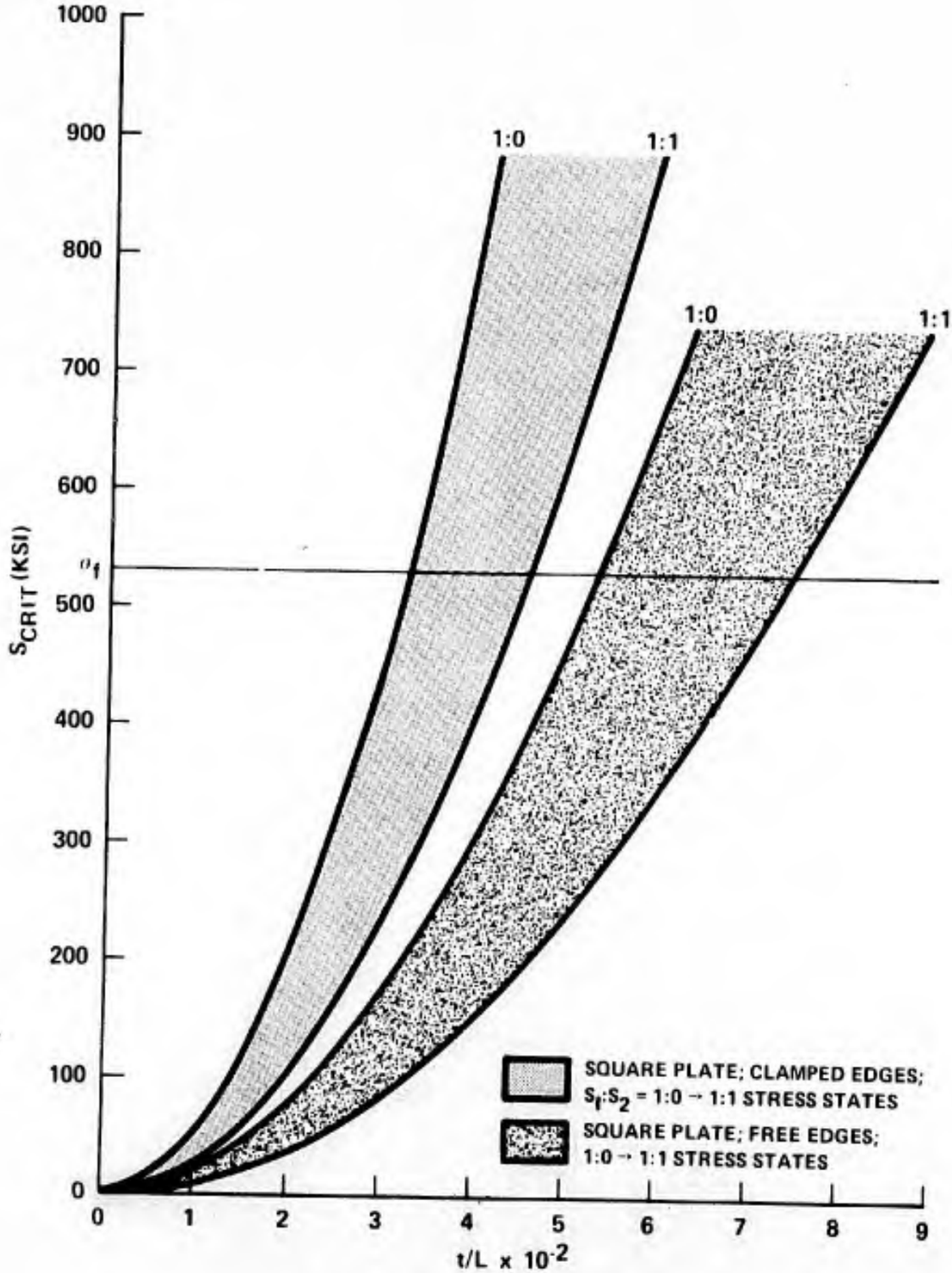

Figure 79. The Buckling Behavior of Various Plates.

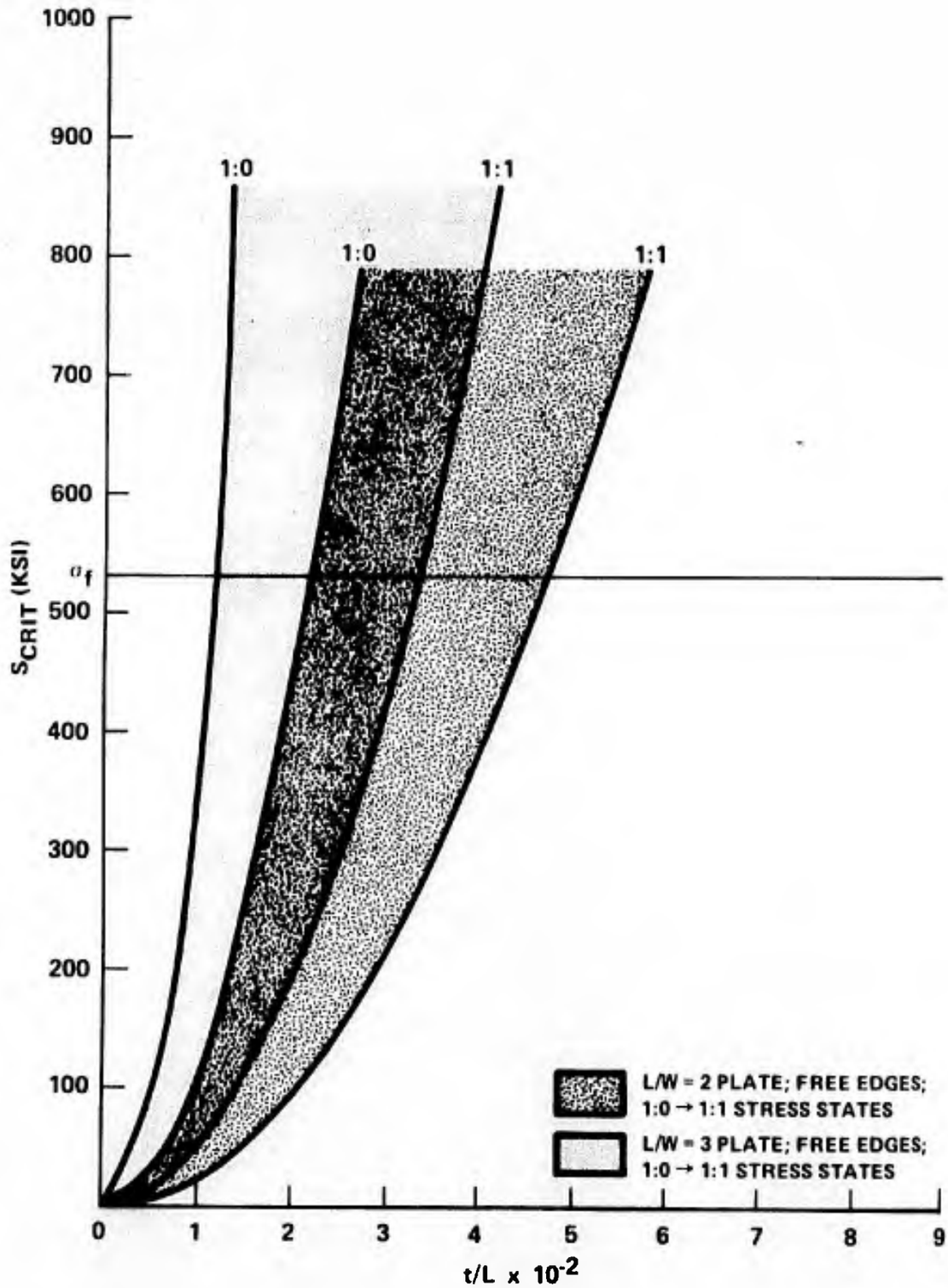

Figure 79. (Continued)

The envelope of curves for S_{crit} between $S_1 = S_2$ and $S_1 = S_{crit}$; $S_2 = 0$ as a function of (t/L) is plotted in Figure 79. The interesting aspect of this envelope of curves is the small dispersion produced in the critical (t/L) dimension with a change in stress state from uniaxial compression 1:0 to equibiaxial compression 1:1.

A comparison of S_{crit} for the three cases considered assuming L = W shows:

Case 1: $S_1 = S$; $S_2 = 0$; simply supported edges: $S_{crit}^{1:0} = 4S_o$

Case 2: $S_1 = S_2 = S$; simply supported edges: $S_{crit}^{1:1} = 2S_o$

Case 3: $S_1 = S_2$; clamped edges: $S_{crit}^{1:1} = 5.3S_o$

Figure 77 summarizes the S_{crit} versus t/L behavior for the various plates discussed with the parameters L/W and stress state considered. This shows that plates will buckle out when their t/L ratios are less than about 1/15. Plates buckle easiest under equi-biaxial compression. Buckling requires higher stresses as S_2 becomes a smaller proportion of S_1 and also as the L/W ratio becomes greater or less than unity. A plate with "built-in" edges requires almost three times as large a buckling stress as a free edge plate.

Distribution List for Contract No. N00019-73-C-0294 Mod. P00004

		No. of Copies
1.	AIR-52032, Naval Air Systems Command Washington, D. C. 20361	4
2.	Naval Air Systems Command Washington, D.C. 20361 Attn: AIR-954	10
3.	Office of Naval Research Washington D.C. 20361 Attn: Code 471	1
4.	Naval Ordnance Laboratory White Oak, Maryland 20910 Attn: Codes 2301 and 234	2
5.	Ceramic Finishing Company Box 498 State College, Pennsylvania 16801	1
6.	Materials Sciences & Engineering Laboratory Stanford Research Institute Menlo Park, California 94025	1
7.	Inorganic Materials Division Institute for Materials Research National Bureau of Standards Washington, D. C. 20234	2
8.	Naval Ship Engineering Center Washington, D. C. 20360 Attn: Code 6101E	1
9.	Battelle Memorial Institute 505 King Avenue Columbus, Ohio 43201	1
10.	Metals and Ceramics Information Center Battelle Memorial Institute 505 King Avenue Columbus, Ohio 43201	1
11.	IIT Research Institute 10 West 35th Street Chicago, Illinois 60616 Attn: Ceramics Division	1
12.	Naval Ship R & D Laboratory Annapolis, Maryland 21402	1

Distribution List for Contract No. N00019-73-C-0294 Mod. P00004

		No. of Copies
13.	SEA-035 Naval SEA Systems Command Washington, D. C. 20360	1
14.	Naval Ship Research and Development Center Washington, D. C. 20007 Attn: Code 725	1
15.	Naval Undersea R and D Center San Diego, California 92117	1
16.	Air Force Materials Laboratory Wright-Patterson Air Force Base Dayton, Ohio 45433 Attn: LMC 1 LAE 1 LMD 1 LAM 1 LMN 1 LY 1 LT 1	7
17.	Naval Research Laboratory Washington, D.C. 20390 Attn: Code 6360 1 Code 8430 2 Code 8437 1	3
18.	Atomic Energy Commission Technical Information Service P.O. Box 62 Oak Ridge, Tennessee 37830	1
19.	NASA Headquarters Washington, D. C. 20546 Attn: J.J. Gangler, RRM	1
20.	Marshall Space Flight Center Huntsville, Alabama 35812 Attn: D.W. Gates	1
21.	Lewis Research Center 21000 Brookpark Road Cleveland, Ohio 44135 Attn: Dr. Hubert Probst	1
22.	Goddard Space Flight Center Greenbelt, Maryland 20771 Attn: A.G. Eubanks	1
23.	Materials Sciences Laboratory Army Materials & Mechanics Research Center Watertown, Massachusetts 02172 Attn: Dr. Robert Katz	1
24.	Ordnance Research Laboratory Pennsylvania State University State College, Pennsylvania 16802	1

Distribution List for Contract No. N00019-73-C-0294 Mod. P00004

		No. of Copies
25.	Structure and Mechanics Laboratory Redstone Arsenal Huntsville, Alabama 35809	1
26.	PPG Industries Glass Research Center P.O. Box 11472 Pittsburgh, Pennsylvania 15238	1
27.	Department of Mineral Technology University of California Berkeley, California 94720	1
28.	A.C. Spark Plug Division General Motors Corporation Flint, Michigan 48556 Attn: Dr. Morris Berg	1
29.	Coors Procelain Company 600 Ninth Street Golden, Colorado 80401 Attn: Research Department	1
30.	Department of Metallurgy Massachusetts Institute of Technology Cambridge, Massachusetts 02139	1
31.	Materials Research Center Lehigh University Bethlehem, Pennsylvania 18015 Attn: Dr. D.P.H. Hasselman	1
32.	Department of Metallurgy Case-Western Reserve University Cleveland, Ohio 44106	1
33.	Midwest Research Institute 425 Volker Boulevard Kansas City, Missouri 64110	1
34.	Bell Aerosystems Company Buffalo, New York 14240 Attn: Materials Research & Structural Systems Dept.	1
35.	Department of Ceramic Engineering University of Utah Salt Lake City, Utah 84412	1
36.	Materials Sciences Laboratory United Aircraft Corporation East Hartford, Connecticut 06101	1

Distribution List for Contract No. N00019-73-C-0294 Mod. P00004

		No. of Copies
37.	Metallurgy and Ceramics Research Dept. General Electric R&D Laboratories P.O. Box 8 Schenectady, New York 12301	1
38.	Libbey-Owens-Ford Glass Company 811 Madison Avenue Toledo, Ohio 43600	1
39.	Engineering Experiment Station Georgia Institute of Technology Atlanta, Georgia 30332 Attn: J. D. Walton	1
40.	Materials Research Laboratory Pennsylvania State University University Park, Pennsylvania 16802 Attn: Prof. Rustum Roy	1
41.	Physical Properties Research Department Corning Glass Works Corning, New York 14832 Attn: Mr. Henry E. Hagy	1
42.	State University of New York College of Ceramics At Alfred University Alfred, New York 14802	1
43.	Raytheon Company Research Division 28 Seyon Street Waltham, Massachusetts 02154 Attn: Dr. J. Pappis	1
44.	Hughes Aircraft Company Aerospace Group R&D Division Culver City, California 90130	1
45.	McDonnell-Douglas Company Missile and Space Systems Division 3000 Ocean Park Boulevard Santa Monica, California 90405	1
46.	Space Sciences Laboratory General Electric Company P.O. Box 8555 Philadelphia, Pennsylvania 19101	1

Distribution List for Contract No. N00019-73-C-0294 Mod. P00004

		No. of Copies
47.	Research Library Research Institute University of Dayton Dayton, Ohio 45409	1
48.	Research Library Owens-Illinois Technical Center 1700 N. Westwood Avenue Toledo, Ohio 43607	1
49.	Westinghouse Research Labs Beulah Road Churchill Borough Pittsburgh, Pennsylvania 15235 Attn: Dr. Ray Bratton	1
50.	Dept. of Engineering Research North Carolina State University Raleigh North Carolina 27607 Attn: Dr. H. Palmour	1
51.	Battelle Memorial Institute Pacific Northwest Laboratory Richland, Washington 99352 Attn: T. Chikalla	1
52.	Dr. Peter Gielisse Materials Engineering University of Rhode Island Kingston, Rhode Island 02881	1
53.	Prof. W.A. Tiller Dept. of Materials Science Stanford University Palo Alto, California 94305	1
54.	University of Kentucky Department of Metallurgical Engineering Lexington, Kentucky 40506 Attn: Prof. M.H.Leipold	1
55.	Turbine Research Department Product Development Group Ford Motor Company 20000 Rotunda Drive Dearborn, Michigan 48121	1

Distribution List for Contract No. N00019-73-C-0294 Mod. P00004

		No. of Copies
56.	Aerospace Corporation Materials Laboratory P.O. Box 95085 Los Angeles, California 90045 Attn: Dr. R.C. Rossi	1
57.	U.S. Army Research Office Box CM, Duke Station Durham, North Carolina 27706 Attn: CRDARD	1
58.	Ceramics Division Sandia Corporation Albuquerque, New Mexico 87101	1
59.	Applied Technology Division AVCO Corporation Lowell Industrial Park Lowell, Massachusettts 01851	1
60.	Solar Division International Harvester Co. 2200 Pacific Highway San Diego, California 92112 Attn: Dr. A.G.Metcalfe	1
61.	North American Rockwell Science Center P.O. Box 1085 Thousand Oaks, California 91360	1
62.	Shock Dynamics Laboratory Department of Physics Washington State University Pullman, Washington 99163	1
63.	Department of Ceramic Engineering University of Illinois Urbana, Illinois 61801	1
64.	Dr. Robert J. McGrattan Chief of Ocean Science and Engineering General Dynamics Electric Boat Division Groton, Connecticut 06340	1
65.	Henry M. Demarest, Jr. Research Laboratory PPG Industries Creighton, Pennsylvania 15030	1

		No. of Copies
66.	Stanford Research Institute Menlo Park, California 94025 Attn: R. Sedlacek	1
67.	Dr. H. W. Babel Materials Research McDonnell-Douglas Huntington Beach, California	1
68.	Lloyd J. Breidenbach Bldg. 150 0/57-20 P.O. Box 504 Lockheed Missiles and Space Company Sunnyvale, California 94088	1
69.	Prof. Norbert J. Kreidl Department of Ceramic Engineering School of Mines and Metallurgy University of Missouri at Rolla Rolla, Missouri 65401	1
70.	Prof. L. Broutman Illinois Institute of Technology Chicago, Illinois 60616	1
71.	Prof. Ralph Barnett Illinois Institute of Technology Chicago, Illinois 60616	1
72.	Honeywell Research Center 500 Washington Avenue South Hopkins, Minnesota 55343 Attn: Dr. R. J. Stokes	1
73.	School of Ceramics Rutgers, The State University New Brunswick, New Jersey 08903	1
74.	TRW Systems One Space Park Redondo Beach California 90277 Attn: J. R. Bohn	1
75.	Southern Research Institute 2000 Ninth Avenue South Birminham, Alabama 35205	1
76.	Dr. John Ritter University of Massachusetts Amherst, Massachusetts 01002	

Distribution List for Contract No. N00019-73-C-0294 Mod. P00004

		No. of Copies
77.	Dr. E. van Reuth Advanced Research Projects Agency 1400 Wilson Boulevard Arlington, Virginia 22209	1
78.	SKF Industries, Inc. 1100 First Avenue King of Prussia, Pennsylvania 19406 Attn: Dr. Harish Dolal	1
79.	Detroit Diesel Allison Division General Motors Corporation P.O. Box 894 Indianapolis, Indiana 46202 Attn: Dr. M. Herman	1